DEVELOPMENT OF COMPUTATIONAL ALGORITHMS FOR DISPERSED TWO PHASE FLOW AND FLOW WITH COMPLEX INTERFACES

Thesis Submitted to the
Indian Institute of Technology Kharagpur
For award of the Degree

of

Doctor of Philosophy

by

Arup Kumar Das

Under the guidance of

Prof. Prasanta Kumar Das

DEPARTMENT OF MECHANICAL ENGINEERING
INDIAN INSTITUTE OF TECHNOLOGY KHARAGPUR
NOVEMBER 2009

Dedicated to

My Wife
&
My Sister

APPROVAL OF THE VIVA-VOCE BOARD

13/04/2010

Certified that the thesis entitled "**Development of computational algorithms for dispersed two phase flow and flow with complex interfaces**" submitted by **Arup Kumar Das** to the Indian Institute of Technology, Kharagpur, for the award of the degree Doctor of Philosophy has been accepted by the external examiners and that the student has successfully defended the thesis in the viva-voce examination held today.

Professor S. K. Som
Deptt. of Mech. Engg.
IIT Kharapur
(Member of the DSC)

Professor S. Roy
Deptt. of Mech. Engg.
IIT Kharapur
(Member of the DSC)

Professor S. K. Dash
Deptt. of Mech. Engg.
IIT Kharapur
(Member of the DSC)

Professor S. Chakraborty
Deptt. of Chem. Engg.
IIT Kharapur
(Member of the DSC)

Professor P. K. Das
Deptt. of Mech. Engg.
IIT Kharapur
(Supervisor)

Professor S. Sarkar
Deptt. of Mech. Engg.
IIT Kanpur
(External Examiner)

Professor A. K. Chattopadhyay
Deptt. of Mech. Engg.
IIT Kharapur
(Chairman)

INDIAN
INSTITUTE OF
TECHNOLOGY
KHARAGPUR-721302, INDIA

भारतीय
प्रौद्योगिकी
संस्थान
खड़गपुर

EPARTMENT OF MECHANICAL ENGINEERING

CERTIFICATE

This is to certify that the thesis entitled "**Development of computational algorithms for dispersed two phase flow and flow with complex interfaces**" submitted by Arup Kumar Das to Indian Institute of Technology, Kharagpur, is a record of bona fide research work under my supervision and I consider it worthy of consideration for the award of the degree of Doctor of Philosophy of the Institute.

Prof. Prasanta Kumar Das

Date: 15.04.2010

ACKNOWLEDGEMENT

I would like to express my immense gratitude to **Prof. Prasanta Kumar Das** of Department of Mechanical Engineering, IIT Kharagpur for providing me the opportunity to work under his able guidance. It has been a great opportunity of learning under his supervision because of the freedom he granted to me throughout my doctoral study. This work could not have been possible without his innovative problem definition, technical advice and continuous inspiration.

I could not have completed my doctoral study without the inspiration of my parents and my beloved sister. Whenever I felt depressed or faced any problem they were always beside me. Words can hardly acknowledge the support I received from them.

I am very much indebted to **Prof. John Thome** of École Polytechnique Fédérale de Lausanne, Switzerland for giving me the opportunity to work in his research group in the summer of 2007.

I am also very much grateful to the members of the Doctoral Scrutiny Committee, **Prof. Sankar Kumar Som**, **Prof. Sukanta Kumar Dash**, **Prof. Subhransu Roy** of the Department of Mechanical Engineering, IIT Kharagpur and **Prof. Sudipto Chakraborty** of the Department of Chemical Engineering, IIT Kharagpur for their constructive criticism and helpful suggestions. I express my indebtedness to the Department of Mechanical Engineering, IIT Kharagpur for providing me all the required facilities.

I convey my sincere thanks to **Prof. Souvik Bhattacharyya, Late Prof. Ranajit Kumar Brahma, Prof. Sandipan Ghosh Moulick, Prof. Biswajit Maity and Prof. Maddali Ramgopal** of the Department of Mechanical Engineering for giving me the chance to attend their classes. I received invaluable inputs for my research work from their lectures.

I convey my thanks to **Dr. Sagnik Mazumdar, Dr. Supriya Bera, Mr. Suman Ghosh, Mr. Dipankar Narayan Basu, Mr. V. R. K. Raju, Mr. G. K. Alok Dash, Mr. Santanu Dutta, Mr. Nagesh Patil, Dr. Santosh Sahu, Dr. Manoj Chopkar, Mr. V. Vishwakarma, Mr. Kiran Kumar Kupireddi, Dr. Tapas Kumar Mandal, Mrs. Arpita Mondal, Miss Aditi Oza, Mr. Shantanu Pramanik** and all my other co-workers for their valuable assistance.

I would remain always thankful to **Mr. Biswajit Mazumder, Mr. Ratan Patra, Mr. Sudip Bhakat** (Technical staffs of the Gas Dynamics and Heat transfer Laboratory) for their great help and sincere cooperation during my research work.

It will be injustice to forget my childhood friends who always inspired me. **Mr. Sandip Saha, Mr. Prithu Chatterjee, Mr. Kalyan Brata Chatterjee, Mr. Rakesh majumder, Mr. Rajdip Ghosh** are to name a few who are constantly helping me throughout my studies.

I should thank AICTE, India for extending the financial support during my research period at Indian Institute of Technology, Kharagpur.

Finally, I would like to express my appreciation to my wife **Mrs. Sumana Ghosh Das** who relinquished untold amount of time with her husband. She always encourages me to achieve my dreams. She took all the responsibilities of our family so that I could concentrate in studies. She was very much helpful and supporting throughout my journey for the degree.

Arup Kr. Das

Date: 26.11.09

Arup Kumar Das

DECLARATION

I certify that

a. The work contained in the thesis is original and has been done by myself under the general supervision of my supervisor(s).
b. The work has not been submitted to any other Institute for any degree or diploma.
c. I have followed the guidelines provided by the Institute in writing the thesis.
d. I have conformed to the norms and guidelines given in the Ethical Code of Conduct of the Institute.
e. Whenever I have used materials (data, theoretical analysis, and text) from other sources, I have given due credit to them by citing them in the text of the thesis and giving their details in the references.
f. Whenever I have quoted written materials from other sources, I have put them under quotation marks and given due credit to the sources by citing them and giving required details in the references.

Amal Kr. Das 13.04.10

Signature of the Student

LIST OF SYMBOLS

a	Empirical constant of equation 2.17 [dimensionless]
a_r	Drop radius [m]
as	Empirical constant of equation 3.16 [dimensionless]
b	Empirical constant of equation 2.17 [dimensionless]
bs	Empirical constant of equation 3.16 [dimensionless]
b^*	Empirical constant of equation 2.16 [dimensionless]
B	Empirical constant of equation 2.6 [dimensionless]
B_s	Empirical constant of equation 3.15 [dimensionless]
$B_B(r,z,t;d)$	Number of new borne bubbles due to break up [dimensionless]
$B_C(r,z,t;d)$	Number of new borne bubbles due to coalescence [dimensionless]
c_1	Constant in equation 2.12 & 2.15 [dimensionless]
c_2	Empirical constant in equation 2.21 [dimensionless]
c_3	Empirical constant in equation 2.22 [dimensionless]
c_i	Velocity of sound through the medium i [ms^{-1}]
c_{pi}	Specific heat capacity of i^{th} phase [J/ kg K]
Cap	Capillary number [dimensionless]
C_D	Drag coefficient for a single bubble [dimensionless]
C_{FL}	Interfacial friction factor [dimensionless]
C_i	Colour attribute of the particles i [dimensionless]
Cn	Cahn number [dimensionless]
C_{TD}	Turbulent dispersion force coefficient [dimensionless]

d	Diameter of the bubbles [m]
d_c	Critical bubble diameter for bubble breakup frequency [m]
d_{in}	Diameter of the bubbles entered at the inlet of the tube [m]
D	Pipe diameter [m]
D_B	Number of dying bubbles due to break up [dimensionless]
D_C	Number of dying bubbles due to coalescence [dimensionless]
D_r	Empirical constant in equation 3.16 [dimensionless]
D_{surf}	Maximum bubble size possible in dispersed bubbly flow [m]
f	Friction factor [dimensionless]
f_c	Empirical constant in equation 3.15 [dimensionless]
f_{io}	Wall friction factor of i^{th} phase [dimensionless]
f_{pi}	No penetration force of i^{th} particle [$kgms^{-2}$]
f_{si}	Surface tension force per unit vol. [$kgm^{-2}\ s^{-2}$]
f_v	Volume fraction of daughter bubble to mother bubble [dimensionless]
$f(x)$	Value of function at special coordinate x
F_{ab}	Parameter used in equation 5.12
F_c	Force generated due to asymmetry in the drop [N]
F_{LGi}	Interfacial force in i^{th} direction [$kg.m.s^{-2}$]
F_{dispi}	Mass transfer force due to turbulent dispersion in i^{th} direction [$kg.m.s^{-2}$]
F_{Wji}	Wall friction force for j^{th} phase in i^{th} direction [$kg.m.s^{-2}$]
F_{ilj}	Mass transfer force to i^{th} phase in j^{th} direction [$kg.m.s^{-2}$]
F_{si}	Surface tension force [$kg\ m\ s^{-2}$]
$F(R)_i$	Lennard-Jones force at the boundary [$kgms^{-2}$]
g_x	Gravitational acceleration in x direction [$m.s^{-2}$]
$g(a)$	Breakage frequency of the bubbles of diameter a [s^{-1}]

h	Smoothing length [m]
h_{new}	Smoothing length for the present time step [m]
h_{old}	Smoothing length for the earlier time step [m]
h(a,b)	Effective swept volume rate for bubble diameter a and b [s^{-1}]
I	Normalization coefficient described in equation 2.17 [dimensionless]
k	Empirical constant in equation 2.12 [dimensionless]
k_i	Thermal conductivity of i^{th} phase [W m^{-1} K^{-1}]
k_m	Mobility of a fluid [$m^2.V^{-1}s^{-1}$]
k_s	Scale of the smoothing length [dimensionless]
k_w	Wetting coefficient [dimensionless]
L	Characteristic length scale [m]
L_h	Latent heat for gas-liquid phase change [J kg^{-1}]
m	Empirical constant of equation 2.16 [dimensionless]
m_g	Mass transfer due to phase change [kg]
m_{gas}	Mass of the gaseous particles [kg]
m_i	Mass of particle i [kg]
m_{pseudo}	Mass of the pseudo particles [kg]
M	Normalization constant of the kernel [dimensionless]
n	Empirical constant of equation 2.6 [dimensionless]
n(r,z,t :d)	Number of bubbles at (r,z) of size d at time t [dimensionless]
oh	Ohensorge number [dimensionless]
p(a,b)	Film rupture efficiency of bubbles of diameter a and b [dimensionless]
P	Pressure of the mixture phase [$kg.m^{-1}.s^{-2}$]
P_d	Distance between different colored particles [dimensionless]
P_i	Pressure of particle i [kgm^{-1} s^{-2}]

q	Number of dimension [dimensionless]
Q_k	Heat flux of the k^{th} heat source [W m^2]
r	Radial direction of the conduit [m]
r_{ij}	Scalar distance between two particles i and j [m]
r_0	Minimum distance between boundary particle and fluid particle [m]
R	Radius of curvature of the drop footprint [m]
R_B	Average bubble diameter [m]
Re	Reynolds number [dimensionless]
R_g	Universal gas constant [$kJ.kg^{-1}K^{-1}$]
R_I	Vector location of the interface [m]
R_k	Location of the k^{th} heat source [m]
s	Position vector [dimensionless]
Sc_{tg}	Turbulent Schmidt number for gaseous phase [dimensionless]
t	Time [s]
T	Temperature [K]
T_0	Saturation temperature [K]
U_m	Mixture velocity [$m.s^{-1}$]
u_i	Radial velocity of i^{th} phase [$m.s^{-1}$]
v	Characteristics velocity [ms^{-1}]
v_{ij}^{β}	Relative velocity of particle i and j in β direction [ms^{-1}]
v_i^{α}	Velocity of particle i in α direction [ms^{-1}]
V_{high}	Ratio of the volume of the bubbles generated above the size entered at the inlet to the total volume of the bubbles [m]
V_{res}	Resultant velocity for drawing iso velocity lines [$m\ s^{-1}$]
w_i	Axial velocity of i^{th} phase [$m.s^{-1}$]

We	Weber number [dimensionless]
W_{ij}	Smoothing function between particles i and j
W(s,h)	Smoothing function at s having smoothing length h [dimensionless]
x	Redistribution criteria given in equation 5.14 [dimensionless]
x_i	Position vector of particle i [m]
x_{in}	Initial location of the drop over wettability gradient surface [m]
x_i^{β}	Position of particle i in β direction [m]
x_{ij}^{β}	Distance between particle i and j in β direction [m]
X_c	Empirical constant of equation 2.6 [dimensionless]
Y_c	Empirical constant of equation 2.6 [dimensionless]
z	Axial direction of the conduit [m]
zi	Empirical constant of equation 2.17 [dimensionless]

Greek alphabets

Ω	Domain of interest [m^3]
Φ_i	Chemical potential of i^{th} particle [Gibbs]
α	Empirical constant in equation 3.17 [dimensionless]
α_i	Void fraction of the i^{th} phase [dimensionless]
β	Empirical constant in equation 3.17 [dimensionless]
β_s	Shear rate [s^{-1}]
β_{TK}	Coefficient of volume expansion [K^{-1}]
δ	Dirac delta function [dimensionless]
δ_s	Dirac delta function along the interface [dimensionless]
ΔP_{LO}	Single phase frictional pressure drop [$kg.m^{-1}.s^{-2}$]
ε	Energy dissipation rate per unit mass [$m^2.s^{-3}$]

γ_{tg}	Turbulent kinetic viscosity [$m^2.s^{-1}$]
η	Empirical constant in equation 3.12 [m^2]
$\eta(a,b)$	Daughter bubble probability distribution [dimensionless]
θ_a	Advancing contact angle (°)
θ_{in}	Contact angle of the drop at initial location (°)
θ_r	Receding contact angle (°)
λ	Ratio of drop and matrix viscosities [dimensionless]
$\lambda(a,b)$	Coalescence frequency of bubble diameter a and b [s^{-1}]
μ_d	Viscosity of the drop [$kg.m^{-1}.s^{-1}$]
μ_i	Viscosity of i^{th} phase [$kg.m^{-1}.s^{-1}$]
μ_m	Viscosity of the matrix fluid [$kg.m^{-1}.s^{-1}$]
$\nu(a)$	Number of bubbles formed from the breakage of a bubble diameter a [dimensionless]
ξ_k	Parameter used in equation 5.12
ξ_{min}	Non-dimensional minimum daughter bubble size [dimensionless]
π_{ij}	Neumann-Richtmyer artificial viscosity [$kg\ m^{-1}s^{-1}$]
ρ_i	Density of i^{th} phase [$kg.m^{-3}$]
ρ_m	Density of the mixture [$kg.m^{-3}$]
$\rho(x)$	Density at x location [$kg.m^{-3}$]
σ	Surface tension [$kg.s^{-2}$]
$\sigma_i^{\alpha\beta}$	Strenns tensor mentioned in equation 3.11
σ_{lv}	Surface tension of liquid and gas pair [$kg\ s^{-2}$]

ABSTRACT

Computational algorithms have been developed to simulate multiphase flow of different types. Attention has been focused particularly to two categories of flow phenomena namely well dispersed (bubbly) flow and flow with complex interfaces.

Population balance equation coupled with two fluid model is used for the prediction of well dispersed bubble evolution of gas liquid two phase flow through vertical conduits. Coalescence of two similar or different sized bubbles and homogeneous and non homogeneous binary break up of a bubble has been tracked using the methodology. Present model is capable of tracking various distributions of void fraction profiles (wall peak, core peak, two peak etc.) efficiently. Using the model an effort has been made to propose unique criteria for transitions from bubbly flow to slug flow and dispersed bubbly flow by tracking the coalescence frequency and breakup frequency along the conduit axis. The developed transition criteria exhibit excellent match with the available literature. The present model has also been applied successfully for simulating bubbly flow through an annular passage.

Lagrangian Smoothed Particle Hydrodynamics (SPH) model is described to tackle the complex interfaces in typical multiphase flow situations. Surface tension force is added in the present numerical technique to avail the exact shape of the interface. The developed algorithm has been used to simulate the process of bubbling through submerged orifices. Effect of different properties of the surrounding liquid, like density, viscosity and surface tension, on bubble formation has been investigated in detail.

The concept of diffused interface is incorporated in the present numerical technique to improve the prediction of the interfaces. Liquid drop over an inclined plane is modeled successfully using the described methodology. Motion of the contact line and the overall dynamics of the drop are predicted analyzing the fluid flow inside the drop. Efforts have also been made to simulate unique phenomena like drop translation, uphill movement, splitting and merging of drops due to wettability gradient. Diffused interface based SPH can efficiently track the complex, dynamic interfaces in the scale of the droplet. New methodology for drop surgery is proposed using the developed numerical tool.

Finally a model has been proposed based on SPH to describe gas liquid phase change. Pseudo particles of zero mass are initially placed to locate the interface. Mass generated due to phase change is assigned to the pseudo particles and their positions are updated at intervals to track the mobility of the interface. The developed algorithm has been used to simulate vapor formation around solid spheres both in the absence of gravity and in the normal gravitational field. Finally, bubble growth over a hot horizontal surface due to boiling has been simulated. Simulated results showed good matching with the reported literature.

Keywords: Two fluid model, Population balance equation, Smoothed particle hydrodynamics, Diffused interface, Gas-liquid phase change, Bubbly flow, Wettability gradient.

CONTENTS

LIST OF TABLES

LIST OF FIGURES

CHAPTER 1 INTRODUCTION AND LITERATURE REVIEW

1.1. Multiphase flow, importance and application

Multiphase flow can be defined as the simultaneous flow of more than one phase. The most common example of such flow is the flow of two immiscible phases and can be termed as two phase flow. Simultaneous flow of liquid and gas (or liquid and vapor), liquid and solid, solid and gas as well as liquid and liquid are different types of two phase flow. On the other hand, flow of a three phase or four phase mixture is not rare. Combined flow of sand, water and air is used for filling up mine voids. Simultaneous flow of oil, water, air and gas occurs during oil exploration. It is needless to mention that such flows are highly complex.

Examples of multiphase flow in general and two phase flow in particular are common in nature, living organisms and man made systems. Rain, mist, sandstorm, hail storms, surf, foam etc. are natural phenomena involving two phase flow. In science and engineering the application of two phase flow are plenty. Gas-liquid two phase flow plays a very crucial role in power generation, refrigeration, air condition and cryogenics, industrial heating and cooling as well as chemical and process industries. Gas-solid and solid-liquid flows are widely used in the transportation of bulk solids by pneumatic conveying and slurry transportation respectively. In all the cutting edge technologies like space technology, cooling of highly integrated electronic systems, MEMS and microfluidics, novel biochemical and medical systems, emerging power sources like fuel cell two phase flow plays a very important role. However, the above list is far from an exhaustive one. It is only indicative of the significance of two phase flow and the relevance of its study in engineering practice.

1.2. *Complexities in multiphase flow*

Fluid dynamics is one of the most complex phenomena of physics. The complexities increases manifold in multiphase flow. The concept of continuum associated with the single phase system is immensely helpful in understanding the flow phenomena, analyzing it mathematically and even conducting experimental studies. In two phase flow the continuum is intercepted by the presence of deformable interfaces across which there is a sharp variation of properties and there could be a significant variation in pressure, velocity and temperature. Further, the interface evolves with respect to time and space. Certain parameters like interfacial tension, surface wettability, gravity and other body forces as well as conduit shape,

size and orientation can influence two phase flow in unique ways compared to the single phase flow.

Turbulence is one of the least understood phenomena in fluid mechanics. Even in single phase flow there is an enormous need for fundamental investigations to uncover the mystery of turbulence. In case of two phase flow, the macroscopic non-homogeneity adds further to the inherent complexities of the topic. The origin, nature, growth and decay of turbulence could be significantly different in two phase flow. Little has yet been done to resolve these issues.

Phase change is another singlemost phenomenon in two phase flow which requires a critical treatment. Apart from the macro scale issues there are many micro scale phenomena like nucleation, growth and collapse of a phase, local thermodynamic non-equilibrium etc. it is needless to say that the researchers have to go a long way to understand them fully and to model them successfully.

It has been mentioned earlier that the presence of interface is a unique characteristics of two phase flow. That during their simultaneous motion, the two phases can distribute themselves in a variety of macro scale morphological patterns is responsible for the occurrence of complex interfaces. These morphological varieties are known as flow regimes or flow patterns. At this point it may be worthwhile to cite an example. The flowing mixture of a liquid and a gas through a conduit can exhibit a large number of flow regimes. The two extreme cases are the gas phase distributed in the form of bubbles in a moving liquid stream (bubbly flow) and the flow of a continuous gas stream laden with liquid droplets (mist or drop flow). In between there could be a host of other distribution of phases or flow regimes. Existence of a particular flow regime depends on a large number of parameters, namely velocity and property of the individual phase, shape, size and orientation of the conduit with respect to gravity (vertical, horizontal or inclined), absolute (up or down) and relative (co-flow or counter-flow) direction of flow etc. Flow regimes can be drastically different under the influence of other than normal 'g' or in the presence of other body force fields. On the other hand, the change of phase gives rise to unique flow regimes. Different stability criteria are responsible for the occurrence of a particular flow regime. In this respect the current state of understanding is far from being adequate. As a summarizing note one can mention that two phase flow often encompasses a number of physical mechanisms working simultaneously

(multi-physics) and phenomena having different scales (multi-scale). As a result many situations involving two phase flow are counter intuitive.

1.3. Understanding two phase flow- methods of investigations

The complex physics of two phase flow offers an insurmountable challenge to the scientists and engineers. Nevertheless, untiring effort is being made by the researchers from different disciplines to understand the flow phenomena, to analyze and to predict it. One can trace the early investigations in this direction to be solely experimental. One can not deny the role of experimental investigations in exploring the unknown physics. The most challenging task in the experiments involving two phase flow is the measurement of the relevant hydrodynamic parameters. Often the techniques of measurement are different from those commonly used for single phase flow. Such unique techniques are not only costly but also not always available of the shelf. Visualization is essential for almost all problems of two phase flow for appreciating the intricate flow structure. This is an additional requirement with the associated cost implication. Besides, experiments are time consuming and are not feasible for all the situations of multiphase flow. Theoretical analysis can replace the costly and time consuming experiments in some cases. It can supplement the experimental results in many cases and can enhance the capability of our prediction. One can also trace a chronological account of the various methods of theoretical analysis or modelling in multiphase flow. As the present work is concerned with the modelling of multiphase flow the development of different models is described in separate sections as follows:

1.4. Early methods

Early attempts of modelling multiphase flow are marked with a high level of idealization and averaging so that concepts can be easily borrowed from the established theories of single phase flow (Wallis, 1969; Ishii and Hibiki, 2006). Most of the cases such models used to consider the spatial variation only along one direction- the direction of mean flow.

The most simplistic model in this genre is described as Homogeneous Equilibrium Model (HEM). It assumes that velocity temperature and pressure of both the phases and components are equal. For the analysis of different transport phenomena HEM arbitrarily calculates the

mixture transport properties based on various schemes of volume average or mass average.

Zuber and Findlay (1965) proposed a better model and considered the interfacial slip between the phases. Their proposed model is commonly known as drift flux model (DFM). This model does not assume that phases are in mechanical equilibrium. The phase velocities are allowed to differ from each other and consequently they also differ from the mixture velocity. The main assumption of drift flux model (Ishii 1977) is that the relative velocity between the phases can be approximated by an algebraic expression. Such type of modeling is more applicable for strongly coupled phases.

1.5. CFD models based on averaged formulations

The advantages of HEM or DFM are obvious. In many cases they are amenable to analytical solutions. As HEM assumes the flow of a pseudo fluid the conventional schemes of single phase CFD are applicable in principle. But both of these models ignore the complex physics of two phase flow grossly. In the next level of averaging both the phases were reckoned as separate fluids considering separate set of conservation equations for them. This resulted in a new class of model known as two fluid model. This is also an averaged model as the actual distribution of the phases are not considered but their relative influence on the flow phenomena is taken care through the void fraction (α). Two fluid model is well suited for dispersed flow in which one phase is continuous and the other phase is distributed in the "lumps" of regular or irregular (mostly) shape and size. However, attempts have also been made to simulate flow phenomena other than dispersed flow using the two fluid model.

Different types of averaging based on space, time or ensemble have been suggested. Joseph and Lundgren (1990) applied ensemble averaging technique to develop equations for fluid-particle suspension. Zhang and Prosperetti (1994) described ensemble averaging of inviscid, incompressible fluid-fluid mixture and developed relationships for time and spatial derivatives of physical properties. Drew and Passman (1999) gave a very broad detailed overview of averaging methods of multi component flows.

Two fluid formulation can successfully analyze the transient phenomena, wave propagations and flow regime transitions. A detailed description of the model formulation is described in the next chapter. Continuous developments have been made in the basic two fluid model to appropriately reflect the physics of flow. Ishii and Mishima (1981) proposed that two phase flow is not only dependent on the volumetric concentration of phases but

interfacial area is also an important parameter. Ishii (1975) developed a scalar transport equation for interfacial area concentration considering time averaged conservation equation for the fluids. Two fluid model along with one dimensional interfacial area transport equation gives a good prediction for dispersed flow in standard conduit diameter range for a given sphericity of the dispersed phases. But with one transport equation for interfacial area concentration change in size of the dispersed phase entity can be modeled but not the shape. Ishii and Kim (2004) recently proposed a more generalized two group area transport concept which models spherical/ellipsoidal bubbles and elongated cap type bubbles separately.

Several higher order eulerian models involving appropriate use of averaged mass, momentum and energy equations showed impressive progress in recent years. Hibiki and Ishii (2002) developed constitutive equations for coalescence and breakup of dispersed phases and used them to calculate interfacial area transport. In general, interfacial transfer rates can be given by the product of the driving interfacial flux and interfacial area concentration defined by the available interfacial area per unit mixture volume. Kocamustafaogullari and Ishii (1995) proposed a dynamic approach to furnish interfacial area concentration via transport equation. Wu et al. (1998) established the source and sink terms of the interfacial area accounting for the dispersed phase interaction mechanisms. It was followed by Kim (1999) where the transport equation applicable to the well dispersed flow in a confined conduit was established. The model was further evaluated by Ishii et al. (2002) and Kim et al. (2002), where an extensive database acquired in various sizes of round conduit was employed. Sun (2001) and Fu (2001) developed the two-group interfacial area transport equation applicable to confined and round flow channels, respectively. Furthermore, the interfacial area transport equation for a co-current downward two-phase flow was developed by Paranjape et al. (2003). Similar efforts to provide dynamic models for interfacial area were also made by Millies et al. (1996), Morel et al. (1999) and Hibiki and Ishii (2000). More recently, the comprehensive mathematical formulation of transport equation analogous to the Boltzmann transport equation was published by Ishii and Kim (2004). Lahey and Drew (2002) propose the ensemble averaging constitutive equations describing forces within the multi-field, multifluid model interactions.

Another extension of two fluid model comes out in terms of multi field two fluid model as proposed by Lahey and Drew (2001). The basic idea of the model is that both the fluids can be present as continuous and dispersed phases. In the model four fields are therefore given by

continuous liquid, continuous gas, dispersed liquid and dispersed gas. For each of these four fields separate transport equations are solved by considering mass and momentum transfer with appropriate closure. The four field two fluid model is effective for flows where phase change phenomena do occur.

Apart from all these models two fluid model is the most widely used approach which considers two interpenetrating streams as continua. In 1975 Ishii proposed two fluid formulation by considering each phase separately. The model is expressed in terms of two sets of conservation equations governing the balance of mass, momentum and energy in each phase. The interactions of one phase on the other appear in these balance equations. It can take into account the dynamic and non equilibrium interactions between the phases.

Third and most promising improvement of two fluid model, particularly for dispersed flow, is to overcome the mono dispersed limitation by introducing several population classes (Ramkrishna 2000). In this approach dispersed phase is divided into several classes based on characteristics dimensions. Suitable model (Venneker et al. 2002) for break up and coalescence of the classes governs the spatial and temporal distributions of the phases. Recently Lo (1996) algebraically related individual velocities of different classes with the mixture velocity and proposed Multiple Size Group (MUSIG) model. In this model only one equation is solved for dispersed phase momentum conservation. Out of which separate velocities for all the classes are determined for multiple continuity equations.

1.6. Models of two phase flow with a distinct interface

Along with the development of averaged models, parallel efforts were made for the accurate modelling of the interface. In a broad sense there are two methodologies namely interface tracking and interface capturing. An interface-tracking technique requires meshes that move to "track" the interface. In an interface-capturing technique for two fluid flows, the computations are based on fixed spatial domains, where an interface function, marking the location of the interface, needs to be computed to "capture" the interface. Time to time researchers developed several methodologies which either can track or capture the time variant interfaces. Hirt and Nichols (1981) presented an overview of the initial techniques such as height and line functions and marker and cell method (MAC) for modelling of the irregular interfaces. But these techniques possess certain drawbacks which discourages their application for complex interfaces. Height and line function cannot handle complex

topologies of the interfaces and MAC requires large computer memories and substantial computer resources. Among all other developed numerical methodologies Simplified Line Interface Calculation (SLIC) (Noh and Woodward, 1976) is most common which redistribute its discretization using a simplified algorithm based on its neighbors. In this method the interface is considered to be a horizontal and vertical line inside a computational grid. SLIC is efficient for interface tracking but performs unsatisfactorily for temporally developing complex geometries. Brackbill et al. (1992) presented continuum surface force model which uses the gradient of fluid cell to calculate the surface normal and its curvature. In 1981 Hirt and Nichols introduced another version of front tracking method which is capable of computing highly complicated phase boundaries. This method is commonly known as volume of fluid method. Volume of Fluid method (Hirt and Nichols, 1981) uses suitable reconstruction algorithms in a eulerian system by defining volume fraction of each phase in each grid volume. A review of the VOF method can be found in Scardovelli and Zaleski (1999). But algorithm with volume of fluid requires very low Courant number to produce stable and accurate solution. This makes the algorithm computationally expensive. Moreover, in volume of fluid minimum advection of interface can be in the order of control volume which limits its application for highly complex nature of interface.

In 1988 Osher and Sethian proposed an alternative, level set method for multiphase flow simulation. In this method two phases are separately represented using the level set function which advects and reinitializes depending on the individual phase velocities. This method can capture complex breakage and coalescence without any special treatment. But at the same time level set cannot conserve mass and possesses limited accuracy. Sussman and Fatemi (1999) presented a good review about the level set functions and its applications.

To take out the advantages of both volume of fluid and level set method efforts are made to combine these techniques. Coupled level set and volume of fluid (CLSVOF) is first introduced by Bourlioux (1995). Sussman and Puckett (2000) subsequently developed a three-dimensional and axisymmetric CLSVOF method for computing incompressible two-phase flows with large density ratios, utilizing the inherent essence of CLSVOF. Son and Hur (2002) also developed a CLSVOF approach for buoyancy driven flows. Drust and his Co-workers (Gerlach et al., 2005; Gerlach et al., 2007; Buwa et al., 2007) simulated evolving gas-liquid interface using VOF and CLSVOF. But the major difficulty lies in the proper handling of advection of volume of fluid function and reinitialization of level set function.

1.7. Particle based methods for multiphase flow

Recently, a number of meshfree methods have been proposed for analyzing fluid-fluid interfacial structures. These methods can be efficiently used for situation related to deformable boundaries, complex geometry and multiple scales. Among all the meshfree methods smoothed particle hydrodynamics (Lucy, 1977; and Gingold and Monaghan, 1977) is one of the earlier methods and widely used for versatile multiphase flow problems. SPH was conceived by Lucy (1977) in 1977 and further developed by Gingold and Monaghan (1977) for treating astrophysical problems. Since then it has been used with appropriate modifications for numerous single phase fluid dynamics problems including viscous flow (Takeda et al., 1994), free surface flows (Monaghan, 1994) as well as low Reynolds number incompressible flow (Morris et al., 1997). SPH requires a special treatment at the solid liquid interface to ensure no penetration condition. Different methods for modeling of boundary conditions in SPH have also been proposed till date making the technique more versatile. Libersky and Petschek (1991) introduced symmetrical surface boundary condition by inserting ghost particles along and outside the boundary. On the other hand, Monaghan (1992) and Monaghan et al. (1994) used ghost particles at the boundary exerting a normal and tangential force on the fluid particles. Gomez-Gesteira et al. (2004) use fixed particles along the boundary and smoothly interpolated the values for interior particles. Morris et al. (1997) assigned an artificial velocity for boundary particles to simulate a no-slip condition. Recently Liu et al. (2001) suggested two layers of virtual particle arrangement making a compromise between Libersky and Petschek (1991) and Monaghan (1994). Implementation of SPH in multiphase flow problems needs a few modifications. For multiphase systems Chen et al. (1999) proposed an approach for density re-initialization across the interface to take care of a large density difference between the phases. This technique is termed as corrective smoothed particle method (CSPM). In 1992 Brackbill et al. proposed continuum surface force (CSF) model for adding surface tension in grid based technique. Taking queue from the CSF model, Morris (2000) simulated surface tension acting at an interface between two fluids of the same density and viscosity.

Among other mesh free methods Lattice Boltzmann Method (LBM) (Higuera and Succi, 1989) has become a popular numerical tool for simulation of multiphase flow dynamics. While the conventional CFD depends on continuum based formulations LBM has its roots in

kinetic theory and exploits cellular automata (Chen and Doolen, 1998). LBM based methods, though much young compared to conventional CFD, has shown considerable promise in handling flow through complicated geometry, flow over a large range of Reynolds number, flow of different types of fluids and fluid mixtures including multi phase flow. Gunstensen and Rothman (1993) studied the linear and nonlinear multicomponent flow regimes due to distributions of one phase into the other. Nayroles et al. (1992) used moving least square approximations in a Galerkin method to formulate Diffuse Element Method (DEM). Based on DEM, Belytschko et al. (1994) introduced element free Galerkin Method (EFG) for multiphase flow simulation. EFG is currently used for several multiphase flow situations with the possibility of using Lagrange multiplier as a means to introduce field discontinuities. Among other meshfree numerical techniques Finite point method (FPM) (Liszka and Orkisz, 1980), Reproducing Kernel Particle method (RKPM) (Liu et al., 1995), Point Interpolation Method (PIM) (Liu and Gu, 2001) are to name a few. RKPM (Liu et al., 2005) uses a reproducing kernel interpolation function to attain a more efficient description of continuum behavior along with the numerical description of smoothed particle hydrodynamics. Liu and Xiao (2006) used PIM to solve immiscible two phase flow in porous media. They have used additional liner or quadratic polynomial for approximating a function other than the particle approximation. Another microscopic meshfree particle method, molecular dynamics (Alder and Wainwright, 1959) has gained popularity with the increase of computational power for simulation of multiphase flow situations. But as molecular dynamics requires a huge computational power it is applied mostly for evolution of separated flow situations such as micro drop dynamics (Yan and Ji, 2008; Hong et al. 2009) and bubble behavior in nanochannel (Kinjo and Matsumoto, 1998). For details of molecular dynamic simulation one can refer (Tuckerman et al., 1991). Other meshfree particle methods employed for multiphase flow simulation are dissipative particle dynamics (Hoogerbrugge and Koelman, 1992), moving particle semi implicit method (Koshizuka et al., 1998) etc.

Combination of eulerian and lagrangian techniques are also used time to time for simulation of multiphase flow dynamics. Arbitrary lagrangian eulerian (ALE) method is the most popular method of this genre. The method is introduced by Hirt et al. (1974) and substantially developed by several researchers for multiphase flow problems. ALE methods are widely used in the modeling of blood flows (Gerbeau and Vidrascu, 2003) or motions of glacier (Picasso et al., 2004), i.e. for problems with small or slow deformation.

Francios and Shyy (2003) combined front tracking marker-chain method in immersed boundary technique to efficiently model surface tension and contact angle even in a completely non wettable surface. Tryggvason and Unverdi (1999) used color for surface particles to track fluid-fluid interactions and employed front tracking methodology to determine the evolution of the interface.

1.8. Sharp interface versus diffuse interface

Conventionally, the interface is assumed as a zone of infinitesimal thickness which separates the bulk phases. The pressure difference across the interface is balanced by a special force termed as surface tension (Panton, 1984). There is an abrupt variation of properties across the interface. This picture emerged from the works of Young (1805), Laplace (1805) and Gauss (1830) in the early part of 1800. Mathematically it is needed to impose suitable boundary conditions at the interface to simulate processes like capillarity. In contrast, to the "sharp interface" described above, Poisson (1832), Maxwell (1876) and Gibbs (1876) conceived the interface as a narrow region characterized by a smooth but rapid variation of physical properties between the bulk values of the two fluids. The later description of the zone intermediate to both the fluids is known as Diffuse Interface (DI). The concept of DI was substantiated further by Raleigh (1892). van der Walls (1893) postulated the gradient theory for the interface and formulated a method for the prediction of interface thickness based on the equation of state. Finally, the constitutive law of capillary stress tensor was developed by Kerteweg (1901) in terms of the spatial gradient of density.

DI approach is based on a rigorous conservation of energy where the length scale of the phenomena is comparable to the interfacial thickness (for example near the critical point) DI gives a definite advantage over the free boundary description of interface. Besides, this method has been reported to give better results for contact line problems and complex topological problems like breakup and coalescence (Anderson et al., 1998). DI also helps to alleviate the numerical difficulties associated with stress singularities (Ding and Spelt, 2007).

Cahn and Hilliard (1958) thermodynamically proved that free energy at a point is not only dependent on the local composition but also it is biased by its immediate neighbors. They extensively studied the diffusion dominated interface and correlated the neighboring composition gradient around the interface with the local energy content in the form of Cahn-

Hilliard equation. Antanovskii (1995) developed a rheological expression for binary fluids subjected to topological changes considering an interfacial layer between the fluids. Anderson et al. (1998) modeled motion of a single component compressible fluid near its critical point using DI under the adiabatic condition. Further, they studied the internal gravity waves in near critical state of the fluid employing approximate van der Wall's equation of state. Later on, Jacqmin (2000) investigated moving contact line dynamics of a Cahn-Hilliard-van der Waals (CHW) diffuse mean field interface. His analysis of DI is utilized in both linearized and non linear finite difference calculation. Liu and Shen (2003) used coupled Navier Stokes Cahn Hilliard equation which includes energetic variational formulation for the extra stress representing the capillary effect of the mixture. Tapia and Lopez (2009) proposed a free energy based formulation of diffuse fluid-fluid-solid interface. They have used Chebyshev pseudo spectral methods with mesh adaptation for the solution of DI type problems. van der Sman and van der Graaf (2008) employed DI scheme in Lattice Boltzmann equation for solving drop spreading phenomena in a shear flow field. They have also showed that artificial compressibility error induced by DI formulation can be eliminated by including surface tension as a body force in Navier-Stokes equation. But till date not many efforts have been made to incorporate to the Lagrangian description of the interface.

Recently, Xu et al. (2009) used mass density as ordered parameter to combine DI concept with SPH and investigated precipitation and dissolution problem of multiphase flow. However, the adoption of DI in particle based CFD simulation is rare. Algorithms should be developed such that the advantage of DI can also be exploited in particle based simulation.

1.9. CFD models for flow with a phase change

The change of phase introduces additional intricacy in two phase hydrodynamics. Firstly, the mass of an individual phase is not conserved. Secondly, the evolution of the interface depends on the conjugate effect of local hydrodynamics and the process of phase change. The computational simulation of the two phase flow with phase change poses a significant challenge. Out of different phase change problems the process of vapor formation from a liquid phase has been considered in the present dissertation. Accordingly, some important literature relevant to liquid-vapor phase transformation is elaborated below.

One can trace back a number of fundamental investigations, mostly analytical in nature,

which contributed towards the understanding of phase change process due to evaporation. . The growth of a bubble in superheated liquid was first analyzed by Bosnjakovic (1930). The early theoretical works of Plesset and Zwick (1954), Forster and Zuber (1955), Scriven (1959) establishes the governing laws for bubble growth in superheated liquids over a wide range of Jacob number. Mikic et al. (1970) proposed an equation for bubble growth which is independent of Jacob number. Lee and Nydahl (1989) calculated the bubble growth rate by solving the flow and temperature field considering a wedge shaped micro layer below the hemispherical bubble. Zeng et al. (1993) estimated the bubble departure diameter during single bubble growth under nucleate boiling situation. Later, several analytical efforts were made to predict the film growth (Robinson and Judd, 2004) its collapse (Naude and Mendez, 2007) and subsequent generation of vapor bubble nucleation (Lee et al., 2003). An extensive review of the previous works is given in Shiotsu and Hama (2000). Despite decades of research still there are many aspects of boiling heat transfer that are not well understood.

With the advancement of numerical techniques, options opened towards the implementation of numerical methodologies for the prediction of phase change heat transfer. Welch used finite volume method for the numerical simulation of bubble growth under saturated condition considering the conduction in the solid wall. Son and Dhir (1997) used moving grid method for the prediction of interface of film boiling on horizontal flat plate. Juric and Tryggvason (1998) used front tracking method for numerical analysis of film boiling heat transfer. Conventional interface tracking methods like volume of fluid (Welch and Wilson, 2000) and level set (Son and Dhir, 1998) is also used for numerical simulation of film boiling heat transfer. Son et al. (1999) considered spatial temporal distribution of wall heat flux and microlayer heat transfer for numerical simulation of isolated bubble on heated surface. They have used level set method for interface capturing. Esmaeeli and Tryggvason (2004) combined front tracking method along with immersed boundary technique to account for the velocity boundary conditions on irregular solid surfaces. Tomar et al. (2005) investigated bubble formation, growth and departure in film boiling situation using combined level set-volume of fluid method. They correlated the frequency of bubble formation with degree of superheat by considering film rupture phenomena due to Rayleigh-Taylor instability. Tomar et al. (2008) performed a linear stability analysis for multimode bubble analysis and showed that increase of heat flux stabilizes the film until Rayleigh-Taylor instability sets in.

As many phase change problem involve a large change in density, the implementation of the basic SPH scheme may pose a difficulty. Monaghan et al. (2005) used the concept of virtual solid particle to model freezing of one or two component system employing smoothed particle hydrodynamics. Particle redistribution was needed at regular intervals for capturing the dynamic interface. However, as the problem considered did not involve any fluid motion the interface location was dependant only on the energy equation.

Though there is apparent similarity between the solid-liquid and liquid-vapor phase change, there are also some differences. For solidification and melting it is usually permissible to neglect change in density. But boiling or condensation is associated with an abrupt change in volume which complicates the phenomena compared to a problem of solid-liquid phase change. Moreover, this change of volume pose a great problem to the particle based models. Special algorithm is needed to tackle the change of volume during liquid vapor phase change.

1.10. Shortcomings in the literature

The above review briefly described the literature on averaged formulation of two phase flow as well as detail simulation of the dynamic interface. The review is far from an exhaustive one. But emphasis has been put on the topics and methods directly relevant to the present dissertation. Though the volume of the literature on the computational modelling of two phase flow is growing very rapidly, one can readily identify a number of shortcomings in the existing literature which need immediate attention from the researchers.

- Despite host of investigations in gas-liquid two phase flow, the dynamics of different sized discrete bubbles are not well understood till date. Temporal evolution of bubble size due to merging of two bubbles and breaking of a single bubble into two needs to be described from the first principle.
- Flow regime maps for two phase flow in literature are developed mainly based either on void fraction data or the superficial velocities of the phases. No effort has been made till date to predict the flow regime transition using computational fluid dynamics.
- Different distribution patterns of void fraction along the radial plane of the conduit are not investigated in detail using CFD.

- Though Lagrangian particle based techniques are suitable for the description of moving interafce, meshless methods are not extensively used for numerical modelling of multiphase flow.
- The concept of diffuse interface may be adopted also in the particle based techniques to exploit the advantage of this technique.
- The simulation of a moving three phase contact line is a challenging task. The motion and spreading of droplets have been modeled assuming them as wedge shaped film. Attempts have also been made to apply different grid based techniques. It is worth while to employ the particle based technique as it is well suited for complex arbitrary shape.
- Extension of particle based technique, for the modelling of phase change problem is another topic which demands attention. A robust algorithm which can take care of the evolution of complex interfaces in phase change problems with a large density difference is yet due.

This thesis aims at developing some computational algorithms to address some of the above issues. Though the algorithms have been applied to solve specific problems they have the generality of solving other problems of similar nature.

1.11. Organization of thesis

The present dissertation is organized in six chapters. The first chapter (the present chapter) describes the importance of two phase flow and the necessity of computational fluid dynamics for analyzing such type of flow. A brief review of literature on typical CFD models for two phase flow is also presented. Emphasis has been given to the literature directly relevant to the present investigations. Based on this survey some lacunas in the literature have also been pointed out. In chapter 2 development of an averaged model based on two fluid formulation and population balance technique has been described. The model, generally suitable for dispersed flow, has been applied to simulate co-current bubbly flow through vertical conduits. Pipe sizes normally encountered in two phase transportation have been considered. For example, the largest pipe diameter simulated is 76.2 mm while the pipe length is around 100D in many cases. Additionally, some physics based criteria have been proposed

for the transition of bubbly flow. Based on these criteria the computational results have been used to construct the flow regime map.

In chapter 3 particle based smoothed particle hydrodynamics is used to model well defined interface between the phases. Bubbling from submerged orifice is studied in details using the methodology. The characteristics length of the domain is considered to be in the order of 10^{-3} m. Parametric variations of the influencing factors are reported along with the influence of gravity over the bubble formation procedure.

In the next chapter diffuse interface concept has been incorporated in the Lagrangian smoothed particle hydrodynamics to avoid the sudden jump of properties across the interface. Several static and dynamic cases of milimetric size range are revisited using the developed hybrid methodology to establish the suitability of the model. In the same chapter drop manipulation using wettability gradient is modeled using diffuse interface based smoothed particle hydrodynamics. Drop sizes are varied in a wide range of scales starting from 10^{-2} m to 10^{-5} m.

In chapter 5 a novel numerical method is described for the modelling of phase change processes. Developed model can track the transformation of high density liquid particles into lighter vapor particles without violating the conservation of mass. In this chapter efforts have been made to model the phenomena film boiling around a spherical solid and on a horizontal plane surface. The evolving interfaces are considered to start from the order of 10^{-6} m in dimension.

Chapter 6 summarizes the main conclusions of the thesis. Significant findings from the developed numerical methodologies and the future scope of research are described here.

1.12. Summary

In this chapter, numerical techniques available in literature for prediction of two phase flow are discussed. Separate attentions are given for techniques capable of solving well dispersed and well separated flow. Finally, literatures related to modelling of non adiabatic phase change are also mentioned. But as multiphase flow is one of the very active fields of research nowadays there exist a huge volume of literatures. We are aware that our literature survey is not exhaustive. Due to the paucity of space we have restricted our discussion mainly to the topics directly related to our investigations.

CHAPTER 2 AVERAGED MODELLING

2.1. Introduction

Multiphase flow is characterized by the presence of interfaces. The behavior of such flow is greatly influenced by the mechanical, thermal and chemical interactions at these interfaces. It is therefore needless to say that the success of simulating such flow phenomena depends on the accurate modeling of the interface and the interfacial interactions. But the complexity of multiphase flow in many of the practical systems often forbids such an activity. On the other hand, even if one possesses the detailed knowledge (Prosperetti and Tryggvasson, 2007) regarding such interactions one can seldom use this huge information for practical purposes. Rather, in most of the situations only some sort of averaged value is usable. This has motivated the researchers to simulate a large number of multiphase flow problems based on averaged formulation. Different types of averaging namely space averaging (Zuber, 1964; Ishii, 1977), time averaging (Ishii, 1975; Ishii and Mishima, 1984), space-time averaging (Lahey and Drew, 1989; Drew and Passman, 1999) and ensemble averaging (Zhang and Prosperetti, 1993; Kolev, 2002) have been tried for multiphase flow.

Averaged models are particularly suitable for dispersed flow. In such flow one phase, called the carrier phase or primary phase has a more or less continuous distribution in the flow field while the other phase, defined as secondary phase is rather discontinuous or dispersed in it. Bubbly flow and droplet flow are good examples. The continuous phase is modeled based on an eulerian approach. The dispersed phase is modeled based on either eulerian or lagrangian approach. As separate sets of conservation equations are used for each of the phases such models are also commonly described as two fluid models. An important idealization of the averaged modelling is popularly known as interpenetrating continua or mixed continua (Rakhmatulin, 1956). According to the hypothesis of the interpenetrating continua both the phases are simultaneously present at each and every point of the computational domain while their influence on the hydrodynamics and the transport processes is given by the local phase fraction. An averaged model is approximate. It needs to be closed by suitable closure relationships. It is of utmost important to select these relationships particularly for the interfacial interactions. In the present chapter different aspects of bubbly flow is modeled based on eulerian-eulerian two fluid model considering interpenetrating continua.

Though the two fluid model is a considerable success towards the modeling of a class of multiphase flow it needs augmentation to take care of the distribution of different length scales of the secondary phase in the matrix of the primary phase. Several researchers have adopted statistical population balance model (PBM) for prediction of the behavior of different sized dispersed phase entity. Fu and Ishii (2002) developed two-group interfacial area transport equation for prediction of bubble dynamics ranging from spherical/distorted bubble to slug/cap bubbles. PBM can encounter the birth and death of a particular sized entity due to breakage or coalescence of the secondary phase. In this chapter we have seamlessly coupled two fluid model along with population balance equation to simulate bubbly flow. Description of the model development is presented in the next section for gas liquid bubbly flow. Pipe sizes normally encountered in two phase transportation have been considered. For example, the largest pipe diameter simulated is 76.2 mm while the pipe length is around 100D in many cases.

2.2. Model development

Fig. 2.1 depicts the typical flow of two phase mixture where the lighter phase is dispersed in the form of bubbles of different sizes in a round vertical conduit. The constitutive equations of each phase are developed based on the volume average properties of the phase. The total population of bubbles of the discrete phase is discretized into subgroups based on volume. Depending on the interactions with primary phase secondary phase bubbles may break or coalesce with other bubbles present in the flow. Size discretization based on volume avoids intermediate bubble generation during coalescence. In the present model each group of bubbles has its characteristic length and occupies a fixed space at any instant. At any location number of bubbles in each group can be individually tracked.

2.2.1. Two fluid model

For the solution of macroscopic flow field eulerian two fluid model (Anderson and Jackson, 1967) has been used considering the idealization of interpenetrating continua. The approach gives the freedom to use coarser grids and longer time steps compared to the eulerian-lagrangian approach. Isothermal dispersed flow in the absence of any phase change can be described by the conservation of mass and momentum for each of the phases. For the

model development we assume that the flow is co-current and axisymmetric. The conservation equations in r-z coordinate system are given below based on the formalism of two fluid model.

Continuity equation:

$$\frac{\partial}{\partial t}\left[\rho_i \alpha_i\right]+\frac{1}{r}\frac{\partial}{\partial r}\left[r\rho_i \alpha_i u_i\right]+\frac{\partial}{\partial z}\left[\rho_i \alpha_i w_i\right]=0. \tag{2.1}$$

r momentum:

$$\begin{aligned}\frac{\partial}{\partial t}\left[\rho_i \alpha_i u_i\right]+\frac{\partial}{\partial r}\left[\rho_i \alpha_i u_i^2\right]+\frac{\partial}{\partial z}\left[\rho_i \alpha_i u_i w_i\right] &= -\alpha_i \frac{\partial P}{\partial r}+\alpha_i \rho_i g_r+\mu_i \frac{\partial^2}{\partial r^2}\left(\alpha_i u_i\right) \\ &+\frac{\mu_i \alpha_i u_i}{r^2}+\frac{\mu_i}{r}\frac{\partial}{\partial r}\left(\alpha_i u_i\right)+\mu_i \frac{\partial^2}{\partial z^2}\left(\alpha_i u_i\right)-F_{Wir}\mp F_{LGir}-F_{ilr}\pm F_{dispr}.\end{aligned} \tag{2.2}$$

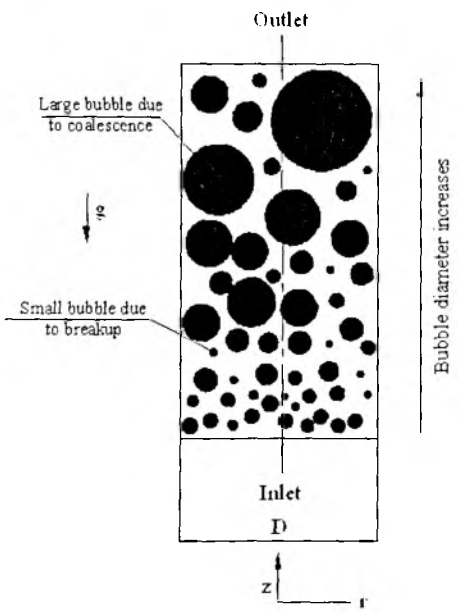

Fig. 2.1 Schematic representation of bubbly flow through a vertical conduit

z momentum:

$$\begin{aligned}\frac{\partial}{\partial t}\left[\rho_i \alpha_i w_i\right]+\frac{\partial}{\partial r}\left[\rho_i \alpha_i u_i w_i\right]+\frac{\partial}{\partial z}\left[\rho_i \alpha_i w_i^2\right] &= -\alpha_i \frac{\partial P}{\partial z}+\alpha_i \rho_i g_z+\mu_i \frac{\partial^2}{\partial r^2}\left(\alpha_i w_i\right) \\ &+\frac{\mu_i}{r}\frac{\partial}{\partial r}\left(\alpha_i w_i\right)+\mu_i \frac{\partial^2}{\partial z^2}\left(\alpha_i w_i\right)-F_{Wiz}\mp F_{LGz}-F_{ilz}\pm F_{dispz}.\end{aligned} \tag{2.3}$$

Here i = l stands for primary phase and i = g stands for secondary phase. The above set of six equations contains seven unknowns. These are the axial and radial component of phase

velocities (4), axial pressure, void fraction and local gas density. This system of simultaneous equation can be closed by the introduction of a suitable closure relationship. The relationship between local pressure and gas density could be a possible choice. In the present work the equation of state for ideal gas has been used for that purpose.

2.2.2. Interfacial momentum transfer

Constitutive relationships for the force terms used in the momentum equations are selected from the published literature (Wang et al., 2006).

F_{LG} is the interfacial drag force that can be expressed as (Richter, 1983):

$$\overline{\overline{F_{LG}}} = \frac{2C_{FL}}{D}\sqrt{\alpha}\rho_g\left(\overline{u_g}-\overline{u_l}\right)\left|\overline{u_g}-\overline{u_l}\right| + \frac{\alpha}{2}\rho_l\overline{u_g}\frac{\partial}{\partial r}\left(\overline{u_g}-\overline{u_l}\right). \tag{2.4}$$

In the above expression C_{FL} is the interfacial friction factor and is given by

$$C_{FL} = C_D\sqrt{\alpha}\left(1-\alpha\right)^{-1.7}\frac{\rho_l}{\rho_g}\frac{D}{2R_B}. \tag{2.5}$$

C_D is drag coefficient for a single bubble and R_B is average bubble diameter at a particular location which is determined through population balance technique. This is one of the interfaces between the two fluid model and population balance technique.

Based on Chisholm's (1973) correlation wall liquid friction force F_{WL} (Eqs. 2.2 and 2.3) can be expressed as:

$$F_{WL} = \left[1+\left(Y_c^2-1\right)\left(B\left(X_c\left(1-X_c\right)\right)^{\frac{2-n}{2}}+X_c^{2-n}\right)\right]\Delta P_{L0}. \tag{2.6}$$

Here ΔP_{L0} is the single phase friction pressure drop, B is an empirical constant dependent on the fluid pair (B = 12500) and n = 0.25 for gas liquid system. X_c and Y_c can be expressed as follows:

$$X_c = \frac{1}{1+\frac{1-\alpha}{\alpha}\frac{\rho_l}{\rho_g}\frac{\overline{u_l}}{\overline{u_g}}} \text{ and } Y_c = \left(\frac{f_{G0}\rho_l}{f_{L0}\rho_g}\right)^{0.5}. \tag{2.7}$$

Wall friction factor for the secondary phase is also calculated in the same manner. As there is no mass transfer between two phases, F_{GI} and F_{LI} can be neglected.

Turbulent dispersion force of secondary phase is considered in the form of Favre averaged variables (Burns et al., 2004) as

$$F_{td} = C_{td} C_D \frac{\gamma_t}{Sc_t} \left[\frac{\nabla \alpha}{\alpha} - \frac{\nabla \alpha_c}{\alpha_c} \right] \tag{2.8}$$

C_{TD} and C_D are the turbulent dispersion force coefficient and Drag force coefficient for a single bubble. C_{TD} is taken as 0.1 in the present simulation. γ_t is turbulence kinetic viscosity and Sc_t is turbulent Schmidt number of the secondary phase.

2.2.3. Population balance equation

A population balance (Ramkrishna, 2000) has been incorporated in the present model to keep account of bubble evolution in the bulk of continuous phase due to coalescence and breakup. As a result of these processes bubbles of new groups (birth) may appear and those of existing groups may disappear (death). Accordingly the population balance can be obtained in terms of birth and death rate.

$$\frac{\partial n(r,z,t;d)}{\partial t} + u_g \frac{\partial n(r,z,t;d)}{\partial r} + w_g \frac{\partial n(r,z,t;d)}{\partial z} = B_B(r,z,t;d) - D_B(r,z,t;d) + B_C(r,z,t;d) - D_C(r,z,t;d). \tag{2.9}$$

In the present model entire population of bubble is discretized into different subgroups of equal volume interval. As the bubbles are equispaced in volume, newly born bubble during coalescence explicitly falls in one subgroup node. This eliminates weighted distribution of intermediate bubbles into their neighbors during coalescence. Any bubble formed due to bubble breakage other than these pivotal sizes are distributed among the neighboring sizes keeping the bubble mass and number fixed (Fig. 2.2a). Nucleation of new bubbles as well as change in bubble size due to evaporation, condensation, shrinkage and elongation is not considered in the present model.

Present model only recognizes the appearance of newly born and disappearance of the extinct bubbles due to dynamic interactions in a fixed control volume. However, their redistribution is considered as random and solely guided by the advection of two phase mixture. Further, only binary coalescence and binary breakage of the bubbles are considered.

2.2.4. Bubble breakage

Collision with turbulent eddies (Fig. 2.2b) are considered as the mechanism of breakup. Breakage of a bubble is possible only when the turbulence kinetic energy of the striking eddy supersedes the effect of surface energy of the interacting bubble (Wang et al., 2003). Breakup occurs when an eddy of size comparable to the bubble characteristics length collides with it. If the eddy size is larger than the bubble characteristics length, collision between them is unable to make any crater over the bubble shape. Thus, in Fig. 2.2b only eddies denoted by 1, 2 and 3 are effective for breakup process. Sizes of the daughter bubbles due to breakage depend on the strength of eddies (Luo and Svendsen, 1996) which in turn depend on the local hydrodynamics.

Birth and death of bubbles due to breakup process can be calculated as follows:

$$B_B(r,z,t;d) = \int_d^\infty \eta(d'-d,d)\, v(d')\, g(d')\, n(r,z,t;d')\, \mathrm{d}d' \tag{2.10}$$

and $$D_B(r,z,t;d) = n(r,z,t;d)\, g(d). \tag{2.11}$$

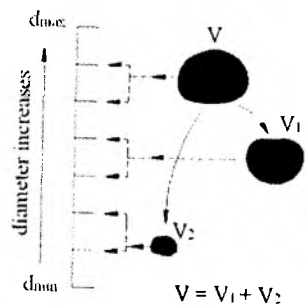

a. Redistribution of daughter bubbles

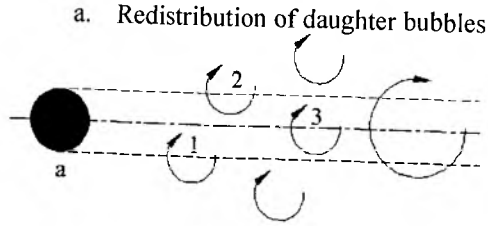

b. Breakage

Fig. 2.2 The scheme of redistribution and the mechanism of breakage

Based on the model proposed by Kostoglou and Karabelas (2006) bubble breakup frequency can be expressed as:

$$g(d) = k(1-\alpha)\left(\frac{\varepsilon}{d^2}\right)^{\frac{1}{3}} \int_0^1 \int_{\xi_{min}}^1 \frac{(1+\xi)^2}{\xi^{\frac{11}{3}}} e^{\left(-\frac{12c_1\sigma}{2.04\rho\varepsilon^{\frac{2}{3}}d^{\frac{5}{3}}\xi^{\frac{11}{3}}}\right)} d\xi df_v . \quad (2.12)$$

Here f_v is the ratio of the volume of mother and daughter bubbles and ε is the energy dissipation rate per unit mass which can be written in the following fashion (Ioannou et al., 2004) in terms of pipe diameter (D) and mixture velocity (U_m):

$$\varepsilon = \frac{fU_m^3}{2D} . \quad (2.13)$$

Here, U_m is calculated as follows:

$$U_m = \sqrt{\left(u_g^2 + w_g^2\right)^2} + \sqrt{\left(u_l^2 + w_l^2\right)^2} . \quad (2.14)$$

c_1 is an empirical constant and can be expressed in terms of f_v as follows:

$$c_1 = f_v^{\frac{2}{3}} + \left(1-f_v\right)^{\frac{2}{3}} - 1 . \quad (2.15)$$

ξ_{min} is the non-dimensional minimum daughter bubble size that can be obtained from the Kolmogroff microscale as described by Tsouris and Tavlarides (1994). For bubbles of size larger than a critical value instantaneous break up may take place because of the instability of the fluid-fluid interface. According to Carrica and Clausse (1993) the probability is given by:

$$g(d) = b^* \frac{(d-d_c)^m}{(d-d_c)^m + d_c^m} . \quad (2.16)$$

where d_c is the critical bubble diameter, set as 27 mm, b^* and m are model parameters set as 100 s^{-1} and 6.0, respectively (Carrica and Clausse, 1993).

Daughter distribution probability $\eta(d_1, d_2)$ proposed by Kostoglou and Karabelas (1998) is used in the present model as

$$\eta(d_1, d_2) = \left(\frac{1}{\frac{d_1}{d_2} + a} + \frac{1}{1 - \frac{d_1}{d_2} + b} + \frac{2(zi-1)}{b+0.5} \right) \frac{6I}{\pi d_2^3} , \quad (2.17)$$

where I is the normalization coefficient and expressed as:

$$I = \frac{0.5}{\ln(1+a) - \ln(b) + \frac{zi-1}{b+0.5}} \quad \text{and} \quad zi = \frac{a}{4b(1+b)(1-a)}. \tag{2.18}$$

a and b are parameters that define the shape of the daughter drop size distribution function. In the present model the values a = 0.1 and b = 1 are used that signifies "U" shaped bubble size distribution.

2.2.5. Bubble coalescence

For coalescence of bubbles to occur in the turbulent flow field of a two fluid mixture, the bubbles must first collide with each other and then remain in contact for sufficient time so that the processes of film drainage, film rupture and finally coalescence may occur (Fig. 2.3).

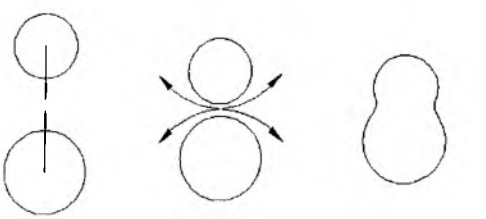

Fig. 2.3 Steps of coalescence process

The process of birth and death due to coalescence process can be expressed by the following expressions:

$$B_C(r,z,t;d) = \frac{1}{2}\int_0^{v(d)/2} \lambda\left(d_{v-v'}, d_{v'}\right) n\left(r,z,t;d_{v-v'}\right) n\left(r,z,t;d_{v'}\right) \mathrm{d}v' \tag{2.19}$$

$$\text{and} \quad D_C(r,z,t;d) = n\left(r,z,t;d_v\right)\int_0^{\infty} \lambda\left(d_v, d_{v'}\right) n\left(r,z,t;d_{v'}\right) \mathrm{d}v'. \tag{2.20}$$

The binary coalescence of two equal sized bubbles generates a daughter bubble having 1.26 times diameter of its parents. Therefore two bubbles having the dimension greater than 0.8D (D is tube diameter) will result a coalesced bubble of diameter greater than D. This obviously goes beyond the computational domain and is also physically unrealistic. Further, it has been reported (Tomiyama et al., 2003) that bubbles with diameter 0.6D represent a

transition to cap bubble or a Taylor bubble. With all these consideration maximum bubble diameter is restricted up to the half of the diameter of the pipe through which the flow occurs to attain transition between dispersed and separated flow.

Coalescence frequency $\lambda(d_1, d_2)$ is the product of the effective swept volume rate, $h(d_1, d_2)$ and film rupture efficiency $p(d_1, d_2)$. Effective swept volume rate is calculated using the analogy between kinetic theory of gasses and bubble coalescence phenomena. According to Coulaloglou and Tavlarides (1977) effective swept volume rate is calculated as:

$$h(d_1, d_2) = c_2 \frac{\varepsilon}{1+\alpha}(d_1 + d_2)^2 \left(d_1^{\frac{2}{3}} + d_2^{\frac{2}{3}} \right)^{\frac{1}{2}}. \tag{2.21}$$

Film drainage is controlled by inertia and surface tension forces (Chesters, 1991). For two bubbles of diameter d_1 and d_2 Coulaloglou and Tavlarides (1977) proposed the film rupture efficiency as follows:

$$p(d_1, d_2) = \exp\left[-\frac{c_3 \rho_l \mu_l \varepsilon}{\sigma^2 (1+\alpha)^3} \left(\frac{d_1 d_2}{d_1 + d_2} \right)^4 \right]. \tag{2.22}$$

The numerical constants c_2 and c_3 are related to the collision frequency and the rupture efficiency respectively. Values of c_2 and c_3 are taken as $0.0055\phi^{-1.3333}$ and $5.4\text{X}10^8$ as referred by Ioannou et al. (2004). They used the experimental data of Lovick (2004) to fit the values of the above constants.

From the above description it may be noted that no rigorous turbulence model has been used. As the two fluid model is not the "exact" one but an approximate representation of the flow dynamics, any turbulence closure incorporated in the two fluid model also suffers from the same limitation. There are different options for turbulent closure in a two fluid model. All the closure relationships depend on empiricism of different magnitudes. Several researchers (Hu and Zhang, 2007; Ekambara et al., 2008) used k-ε model for turbulence in two phase flow as this model gives reasonably good predictions in a number of single phase problems. k-ε model uses a number of empirical constants derived from single phase experiments. The applicability of these constants in two phase flow is questionable.

Further, wall function for two phase flow is not as standardized as in the case of single phase flow. It may be appreciated that the presence of dispersed phase will change the wall function; particularly as the dispersed flow can have different structures like core peaking,

wall peaking etc. According to Prof. Prosperetti (Prosperetti and Tryggvason, 2007) the adoption of k-ε model can not be justified other than "a very crude approximation". In the absence of any unequivocally accepted turbulence closure in two phase flow a simple turbulence energy dissipation function (Eqs. 2.13) has been used in the present model. However, the model developed by this adoption gives reasonably good predictions for a number of experimental results.

2.3. Boundary condition and solution procedure

For dispersed flow in a vertical duct following boundary conditions are employed:

i. For both the phases, at the inlet uniform velocity profile in stream wise direction and zero velocity at the crosswise direction is assumed. No slip condition is prescribed at the wall of the conduit.

ii. Void fraction of secondary phase (α) and pressure at the inlet are specified.

iii. For a better simulation of the flow field finer grid have been used near the wall. A small velocity as per the logarithmic law of buffer layer is implemented at a very small distance from the conduit wall (Schumann, 1975).

iv. Uniform distribution of equal sized bubble of secondary phase is considered at the inlet whereas initially (t=0) the conduit is filled up only with the primary phase. It can be expressed as:

$$n(r,0,t;d) = \begin{matrix} \text{constant} & \text{for } d = d_{in} \\ 0 & \text{for } d \neq d_{in} \end{matrix} \qquad (2.23)$$

and

$$n(r,z,0;d) = 0\,, \qquad (2.24)$$

where d_{in} is the bubble size of secondary phase entering at the inlet plane and can be selected as desired. This mimics a situation where the secondary phase is introduced into the conduit by a large number of nozzles uniformly distributed at the inlet section.

v. Overall possible bubble sizes of secondary phase $\left(\xi_{\min} \le \frac{d}{2} \le \frac{D}{2}\right)$ are divided into 40 equal volumes to simulate a realistic flow phenomenon.

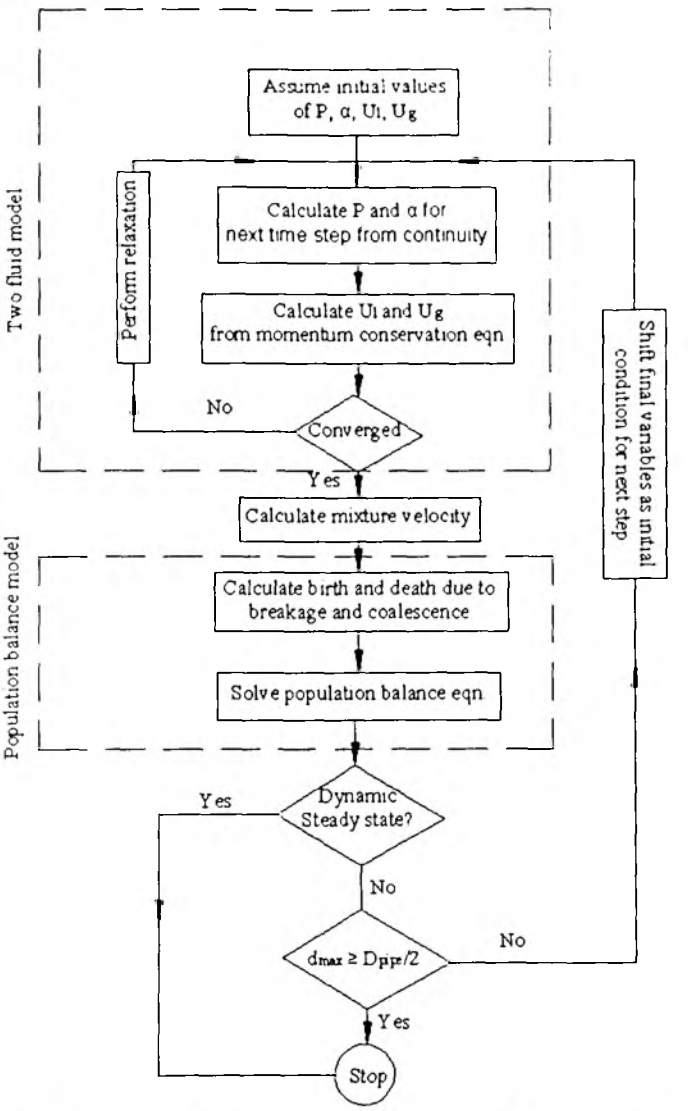

Fig. 2.4 Solution methodology of the proposed hybrid model

Solving Eqs. 2.1-2.3, velocity field at each grid point is calculated and is subsequently used for determining the mixture velocity at that particular position. 0.1% convergence criteria is used for both velocity and density field of the bubbly flow situation. Mixture velocity is used to determine the distribution of bubble size for the next instant based on the population balance equation (Eqs. 2.9). Fig. 2.4 shows the solution methodology of the proposed model. Simulation is forward marched till either a steady dynamic solution

$(\frac{\partial}{\partial t} n(r,z,t;d) \approx 0$ for all $d)$ is reached or the hydrodynamics gives a clear indication towards the transition into a different flow regime. Using the developed methodology and boundary conditions three different situation of bubbly flow is studied in the next sections.

2.4. Gas liquid upflow through a vertical circular duct

2.4.1. Grid independent test

Downward bubbly flow in circular conduit has been simulated using developed two fluid model along with the population balance technique. Solution of the model based on the algorithm shown in Fig. 2.5 gives the phase velocity and void fraction at any particular point of conduit. Computations have been done selecting different mesh size and time step to check the grid independence and to find out optimal values of grid spacing as well time step. Results on the effect of mesh size on void distribution are depicted in Fig. 2.5. From this study it is decided that 20 radial grids will be sufficient for a compromise between the accuracy and the computational time. For the flow field to become fully developed total length of the pipe is assumed to be minimum of 100D. Grid independent studies have also been made for axial direction and 1000 nodes were found to be sufficient for that. Total number of cells then turns out to be 18981.

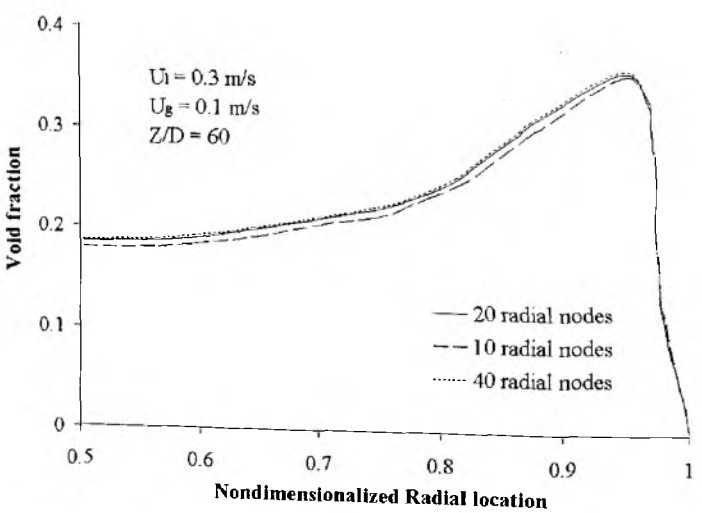

Fig. 2.5 Effect of radial mesh refinement on void distribution

2.4.2. Model validation

There is a considerable volume of gas liquid bubbly two phase flow data in open literature. Among them one pioneering work by Serizawa et al. (1975) and one recent work by Ohnuki and Akimoto (2000) are selected for the verification of the present model. Comparisons of the present simulation against these data are described below.

In Fig. 2.6 computational results are compared with the data of Serizawa et al. (1975) for various inlet qualities and reported bubble diameters. Simulation results are taken at a considerable distance (30D) from the inlet plane to avoid the effect of entrance region. Liquid velocity is kept at 1.03 m/s to make the comparison relevant. Void fractions at different qualities are presented with respect to nondimensionalized radial position. Though there is a mismatch in the profiles near the wall it is clear from Fig. 2.6 that the model predicts the radial void fraction distribution satisfactorily. Near the wall, an improved modeling of the motion of the continuous phase including the effect of boundary layer and buffer layer may give a better result.

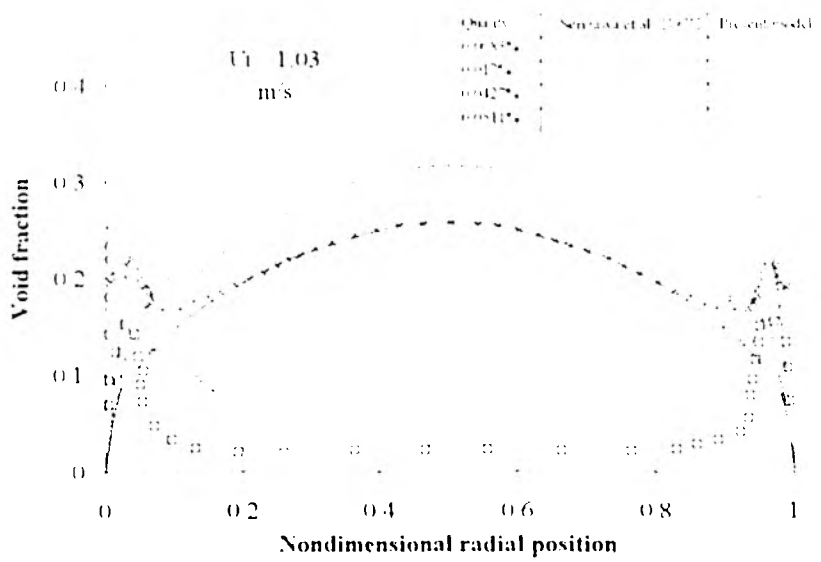

Fig. 2.6 Radial distribution of void fraction- comparison of present model with the experiment of Serizawa et al. (1975)

Ohnuki and Akimoto (2000) have used optical void probe for void fraction measurement and dual sensor resistivity probe for the measurement of bubble velocity and its fluctuation

measurement. In Fig. 2.7 radial distribution of void fraction generated by numerical simulation with identical conditions is compared with the results of Ohnuki and Akimoto (2000) for a liquid velocity of 0.18 m/s and gas velocity of 0.11 m/s and a satisfactory agreement has been observed. Void fraction profile for a higher liquid flow rate of 0.35 m/s keeping the air flow rate same (0.11 m/s) is also depicted in the same figure. Simulations using the same velocities of both the phases as reported by Ohnuki and Akimoto (2000) show a good agreement.

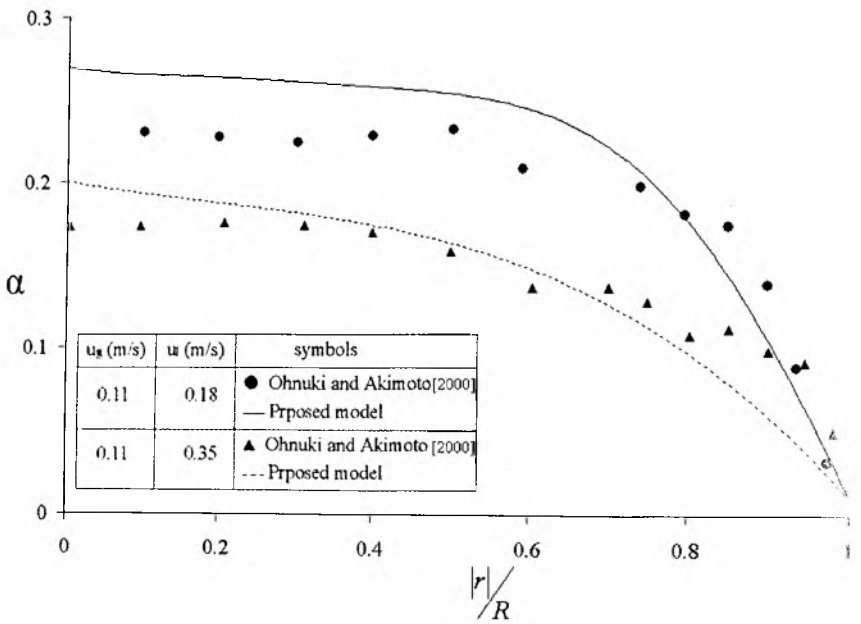

Fig. 2.7 Radial distribution of void fraction- comparison of present model with the experiment of Ohnuki and Akimoto (2000)

Comparisons of the predicted radial profile of volume averaged bubble diameter with experiment are depicted in Fig. 2.8. The developed model predicts the correct trend though it under predicts bubble diameter towards the tube wall.

Present model is also used to investigate the distribution of bubble Sauter diameter in a radial plane. Computed result of bubble Sauter diameter is compared with experimental observation of Shen et al. (2005) for air water flow through a tube diameter of 200 mm. Fig. 2.9 shows a very good prediction of Sauter mean diameter at a gas superficial velocity 0.186 m/s for three different liquid superficial velocities covering a wide range. Prediction is also

satisfactory for higher gas superficial velocity as depicted in Fig. 2.10. With the confidence gained from the above comparisons the present model has now been employed to investigate the development of flow along the axial direction and the transition from bubbly to slug flow.

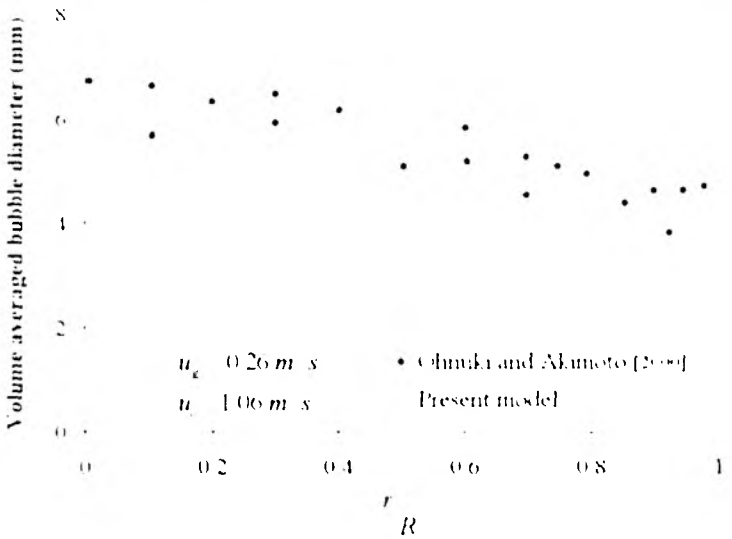

Fig. 2.8 Radial distribution of volume averaged bubble diameter- comparison of present model and experimental data of Ohnuki and Akimoto (2000)

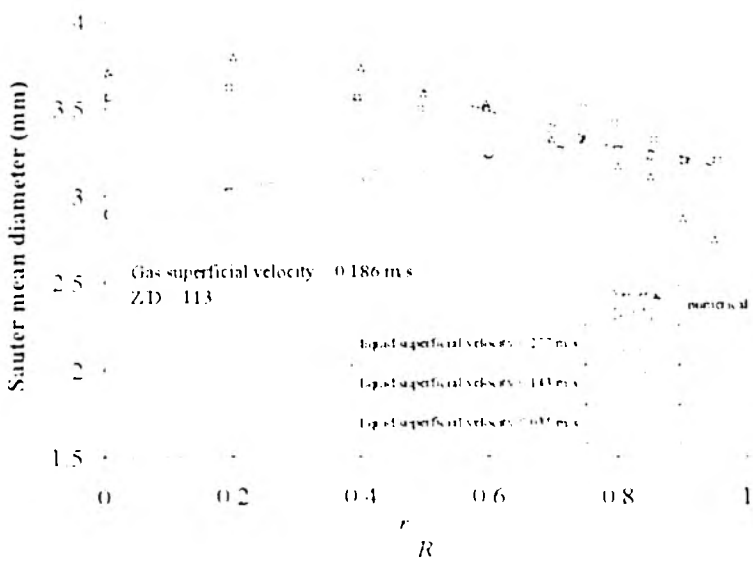

Fig. 2.9 Comparison of computed bubble Sauter diameter along a radial plane with the experimental result of Shen et al. (2005) at low gas superficial velocity

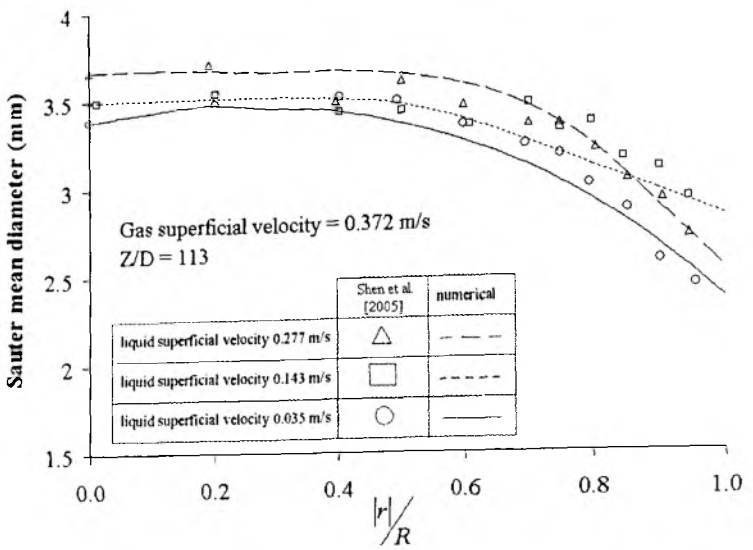

Fig. 2.10 Comparison of computed bubble Sauter diameter along a radial plane with the experimental result of Shen et al. (2005) at high gas superficial velocity

2.4.3. Prediction of bubbly-slug transition

It is clear from the available literature and above mentioned validation that the application two fluid model along with PBM or interfacial area transport equation has produced reasonable success in the prediction of bubbly flow. However, till date not much effort has been made to predict the transition of co-current bubbly flow through a circular conduit using CFD. At low and moderate liquid flow rate bubbly flow transforms into slug flow with the increase of air flow rate, whereas transition from bubbly to dispersed bubbly flow is observed at high liquid flow rates (Wallis, 1969). Classically these transition criteria have been derived from control volume based approach using a number of simplifying assumptions (Taitel et al., 1980; Mishima and Ishii, 1984).

From these criteria transition is predicted based on the phase superficial velocities without taking other process parameters (like tube diameter, inlet bubble size distribution etc.) into cognition. Further, a considerable variation has been reported in the transition boundaries observed in different experiments. It is expressed that CFD technique can be a better tool for identifying the transition criteria for bubbly flow. Bubbly flow shifts towards dispersed

bubbly flow due to breakage of droplets into the smaller ones as the liquid velocity increases. On the other hand, increase of gas velocity transforms the bubbly flow into slug flow by virtue of coalescence. A schematic diagram of the bubbly flow regime along with its neighboring regimes plotted on a liquid velocity vs. gas velocity 2D plane is depicted in Fig. 2.11.

Due to the coalescence and breakup of the bubbles during their random motion, number of bubbles in a particular subgroup may increase or decrease in the downstream. This is solely guided by the hydrodynamics. Some interesting cases are discussed below from the hydrodynamic study of gas-liquid bubbly flow.

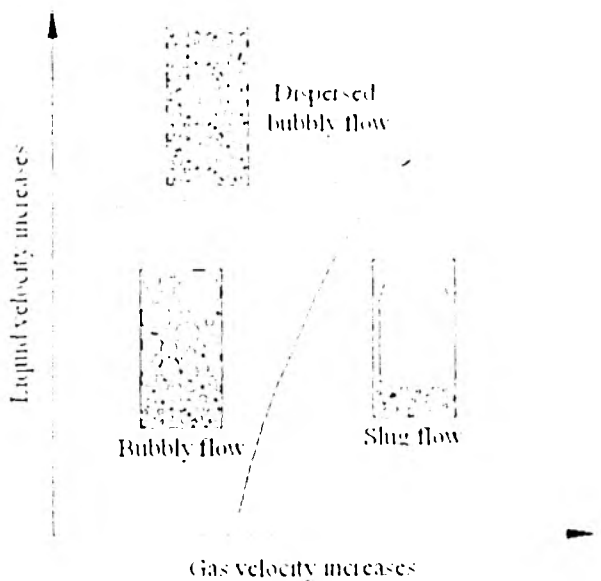

Fig. 2.11 A Schematic diagram of flow patterns- bubbly flow and its transition

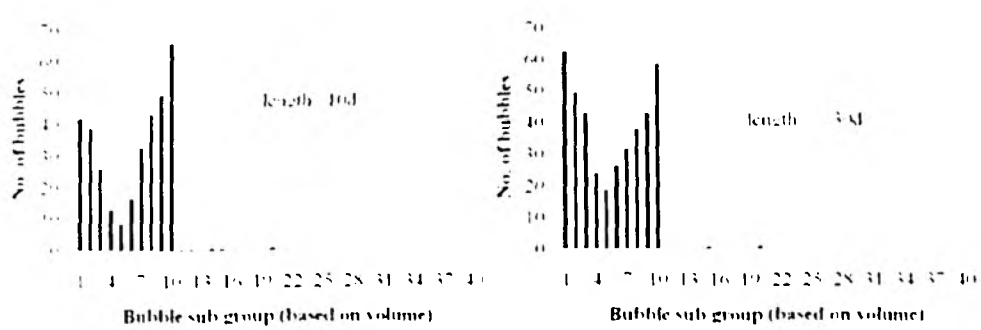

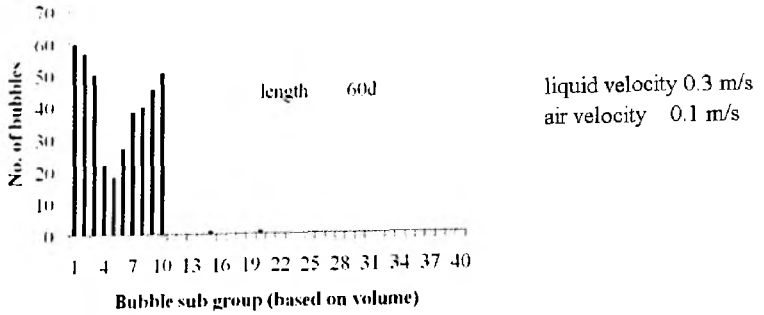

Fig. 2.12 Radial bubble count histogram at different axial locations for low flow rates

In Fig. 2.12a-c the bubble count of different subgroups in a radial plane is shown for different axial positions. Bubbles of 10^{th} subgroup (2.145 mL) are introduced at the inlet. It may be noted that for a liquid velocity 0.3 m/s and air velocity 0.1 m/s there is no bubble growth due to coalescence, rather there is formation of smaller size bubbles as one moves towards the downstream.

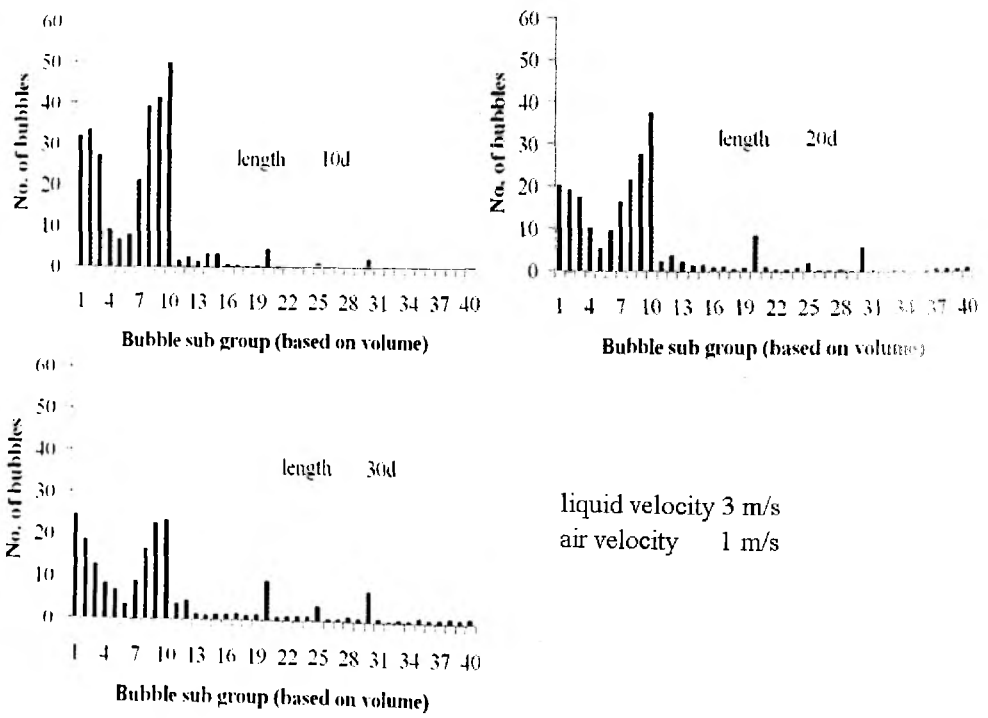

Fig. 2.13 Radial bubble count histogram at different axial locations for high flow rates

The coalescence of bubbles is clearly discernable from Fig. 2.13a-c at a high phase velocities (liquid velocity of 3 m/s and gas velocity of 1 m/s) even at an axial length of 10D. At this position one can see formation of bubble up to a subgroup of 30 that is considerably large compared to the bubbles introduced at the inlet plane (10th subgroup). Further downstream the number of large size bubbles (V_{30}-V_{40}) increases and new bubbles with even larger diameter come into existence.

To confirm the generation of larger bubbles at higher gas and liquid flow rates a total volume count of bubbles above and below those introduced at inlet are depicted in Table 2.1.

Generation of larger bubbles at higher phase flow rates can also be confirmed by taking an account of the volume of the bubbles of different subgroup. For these a non-dimensional parameter namely $V_{i,p}$ has been defined as follows:

$$V_{i,p} = \frac{\sum_{i=p+1}^{m} v_i n_i}{\sum_{i=1}^{m} v_i n_i} \qquad (2.25)$$

where pth subgroup of bubbles enters at the inlet. $V_{i,p}$ at different axial planes for low and high phase flow rates are presented in Table 2.1 and 2.2.

At low phase flow rates (Table 2.1) the value of $V_{i,p}$ is relatively low and assumes a constant value after some distance from the inlet plane. This indicates the existence of a steady bubbly flow for the given hydrodynamic parameters. As the flow develops, downstream of the inlet plane coalescence and breakup occurs, the process of break up being more dominant compared to coalescence.

Table 2.1 Bubble volume account below and above the bubble size introduced at the inlet for liquid velocity 0.3m/s and gas velocity 0.1m/s

Axial location	$\sum_{i=p+1}^{m} v_i n_i$ in (m^3) X 10	$\sum_{i=1}^{m} v_i n_i$ in (m^3) X 10^{-3}	$V_{i,p}$
10D	4.588	2.962	0.01525
30D	4.689	2.96	0.01559
60D	4.701	2.98	0.015526

Table 2.2 Bubble volume account below and above the bubble size introduced at the inlet for liquid velocity 3m/s and gas velocity 1m/s

Axial location	$\sum_{i=p+1}^{m} v_i n_i$ in (m^3) X 10^{-4}	$\sum_{i=1}^{m} v_i n_i$ in (m^3) X 10^{-3}	V_{high}
10D	6.67	2.331	0.2225
20D	13.99	1.609	0.4663
30D	18.95	1.104	0.6317

However, these two competing processes reach a dynamic steady state where the maximum bubble size can never cross a certain limit to perturb the flow towards slug flow regime. The flow essentially remains bubbly though there is a readjustment of bubble size and void distribution compared to the inlet plane.

Table 2.2 presents a different picture. V_{high} increases continuously along the downstream. This signifies domination of coalescence over break up. Importantly, it indicates gradual growth of some bubbles as they move up. This is conducive for the generation of cap bubbles to start with and for the formation of Taylor bubble finally.

To probe the bubble size evolution with axial length a cumulative estimate volume of bubbles with diameters larger than those introduced at the inlet is shown in Fig. 2.14. The inlet velocity of air is taken as 0.1 m/s and inlet velocity of liquid is 0.3 m/s. The figure clearly supports the statement made above from the observations of Table 2.2. Though coalescence is present, it is not strong enough to generate new bubbles of larger diameter ($d_i > d_p$) in sufficient quantity. On the other hand, the process of breakup is more significant and is able to create smaller bubbles ($d_i < d_p$).

Another interesting feature may be noted from the Fig. 2.14. Beyond L/D of 100, volume count above and below the bubble size introduced at the inlet does not change with the pipe length. This gives an idea regarding the pipe length required for the development of the flow. There is enough controversy regarding the developing length in case of two phase flow. CFD simulation is capable of resolving this issue. Obviously the criterion for the developing length depends on the operating conditions as will be clear from the results presented below.

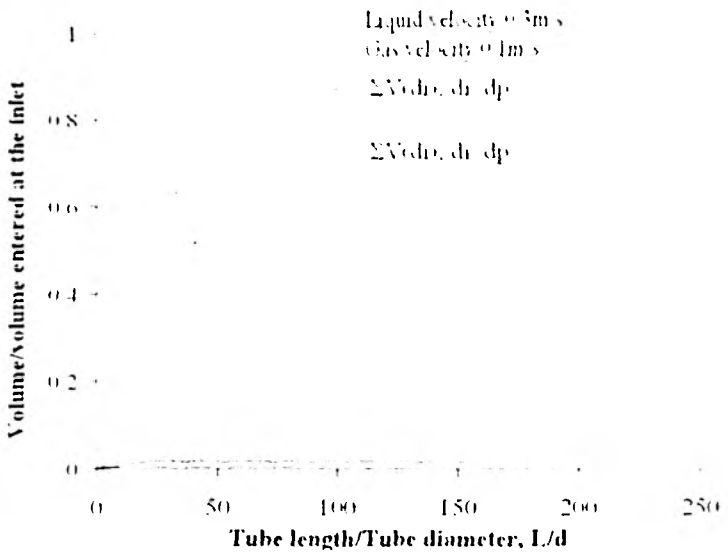

Fig. 2.14 Evolution of bubble volume from the input volume with axial location at lower flow rates

In the Fig. 2.15 an assessment of the breakage and coalescence process along the axial direction has been made by taking an account of the bubbles with size below and above those (d d_P) entering the inlet plane. At a liquid velocity of 0.3 m/s and gas velocity of 0.1 m/s the coalescence rate is very low and remains more or less constant along the axial length. On the other hand, downstream of the inlet plane the local breakage rate undergoes a large fluctuation. The fluctuation continues along the axial direction with diminishing amplitude and ultimately stabilizes into a steady periodic nature with a very small amplitude. Referring back to Fig. 2.12a-c one can appreciate the presence of a stronger breakup process compared to the process of coalescence for the selected phase velocities. It is also evident from Figs. 2.14 and 2.15 that the two phase flow assumes a dynamic steady state downstream of the inlet plane where the time averaged flow characteristics do not change axially.

The morphology of the dispersed phase goes through a different developmental pattern at higher phase flow rates. Fig. 2.16 shows that a vigorous process of coalescence starts immediately after the bubbles enter the conduit. However, the coalescence rate reduces and ultimately stabilizes to a fluctuating pattern with a small amplitude. The process of break up on the other hand is rather insignificant. The net effect of coalescence and breakup on the

bubble size distribution is depicted in Fig. 2.17 which clearly indicates the zone for flow development.

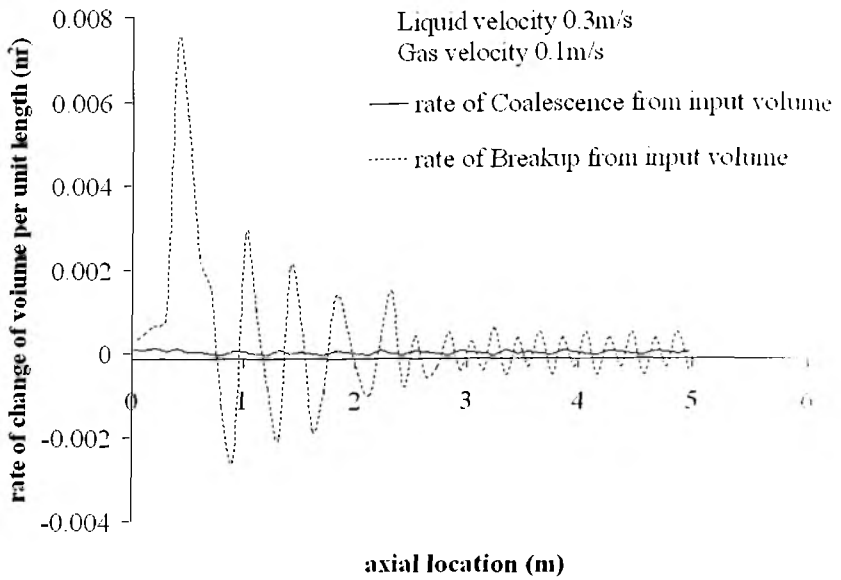

Fig. 2.15 Variation of breakage and coalescence with axial length at lower flow rates

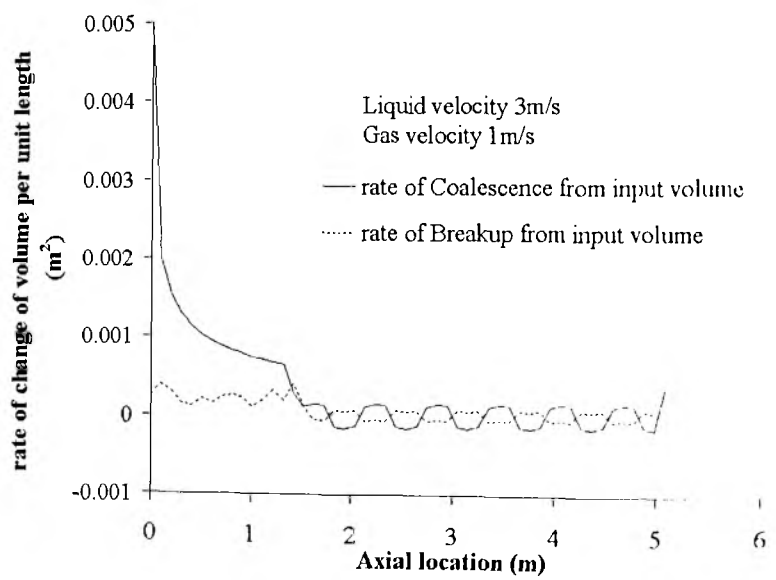

Fig. 2.16 Variation of breakage and coalescence with axial length at higher flow rates

The evolution of bubble size along the conduit length as a function for typical inlet flow rates is depicted in Fig. 2.18. From the figure it is evident that at lower flow rates of gas and

liquid (0.1 m/s & 0.3 m/s respectively) maximum bubble size remains unaltered (more or less identical to the bubbles at the inlet). This clearly shows that in the flow field bubble break up is dominant leading towards the flow of different sized spherical bubbles i.e. bubbly flow. At higher flow rate the bubble size reaches the prescribed maximum limit of bubble diameter. This clearly indicates a possible transition from bubbly flow.

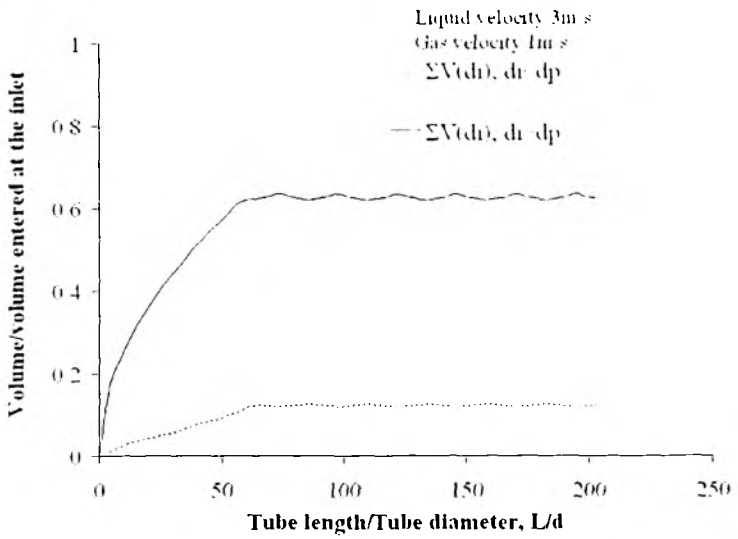

Fig. 2.17 Evolution of bubble volume from the input volume with axial location

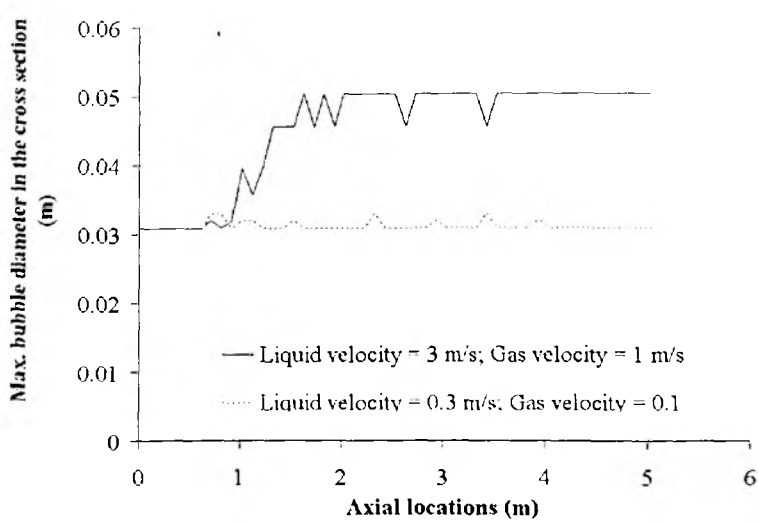

Fig. 2.18 Change of maximum bubble diameter along axial length for air water bubbly flow

Identification of flow regime boundary has been achieved either through experimental (Nakoriakov et al., 1996; Lucas et al., 2005) or by control volume based analytical modelling. Assuming the transition to slug flow takes place due to high frequency of collisions at an increased density of dispersed bubble Radovicich and Moissis (1962) proposed a semi theoretical analysis. They have considered a cubic lattice of spherical bubbles fluctuating around their mean position and suggested that the transition occurs at a maximum limiting void fraction of 0.3 for bubbly flow. This physical model has also been supported by Dukler and Taitel (1977) and Mishima and Ishii (1984). However, there is a difference in opinion regarding the value of the maximum limiting void fraction though a value of 0.25 is well accepted in the literature.

A slightly different view is proposed by Bilicki and Kestin (1987). The spherical bubbles dispersed in a bubbly flow do not move with identical velocities. The wake of a preceding bubble induces acceleration to its successors. A bubble may catch up its predecessors and may coalesce to form a larger bubble. According to them this is the root cause of transition. For the success of coalescence process, the distance between the two bubbles should be below a characteristics length which is stochastic in nature depending on the flow phenomena. Based on this argument they proposed a transition criterion which depends on a limiting void fraction, phase superficial velocities, "local friction velocity" and some numerical constants. The numerical constants were determined by experiments.

Some researchers have proposed void fraction wave as the cause of transition from bubbly to slug flow. Marcedier (1981) observed that void fraction waves are damped in bubbly flows where the damping decreases with the increase in the mean void fraction. It has further been hypothesized that at some value of mean void fraction the damping could disappear and the instability of the void fraction wave may give rise to bubble-slug transition. Matuszkiewicz et al. (1987) took the queue from this postulation and experimentally demonstrated that transition from bubbly to slug flow occurs for a range of average void fraction $0.1<\alpha_{mean}<0.45$. It may be noted that this value is different from the limiting void fraction reported by Taitel et al. (1980).

Sun et al. (2002) conducted an experiment on gas-liquid two phase up flow in a tube diameter of 112.5 mm where disturbance was created by a swinging metallic plate at the upstream of the flow. Bubbly flow was observed upto a mean void fraction of 19.2%. Sudden emergence of Taylor bubble was observed at a gas concentration of 21.5%. This induces a

transition to slug flow. They also observed at high liquid velocity the intense turbulence suppresses the formation of Taylor bubbles. As a result an increase in mean void fraction transforms the bubbly flow directly to churn flow.

Alternatively, efforts have been made to characterize the termination of bubbly flow based on maximum bubble diameter. Again different criteria have been used. Tomiyama et al. (2002) considers a bubble to be a slug bubble when its equivalent diameter is 0.6 of tube diameter. Ruzansenberg et al. (1999) and Lucas et al. (2005) also suggest a differentiation between bubbly flow and slug flow based on the equivalent diameter of the largest bubble.

It may be noted that the transition criteria predicted from experimental observations are system specific and are dependent on operating conditions. On the other hand theoretical predictions developed so far are based on "control volume" type analysis of mechanistic models. They typically rely on a specific mechanism and a number of simplified assumptions. Till date little effort has been made to apply CFD simulation for the identification of flow regime boundary. In the present work we present a methodology for the same.

It has been accepted beyond doubt that coalescence is the mechanism for the transition from bubbly to slug flow. However, coalescence is a spatio-temporal process. It is necessary to investigate the hydrodynamics both locally and axially to bring out a clear picture about the transition. Further, as coalescence and breakup simultaneously occur we propose monitoring of three different characteristics.

- Formation of large size bubble is of crucial importance.
- Number of large bubble should increase and individual large bubble should further grow in size
- Finally, the consistency of the above two process should also be reflected in a diminishing rate of bubble breakup.

To monitor these three aspects we have studied

i) the bubble histogram at different axial levels

ii) bubble volume account below and above the bubble size introduced at the inlet

iii) breakage and coalescence frequency along the axial length.

Based on the above criteria transition from bubbly to slug flow has been predicted and compared with the experimental observation of Dukler and Taitel (1977) in Fig. 2.19. An

excellent match between our prediction and experimental result has been observed. It can also be noted that the prediction by the present method is better than that of Taitel et al. (1980).

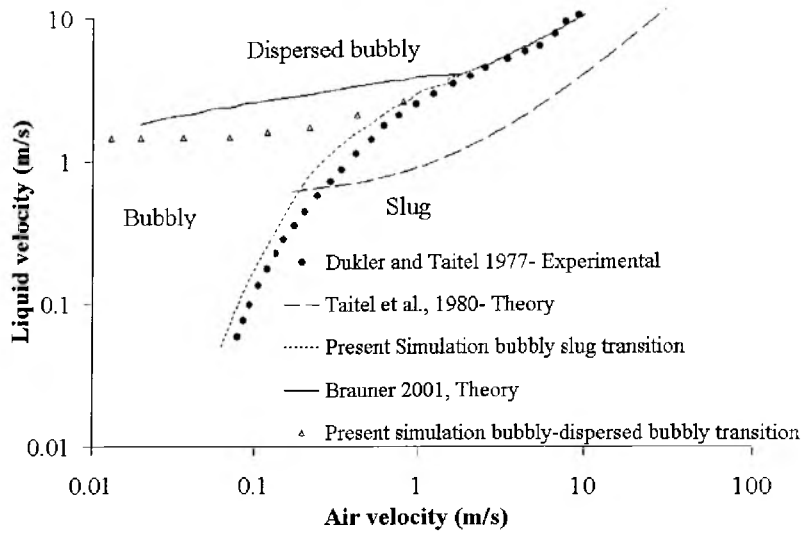

Fig. 2.19 Transition of bubbly flow to other flow regimes- comparison with the experimental results of Dukler and Taitel (1977) and Brauner (2001)

2.4.4. Prediction of bubbly-dispersed bubbly transition

A second type of transition from bubbly flow at high liquid velocity was proposed by Taitel et al. (1980). This flow regime is different from bubbly flow at low liquid velocity and is termed as dispersed bubbly flow. Hinze (1955) proposed a mechanism for estimating the maximum bubble size from a balance between turbulence kinetic energy and drop surface energy. Hinze's (1955) analysis is applicable for dilute suspension. Brauner (2001) extended Hinze's (1955) model for dense dispersion and obtained a modified expression for maximum bubble diameter. They have further suggested considering the largest of the diameter value calculated by the original Hinze (1955) theory and its extension. For the present system the diameter of the largest dispersed bubble is given by the following equation

$$D_{surf} = 0.55D\left(\frac{\rho_l u_l^2 D}{\sigma}\right)^{-0.6}\left(\frac{\rho_m f}{\rho_l(1-\varepsilon)}\right)^{-0.4}. \qquad (2.26)$$

To investigate the bubbly to dispersed bubbly transition in the perspective of the present CFD model the simulations have been done for higher liquid flow rates. A typical result of

bubble count histogram can be seen in Fig. 2.20. It may be noted that the operating condition lies within the dispersed bubbly flow regime proposed by Taitel et al. (1980).

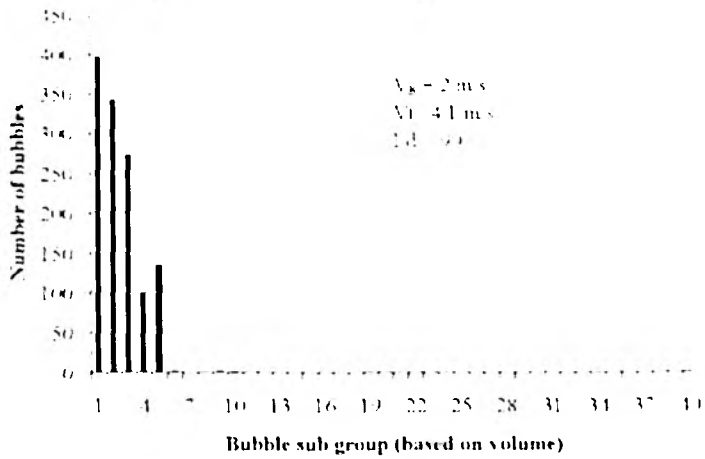

Fig. 2.20 Radial bubble count histogram at an axial distance of 90D for high liquid flow rate showing dispersed bubbly flow

The figure clearly depicts the generation of smaller sized bubbles from the introduced 10^{th} subgroup of bubble and the strong suppression of the process of coalescence. To get an overall picture of the flow development with the change of liquid velocity one may refer to Fig. 2.21, where simulation results for a single gas velocity at three different liquid velocities have been shown. The volume histogram clearly indicates slug flow, bubbly flow and dispersed bubbly flow with the increase of liquid flow rates. Finally, the occurrence of critical dispersed bubble (Eqs. 2.25) as a function of phase superficial velocities has been depicted in Fig. 2.19. The simulation result shows a good match with the regime boundary mechanistically predicted by Brauner (2001).

2.4.5. Development of radial void distribution

Though bubbly flow often appears as a homogeneous dispersion of gas bubbles in a liquid medium, in reality, the flow regime is rather complex due to the presence of different spatial-temporal structures and interplay of various complex mechanisms. Hydrodynamics of bubbly flow strongly depends also on the phase distribution and bubble population along the radial direction. It is well known that the pattern of void distribution in a cross sectional plane could

be wall peaked or core peaked depending on the operating condition (Serizawa et al., 1975; Sekoguchi et al., 1981; Zun, 1990; Song et al., 2001). This gives rise to different peaked structure (Serizawa et al., 1975; Zun, 1990; Ohnuki and Akimoto, 2000) of the void fraction and also influences the transition.

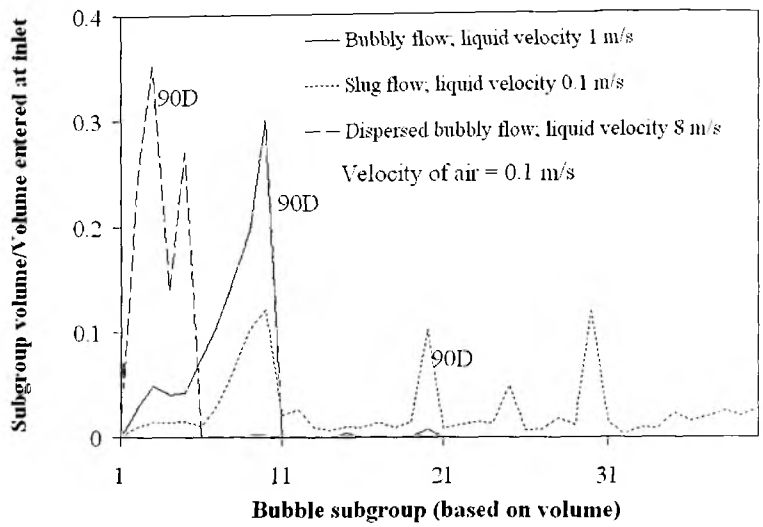

Fig. 2.21 Bubble volume histogram for different liquid velocities at air velocity 0.1 m/s showing different flow regime

Further, bubbly flow is also influenced by the characteristics of the input bubbles. Development of void profile is not identical in the case of mono dispersed bubble input and poly dispersed bubble input. In a number of experiments on gas liquid up flow through vertical conduits non uniform void distribution has been observed at the downstream while gas bubbles were introduced uniformly at the inlet plane. Theoretical simulations of bubbly flow (Cheung et al., 2006) also corroborate the peaked characteristic of the void profile. It is important to note that not only the absolute value of void fraction varies in different flow regimes, each regimes may have a few typical patterns for radial distribution of void fraction. Therefore, efforts have been made to investigate further into the transformation of void profile due to the operating and inlet conditions.

The present model is compared with the experimental void fraction obtained by Zun (1990), Song et al. (2001) and Lucas et al. (2007) in case of two phase flow mixture of air and water in vertical ducts.

An extensive study of bubbly flow (Lucas et al., 2007) has been made in the MTLoop facility. The test section in this loop has an inner diameter of 52.3 mm and a length of 3.5 m. Wire mesh sensors have been used for the measurement of void fractions at a distance of 60D from the inlet. Fig. 2.22 shows the results at an air flow rate of 0.0096 m/s and water flow rate of 0.0405 m/s. Most of the bubbles are gathered near the wall of the tube. Results from the present model also show a similar pattern of the void fraction distribution.

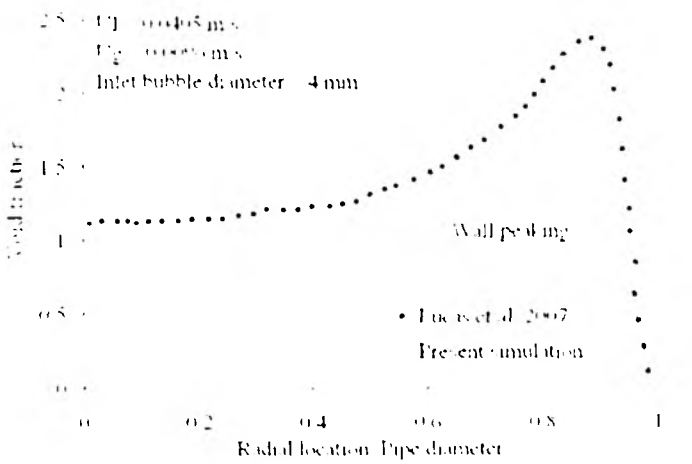

Fig. 2.22 Comparison of void distribution at low phase flow rates, present model versus experimental observations of Lucas et al. (2007)

Similar experiments were conducted by Prasser et al. (2007) where they have used larger tube having 195.3 mm diameter and 8.78 m length. At an air flow rate of 0.53 m/s and water flow rate of 1.02 m/s they have observed the distribution pattern to change (Fig. 2.23) into a parabolic shape exhibiting core peak of the bubbles. Simulations have been made for identical conditions and the results agree with experiment satisfactorily (Fig. 2.23). This shows that the present model can handle both inward and outward lateral migrations of bubbles depending on the flow velocities and tube diameter.

Zun (1990) proposed that uniform input of big bubbles at the inlet produces a core peak while smaller bubbles at the inlet produce a wall peak. Interestingly, when a mixture of big and small bubbles is introduced at the inlet simultaneous occurrence of wall and core peaks is possible at further downstream. According to Zun (1990) the bubbles having high intrinsic oscillatory motion stay near the wall and others settle at the core of the conduit, the amplitude of the oscillation being a strong function of the bubble diameter. To demonstrate this, Zun

(1990) conducted an experiment using a vertical conduit of square cross section having 25.4 mm sides. Downstream gas void fraction was measured using microresistivity probes. Experiments were conducted for different inlet bubble sizes and different void fractions. In general, experiments were conducted for low gas flow rates. Results are depicted in Fig. 2.24. As the present model is an axisymmetric one an exact simulation of Zun's (1990) result is not possible. However, simulations have been done for a circular tube (25.4 mm diameter) using identical operating conditions. Simulation results exhibit excellent trend matching with the experimental results of Zun (1990).

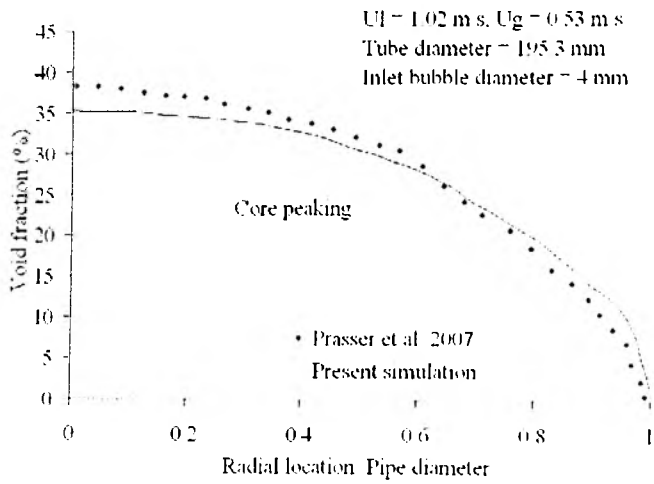

Fig. 2.23 Comparison of void distribution at high phase flow rates, present model versus experimental observations of Prasser et al. (2007)

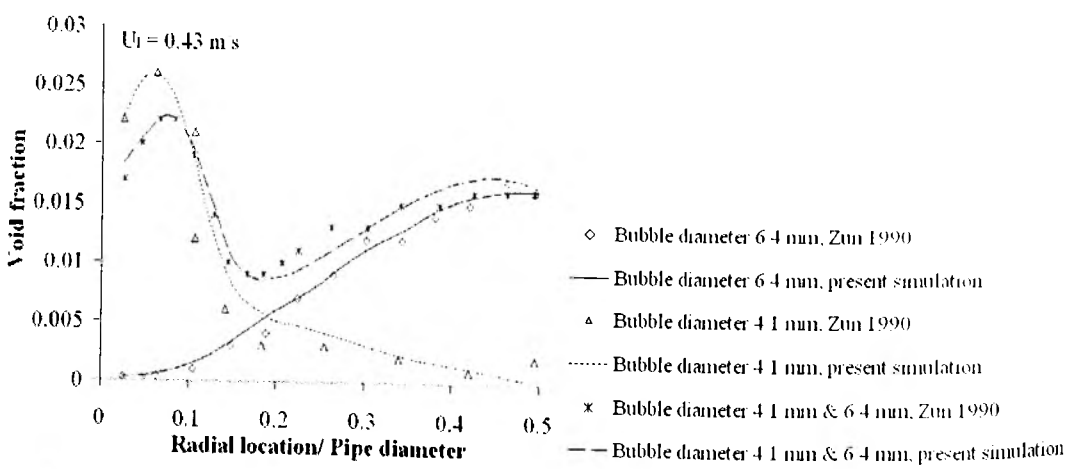

Fig. 2.24 Two peak void distribution; present model vis-à-vis experimental observations of Zun (1990)

The shape of void distribution in the downstream due to the injection of two different bubble sizes at the inlet has also been investigated by Song et al. (2001). They have used 29 mm inner diameter vertical tube of 3.7 m length to study the voidage profile development in a mineral oil-air flow. Nozzles of different size were used to produce bubbles of two different diameters. 3D photographic method was used for measuring the position of the bubbles and void fraction profile was derived from it. Fig. 2.25 shows the comparison of estimated void distribution with the experimental observation by Song et al. (2001) for the simultaneous entry of 3.4 and 2.5 mm diameter bubbles. Liquid flow rate is kept at 0.079 m/s and air flow rate is maintained at 0.0082 m/s. Generated results were presented at an axial length of 60D to avoid the effect of entrance length in Fig. 2.25. The model prediction is matching significantly well with the experimental data.

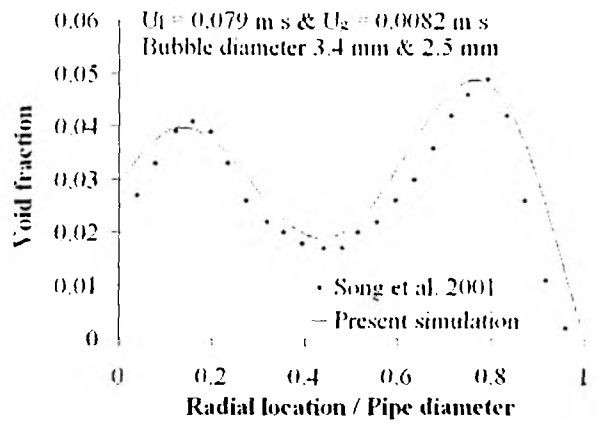

Fig. 2.25 Two peak void distribution; present model vis-à-vis experimental observations of Song et al. (2001)

Occurrence of different peaked structure of the voidage profile in bubbly flow has been observed in different independent experiments (Serizawa et al., 1975). As the evolution of the different pattern of the voidage profile is complex in nature CFD simulation can be the best possible option for studying the phenomena.

2.4.6. Regime map for different peaked structure

It is a well recognized fact that flow regime transition is not a discrete event. It is more likely that a fully developed bubbly flow transforms into a fully developed slug flow through

a gradual change. In this regard the different peaked structure of the voidage distributions in bubbly flow may have a role to play. The present model has been used to investigate this. For a case study, uniform distribution of bubbles of 0.05D has been considered at the inlet plane and the void fraction profile is investigated at 60D from the inlet. Fig. 2.26 shows the boundary obtained between wall peaking void fraction profile and core peaking void fraction profile based on liquid and gaseous phase flow velocities. To make a comparison with the available void distribution map results of Serizawa and Kataoka (1987), Ohnuki and Akimoto (2000) and Lucas et al. (2005) are depicted in the same figure. Serizawa and Kataoka (1987) proposed a band of flow velocities beyond which core peaking void fraction profiles changes into wall peaking void fraction profile. Present results of the simulation falls well in the band proposed by Serizawa and Kataoka (1987). The boundaries proposed by Ohnuki and Akimoto (2000) and Lucas et al. (2005) though fall within the band do not match well with the present simulation. In their model Lucas et al. (2005) have assumed that the whole bubble mass is divided into three separate bubble groups whereas in the present simulation 40 subgroups have been considered. This may be one of the reasons in the discrepancy of the results.

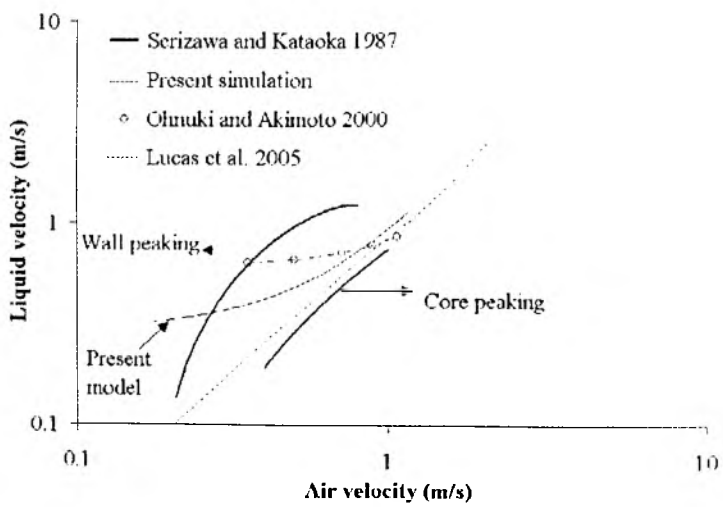

Fig. 2.26 Void distribution map for wall peaking and core peaking, present model along with published results

To appreciate further the development of voidage profile and its effect on flow regime transition one may refer to Fig. 2.27. Here, a line PQ drawn parallel to the abscissa indicating increasing gas superficial velocities at a constant liquid superficial velocity is tracked. Point A

on this curve indicates a peak very near the wall at a low gas flow rate. With the increase of gas flow rate (point B) the peak shifts away from the wall. With a further increase in gas flow rate (point C) two peaks, one at the pipe center and another near the wall appears. Subsequent increase in gas superficial velocity (point D) strengthens the core peak while the wall peak disappears. Finally, one gets slug flow increasing the air velocity further (point E). This also reveals the physics of flow regime transition. Slug flow constitutes of a pseudo periodic movement of Taylor bubbles and spherical bubble laden liquid slugs through any cross sections. From the above observation it can be said that the formation of the Taylor bubbles is preempted by a dense voidage (as well as larger bubbles) at the core of the conduit. This is also supported by experimental observations (Rao, 2002).

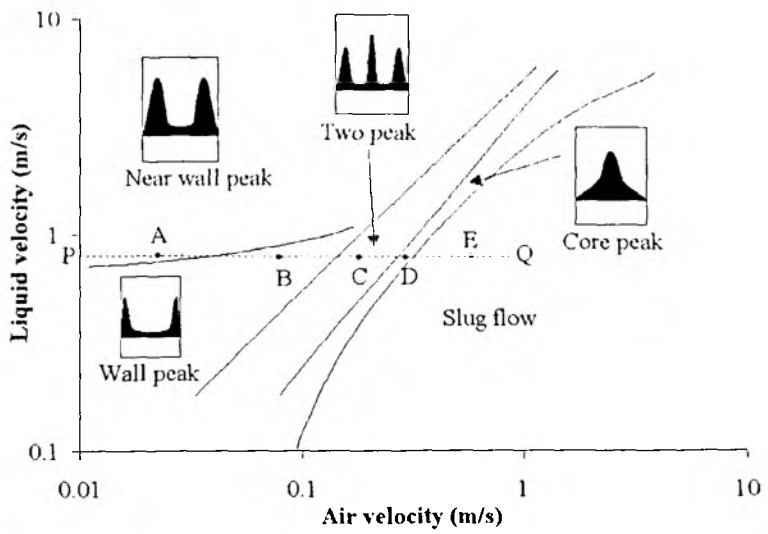

Fig. 2.27 Detailed map for different shapes of void distribution profiles based on superficial velocities

2.4.7. Effect of inlet bubble diameters on transition criteria

It is interesting to note that a unique regime boundary was not observed by different investigators. In Fig. 2.28 bubbly slug transitions as observed in different experiments point out a substantial difference between themselves. While the trend of the transition boundary of Griffith and wallis (1961), Dukler and Taitel (1977) and Mishima and Ishii (1984) are similar (which also matches with the prediction of the present simulation) the nature of the other transition boundaries (Taitel et al., 1980; Sternling, 1965; Govier and Aziz, 1972; Gould,

1974; Oshinowo and Charles, 1974) are different. It may be quite possible that the difference in the inlet condition of the specific experiments is mainly responsible for this mismatch. Unfortunately, in most of the experimental results the inlet conditions, particularly the bubble size distribution, have not been specified explicitly. Therefore, it is difficult to substantiate the above proposition directly. As an alternative we have tried to predict the transition boundary for different inlet conditions. The results are discussed below:

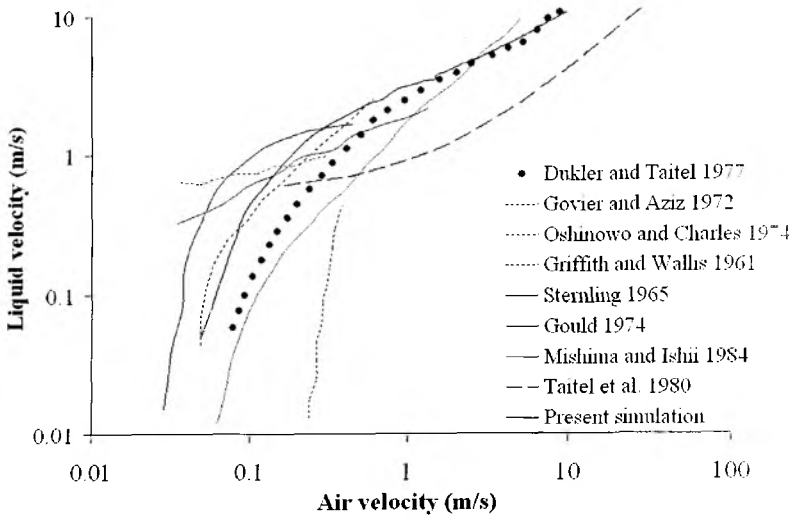

Fig. 2.28 Flow pattern map of the present model along with other published results

To see the effect of bubble size at the inlet on the flow pattern map, results were generated using the present model for homogeneous inputs of various bubble sizes. Fig. 2.29 shows the change of flow regime map due to the change of bubble size at the inlet from 0.5 mm to 1 mm and then into 3 mm. Bubbly flow turns into slug flow at a lower flow rate of liquid for a fixed gas flow rate with the increase in inlet bubble size. It is obvious that bubbles of higher size at the input takes less effort to merge into a big gaseous slug. Results generated from the developed model efficiently support the intuitive concept about bubble coalescence. Flow pattern map of Bilicki and Kestin (1987) for different sized bubble input are also plotted in Fig. 2.29 to support the results generated from the developed model. They have used plexiglass tube of 20 mm diameter and 1.5 m length to view the two phase flow patterns for air and water. Tests were carried out for bubble diameter of 1 mm and 3 mm. The observations of Bilicki and Kestin (1987) are in close concordance with the simulation results.

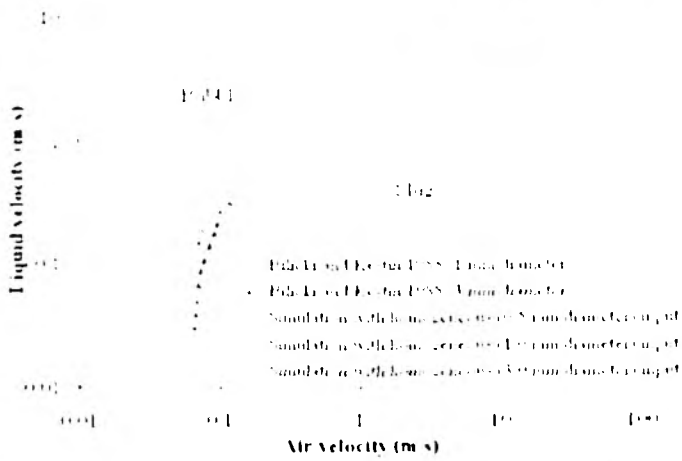

Fig. 2.29 Effect of bubble diameter at the inlet (homogeneous distribution) on flow pattern map

In most of the experiments monosized bubbles are rarely injected at the inlet. In general there could be a distribution of bubble size. Simulations are made to study the effect of a mixed bubble population at the inlet on flow regime transition. Different inlet populations mainly 0.5 mm bubble diameter (a), 1 mm bubble diameter (b) and 2 mm bubble diameter (c) as well as 50% bubbles of 0.5 mm diameter + 50% is of 1 mm diameter (d), 50% bubbles of 1 mm diameter + 50% of 2 mm diameter (e) were considered at the inlet as shown in Fig. 2.30. In all the cases inlet volume fraction is kept constant. It can be seen that with the mixing of higher sized bubbles the flow pattern map for 1 mm diameter bubbles at the inlet shifted downwards causing transition at lower air flow rate. Similarly when 0.5 mm diameter bubbles are mixed with 1 mm diameter bubbles slug bubble appears at a higher gas flow rate for a fixed liquid flow rate compared to the homogeneous input of 1 mm diameter bubble. This analysis can be extended further to investigate the effect of polydispersed bubble input at the inlet plane on void distribution profiles and flow pattern map. It is also clear from the results generated from the simulation that along with the superficial velocities bubble diameter is an important parameter for transition of bubbly flow to slug flow. It is interesting to note that curve a and d and curve c and e intersect each other indicating an implicit effect of the inlet bubble size on the transition boundary. Effect of mixing two different bubble sizes cannot be predicted (even qualitatively) from the logic of linear averaging. The input bubble diameter distribution influences the hydrodynamics in a number of ways. It has got direct effects on the

rates of breakage and coalescence as well as on the drag force. The laws governing these phenomena are strongly non linear. The regime boundaries depicted in Fig. 2.30 is a reflection of that fact.

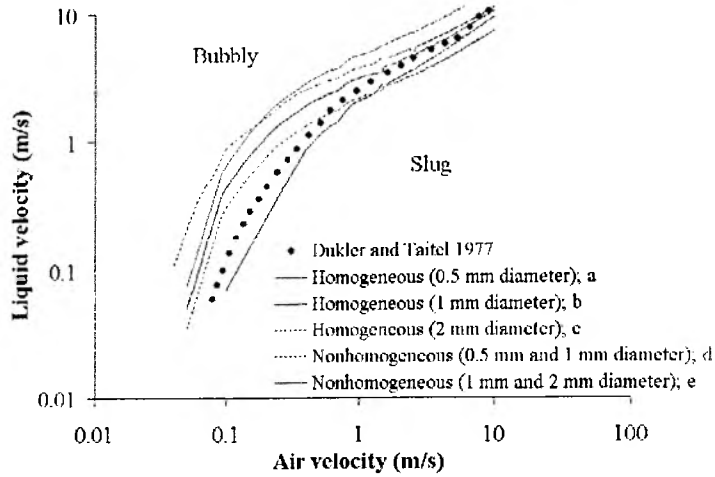

Fig. 2.30 Effect of bubble diameter at the inlet (non homogeneous distribution) on flow pattern map

Over the years numerous efforts (Taitel et al., 1980; Serizawa and Kataoka, 1988; Hibiki and Ishii, 2000) have been made to predict the bubbly-slug transition criteria for cocurrent upflow through a vertical tube. Different dimensional and nondimensional parameters have been selected as the coordinate axes for representing the flow regime boundary on a two dimensional plane. Out of all such efforts the model of Dukler and Taitel (1986) is the most popular one. Based on the argument of maximum packing density of the spherical bubbles the maximum void fraction has been predicted in this model. While doing so, a uniform distribution of bubbles in an infinite mixture medium has been considered without taking any cognition of the tube wall effect. With a simplifying assumption the limiting void fraction has been achieved as 25%. The authors have further used the material conservation and the relationship for slip velocity to obtain the transition criteria in terms of the phase superficial velocities. This is a simple yet elegant derivation which showed reasonable agreement with a number of experimental results. The idealizations made in the model namely one dimensionality and invariance with bubble and tube diameter were essential for obtaining a simple closed form expression as the transition criteria.

2.4.8. Effect of tube diameters on transition criteria

It has already been demonstrated that bubble size influences the transition boundary. Evidence is also available in the literature indicating different flow structure and transition boundaries for different tube diameters. To examine exclusively the effect of tube diameter on the transition boundary one needs to conduct experiments with different tube size and identical inlet bubble population. However, such results are readily not available. We have simulated bubbly flow for different conduit diameters (25.4 mm, 50.8 mm and 76.2 mm) with uniform distribution of 2.54 mm diameter bubbles at the inlet. For 25.4 and 50.8 mm pipe geometry 40 grids have been taken in radial direction whereas 60 grids have been taken for 76.2 mm diameter tube. Axial length is kept constant for all the tube diameters at 5 m. All the results depicted in the present paper are taken at a distance of 40D from the inlet plane. Void fraction distribution at air flow rate of 0.1 m/s and liquid flow rate of 1 m/s is depicted in Fig. 2.31 for all the three tube sizes. In all the cases a distinct peak is visible at the wall of the conduit. At 25.4 mm diameter the rise of the peak is highest at the vicinity of the wall and fall in the valley is lowest at the core.

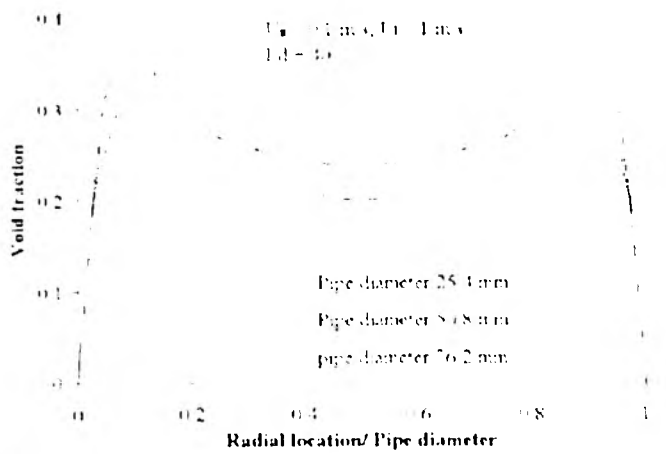

Fig. 2.31 Effect of tube diameters on void fraction profile at low air and water velocities

With the increase in the diameter the peak sharpness decreases and valley depth increases. The position of the peak near the wall also shifts towards the center of the tube geometry. Results of void fraction distribution for various tube diameter at higher liquid (3 m/s) and air (2 m/s) flow rates are depicted in Fig. 2.32. In all the cases core peaking is observed.

However, the profile becomes flatter with the increase in tube diameter. The figures bring out the diminishing wall effect on the gaseous phase with the increase in tube diameter.

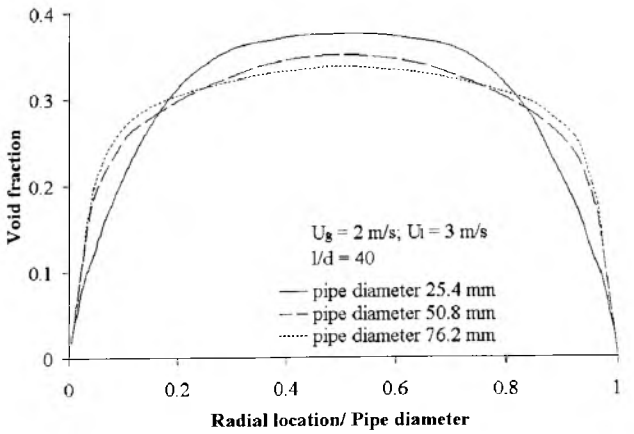

Fig. 2.32 Effect of tube diameters on void fraction profile at high air and water velocities

As the change in tube diameter causes a change in the voidage profile, it is not unwise to expect that tube diameters may have an effect on flow regime transition. Flow regime boundary has been constructed using the present simulation for the three different tube diameters as shown in Fig. 2.33. There is a distinct upward shift of the transition line with the increase in the conduit size. The data available for 25.4 mm (Vince and Lahey, 1982) and 50.8 mm (Taitel et al., 1980) tube diameters exhibit reasonable agreement with the simulation results.

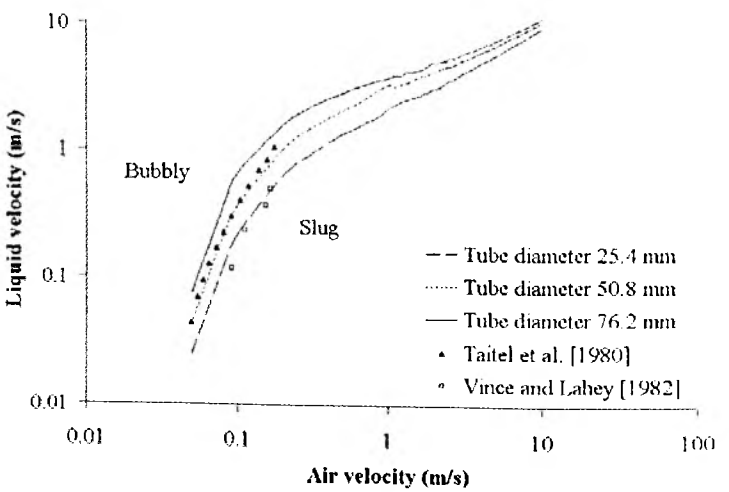

Fig. 2.33 Effect of variation in tube diameter on flow pattern map

2.5. Gas liquid upflow through circular annuli

Gas liquid two phase flow through annular passage of circular cross section (schematically shown in Fig. 2.34) occurs frequently in diverse engineering systems. Well bores for the exploration and extraction of oil and natural gas, double pipe heat exchangers, different cooling passages, various gas lift devices are examples where two phase flow occurs through concentric circular annulus. Accordingly, flow of a two phase mixture through annular passage has been investigated by several researchers (Sadatomi et al., 1982; Caetano, 1984; Kelessidis and Dukler, 1989; Hasan and Kabir, 1992; Caetano et al., 1992; Das et al., 1999; Sun et al., 2004).

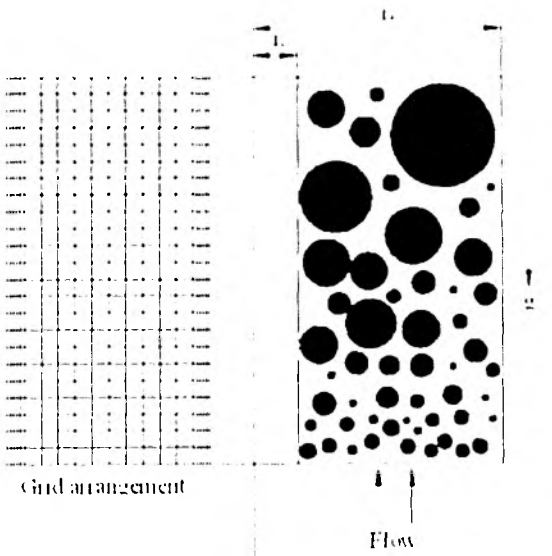

Fig. 2.34 Schematic representation of bubbly flow in an annulus

Sadatomi et al. (1982) studied air water two phase flow through vertical annulus of 15 mm inner diameter and 30 mm outer diameter and determined the average void fraction using quick closing valve technique. They also proposed the transition boundary for bubbly to slug flow. Caetano (1984) investigated air water and air kerosene two phase flow through annuli and observed the transition of bubbly flow to slug flow at a void fraction of 18% and 25% for these two cases respectively. Kelessidis and Dukler (1989) conducted experiments for air water flow in vertical concentric and eccentric annuli of 50.8 mm inner diameter and 76.2 mm outer diameter. They have used probability density function analysis of their conductivity

probe signals to identify various flow regimes. Based on this a map has also been introduced for the transitions of different flow patterns. Mathematical models based on the physical understanding of different flow patterns have also been developed that matches well with their experimental results.

Hasan and Kabir (1992) studied the effect of annular gap on two phase hydrodynamics using three different annuli. They have used drift flux model to predict average void fraction. Caetano et al. (1992) proposed a transition criterion for bubbly to slug flow using a hydrodynamic model based on eight empirical constants. Their flow pattern map matches well with the data of Hasan and Kabir (1992).

Das et al. (1999) made experimental observation for air-water upflow through concentric annuli of three different annuli (A: 50.8mm/25.4mm, B: 38.1mm/12.7mm, C: 25.4mm/12.7mm). To identify the distribution of void fraction in different flow regimes parallel plate type conductivity probe was used. Flow regimes were identified using PDF of the signals obtained. Further, they have developed a transition model and compared the model prediction for bubbly to slug flow with different experimental results.

Recently, Sun et al. (2004) observed bubble distribution pattern in their 4.1 m long borosilicate glass tubing of annular cross section. The outer diameter of the tube is 38.1 mm and inner diameter is 19.1 mm. Impedance void meter is used to measure the average void fraction of the test rig. Using the signals obtained from an impedance probe flow patterns have been recognized through a neural network. Their analytical model predicts the transition from bubbly to slug flow at a void fraction of 0.191. Some efforts have also been made for two phase flow through annular conduit in horizontal and inclined orientations. The investigations made by Osamasali and Chang (1988), Ekberg et al. (1999) and Wongwises and Pipathattakul (2006) are worth mentioning.

The review of literature reveals that most of the previous works on two phase flow through annulus are experimental. Time to time some efforts has been made to analyze the flow phenomena through theoretical models. Several attempts have been made for the prediction of transition criteria between different flow regimes. These are primarily phenomenological models developed for specific control volumes based on simplified assumptions. Moreover, in most of the cases these phenomenological models were derived as extensions of the transition criteria previously proposed for circular geometry. Though these models are reasonably successful in predicting the regime boundary they do not provide much

insight into the flow behavior at any location or its development along the conduit axis. Hence, efforts have been made to model bubbly flow and its transition through annuli with the help of developed two fluid-population balance model.

2.5.1. Grid independence test for annuli

Gas liquid flow through an annular cross section is solved using 2D axisymmetric grids in a cylindrical polar coordinate system. To check the grid-independence of the solution, the influence of the number of radial grids on the numerical simulation is studied. The grid structure used in the present paper is non uniform, with finer mesh close to the inner and outer walls, as shown in Fig. 2.34.

The results for the radial profiles of the void fraction at air velocity of 1 m/s and water velocity of 3 m/s for 30, 40 and 50 radial grids are depicted in Fig. 2.35. There is no perceptible difference between the results using 40 radial grids and 50 radial grids, therefore 40 grids were used for all simulations in this work.

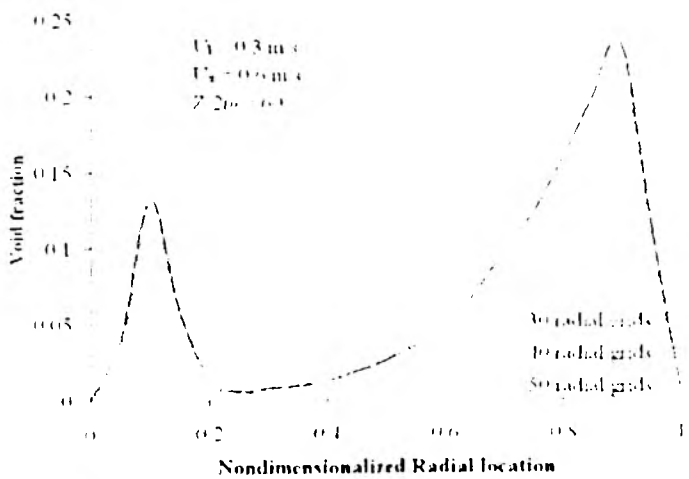

Fig. 2.35 Effect of radial mesh refinement on void distribution

2.5.2. Validation of the developed model

At first the developed model is validated with the reported radial void distribution from literature. Air and water at atmospheric pressure and at a temperature of 25 °C are considered

as the two phases for the simulation of bubbly flow. Inlet bubble diameter is kept as 0.05 times of the annular spacing. With 40 radial grids and 100 axial grids simulations have been made for prediction of radial void distribution. In Fig. 2.36a the present model is validated with a core peaking void distribution pattern as reported by Sorour and El-Beshbeeshy (1986). They have used electrical resistivity probe to measure the radial void distribution pattern for annuli having 38 mm inner and 75 mm outer diameter. Present model is simulated for the same flow conditions and void distribution pattern is reported at an axial distance of 43.5 times of the annular spacing. It can be observed from the figure that the result of the present model matches very well with the core peaked void distribution reported in the literature.

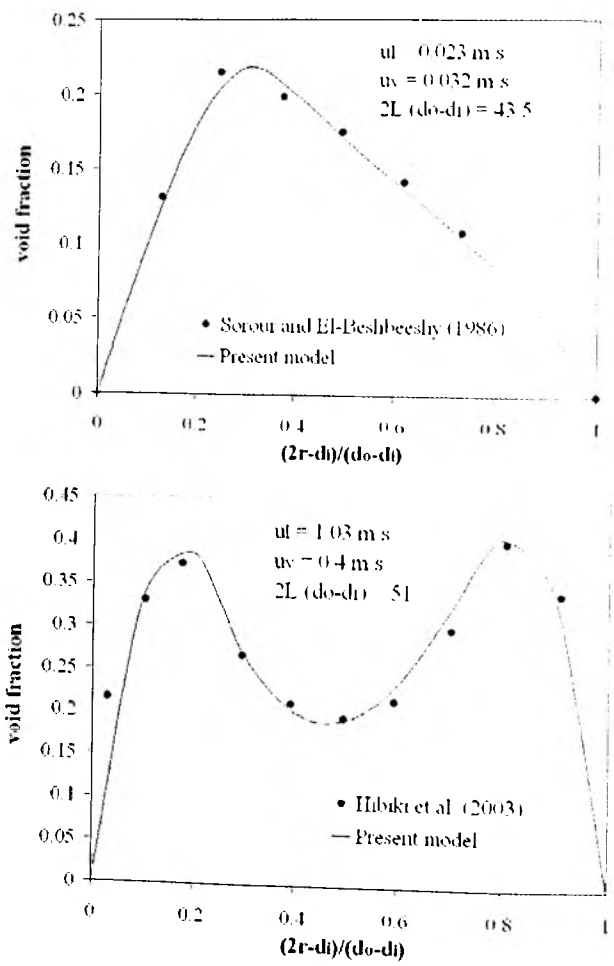

Fig. 2.36 Prediction of radial void distribution pattern for bubbly flow inside annuli

Efforts have also made to examine the predictability of the model for situations where bubbles are pushed towards the walls of the annuli showing two wall peaks. Present model is used to predict the void distribution pattern for bubbly flow inside annuli having 38.1 mm outer diameter and 19.1 mm inner diameter. Hibiki et al. (2003) performed experimental investigation on similar situations and reported void distribution pattern at a radial plane 51 times of the annular spacing away from the inlet. They have used double sensor conductivity probe to measure the instantaneous radial pattern of void distribution. Results of the present numerical simulation and experimental data reported by Hibiki et al. (2003) are reported in Fig. 2.36b for comparison. It can be observed from the figure that present model also predicts the gathering of bubbles near both the wall efficiently.

2.5.3. Prediction of bubbly-slug transition in annuli

Air and water are considered at atmospheric pressure and at a temperature of 25 °C for the simulation of bubbly flow. Inlet bubble diameter is kept as 0.05 times of the annular spacing. With 40 radial grids and 100 axial grids simulations have been done for a fixed water flow rate varying the air flow rate until the criteria for transition from bubbly to slug flow is met. For comparison of developed flow pattern map with available experimental results observation of Caetano (1984) and Kelessidis and Dukler (1989) is plotted in the Fig. 2.37. It can be seen from the figure that the computed result is matching well with experimental observation of Caetano (1984). But observation of Kelessidis and Dukler (1989) is over predicted by the present model. It may be noted that certain amount of subjectivity is associated with the prediction of flow regime boundary in any experiment. Therefore, the mismatch observed in two experimental results (Fig. 2.37) is not surprising. However, the annular gap of the test section used by Kelessidis and Dukler (1989) is 25.4 mm which is half of that used by Cateno (1984). This may have some effect on the transition of flow regimes. Further, experimental verifications are needed to ascertain this.

Comparison of the present simulation was also made with other theoretical flow pattern transition criteria available in literature. Transition map of bubbly flow to slug flow presented by Das et al. (1999) and Sun et al. (2004) is depicted in the same figure. All the predictions follow the same trend as shown by the present model. Das et al. (1999) and Sun et al. (2004) matches well with experimental observations of Kelessidis and Dukler (1989) but under predicts the experimental observations of Caetano et al. (1992). Though the agreement of the

present model with the data from the narrow annuli is not excellent the concordance of the present model and the published theoretical maps is still satisfactory. Transition model for bubbly to slug flow in circular tube presented by Mishima and Ishii (1984) is also plotted in Fig. 2.37 as a benchmark. All the transition boundaries exhibit the same trend depicted by the Mishima and Ishii (1984) model. It essentially signifies identical physical phenomena responsible for the transition of bubbly to slug flow in both the geometries. The influence of geometry is manifested in the shift between the transition boundaries of the annuli and the circular tube.

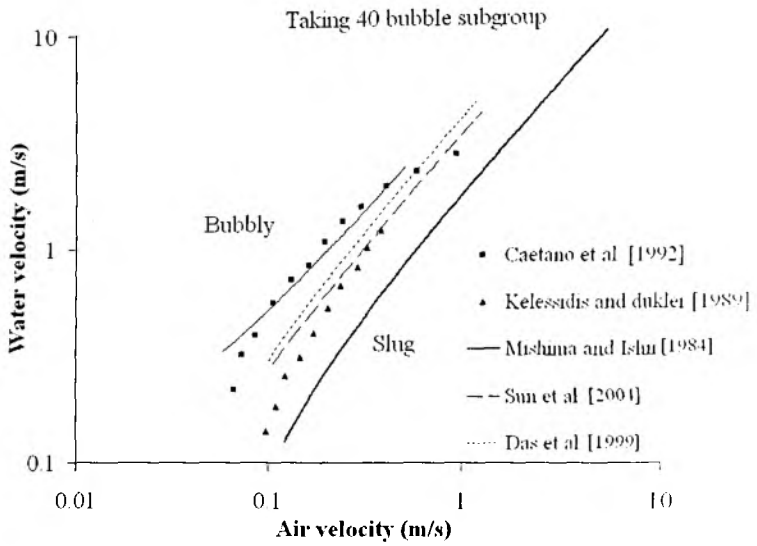

Fig. 2.37 Bubbly-slug transition map for air water two phase flow through annuli- comparison with the available experimental and theoretical results

2.5.4. Radial void distribution in annuli

Simulations were made for various air and water flow rates for annuli of 50 mm inner diameter and 20 mm outer diameter. Diameter of the bubbles at the inlet is kept at 1.5 mm. It has been observed that the void distribution pattern changes with the change in superficial flow velocities. Distribution of gaseous phase at various superficial flow velocities are depicted in Fig. 2.38. At low air and water flow rates bubbles entering into the annulus try to shift towards the outer wall. Result for 0.3 m/s water velocity and 0.1 m/s air velocity shows a sharp peak in the void distribution profile at the outer wall of the annular geometry.

With the increase of gas flow rate some bubbles move towards the inner wall while most of them continue to stick with the outer wall of the annulus. As a result a secondary peak in the void distribution pattern can be seen near the inner wall along with the dominant peak at the outer wall. One example of such type of distribution is plotted in Fig. 2.38 for liquid and air velocities of 0.3 m/s and 0.6 m/s respectively. Further increase in liquid velocity forces the bubbles to move through the core of the annuli due to the increased vibration induced by turbulence. As a result at a liquid velocity of 0.6 m/s and gas velocity 0.6 m/s a third peak at the core of the annular gap can be observed. It may be noted that the peaks at the walls are lowered with the appearance of a new peak at the center of the annuli. At high liquid flow rate the amplitude of the intrinsic bubble vibration increases and as a result a single dominant peak at the center of the annular gap is observed. In Fig. 2.38 void distribution pattern for liquid flow rate of 1 m/s and gas flow rate of 0.1 m/s shows similar kind of phenomena. From this distribution it is clear that most of the bubbles concentrate in the central region of the annular spacing at high liquid superficial velocities.

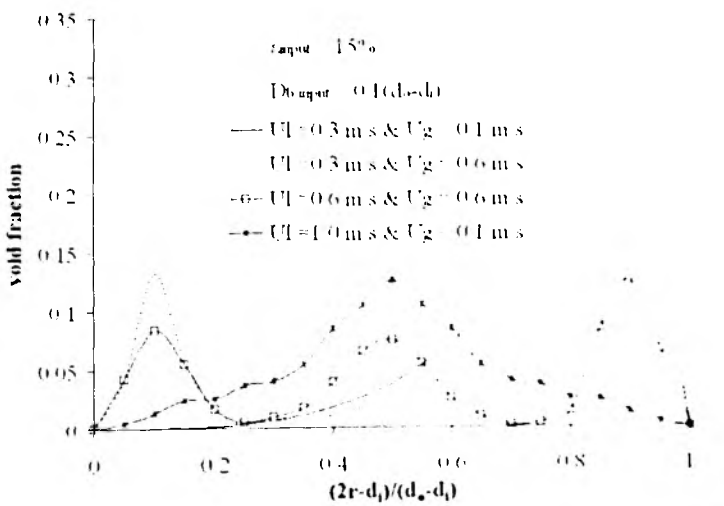

Fig. 2.38 Various void distribution patterns in a radial plane for different superficial velocities of air and water

From the above exercise it is clear radial voidage distribution vary substantially depending on the operating conditions. Further, one mode of voidage distribution may change into another. In Fig. 2.39 four well demarcated regimes has been shown inside the bubbly

flow pattern where outer wall peaking, both wall peaking, three peak and core peak can be viewed prominently. The simulation is for an input bubble diameter of 1.5 mm inside a 30 mm annular spacing with 20 mm inner radius. It may be appreciated that before the transition into slug flow regime the bubble tries to gather at the core of the annuli. This causes coalescence of the bubbles. Coalescence of the spheroidal bubbles produces cap bubbles which in turn grows to form gas slugs and signifies the inception of slug flow. On the other hand, at a relatively high water flow rate as coalescence is prevented bubbly flow terminates into dispersed bubbly flow. In the present model coalescence and break up are the main mechanisms behind the change in bubble size. Diameter of inlet bubble also influences the evolution of bubble size further downstream.

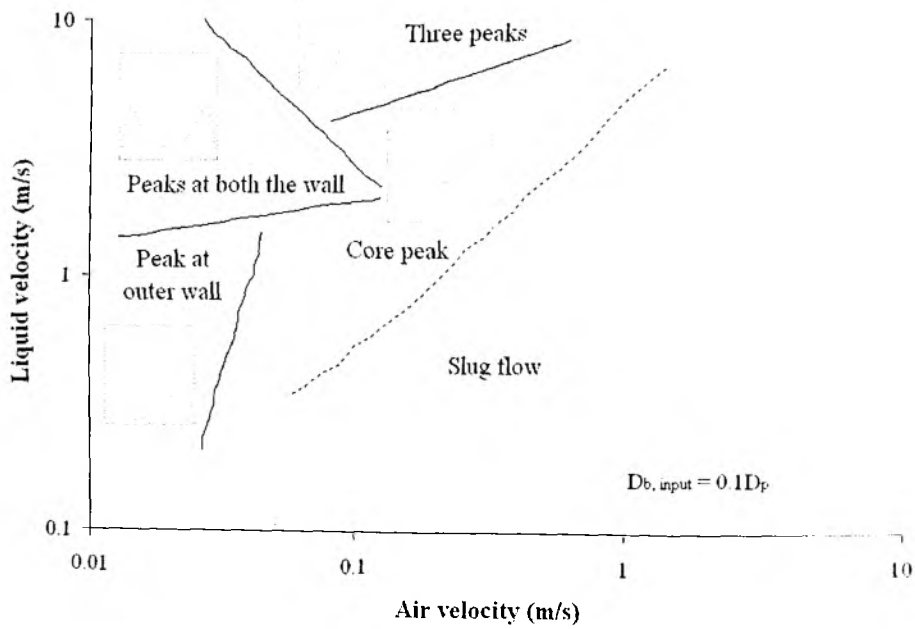

Fig. 2.39 A map in terms of flow velocities for different peaks of void distribution

Studies have been made for different homogeneous and non homogeneous input of bubbles at the inlet plane. Fig. 2.40 depicts the void fraction profile for two different input diameters of bubbles inside the annular passage (ID=20 mm, OD=50 mm) for a liquid velocity of 0.3 m/s and air velocity of 0.6 m/s. The void fraction profiles are computed at 30D from the inlet plane to avoid entrance effect. Dominant peaks at the walls in the void distribution profile can be seen for bubbles of 2 mm diameter. For such small bubbles wall

force is not dominant compared to interfacial forces. Dominance of wall forces over interfacial forces can be seen when bubbles of 4 mm diameter are introduced at the inlet plane for same flow velocities. Strong core peaking can be viewed in this case. Simulation has also been made for simultaneous entry of 2 mm and 4 mm bubbles at the inlet plane keeping the inlet void fraction constant. The figure depicts three peak distributions as the hydrodynamics is influenced by the individual behavior of both the sizes. It can be easily understood that 4 mm bubbles crowd towards the core of the annuli while 2 mm bubbles tends to move towards the wall of the annuli.

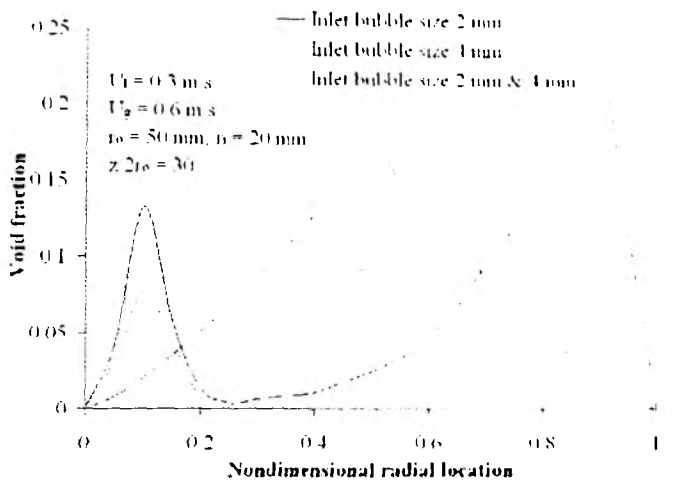

Fig. 2.40 Effect of different sized homogeneous and non homogeneous bubble input on void fraction distribution

2.5.5. Effect of inlet bubble diameter and annular gap on transition for annuli

Influence of inlet bubble size on flow pattern map has also been studied using the present population balance technique. In Fig. 2.41 three flow pattern transition boundaries corresponding to 2 mm, 4 mm and simultaneous entry of 2 mm and 4 mm bubbles at the inlet plane are presented for a comparison. As the inlet bubble size increases slug flow appears at a lower liquid flow rate compared to smaller bubbles for a fixed air flow rate. Transition boundary for 2 mm bubble size at the entry shifts upward compared to the previous case. While both 2 mm and 4 mm diameter bubbles are introduced simultaneously transition line in the flow pattern map lies in between their individual transition boundaries. This evidently

shows that present model can take care of the effect of inlet bubble characteristics on the transition of flow regime.

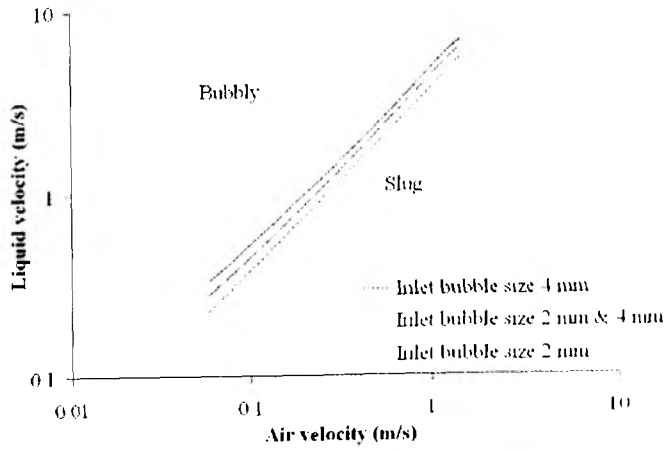

Fig. 2.41 Flow pattern transition from bubbly flow to slug flow for input of 2 mm, 4 mm and a mixture of 2 mm and 4 mm bubbles at the inlet of the annulus

As mentioned earlier, the annular gap (defined by a nondimensional term $r^* = (r_o-r_i)/r_o$) also influences the distribution of void fraction. Outcome of void distribution profile for various annular spacing is also studied using the present model. To evaluate the effect of wall forces on the dispersed phase outer diameter of the annuli is kept constant and inner radius is varied in order to avail various spacing between the walls. At a liquid flow rate of 0.3 m/s and air flow rate of 0.1 m/s void distribution profile for various annular spacing is depicted in Fig. 2.42. A sharp peek near the outer wall can be seen for narrow spacing of the annuli (r^* = 0.2 and 0.4). The height of the peak for r^*= 0.2 is higher compared to the peak at r^* = 0.4. But as r^* increase to 0.6 a small peak appears at the inner wall in addition to the peak at the outer wall. This trend continues for r^* = 0.8. Increase in secondary peak height and decrease in primary peak height can be seen as r^* changes from 0.6 to 0.8. This clearly shows that effect of wall forces becomes significant in case of narrow spaced annuli. As wall force diminishes with the channel spacing two peaks are formed at inner and outer periphery.

Flow pattern map for various gap widths of the annuli is presented in Fig. 2.43. The figure shows an interesting trend reversal for bubbly to slug transition. At the range of low air velocity transition to slug flow occurs at lower water flow rates with the increase of annular gap. As the wall force reduces with the annular gap the gas bubbles stay near the wall. This is

not conducive for the formation of gas slugs. Only with the increase of gas flow rate or with the increase of the annular gap the void fraction in the core region increases giving rise to slug formation. On the other hand, at higher gas flow rate coalescence becomes predominant as the annular gap increases. This results in a transition to slug flow at lower water velocity.

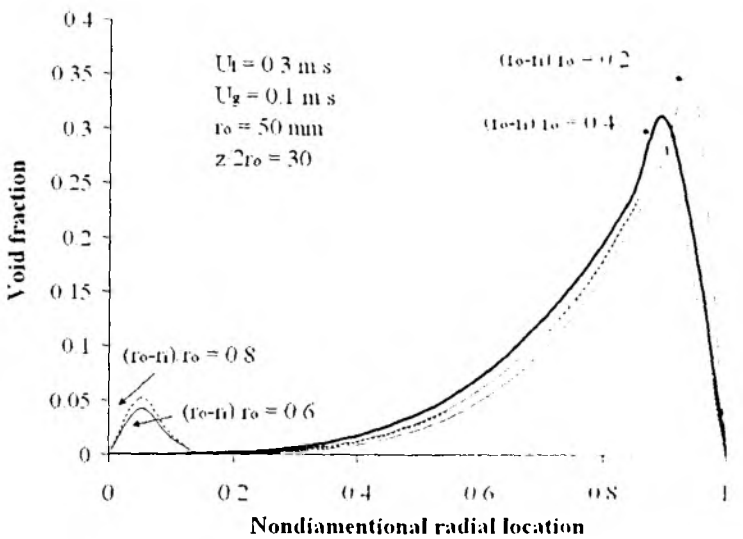

Fig. 2.42 Effect of annular spacing over radial void distribution for air water two phase flow

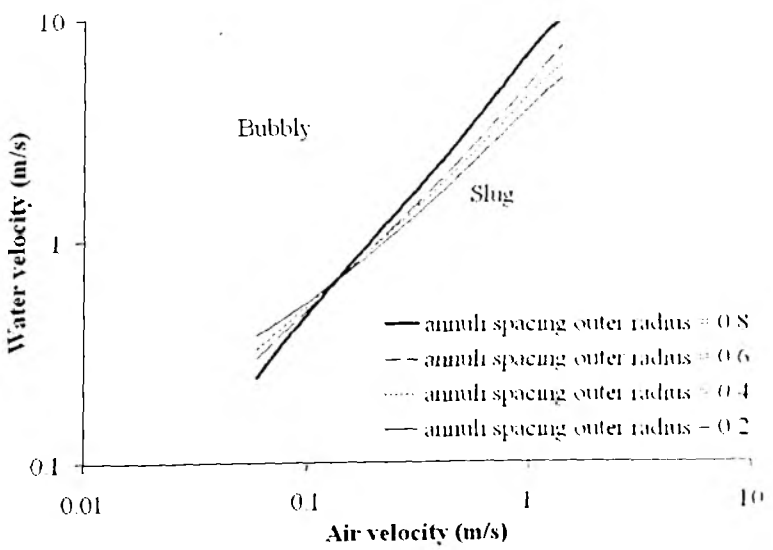

Fig. 2.43 Prediction of Bubbly to slug flow pattern transition for various annular spacing in air water two phase flow

At higher liquid flow rate spheroidal bubbles break into smaller size and produce a homogeneous mixture of tiny air bubbles inside the annular geometry. To investigate the bubbly to dispersed bubbly transition in the perspective of the present CFD model the simulations have been carried out at higher liquid flow rates. The evolution of bubble size has been closely monitored to check the criteria given in equation 2.27. The boundary for bubbly to dispersed bubbly transition, as obtained from the simulation, is depicted in Fig. 2.44. In the same figure the available experimental data and theoretical regime boundaries proposed by other researchers have also been depicted. Present model gives a better prediction of the experimental data of Hasan and Kabir (1992) throughout the domain in comparison with the data of Caetano et al. (1992) and Kelessidis ands Dukler (1989). However, at lower air velocity there exists some deviation between the model prediction and experimental observation.

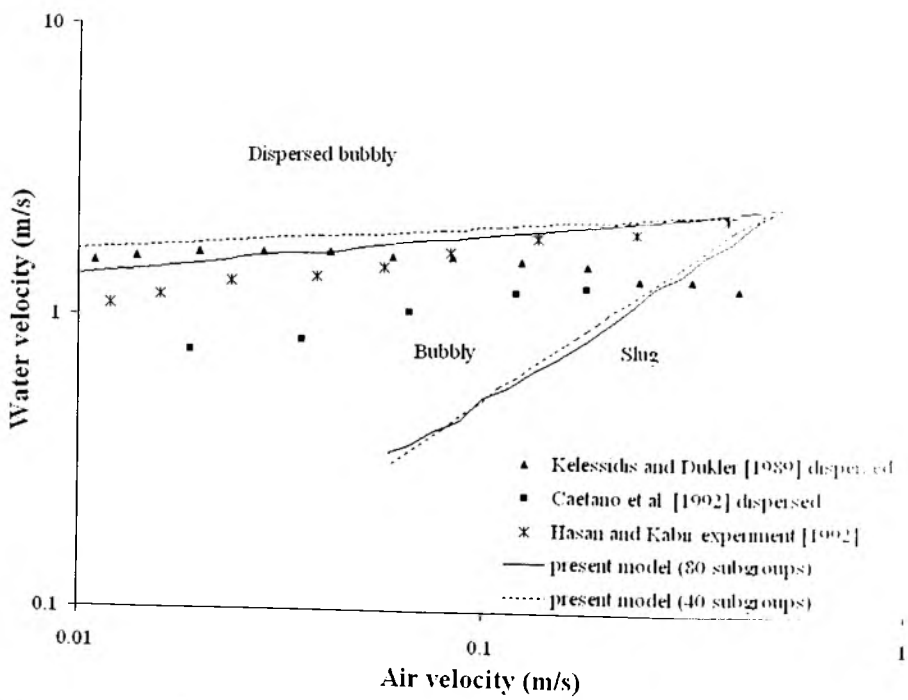

Fig. 2.44 Bubbly-dispersed bubbly transition for air water two phase flow through annuli

In the present model the possible span of bubble diameter is divided into 40 equal subgroups based on volume. As the volume of a bubble is a cubic function of its diameter, such a division generates a bubble population where the difference in the diameters between

two subsequent subgroups is larger for small bubbles. This makes the distribution lopsided towards the large bubbles. In the simulation, daughter bubbles generated due to breakup are divided into its neighboring subgroups keeping its mass and number constant. The formation of small bubbles of intermediate size cannot be captured effectively in the lower range of diameter. The closure law for bubbly to dispersed bubbly transition depends directly on the spacing of bubble diameters of lower subgroups. To circumvent this, an alternate simulation has been made using 80 subgroups within the span of possible bubble volume. This minimizes the error in predicting the flow pattern due to birth of arbitrary sized bubbles caused by breakage.

2.5.6. Bubbly-dispersed bubbly transition for annuli

Fig. 2.44 also depicts the transition curve for bubbly to dispersed bubbly flow inside annuli using 80 subgroups of bubble volume. It is evident that an increase in number of subgroup improves the prediction of regime boundary for bubbly to dispersed bubbly flow. It would be prudent to investigate whether introduction of more number of subgroups alters the bubbly slug regime boundary. In Fig. 2.44 both the regime boundaries are plotted for 40 and 80 subgroups of bubble volume and it is observed that there is no significant change in bubbly slug transition in comparison to shift of regime boundary for bubbly-dispersed bubbly transition. Finally, it can be stated that present model is capable of simulating bubbly flow and predicting its transitions in vertical annuli.

2.6. Summary

Coupled two fluid population balance model is used to simulate upward gas-liquid bubbly flow through a vertical conduit. The simulation enables one to track the axial development of the voidage pattern and the distribution of the bubbles. Thereby it has been possible to propose new criteria for the transition from bubbly to slug flow regime. The transition criteria depend on i) the breakage and coalescence frequency ii) bubble volume count below and above the bubble size introduced at the inlet and iii) bubble count histogram. It has also been possible to simulate the transition from bubbly to dispersed bubbly flow at a high liquid flow rate using the same model. Appearance of core peak, intermediate peak, wall peak and two peaks are modeled using the model in radial voidage distribution depending on the phase

superficial velocities. Finally, efforts have been made to simulate bubbly flow and its transitions through circular annuli. The model prediction gives a good match with the experimental data and existing theory.

It may be noted that two fluid population balance model have also been used by a number of earlier researchers to simulate bubbly flow. The contributions made in the present work in this already used methodology are briefly mentioned below.

1. The effect of turbulence is captured by a simple relationship in terms of the mixture velocity.
2. Bubble grouping has been done based on equal volume distribution.
3. A typical two way coupling has been used for the simulation of two phase hydrodynamics. The local velocity field influences the coalescence and breakup. On the other hand the bubble size and its distribution (which are outcome of coalescence and breakup) have been used for calculation of interfacial momentum transfer.

CHAPTER 3

SIMULATION OF TWO PHASE FLOW THROUGH SPH – SHARP INTERFACE

3.1. Introduction

It has been mentioned earlier that multiphase flow is characterized by the presence of deformable interfaces which generally evolve both with time and space. In some cases exact modeling of the interfaces is avoided for the sake of simplicity. Example of such an approach has been provided in the previous chapter.

It is needless to mention that an accurate modeling of multiphase flow is impossible unless the interface and its evolution are considered rigorously. In fact, this is the most formidable task in the simulation of multiphase flow. The interface often involves an arbitrary geometry and the process of mass, momentum and energy transfer across it is rather complex. Additionally, there are abrupt changes of fluid properties and flow variables (velocity, pressure, temperature etc.) across the interface. This poses an enormous computational challenge. Time to time various computational algorithms has been developed to take care of this special need. A review of such algorithms has been provided in the first chapter. In the present chapter we have used a meshfree particle based method namely SPH for the simulation of some typical two phase flow problems of the order of 10^{-1} m.

3.2. Model development

In recent times some attempts have been made to use different meshfree methods for the simulation of interfaces with arbitrary geometry. Among all the mesh free methods Smoothed Particle Hydrodynamics (SPH) has become a popular numerical tool. SPH is a pure lagrangian method (Lucy, 1977) where the flow field is discretized into particles. It uses interpolating nodes in order to determine the field values and their derivatives within the fluid. Each node has individual mass and thermo physical properties associated with it and can be considered as fluid particles whose field value will be governed as per the conservation laws of continuum fluid mechanics within its neighbor. Use of this technique lessens the effort of making adaptive or body fitted grid for complex geometry and provides basic local information for the area of interest. SPH assures preservation of mass by choosing appropriate property distribution coefficient among its neighbor. There is no extra computational effort required for the construction of interface like other grid based techniques as extremities of fluid particles are specifically defined by the particle positions.

3.2.1. Method of discretization

The foundation of smoothed particle hydrodynamics depends on interpolation theory. The conservation law of continuum fluid dynamics is transformed into ordinary differential equations (ODE) through the use of appropriate interpolation functions that give the kernel estimate of the field variable at a point. It resembles the numerically stable weak form formulation in finite element method for any differential equation. Then the set of discretized ODEs is solved using any standard integration routines of the conventional CFD. Solution of SPH produces banded or sparse matrices representing the discretized systems. As the properties depend only on the neighbouring particles the computational effort is drastically minimized.

The following key ideas are implemented to achieve the solution of a complex phenomena using SPH.

i) The domain of interest is discretized into a set of arbitrarily distributed particles with no interconnectivity between them as shown schematically in Fig. 3.1. This approach makes the domain meshfree and filled with particles.

ii) Next, the field function approximation is made using an integral representation method. This is termed as 'Kernel approximation'.

iii) Then the integration of the field variables and their derivatives are replaced by summation approach over all the corresponding values at the neighbouring particles of the local domain. This methodology is termed as particle approximation. The neighbouring domain of a particle is defined as the support domain.

iv) Particle approximation is made at every step during the forward marching of time. Properties at a particular point depend on the current local distribution of the neighboring particles. This makes the simulation process adaptive to any sudden change even at the local level.

v) Particle approximation is done for all the terms of the governing equation of the continuum to make the complex system of PDEs into a family of ODEs that can be easily discretized with respect to time.

vi) Explicit integration algorithm is used to solve the ODEs to avail the time history of the field variables. Optimum time stepping has to be adopted in order to obtain stable solutions with minimum computational effort. Use of compactly supported domain mostly eradicates the problem of numerical instability for the field variables.

Algorithmically SPH is segmented in three interlinked parts. At the first step integral representation or kernel approximation has been done. It is followed by particle approximation of the field variables. Final step is the forward time marching scheme for all the ODEs.

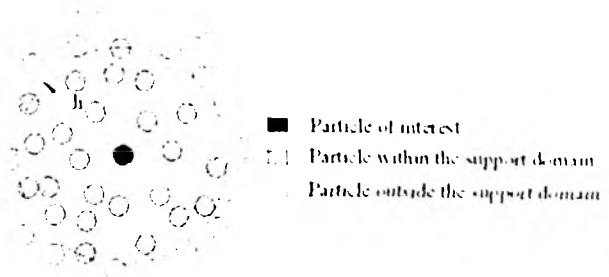

Fig. 3.1 Particle representation of a fluid continuum and its support domain

3.2.2. Approximation of a function and its derivatives

The concept of integral representation of a function can be described as follows:

$$f(x) = \int_{\Omega} f(x')W(x-x',h)dx' \tag{3.1}$$

where f(x) is a function of the three dimensional position vector x, and W(x-x', h) is the smoothing kernel function. h is the smoothing length defining the influence area of the smoothing function W. The function W has the two main properties:

$$\int_{\Omega} W(x-x',h)dx' = 1 \tag{3.2}$$

$$\text{and, } W(x-x',h) = 0, \text{ for } |x-x'| > k_c h \tag{3.3}$$

The function should satisfy the condition of Dirac delta function as the smoothing length is made infinitesimally small. The function should be sufficiently smooth to capture the influence of local phenomena.

The choice of kernel is also very important part of the SPH simulations. The influence of neighbouring particle over the field function depends on the choice of kernel. Liu and Liu (2003) gave a detailed discussion of the main properties which any kernel function should satisfy, and also provided a comprehensive list of some of the most frequently used functions in the SPH literature. In the present work we have used cubic spline for the particle to particle interaction. The form of the kernel is as follows:

$$w(s,h)=\frac{M}{h^q}\begin{cases}\left(1-\frac{3}{2}s^2+\frac{3}{4}s^3\right), & \text{if } 0\le s\le 1\\ \frac{1}{4}(2-s)^3, & \text{if } 1\le s\le 2\\ 0, & \text{if } s\rangle 2\end{cases} \tag{3.4}$$

where $s = x_i / h$, q is the number of dimension, M is the normalization constant with values $10/7\pi$ in two dimensional problem.

Next part of the methodology is to perform particle approximation. Consider a fluid with density $\rho(r)$ defined by a set of points r_i initially distributed arbitrarily throughout the body of the fluid. At any time the fluid dynamic field variables are also known at these points. It has been assumed that the fluid is to be divided (Fig. 3.1) into N small volume elements with masses $m_1, m_2, \ldots, m_N$, where the centres of these small volumes are located at r_i. Hence for numerical simulations, the integral interpolant f(x) can be approximated as follows:

$$f(x)=\int_{\Omega}\frac{f(x')}{\rho(x')}W(x-x',h)\rho(x')dx' \tag{3.5}$$

The derivatives of the field variables can also be expressed as a summation of the derivatives of the smoothing kernel. Equation 3.5 shows the n^{th} order derivative of the function f(x).

$$\frac{\partial^n f(x)}{\partial x^n}=\int_{\Omega}\frac{f(x')}{\rho(x')}\frac{\partial^n W(x-x',h)}{\partial x^n}\rho(x')dx' \tag{3.6}$$

The error involved in approximating the function f(x) by the summation given by equation (3.5) has been studied in detail by Monaghan (1992). It depends on the uniformity of the distribution of the particles, but generally is of second order or better.

3.2.3. Derivation of governing laws

Density of a particle can be tracked using particle approximation as follows:

$$\rho_i=\frac{\sum_{j=1}^{N}m_jW_{ij}}{\sum_{j=1}^{N}\left(\frac{m_j}{\rho_j}\right)W_{ij}} \tag{3.7}$$

This approach of density calculation is termed as summation density approach. Density of the individual particles can be calculated also from the particle approximation of continuity

equation (equation 3.7). Using kernel approximation and particle approximation continuity and momentum equation of the continuum simplifies into the following form

Continuity: $$\frac{D\rho_i}{Dt} = \rho_i \sum_{j=1}^{N} \frac{m_j}{\rho_j} v_{ij}^{\alpha} \frac{\partial W_{ij}}{\partial x_i^{\alpha}} \tag{3.8}$$

Momentum: $$\frac{Dv_i^{\alpha}}{Dt} = \sum_{j=1}^{N} m_j \left(\frac{\sigma_i^{\alpha\beta} + \sigma_j^{\alpha\beta}}{\rho_i \rho_j} + \pi_{ij} \right) \frac{\partial W_{ij}}{\partial x_i^{\beta}} \tag{3.9}$$

or,

$$\frac{Dv_i^{\alpha}}{Dt} = \sum_{j=1}^{N} m_j \left(\frac{\sigma_i^{\alpha\beta}}{\rho_i^2} + \frac{\sigma_j^{\alpha\beta}}{\rho_j^2} + \pi_{ij} \right) \frac{\partial W_{ij}}{\partial x_i^{\beta}} \tag{3.10}$$

where $$\sigma_i^{\alpha\beta} = -P\delta^{\alpha\beta} + \mu_i \left(\frac{\partial v_i^{\alpha}}{\partial x^{\beta}} + \frac{\partial v_i^{\beta}}{\partial x^{\alpha}} - \frac{2}{3}(\nabla v)\delta^{\alpha\beta} \right) \tag{3.11}$$

ρ_i is the density of the particle i with summation density approach, m is the mass associated with particle i, W_{ij} is the smoothing function of particle i evaluated at particle j, v_{ij}^{β} is the relative velocity of particle i and j, v_i^{α} is the absolute velocity of particle i, π_{ij} is the Neumann-Richtmyer artificial viscosity and P_i is the pressure of particle i. Monaghan and Gingold (1983) related particle distribution with the viscosity in the following manner:

$$\pi_{ij} = \begin{cases} \dfrac{-(c_i + c_j)\sum_j \frac{h v_{ij} x_{ij}}{x_{ij}^2 + \eta^2} + 2\left(\sum_j \frac{h v_{ij} x_{ij}}{x_{ij}^2 + \eta^2}\right)^2}{\rho_i + \rho_j} & for \quad v_{ij} x_{ij} < 0 \\ 0 & for \quad v_{ij} x_{ij} > 0 \end{cases} \tag{3.12}$$

where, $\eta^2 = 0.001h^2$, v_{ij} and x_{ij} is the relative velocity and distance of two particles i and j. For SPH simulations involving two or more fluids with largely different viscosities, use of above equation allows the viscosity to be variable and ensure that stress is automatically continuous across the material interfaces.

3.2.4. Variation of smoothing length

The smoothing length h represents the effective width of the kernel and its value determines the number of particles with which a given particle interacts. The accuracy of an SPH simulation can be ensured by taking a sufficient number of particles within the

smoothing length. This helps to replace an integral by a summation. Smoothing length can remain unchanged throughout the time span of the computation or it can change at every time span depending on the local density of the particles. One representation of changing smoothing length in two dimensional flow field is presented in equation 3.13.

$$\frac{dh_i}{dt} = -\frac{1}{2}\frac{h_i}{\rho_i}\frac{d\rho_i}{dt} \tag{3.13}$$

For flow field where density changes are not abrupt constant smoothing functions can be used to avoid numerical complicacies.

To capture the hydrodynamics near the interface of a fluid pair with a large density difference, smoothing length (h) has to be optimized at each time step. An iterative predictor corrector method (Liu et al. 2002) is followed so that each particle interacts with a roughly constant number of neighboring particles. At the end of one time loop h is updated with the following expression:

$$h_{new} = h_{old} + f\left(\frac{Dh_{old}}{Dt}\Delta t\right) \tag{3.14}$$

Here f is the relaxation factor which is considered to be 1.0 initially and corrected subsequently so that number of neighboring particles remains always same with some tolerance.

3.2.5. Equation of state

To handle incompressible fluids like water in SPH some modification in the formulation is required. In SPH simulations the real fluid is approximated by an artificial fluid whose compressibility can be controlled depending on the flow situation. The artificial fluid will still provide a valid approximation to the motion of the real fluid provided the sonic velocity is much larger than the velocity of the bulk flow. For computation of the pressure variation, the artificial fluid is simulated to have some compressibility using a suitable equation of state. Nevertheless, the compressibility should be small enough to restrict the relative density fluctuations. A standard equation of state which is used for water in many hydrodynamic simulations (Monaghan; 1994, Liu et al., 2005) is as follows:

$$p_i = B_s\left(\left(\frac{\rho_i}{\rho_0}\right)^{f_c} - 1\right) \tag{3.15}$$

Here p and B, is measured in atmospheric unit and p_0 is measured at the atmospheric pressure. Value of f_c and B, is 7 and 3.04X10^3 respectively as reported by [illegible]

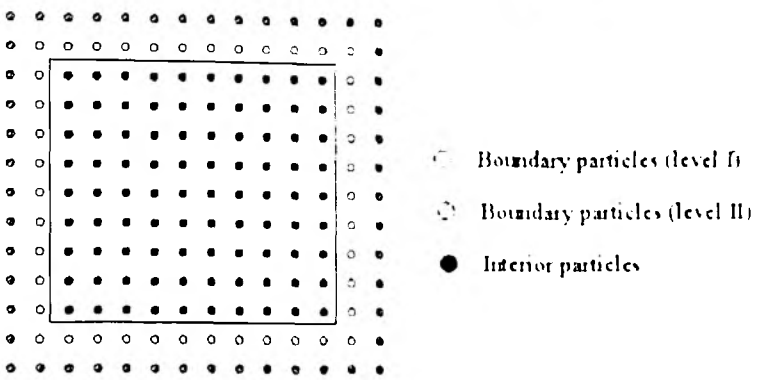

Fig. 3.2 Arrangements of boundary particles

3.2.6. Approximation of solid boundary

For the solid boundaries at the periphery of the domain common technique is to provide layers of artificial boundary particles that resist the fluid particle to remain confined in the problem domain (Fig. 3.2). The force applied by the boundary particles to the fluid particles are described with the help of molecular forces. The force is then directed centrally between the boundary particles and fluid particles which has the Lennard-Jones form as given below (Liu and Gu, 2001):

$$F(R)_i = D_r\left[\left(\frac{r_0}{x_{ij}}\right)^{as} - \left(\frac{r_0}{x_{ij}}\right)^{bs}\right]\frac{x_i}{x_{ij}^2} \quad \text{for} \quad x_{ij} < r_0 \qquad (3.16)$$

$$= 0 \quad \text{for} \quad x_{ij} \geq r_0$$

Here, r is the scaler distance between the boundary particle and the fluid particle. r_0 is the minimum distance between boundary and fluid particles that can be assumed as the initial spacing of the particles. The values of '*as*' and '*bs*' are 12 and 6 respectively. Value of coefficient D_r depends on the problem itself.

3.2.7. Time step calculation

A mid point predictor corrector method have been used to solve the ODEs adopting a forward time marching scheme. The time step is limited by the familiar Courant-Friedrichs-Lewy condition, which basically restricts the physical rate of propagation of information to be

less than that of the numerical propagation rate. For viscous flow an additional diffusive limitation is imposed on the time step and the two effects are usually combined in the following expression:

$$\Delta t = \min_i \frac{h_i}{c_i + 0.6\left(\alpha c_i + \beta \max_j \mu_{ij}\right)} \tag{3.17}$$

Values of α and β is reported in Liu and Liu (2003).

3.2.8. Search for neighboring particles

Neighboring particles are determined based on nearest neighboring particle searching (NNPS) technique. In the SPH method, since the smoothing function has a compact support domain, only a finite number of particles exist within the support domain of the concerned particle and are referred to as nearest neighboring particles (NNP). Only they are considered for the computation in particle approximation. A direct and simple NNPS algorithm is the all-pair search approach. For a given particle i, the all-pair approach calculates the distance r_{ij} from i to each and every particle j (=1, 2... N), where N is the total number of particles in the problem domain. If the distance r_{ij} is smaller than the dimension of the support domain for the particle i, particle j is found belonging to the support domain of particle i. Therefore, particle i and particle j is a pair of neighboring particles. This searching is performed for all the particles (i=1, 2,...,N).

3.2.9. Corrective smooth particle hydrodynamics

In order to increase the accuracy of the field values and its derivative corrective smoothed particle hydrodynamics as proposed by Randles and Libersky (1996) has been adopted. This method reduces the error due to truncation of higher order terms of the Taylor series expansion. Sudden change of field variables are also tackled using this procedure that makes SPH more applicable for multiphase flow of immiscible fluids. First and second derivative of the field variables are shown in equation 3.18 and 3.19 to elaborate the procedure.

First derivative:

$$\frac{\partial f(x)}{\partial x} \cong \frac{\sum_{j=1}^{N} \frac{m_j \left(f(x_j) - f(x_i)\right) W(x_i - x_j, h)}{\rho_j}}{\sum_{j=1}^{N} \frac{m_j \left(x_j - x_i\right) W(x_i - x_j, h)}{\rho_j}} \tag{3.18}$$

Second derivative:

$$\frac{\partial^2 f(x)}{\partial x^2} \cong \frac{\sum_{j=1}^{N} m_j \left(f(x_j) - f(x_i)\right) W(x_i - x_j, h) / \rho_j - \frac{\partial f(x)}{\partial x} \sum_{j=1}^{N} m_j \left(x_j - x_i\right) W(x_i - x_j, h) / \rho_j}{\frac{1}{2} \sum_{j=1}^{N} m_j \left(x_j - x_i\right)^2 W(x_i - x_j, h) / \rho_j} \quad (3.19)$$

3.2.10. Model of surface tension

To model the surface tension force, Continuum Surface Force method (CSF) has been applied in the momentum equation of the particles upon the flow geometry. In the CSF model, surface tension is transformed into a force per unit volume, F_s, by the following equation:

$$F_s = f_s \delta_s \quad (3.20)$$

where δ_s is the surface delta dirac function which peaks at the interface and f_s is the force per unit area.

To simultaneously model surface tension, the color attribute C_i of one fluid particle is set to 1 while the surrounding other fluid implicitly gets $C_i = 0$. Generally the color of the liquid phase is assumed as 1 and gaseous phase color is taken as 0. Surface tension forces per unit area can be computed as (Morris, 2000):

$$f_s = -\sigma_{lg} \sum_{j=1}^{N} \frac{m_j}{\rho_i \rho_j} \frac{\left(C_i - C_j\right)}{\left|r_{ij}\right|} \frac{\partial^2 W_{ij}}{\partial r_{ij}^2} \frac{n}{\left|n\right|} \quad (3.21)$$

here, σ is the surface tension force and n is the normal direction of the interface. n can be calculated as $n = \nabla C_i$.

3.2.11. Effort to ensure immiscibility

To avoid the penetration of two immiscible phases among themselves special care has been taken at the interface of the two phases. A special no penetration force is added to the interfacial particles depending on the scalar distance of them. The form of the no penetration force is shown in equation 3.22.

$$f_{pi} = \begin{cases} \dfrac{\xi\left(P_d^6 - P_d^4\right)\left(x_i - x_j\right)}{r_{ij}^2 m_i} & \text{if } P_d \geq 1 \\ 0 & \text{if } P_d < 1 \end{cases} \tag{3.22}$$

where, $P_d = \dfrac{\left(h_i + h_j\right)}{2r}$ and r is the scalar distance between the interfacial particles. ξ is an empirical constant that depends on the type of fluids and flow situations.

3.3. Results and Discussions

Based on the above description a code has been made to simulate two phase hydrodynamics. At the beginning the code has been validated against the following problems whose solutions are well known, i.e.:

1) accelerated tank
2) rotating tank

3.3.1. Accelerated tank

This problem consists of a two-dimensional, upright rectangular tank containing two fluids of different densities. The semi filled tank is impulsively started from rest with a constant acceleration along the horizontal direction and the motion of the interface is recorded till a steady state configuration is reached. The interface will evolve transiently and at steady state it assumes a flat surface whose slope depends on the relative magnitude of gravitational acceleration and the imposed acceleration in the horizontal direction. Air and water particles are placed uniformly throughout the cylindrical domain (100 mm diameter and 100 mm high) initially. Fig. 3.3a shows the equilibrium shape of free surface represented by different particles. It is clear from the particle position that due to acceleration the interface between two fluids becomes inclined. For determination the effect of particle spacing on the accuracy of computation rigorous study has been made by varying the distance between the particles. Interface location obtained from the simulation by taking three different particle spacing are depicted in Fig. 3.3b. Based on the study, 2 mm spacing between the particles are chosen as optimum for the simulation. Time step used for attaining steady (0.1% change in the interface location) location of the interface is 0.01 s. Computed inclination angle along with analytical solution for different intensities of linear acceleration is plotted in Fig. 3.4. An excellent

match shows the predicting ability of the present algorithm for [illegible] a distinct interface.

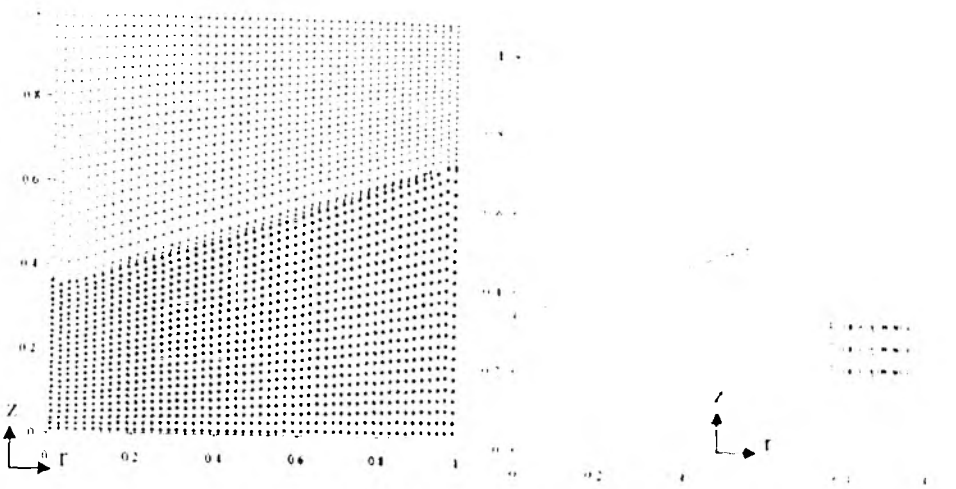

• water particles • air particles

Fig. 3.3 Interface location for semi filled tank under an acceleration of 3 m/s

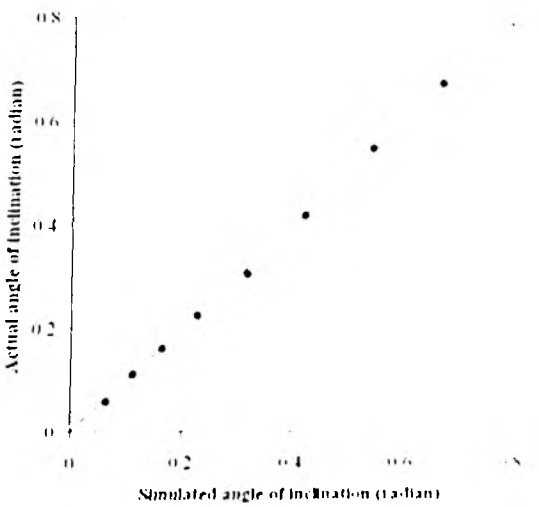

Fig. 3.4 Comparison of angle of inclination between prediction and exact solution

3.3.2. Rotating tank

Next, an effort was made to simulate the flow in a semi filled cylindrical container (100 mm diameter and 100 mm high) which is subjected to an impulsive change in rotational

speed. The sudden impulsive motion of the container causes the interface to evolve transiently and finally at steady state when fluid undergoes a solid body rotation, the interface assumes the shape of a paraboloid of revolution whose geometry depends on the relative magnitude of gravitational acceleration and the imposed rotational speed. For the simulation of the problem initially uniformly distributed water and air molecules are placed in the domain. The plot on the Fig. 3.5a displays the free surface shapes at steady state carried on air and water as two fluids. To calculate the optimum particle spacing, simulations are made by varying the particle spacing and the interface locations are plotted in Fig. 3.5b. It has been observed that 2 mm particle spacing is sufficient for prediction of optimum location of the interface. The same has been used for the simulation of interface location in rotating tank. Time step and convergence criteria used for the present problem is identical to that of the previous study.

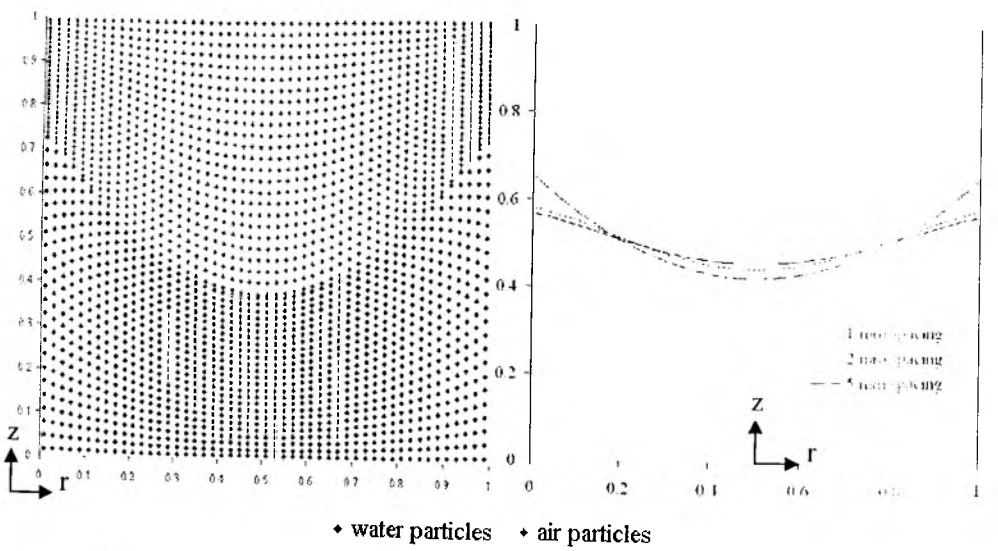

Fig. 3.5 Interface location for semi filled tank under 30 rpm rotational speed.

Comparisons (Fig. 3.6) have also been made for the climb of liquid level at the wall due to rotation between numerical results and actual situations. From the figure it is again confirmed that present model is well suited for capturing interface of an arbitrary shape.

The above exercise also establishes that there is a need to select a proper particle density to ensure the computational accuracy. This exercise has been done meticulously for all the problems.

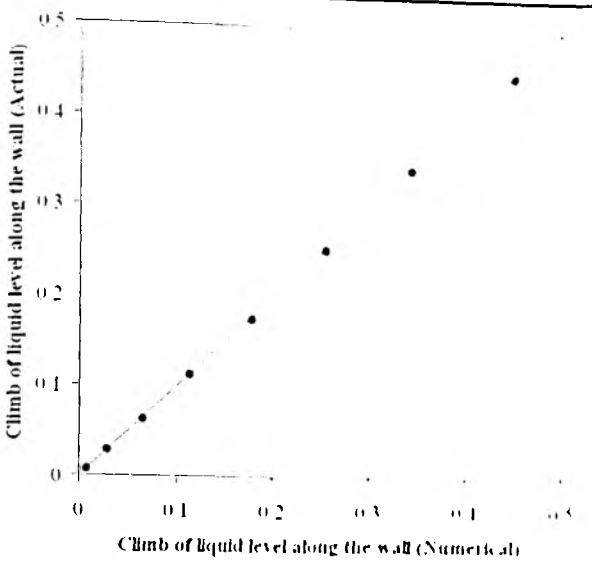

Fig. 3.6 Comparison of liquid climb at the wall between prediction and exact solution

3.4. Bubble evolution through a submerged orifice

3.4.1. Application of the model and validation

The developed algorithm has been used to simulate the process of bubbling from a submerged orifice. The physical problem (Schematically shown in Fig. 3.7) has been idealized as two compartments (150 mm radius and 150 mm high) separated by a rigid partition with a central circular hole. Chambers are large enough compared to the volume of a bubble so that wall effect and change of chamber pressure due to bubbling can be neglected. Pressurized air occupies the lower compartment while the upper compartment comprises water with a free surface (150 mm high). Both the chambers (10.6 L) are sufficiently large so that the generation of a single bubble and its departure from the orifice does not influence the system. Both the domains are represented by a set of uniformly distributed particles. To get the optimum spacing between the particles, bubble period is calculated and reported in Table 3.1 for different particle spacing keeping other parameters same. From the table optimum spacing can be chosen as 1 mm which is maintained for the other simulations for the test case in this chapter. Simulations are forward marched with a time step of 1 ms. In case of bubbling through submerged orifice D_r (mentioned in equation 3.16) is assumed to be 15g times of the initial spacing of the particles.

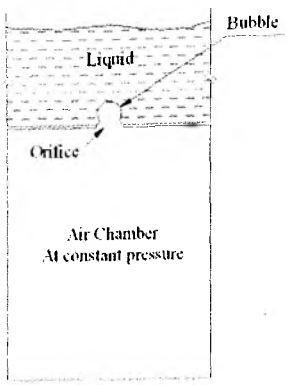

Fig. 3.7 Schematic view of the bubbling process

Table 3.1 Comparison of bubble period for different particle spacing

Particle spacing (mm)	Bubble period (s)
0.5	0.0967
1	0.0952
2	0.0976
5	0.0914

Fig. 3.8 shows the position of the air and water particles over the orifice mouth at various time steps. The diameter of the orifice under consideration is 3 mm. Pressure of the lower chamber is kept constant at 2.5 bar and upper chamber is kept atmospheric. Temperature of both air and water is kept at 25° C. At the inception of the process, the air particles at the bottom chambers try to gather near the orifice. After some time depending on the pressure difference first particle crosses the upper boundary of the orifice and enters into the liquid region. Addition of no penetration force ensures that an individual air particle does not penetrate into the liquid leaving the two phase interface. Gradually the bubble shape becomes hemispherical. As the simulation forward marches in time, size of the bubble elongates and the centre of the bubble shifts up from the orifice mouth. This phenomenon transforms the hemispherical bubble into a truncated sphere of air mass. Due to the presence of surface tension force the shape of the bubble turns out to be spherical. Presence of the wedge shaped liquid layer below the bubble periphery is clearly visible from the figure. It can be seen from the Fig. 3.8 that the water particles forming liquid wedge advances towards the orifice mouth. This process is quite similar to the weeping phenomena during bubbling process. The growing air mass continues to shift upward. As a result, necking of the air bubble starts. This eventually causes the detachment of the bubble from the orifice mouth. During necking considerable changes in bubble volume is not observed. From Fig. 3.8 it is clear that the radius of the neck decreases with the advancement of the time step. At a certain time step depending on the pressure difference between two compartments, the inertia of the bubble becomes sufficient and detaches from the orifice mouth.

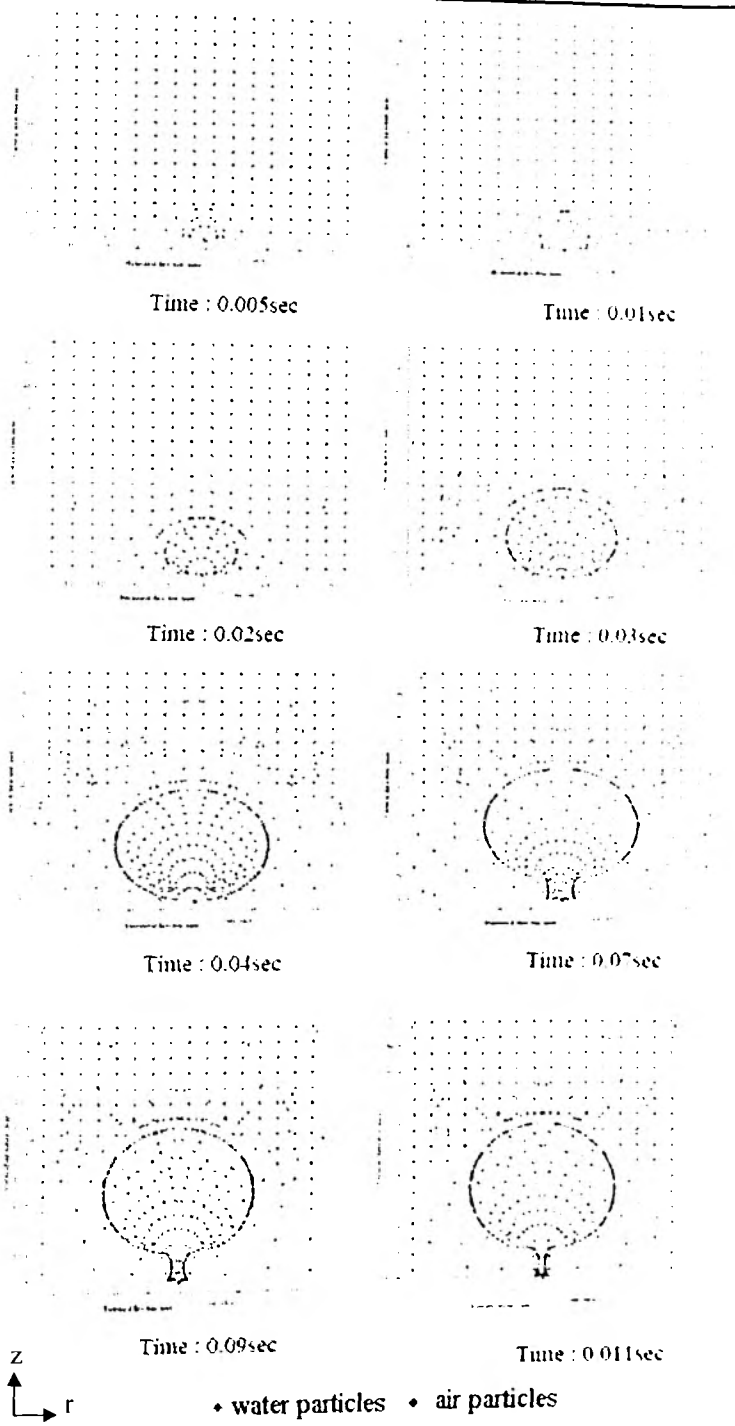

Fig. 3.8 Bubble evolution from a submerged orifice

Evolution of bubble contour has been compared (Fig. 3.9) with the computation of Gerlach et al. (2005) for 2 mm orifice diameter. They have analyzed the formation of air bubble formation in water column based on principles of force balance and used fourth order Runge Kutta scheme to determine the bubble profile. To model their situation we have kept the pressure difference between two chambers at 20 Pa which is the average pressure reported throughout the bubble evolution period in Gerlach et al. (2005).

Position of the extreme air particles at different time level is also plotted in the same figure. It is clear from the figure that present model captures the interfacial phenomena efficiently. Hemispherical bubble, truncated spherical bubble, necking of bubble base at orifice mouth matches clearly with the reported bubble contour. Bubble sticking time at the orifice mouth is also closely matching with the results of Gerlach et al. (2005).

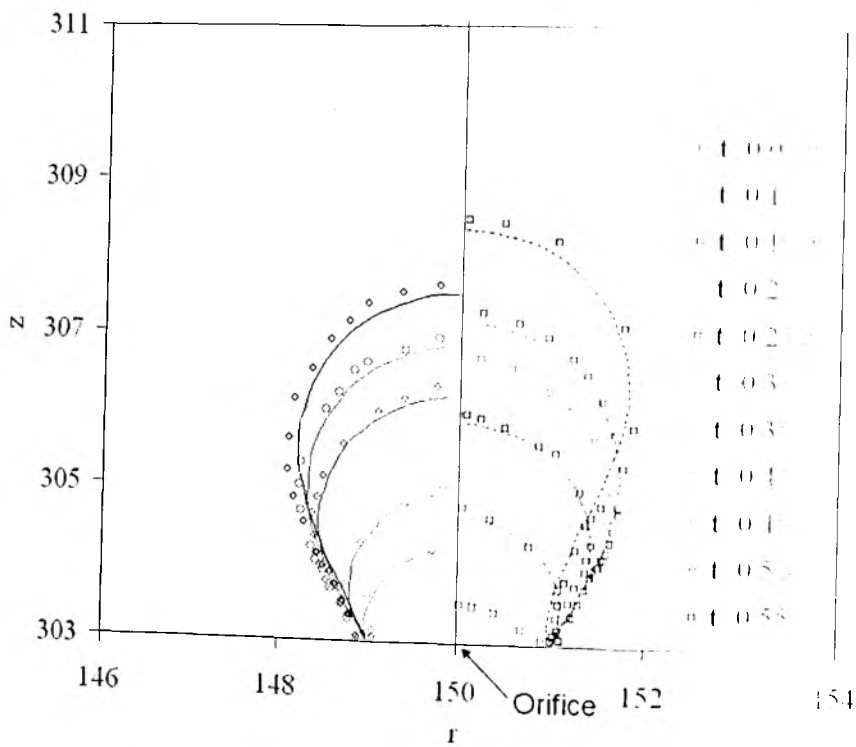

Fig. 3.9 Comparison of bubble contour with Gerlach et al. (2005)

Bubble contour generated by present numerical scheme are also compared with the experimental results of Terasaka and Tsuge (1990). They have used N_2 gas as gaseous phase and 0.7 wt% polyacrylamide (Density: 1.001 kg/m^3, surface tension: 70.5 mN m, viscosity:

1450cP) as the liquid in the pool. Lower chamber is kept at 1.06 bar where as the upper chamber is at atmospheric pressure to ensure quasi static bubble formation. Fig. 3.10 shows the bubble contour for submerged orifice of 3.01 mm diameter at different time level. Terasaka and Tsuge (1990) studied bubble formation due to constant flow and modelled nonspherical air bubble formation in a liquid pool. For five different time steps extreme air particles are stacked along with reported bubble contour. A good matching in all the cases can be seen from the figure.

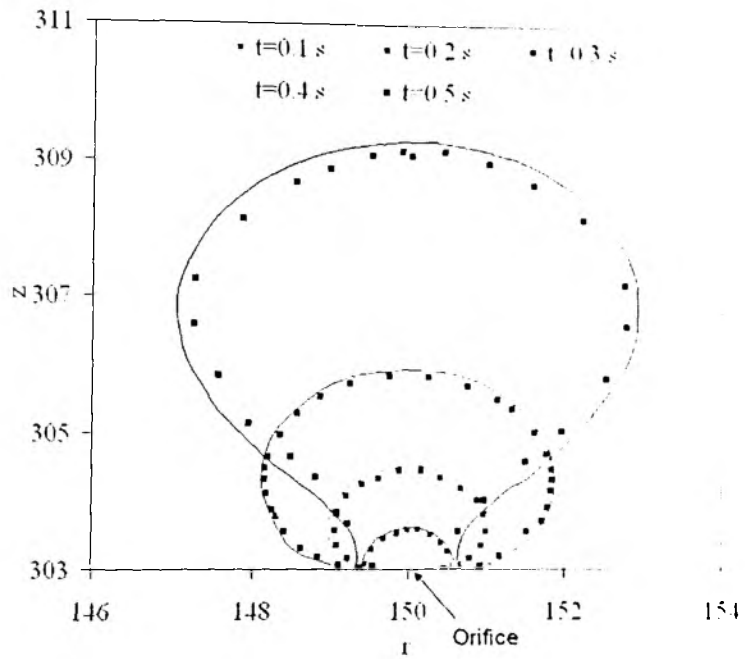

Fig. 3.10 Comparison of bubble contour with Teresaka and Tsuge (1990)

Present model gives an opportunity to study the intricate details of the movement of liquid, gas and their interface. In order to do so iso velocity lines (in mm s) for gas-liquid two phase medium has been demonstrated in Fig. 3.11-3.13 for three different instants. Calculation of velocity is made as follows:

$$V_{res} = \frac{\left|v_i^{\beta}\right|}{v_i^{\beta}} \sqrt{v_i^{\alpha 2} + v_i^{\beta 2}} \tag{3.23}$$

where negative velocity denotes downward movement of the particles and positive velocity resembles helping force for bubble nucleation.

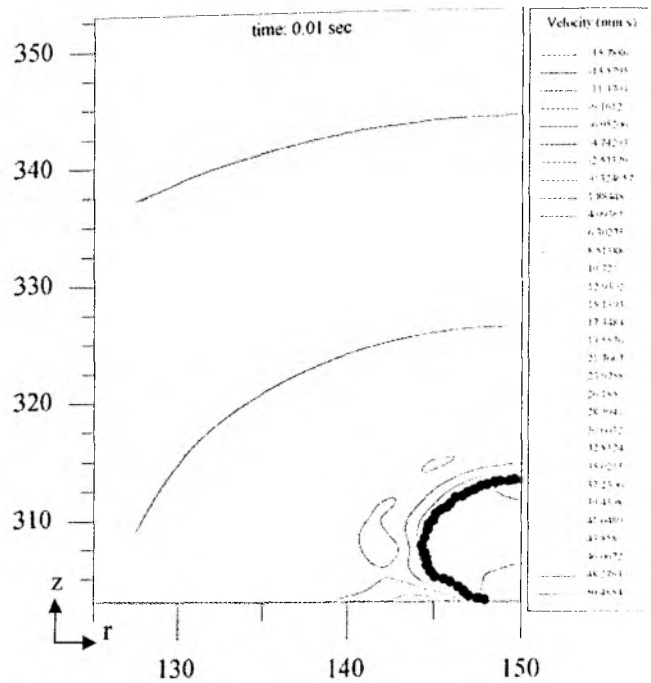

Fig. 3.11 Iso velocity lines in the computational domain during the initiation of the bubble

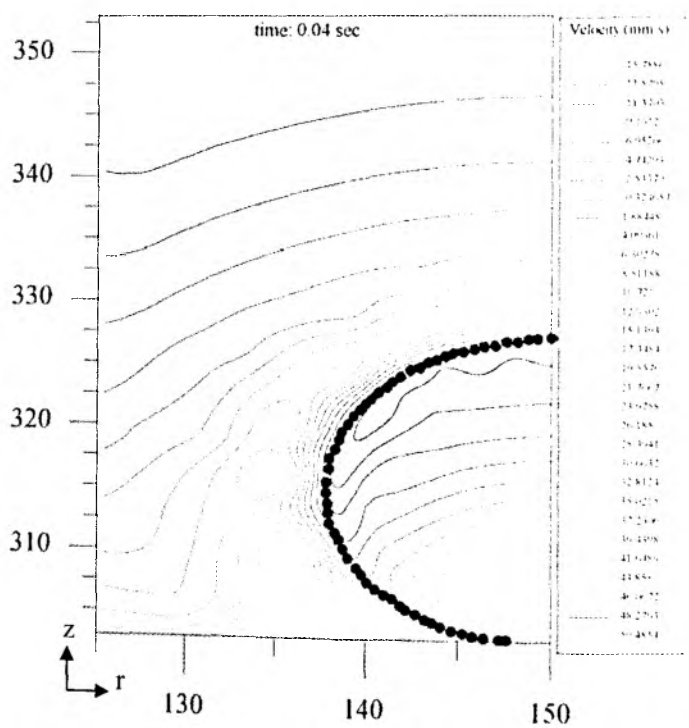

Fig. 3.12 Iso velocity lines for a developing bubble over an orifice mouth

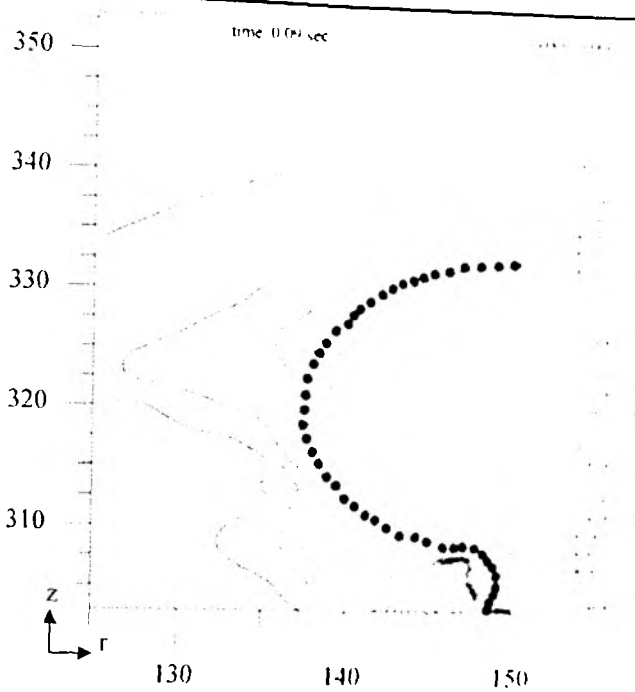

Fig. 3.13 Iso velocity lines in and around a developed bubble before necking

For a better appraisal of the fluid movement the velocity scale has been indicated in the figures. In all the three figures identical scales have been used for the sake of comparison. Dimension of the orifice is taken as 3 mm and pressure difference is kept at 2.5 bar. At 0.01 sec, at the very initial stage of the bubble growth the velocities both in the liquid and the gaseous phase are relatively small. As the bubble grows like a hemispherical body a velocity gradient normal to the interface is created. This is obvious from the iso velocity contours in the liquid phase adjacent to the interface. At the bubble base liquid is squeezed out and moves in the upward direction like a jet as the downward movement is restricted by the partition wall. Isolated vortices are formed as a result of the flow phenomena described above. These features grow further with the growth of the bubble as depicted in Fig. 3.12. In this figure the radial flow of gas outward to the orifice is also obvious from the velocity contours. One may also note the movement of the vortices and the change in their strength. At the final stage of the bubble growth, a gas stem forms at the orifice. The rate of bubble growth decreases as necking of the gas stem starts. Fig. 3.13 represents the necking of the bubble. During necking as there is local contraction of the gas stem surrounding liquid rushes to this point. This is

indicated by the strong negative liquid velocity near the neck. Further the radial expansion of the gas bubble also decreases. This can be discerned comparing the gas and liquid velocity from Figs. 3.12 and 3.13 at the bubble tip.

A close look at the iso velocity contours presented above reveals a circulatory motion of the fluid particles inside and outside the interface. Inside the bubble, circulation cells are dominant near the neck portion as shown in Fig. 3.13. It represents almost no gas flux situation through the orifice which eventually leads towards the thinning of neck and subsequent departure of the bubble. Circulation cells are also present in the liquid film below the bubble. However, circulation in the liquid is not as strong as seen inside the bubble due to the large density difference of the two fluids.

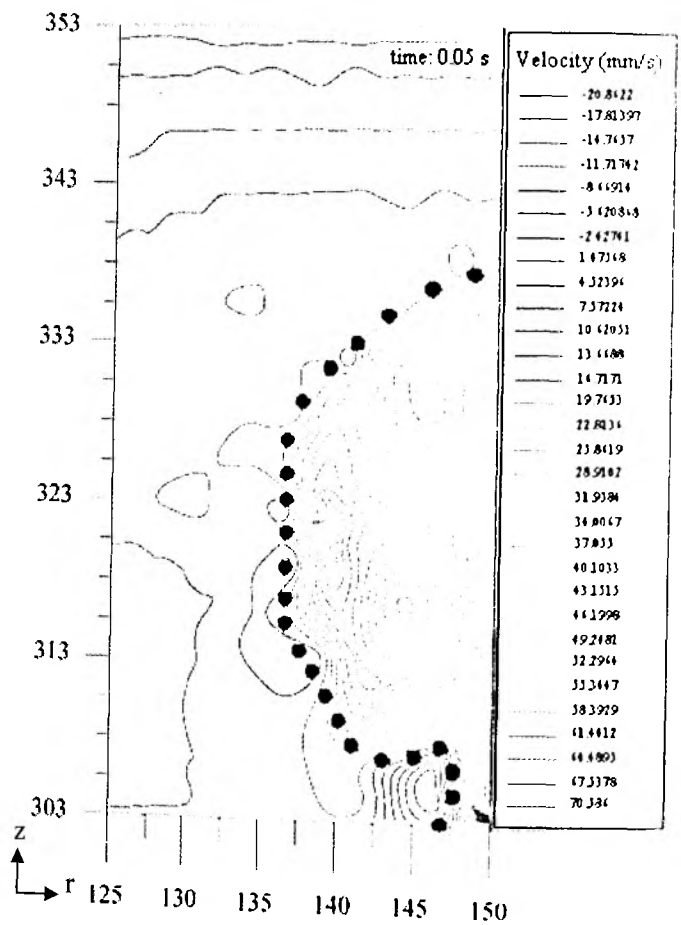

Fig. 3.14 Iso velocity lines of a developed bubble before necking at high gas flow rates

At a large gas flow rate the circulation cells also appear inside the bubble and become dominant as the bubble is about to depart from orifice mouth. In Fig. 3.14 iso velocity lines inside and outside the departing bubble are plotted for 5 bar pressure at the lower chamber. It may be noted that the chamber pressure has been made double compared to the case represented in Fig. 3.13 while the orifice diameter is kept identical for the purpose of comparison. Several differences may be noticed between the two cases. Bubble departure becomes much quicker with the increase of gas velocity. The mushroom shape of the bubble (Fig. 3.13) becomes elongated along the vertical axis (Fig. 3.14). It is well known that at a high gas flow rate air exits from the orifice mouth not as discrete bubbles but as a continuous jet. Bubble shape at high velocity gives an indication towards this phenomenon.

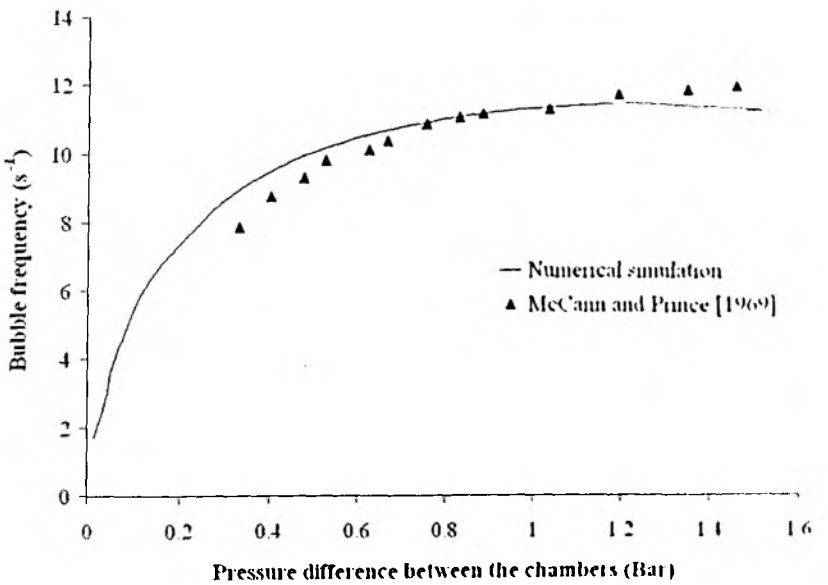

Fig. 3.15 Bubble frequencies for different pressure gradient between the chambers

Comparison of the present result with the experimental observations of McCann and Prince (1969) for various pressure differences between two compartments is then made to validate the methodology. McCann and Prince (1969) reported the gas velocity around the orifice. For a comparison, with the results of McCann and Prince (1969) reported velocity head is transformed into static pressure head. Fig. 3.15 shows the variation of bubble frequency for different pressure heads. Present results show a good agreement with McCann and Prince (1969).

Further, bubble frequency for different air flow rate has been compared with experimental results of Peng et al. (2002) for an orifice diameter of $1/8^{th}$ inch. Peng et al. (2002) used high speed video camera and optical fibre probe for determination of bubble frequency and volume at the time of departure. A good match in bubble frequency as shown in Fig. 3.16 for a wide range of air flow rate proves the versatility of the model.

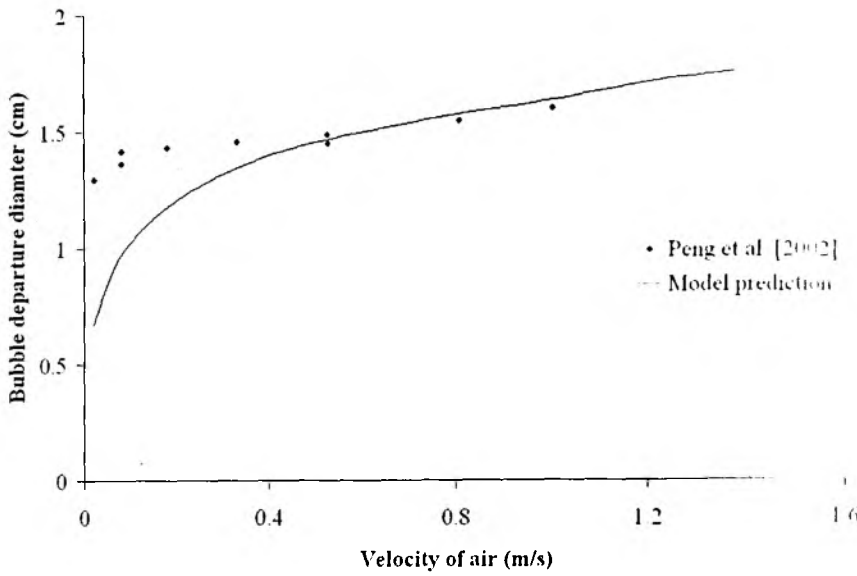

Fig. 3.16 Comparison of bubble frequency for different flow rates through the orifice with Peng et al. (2002)

Effort has also been made to predict the bubble frequency for another gas-liquid combination. Comparison of bubble frequency for different gas flow rates through the orifice has been made in Fig. 3.17 between the experimental observations of Di Macro et al. (2003) and present numerical simulation. Di Macro et al. (2003) used nitrogen gas to bubble from an orifice of 0.13 mm diameter in a pool of FC72. At lower flow rate prediction over estimates the experimental results. In the experiment bubble initiation depends on the chamber volume at those regions which is not tackled efficiently. But from the matching at higher flow rates of Fig. 3.17 it can be said that present model also captures the bubble hydrodynamics efficiently for other fluid combinations.

Diameter of the bubble at the time of departure from the orifice is an important parameter for steady bubbling through a submerged orifice. Bubble volume determines the pressure homogenization rate between the chambers. Using the present model bubble volume at the

time of departure is plotted for different air flow rates through the orifice in Fig. 3.18. Experimental results of Davidson and Schuler (1960) plotted in the same figure compares satisfactorily with the simulation.

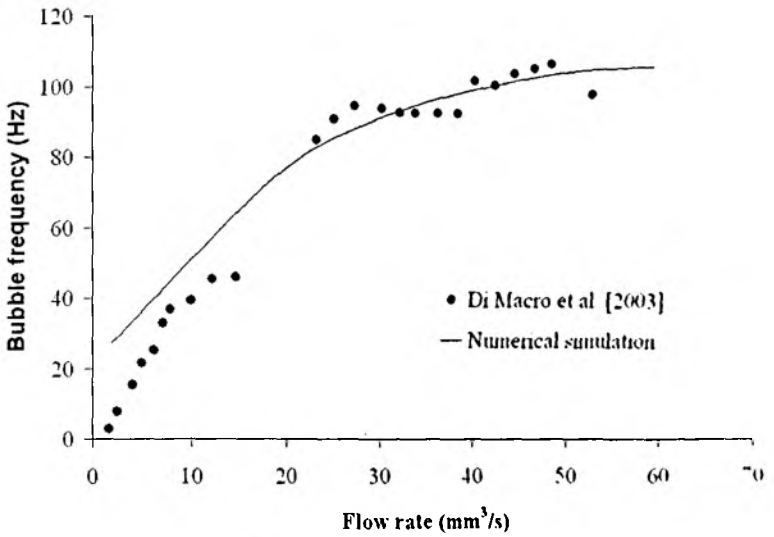

Fig. 3.17 Comparison of bubble frequency for different flow rates through the orifice with Di Macro et al. (2003)

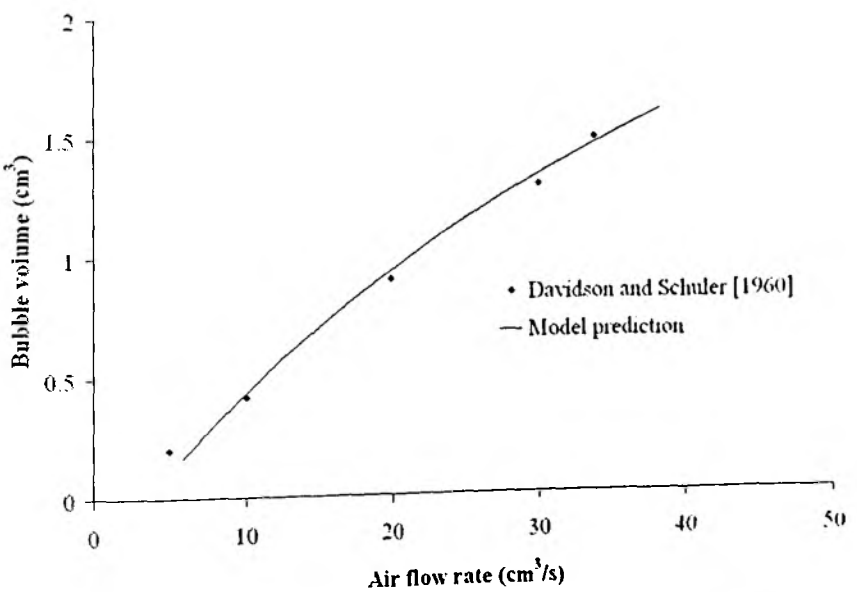

Fig. 3.18 Comparison of bubble volume at the time of departure for different air flow rates with Davidson and schuler (1960)

Bubble diameter at the time of departure is also evaluated for N_2-FC72 combination. In Fig. 3.19 we have compared the numerical simulation with experimental data as reported in Di Macro et al. (2003). In this case also we observe a better agreement with the experimental data at higher gas flow rates which can be explained as before.

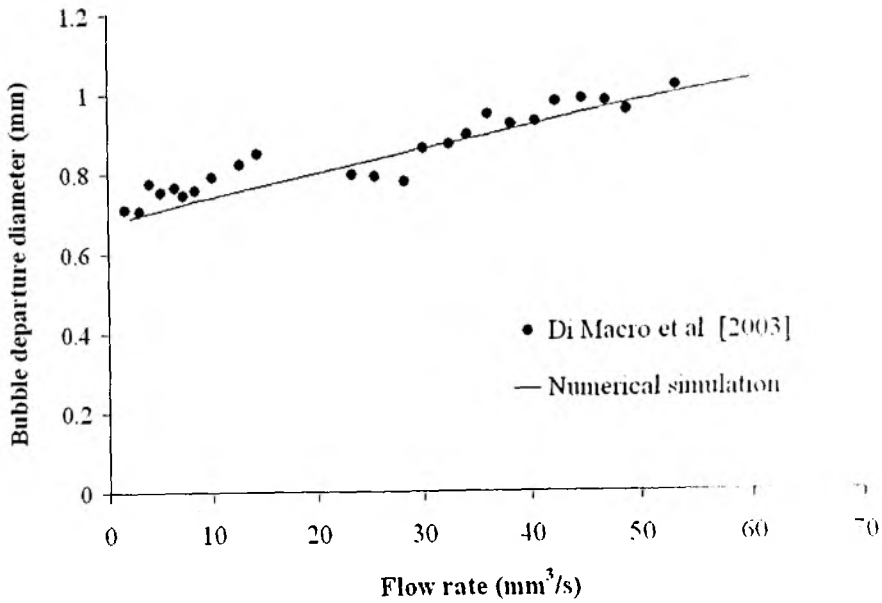

Fig. 3.19 Comparison of bubble departure diameter for different air flow rates with Di Macro et al. (2003)

Table 3.2 Comparison of bubble volume at departure for a pressure difference of 1.6 bar

Volume of the bubble (m^3) X 10^5	McCann and Prince (1969)	Present simulation
	1.25	1.4137

At a very high flow rate of air through orifice mouth bubble volume generated by the numerical simulation is compared with experimental results of McCann and Prince (1969) in Table 3.2. Just after the complete detachment of bubble from the orifice the volume of the bubble is estimated from the simulation. A good matching in the order of magnitude has been observed though the absolute values are different. The associated phenomena in high flow

rate like non sphericity of the bubble and liquid weeping may be responsible for this mismatch.

3.4.2. Effect of different thermo physical properties on bubble formation

The initiation, growth and detachment of bubbles at the mouth of a submerged orifice is governed by the complex interplay between different forces namely inertia, buoyancy, viscous, interfacial etc. Accordingly a number of fluid properties like density, viscosity and surface tension directly influence the bubbling process. Out of the two phases involved in the process of bubble evolution, the role of the liquid properties is more crucial as they may vary widely for different industrial processes. There can be a substantial variation of the liquid properties during the process if it involves chemical or biochemical reactions in a batch operation. For long, there have been attempts to identify the effect of specific liquid properties on bubbling at submerged orifice. Initial investigations in this direction were made through experiments. However, a lack of general agreement is found (Kulkarni and Joshi, 2005) in different studies. Some of the investigations are also marked by inconclusive observations. For example, increase in viscosity has been reported to increase (Khurana and Kumar, 1969; Quigley et al., 1955) or decrease (Vasilev, 1970) the bubble size as well as to have no effect on it (Datta et al., 1950; Benzing and Mayers, 1955). The effects of surfactants and contaminants on the behaviour of bubbles are yet to be understood comprehensively. Long back Davidson Schuler (1960) reported that surface tension force has no dominant effect at high flow rates through a small orifice. They also reported that minimum value of the bubble pressure at the time of departure is governed by surface tension force applied at the contact line. Liow (2000) reported that the surface tension force along with the orifice diameter and orifice thickness decides the bubble period from the orifice mouth. Hsu et al. (2000) experimentally showed the importance of surface tension force over the procedure of bubble formation by using different surfactant in water. But still the effect of surface tension over bubble formation at orifice mouth remains unresolved as conclusive findings are not reported in the literature. Experimental investigations are seriously handicapped by the single most fact that the specific liquid property can not be altered keeping the other properties unchanged. Often the effects of simultaneous variation of more than one property are counter active and lead to ambiguous results.

As an alternate measure attempts have been made to understand the influence of fluid properties on bubble evolution through theoretical analysis and numerical simulations. Kumar and Co workers (Ramkrishnan et al., 1969; Satyanarayana et al., 1969; Khurana and Kumar, 1969) rightly identified the anomaly in the literature regarding the influence of viscosity on the process of bubble formation. They resolved the controversy through a theoretical model. Their model established the effect of viscosity convincingly both at high and low gas flow rates in conjunction with the magnitude of surface tension and orifice diameter. Martin et al. (2006) extended their previous two stage model (Martin et al., 2006) for bubble growth and detachment for investigating the influence of liquid property. The first stage of the model is momentum balance for bubble growth considering viscous and surface tension force. The second stage simulates the period of free rising considering a force balance between buoyancy, drag and inertial force. They have extended this model even for non Newtonian fluids based on the assumption of potential flow field. They have identified three non dimensional parameters namely Reynolds number (Re), Bond number (Bo) and Weber number (We) which influence the hydrodynamics. Thereby it is possible to predict the effect of liquid properties on the evolution of bubbles from their model.

Fully computational simulations of bubble formation at submerged orifice are of recent origin and are few in number compared to the analytical or semi-analytical methods of the process. As a first attempt Oguz and Prosperetti (1993) investigated the bubble formation at high flow rates using Boundary element method (BEM). Same procedure has been applied by Wong et al. (1998) and Higuera (2005) for bubble formation through a highly viscous liquid. In this regard the contribution of Drust and his Co-workers (Gerlach et al., 2005; Gerlach et al., 2007; Buwa et al., 2007) is worth mentioning. They have solved the Navier Stokes equation in its full form for both the phases. For tracking the interface they have used Volume of Fluid (VOF) (Gerlach et al., 2007) and combined VOF and Level Set (LS) (Buwa et al., 2007) technique. Extensive numerical simulations by Gerlach et al. (2007) have been carried out to investigate the influence of various conditions on bubble shapes, bubble volume and transition from a single to a double periodic formation process. Influence of variation of the liquid properties like density, viscosity and surface tension was studied (Gerlach et al., 2007) individually. A comparison of their simulation results with the correlation provided by Jamialahmadi et al. (2001) produce good agreement.

In this section, the effect of liquid properties on the formation, growth and departure of bubbles has been investigated. To begin with, the simulation has been validated with different published results over a range of liquid properties. Attention has been focused on three key liquid properties namely density, viscosity and surface tension.

Density of the liquid phase influences the process of bubble growth and departure in a number of ways. Several forces namely the inertia of the liquid phase, buoyancy force, drag and lift force are directly dependent on density. As these forces are also dependent on other properties the individual effect of density can not be understood without a rigorous simulation. Khurana and Kumar (1969) experimentally showed that for a low gas flow rate and in a less viscous liquid, the bubble shape decreases with the increase of liquid density. For high gas flow rates through the orifice, density does not alter the size of the bubble at the time of departure. All the results from their experiments are for small orifice diameter.

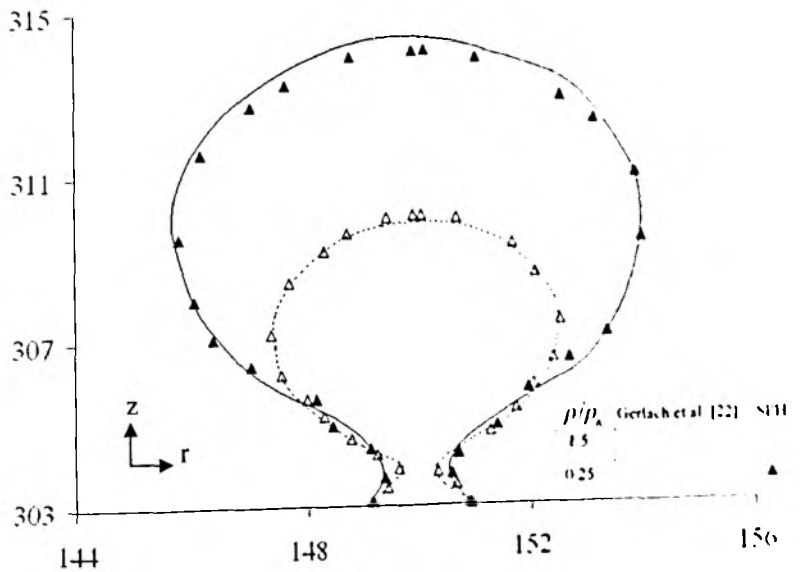

Fig. 3.20 Bubble contour at the time of departure for different liquid density over the orifice mouth

Fig. 3.20 represents the bubble profiles at a 2 mm orifice mouth at the point of departure for liquids 1.5 times heavier and 4.0 times lighter than water respectively. The significant increase in bubble size with the increase in liquid density can be observed. The solid line representing the bubble contour obtained by Gerlach et al. (2007) compare very well with the

present simulation. Further, it has been seen that the period for bubble formation reduces drastically and finally reaches an asymptotic value with the increase in liquid density. This is depicted in Fig. 3.21 along with the numerical results of Gerlach et al. (2007). The present simulation over predicts the period compared to that of Gerlach et al. (2007).

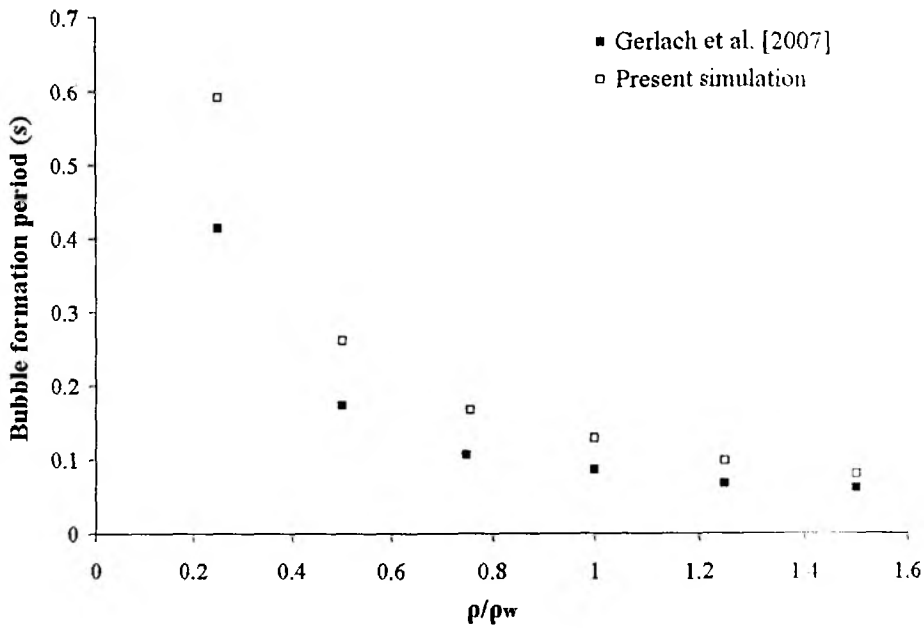

Fig. 3.21 Effect of liquid density on bubble formation period

Contradicting observations have been reported in the literature regarding the effect of viscosity on the process of bubble evolution. Recently, Jamialahmadi et al. (2001) proposed that bubble size at the time of departure is proportional to $\mu^{0.66}$. This signifies a monotonic increase in bubble size with the liquid viscosity. According to Kumar and Kuloor (1970) the effect of viscosity is not independent of flow rate. At higher flow rates effect of viscosity can be dominant, but at low flow rate viscosity becomes quite insignificant. In the present simulation a wide variation of viscosity (compared to that of water) has been considered keeping all the other properties unchanged. To test the predictability of the numerical model bubble profiles at departure obtained by numerical simulations are compared with those obtained by Gerlach et al. (2007) in Fig. 3.22 for two cases i.e. $\mu_l/\mu_w = 0.1$ and $\mu_l/\mu_w = 150$. It is interesting to note that the change in departure volume is rather small compared to such a large change in viscosity. Fig. 3.23 depicts the variation of bubble formation period as a

function of viscosity. Bubble formation period remains almost constant for low values of viscosity and increases only marginally at high liquid viscosity. Similar trend has also been obtained by Gerlach et al. (2007).

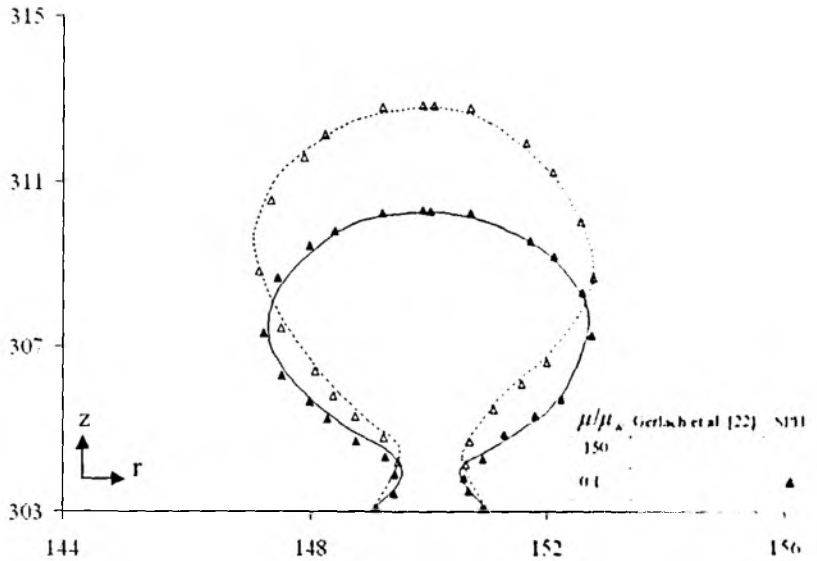

Fig. 3.22 Bubble contour at the time of departure for different liquid viscosity.

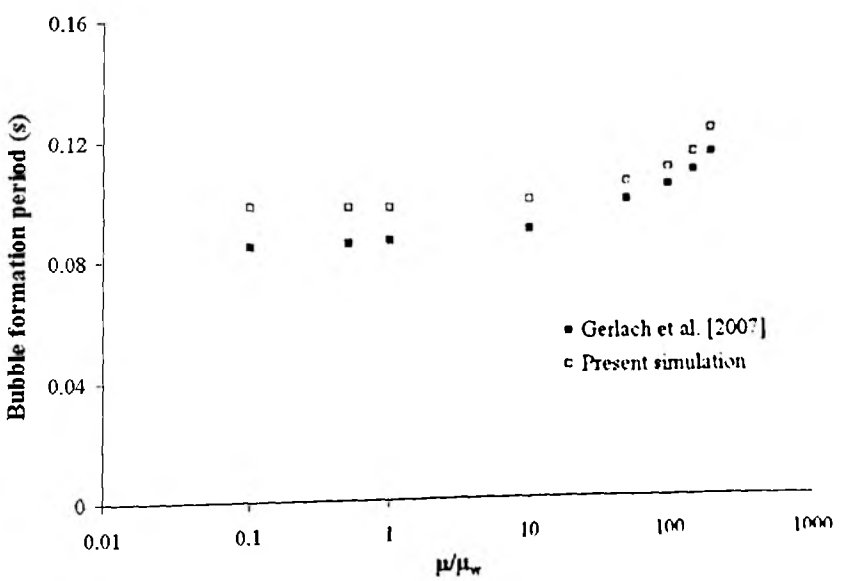

Fig. 3.23 Effect of liquid viscosity on bubble formation period

Effect of surface tension on bubbling also could be quite intriguing. The difference in bubble formation in distilled water and in a system with contamination has been reported but not well explained. Careful investigations are also needed to understand the role of surfactants in the process of bubbling. How the presence of contamination and surfactant modifies different fluid properties and brings out overall change in the process is beyond the scope of present work. We have studied the change in bubbling behaviour simply due to a variation of liquid surface tension.

Fig. 3.24 depicts the bubble shape at departure for two different liquids with surface tension substantially higher as well as lower than water. Both these shapes have been compared with the simulation of Gerlach et al. (2007).The comparison is better in case of liquid with high surface tension. In their simulation, the qualitative change in bubble shape for a liquid with low surface tension is worth noting. It not only has a very small and narrow neck but also shows a small bulged portion below the neck which possibly represents the crown of the succeeding bubble. This attribute is not present in our simulation. However, the variation of bubble formation period with surface tension (Fig. 3.25) as predicted by the present simulation compares very well with that of Gerlach et al. (2007). In general, surface tension increases both the bubble size and the period for bubble formation.

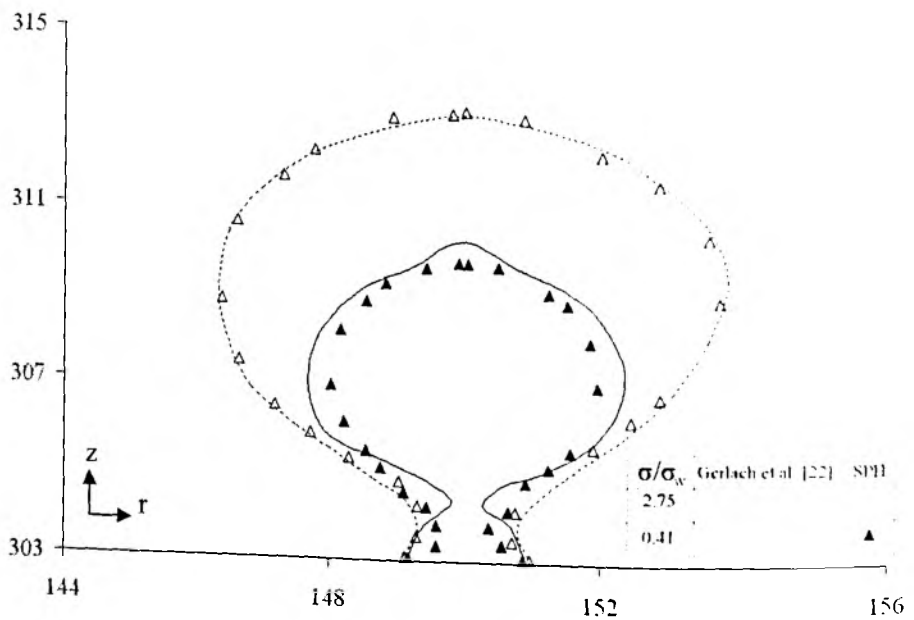

Fig. 3.24 Bubble contour at the time of departure for different liquid surface tension

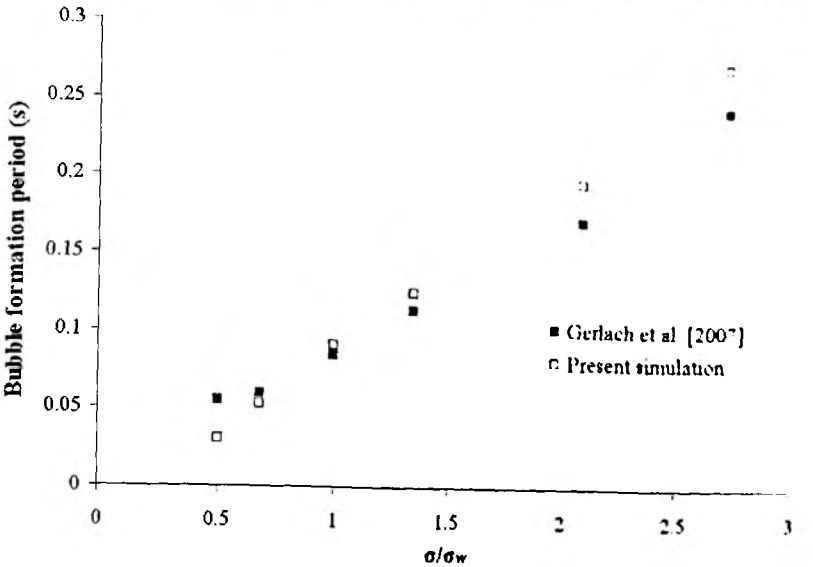

Fig. 3.25 Effect of liquid surface tension on bubble formation period

3.4.3. Influence of liquid properties on different stages of bubble growth

The growth of a bubble at the mouth of a submerged orifice does not follow a monotonic trend. To start with the shape of the gas bubble projected out of the orifice can be approximated as a hemisphere or a truncated sphere. The growth of the bubble continues both in the radial and in the vertically upward direction. Depending on the gas flow rate, orifice diameter and the fluid properties the bubble may assume a non spherical shape at this stage. With further inflow of gas into the bubble a stem develops at the mouth of the orifice and the bubble gets 'lifted up' from the orifice mouth. As the stem grows longer a neck develops in the stem. At a subsequent stage the bubble gets pinched off from the stem at the neck. During the development of the neck, generally the bubble growth is retarded. Therefore, in the development of a bubble there are two distinct phases- initial growth phase and the neck formation phase. In the first phase there is a substantial increase in bubble volume while in the second phase there is a noticeable change in its shape. Formation of neck is characterized by a change in curvature in the bubble profile. Such a change can be easily detected by our simulation.

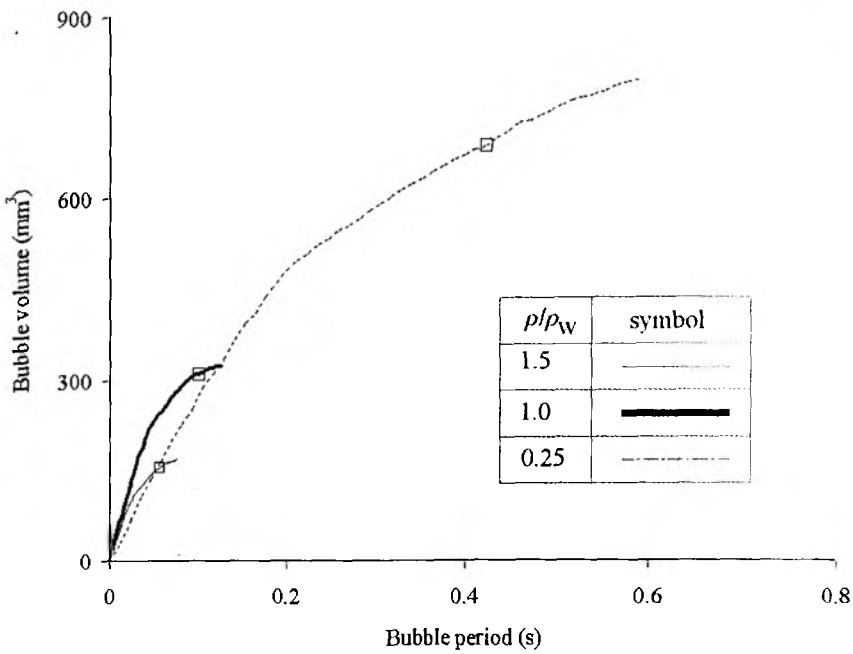

Fig. 3.26 Change of bubble volume throughout the period, effect of liquid density

In Fig.s 3.26-3.28 the change of bubble volume with time has been shown for variations of density, viscosity and surface tension respectively. All the curves span from the inception of the bubble at the orifice mouth till its pinch off. The square marks on the curves indicate the initiation of the neck formation. For all the cases, the duration of neck formation is a small fraction of the total time span of the bubble. Further, the growth of bubble is only marginal during this period. Fig. 3.26 shows both the bubble volume and its life span increases with the decrease of density. However, the rate of bubble growth shows an intriguing trend. The rate is highest for water and decreases both with the increase and decrease of liquid density compared to water. This trend can not be readily explained. Probably it indicates that the bubble growth is not linearly dependent on density. As density appears in different force terms its effect could be rather complex. Fig. 3.27 depicts that both the bubble volume and its life span increases with the increase in viscosity. However, the effect of viscosity is more prominent at its lower values. Finally, the effect of surface tension on bubble volume and departure time is shown in Fig. 3.28. Both of this parameters increases with surface tension. However, the growth curve for bubble volume becomes flatter as surface tension increases.

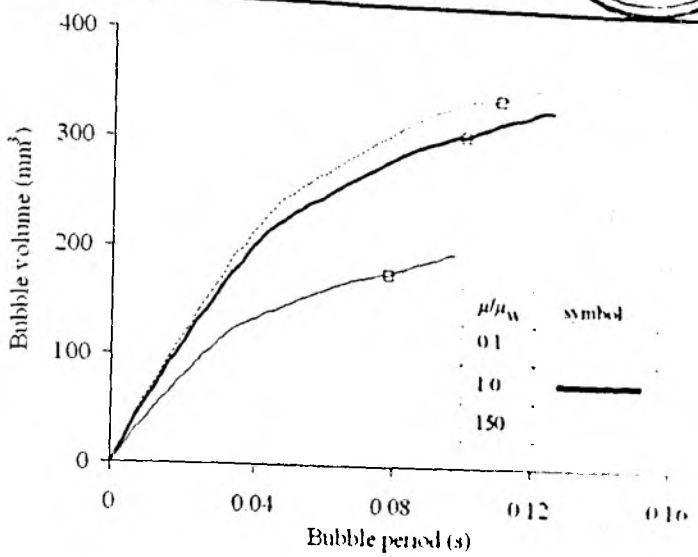

Fig. 3.27 Change of bubble volume throughout the period, effect of liquid viscosity

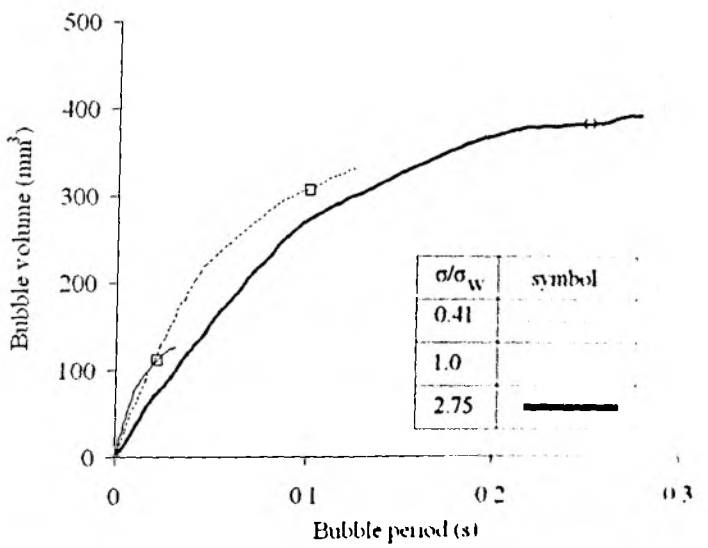

Fig. 3.28 Change of bubble volume throughout the period, effect of liquid surface tension

We have also critically examined the effect of liquid properties on the process of neck formation. The development of the bubble neck starting from its inception till the process of pinch off is depicted in Fig. 3.29 for the variation of the three liquid properties considered in the present work. As the liquid density decreases, the bulb like bubble shape changes to a

rather spherical one during the necking period. The pinch off point also shifts in the upward direction. Change in bubble shape becomes more pronounced in case of viscosity variation. At higher viscosity the bubbles become elongated during the necking period. This is also associated with an upward shift in pinch off point. It is observed that the neck radius increases with surface tension. At a low value of surface tension there is a large increase in necking period as the surface tension increases. However, with further increase in surface tension this effect dies out.

As we have mentioned earlier that the entire duration of bubble evolution may be divided into two parts namely initial growth stage and necking stage. The duration and the bubble growth during the last stage will be far more informative about the necking phenomena.

In Fig. 3.30 ratio of the duration of necking stage to the total growth period is shown in curve (a) (b) and (c) for the variation of density, viscosity and surface tension respectively to quantify the stage in detail. It may be noted that necking period increases with the increase of liquid density over the orifice mouth. The effect of viscosity on the necking period is not as pronounced as the effect of density. There is a marginal decrease in necking period with the increases of the liquid viscosity. From curve (c) it can be seen that necking time is strongly influenced by surface tension when its value is relatively low. As the magnitude of surface tension becomes more than that of water and it increases further, qualitative change in neck formation is noticed but the necking time does not change drastically.

Parallely, efforts have also been made to study the evolution of bubble volume during the necking stage with a variation of fluid properties. Change of bubble volume during necking operation is termed as V_{neck} while the final bubble volume is denoted as V_{total}. In Fig. 3.31 the ratio of V_{neck} to V_{total} is reported for the variation of different liquid properties. It may be noted that the nature of curves in Fig. 3.31 are much similar to the corresponding curve depicted in Fig. 3.30. Neck volume increases with the increase of liquid density but decreases as the liquid viscosity and surface tension force intensifies.

It has been observed that though necking period is occupying almost $1/5^{th}$ of the total bubble period (on an average) the percentage change of bubble volume is not significant (10%) in that period. It eventually shows homogenization of pressure outside and inside of the bubble. The bubble shape also experiences a thorough transformation which leads to the pinch off after some time.

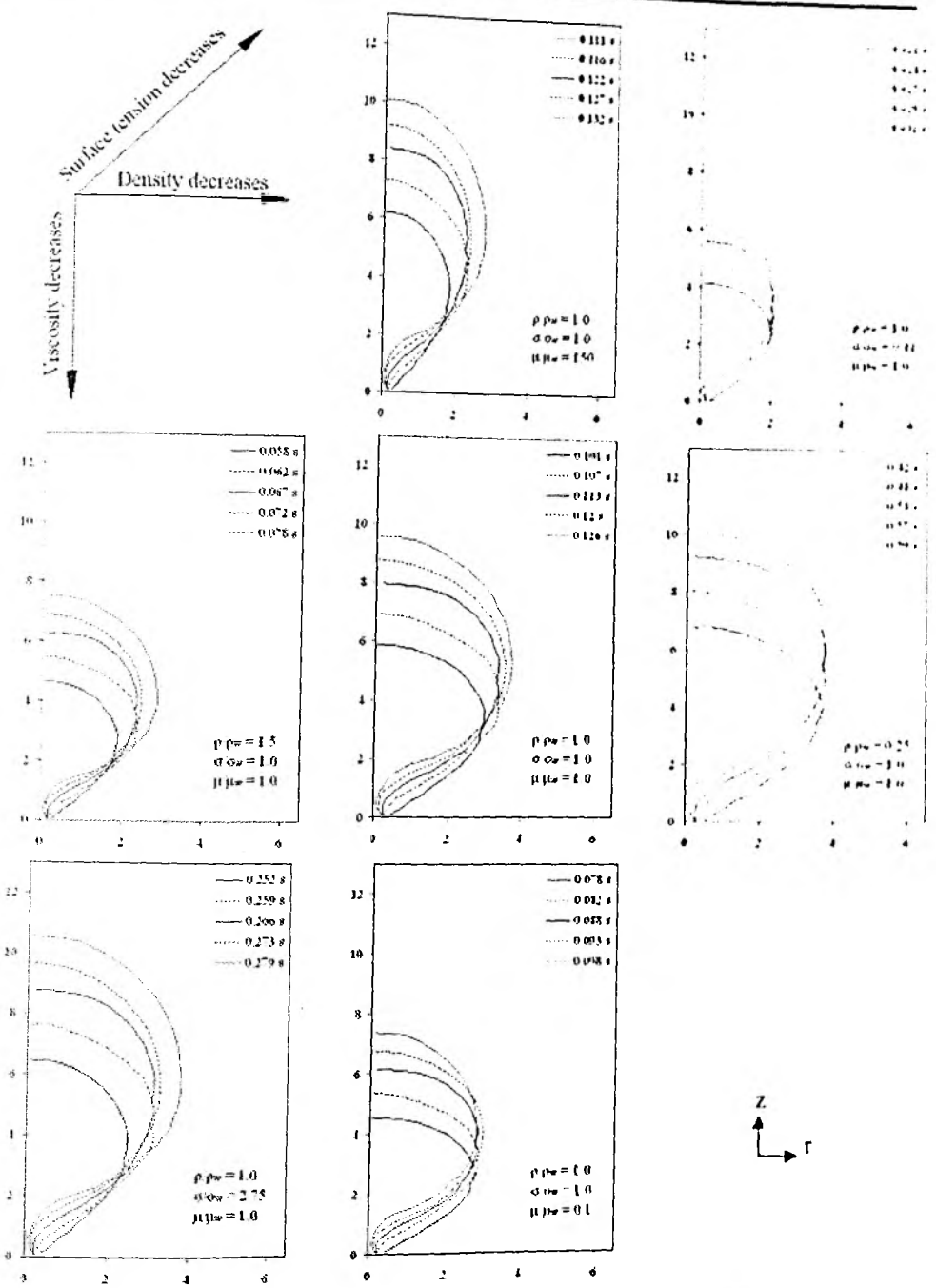

Fig. 3.29 Bubble evolution in the necking phase, effect of density, viscosity and surface tension

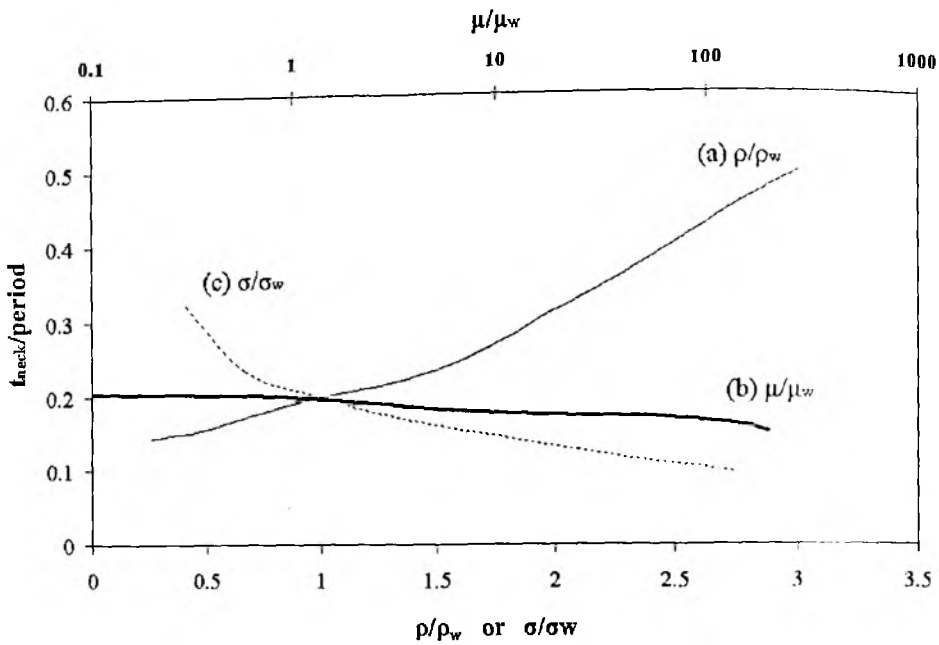

Fig. 3.30 Influence of density, viscosity and surface tension on necking period

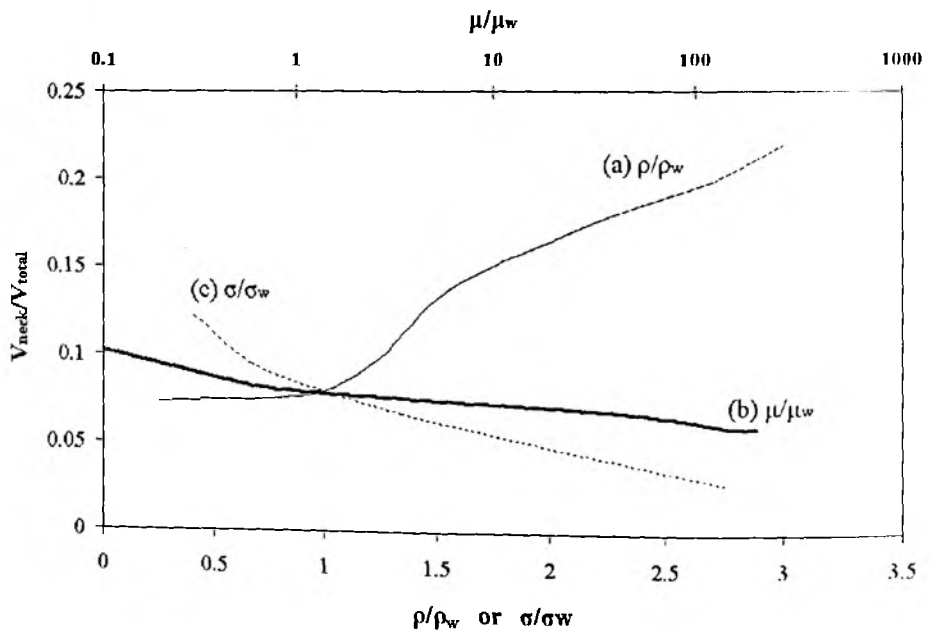

Fig. 3.31 Variation on the bubble volume during neck formation with density, viscosity and surface tension

These two study show that not only bubble volume and bubble period is dependent over the liquid properties like surface tension, density and viscosity, neck formation also relies upon these properties.

3.5. Summary

The Lagrangian Smoothed Particle Hydrodynamics is employed for the simulation of separated flow with a well distinguished interface. At first the model is validated with benchmarking two phase flow situation. Then the model is applied for the prediction of bubbling in a stagnant liquid pool through a submerged orifice. The model successfully captures the cycle of bubble formation, its growth and its departure from the orifice through a process of necking. The computed velocity contours help in explaining the hydrodynamics during the growth of a bubble. Additionally, Effects of fluid properties like density, viscosity and surface tension on the bubbling process and neck formation are also studied in details.

CHAPTER 4 DETAIL MODELING OF INTERFACE-DIFFUSE CONCEPT

4.1. Introduction

Modeling the interface between two fluids is a challenge to both theoretical and computational fluid dynamics. In the previous chapter smoothed particle hydrodynamics is employed to model a time evolving interface as a stretched surface of zero thickness separating two fluids at two different pressures. Another description of interface which defines it as a narrow region characterized by a smooth but rapid variation of physical properties between the bulk values of the two fluids presides for long. Such definition of interface is known as Diffuse Interface (DI). But till date little effort has been made to incorporate DI in particle based techniques due to their lagrangian nature. SPH is successfully used by the researchers (Libersky and Petscheck, 1991; Takeda et al., 1994; Lastiwka et al., 2005; Souto Iglesias et al., 2006) for simulation of multiphase flow as it requires minimal effort to track the interface among the particles of different identities. To the best of the knowledge of the author a few attempts (Xu et al., 2009; Tartakovsky et al., 2009) are there in literature to incorporate DI in SPH. Both of these efforts used mass density based formulation for constructing diffuse interface. On the other hand, in the present work the chemical potential has been used to construct the diffuse interface based on Cahn-Hilliard equation (Jacqmin, 2000). In the present chapter the basic formulation of DI for the particle based system has been devised and the solution algorithm has been developed. Finally, some typical two phase flow problems have been simulated using DI-SPH. The length scale of the interface in the case studies considered in this chapter varies from 10^{-2} m to 10^{-6} m

4.2. Model development

The schematic representation of both sharp and DI is shown in Fig. 4.1. In this figure two different phases are represented by particles of white (phase I) and black (phase II) colors. The propagating sharp interface is characterized by a sudden jump of any thermo physical properties, say from f_1 to f_2 across a zero thickness of the phase boundary. On the other hand, the change of properties across the finite thickness ξ of the DI is rapid but gradual. Though the concept of DI is deeply rooted in thermodynamics suitable computational scheme is needed for its implementation. For the physical description of the phase boundary one may consider a surface with an average value of property $(f_1 + f_2)/2$. Fig. 4.1 depicts the motion of the interface as conceived by both sharp interface and DI.

Van der Waals (1894) first proposed the idea considering the free energy minimization concept. Historically, Cahn (1961) extended the classical model of Van der Waals (1894) for unsteady problems where movement of triple line is present. He correlated interfacial diffusion with the chemical potential gradient in order to track the mobility of the triple line. The governing differential equation for the interface is commonly known as Cahn-Hilliard equation. In the present work we have adopted Cahn-Hilliard equation for a particle based system considering a finite thickness of the liquid-gas interface. Like other thermo physical properties of the fluids one color code (C) has also been assigned to the fluid particles having +1 value for the liquid and -1 for the gas.

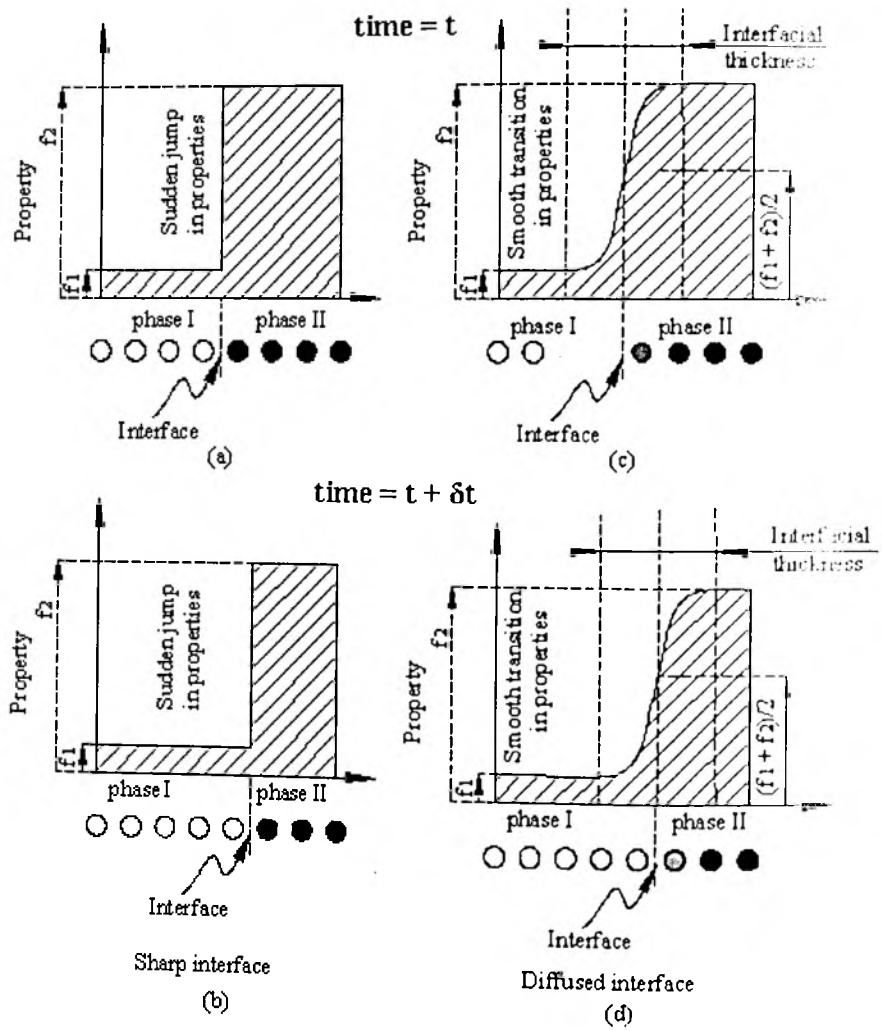

Fig. 4.1 Scheme of DI in SPH

Chemical potential of the fluid (Φ) is calculated based on the color code near the interface around which a smooth transition of C is considered. Chemical potential is calculated for the particle based system in the following manner:

$$\phi_i = \sum_{j=1}^{N} \frac{m_j}{\rho_i \rho_j} \frac{\left((C_i+1)^2(C_i-1)^2 - (C_j+1)^2(C_j-1)^2\right)}{|r_{ij}|} \frac{\partial W_{ij}}{\partial r_{ij}} - \sum_{j=1}^{N} \frac{m_j}{\rho_i \rho_j} \frac{\left(Cn_i^2 + Cn_j^2\right)(C_i - C_j)}{|r_{ij}|} \frac{\partial^2 W_{ij}}{\partial r_{ij}^2} \quad (4.1)$$

In the above, the first and the second part of the RHS of equation 4.1 signifies gradient energy and bulk energy respectively. Cn is the Cahn number which is the ratio of mean interfacial thickness (ξ_i) and characteristics length (L_c). The characteristics length can be selected suitably depending on the problem and ξ_i is taken as three times of the smoothing length, h. Value of ξ_i in the range of 10 μm and can be minimized further if the particle density is increased. Prediction of accurate Cahn number is very important for an effective simulation of the interface and the transport phenomena across it. It basically defines the interfacial thickness in case of DI assumption. One can derive the transport equation of C for the particle based continuum in the following form:

$$\frac{dC_i}{dt} = \sum_{j=1}^{N} \frac{m_j}{\rho_i \rho_j} \frac{k_m(\phi_i - \phi_j)}{|r_{ij}|} \frac{\partial^2 W_{ij}}{\partial r_{ij}^2} . \quad (4.2)$$

In equation 4.2, k_m is the mobility and taken as 10^{-4}. Mobility determines the fluidity of the concerned fluid (Gomez et al., 2008). As a physical thickness is assigned to the interface following the concept of DI, the momentum balance equations (equations 3.8-3.9) will change accordingly. After the incorporation of the source term to take care of the interfacial free energy, the momentum equation can be written as follows:

$$\frac{Dv_i^\alpha}{Dt} = \sum_{j=1}^{N} m_j \left(\frac{\sigma_i^{\alpha\beta} + \sigma_i^{\alpha\beta}}{\rho_i \rho_j} + \xi_{ij} \right) \frac{\partial W_{ij}}{\partial x_i^\beta} - \sum_{j=1}^{N} \frac{m_j}{\rho_i \rho_j} \frac{\left(\frac{C_i}{Cap_i Cn_i} + \frac{C_i}{Cap_j Cn_j} \right)(\phi_i - \phi_j)}{|r_{ij}|} \frac{\partial W_{ij}}{\partial r_{ij}} \quad (4.3)$$

or

$$\frac{Dv_i^\alpha}{Dt} = \sum_{j=1}^{N} m_j \left(\frac{\sigma_i^{\alpha\beta}}{\rho_i^2} + \frac{\sigma_i^{\alpha\beta}}{\rho_i^2} + \xi_{ij} \right) \frac{\partial W_{ij}}{\partial x_i^\beta} - \sum_{j=1}^{N} \frac{m_j}{\rho_i \rho_j} \frac{\left(\frac{C_i}{Cap_i Cn_i} + \frac{C_i}{Cap_j Cn_j} \right)(\phi_i - \phi_j)}{|r_{ij}|} \frac{\partial W_{ij}}{\partial r_{ij}} . \quad (4.4)$$

$\sigma_i^{\alpha\beta}$ is defined in equation 3.10 and Cap is the particulate capillary number which is defined as follows:

$$Cap_i = \frac{2\sqrt{2}\mu_i u_i}{3\sigma_i}. \tag{4.5}$$

Though SPH does not explicitly depend on the boundary following boundary conditions are set for the color code to close the system. No flux condition for chemical potential is assumed at the interface and solid liquid contact plane, if any.

$$\sum_{j=1}^{N} \frac{m_j}{\rho_i \rho_j} \frac{(\phi_i - \phi_j)}{|r_{ij}|} \frac{\partial W_{ij}}{\partial r_{ij}} = 0. \tag{4.6}$$

Second boundary condition for the color code is proposed by Jacqmin (2000) that ensures the interface at the triple line remains at the local equilibrium condition, if present. The boundary condition is as follows:

$$\sum_{j=1}^{N} \frac{m_j}{\rho_i \rho_j} \frac{(\phi_i - \phi_j)}{|r_{ij}|} \frac{\partial W_{ij}}{\partial r_{ij}} + \sum_{j=1}^{N} \frac{m_j}{\rho_i \rho_j} \left(\frac{3kw_i}{4Cn_i}\left(1 - C_i^2\right) - \frac{3kw_j}{4Cn_j}\left(1 - C_j^2\right) \right) = 0. \tag{4.7}$$

Second term of the RHS of equation 4.7 signifies the local surface energy at a particular location. In the above equation, kw is the wetting coefficient whose value equals to the cosine of the physical contact angle of the fluid solid pair. An algorithm for hybrid DI-SPH formulation is shown in Fig. 4.2.

4.3. Prediction by SPH and DI-SPH - a comparison

The previous section describes the modifications needed for the incorporation of DI in the basic algorithm of SPH. The modifications have been done in a generic manner so that the DI-SPH technique can be used to simulate a large variety of problems. The developed technique has been put to test through two different case studies. The examples have been selected such that the properties of the two phases are grossly different and the interface experiences a complex evolution in profile due to the associated fluid dynamics. In both the examples the effect of interfacial tension is important and the success of simulation depends on its correct modelling. In one of the test cases buoyancy force (or the effect of gravity) plays an important role. Additionally, inertia driven flow situations have also been considered. Both the problems have been simulated by SPH as well as DI-SPH to examine the

improvement in the prediction by the incorporation of the concept of DI in the basic SPH scheme. The results of these simulations have been compared with the published literature

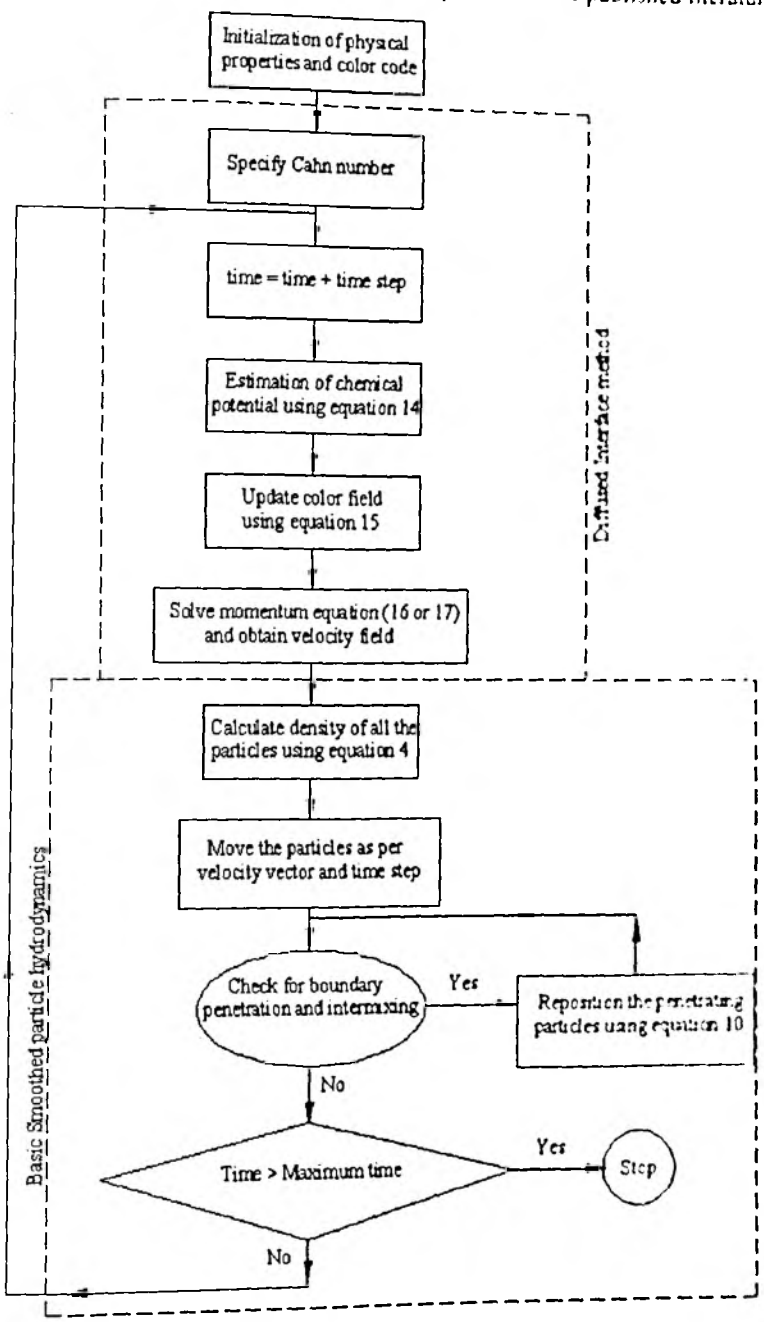

Fig. 4.2 Algorithm for hybrid DI-SPH method

4.3.1. Formation, growth and departure of bubbles from a submerged orifice

Formation of gas bubbles at a submerged orifice, their evolution and finally their departure from the orifice mouth is important for industrial processes which involve aeration. In the previous chapter bubble formation at a submerged orifice is modeled in details using basic SPH. Here, investigations have been made on the same procedure showing special interest on the subsequent rise of the formed bubble due to buoyancy from the orifice mouth. The scheme of particle distribution, spacing between the particles and time steps are kept identical as has been mentioned in the previous chapter.

Recently Smoothed Particle Hydrodynamics has been used by Das and Das (2009) for the simulation of bubble evolution from a submerged orifice. The basic formulation of the methodology assumes the interface to be sharp (chapter 3). In the present chapter DI concept has been incorporated in SPH to equip the methodology for complex simulation of formation of bubbles and their subsequent rise in a liquid column. Figure 3.6 schematically represents the formation of a gas bubble at a submerged orifice. After the growth of the bubble it departs the orifice and rises through the liquid pool as also depicted in the figure.

The process of evolution and free rise of bubble has been simulated by both the methodologies of DI-SPH and the basic SPH. To make a comparison, simulations have been made for conditions identical to those described by Buwa et al. (2007). They have used combined level set and volume of fluid method for capturing the interface. Air and water (surface tension 0.072 N/m) has been used as the gaseous and liquid phase respectively. Volume flow rate through the orifice of 2 mm diameter is kept at 100 cm^3/min.

In Fig. 4.3 bubble evolution for a duration of 70 to 162 ms has been depicted as obtained from our simulations vis-à-vis the simulation results of Buwa et al. (2007). At a first glance the striking trend matching between the figures depicted in the different columns of the figures is obvious. However, a critical inspection helps to bring out the differences. Both SPH and DI-SPH simulation generate almost similar shape of the gas bubble as long as it is attached to the orifice, though in the former simulation shows a tendency for the bubble to get an elongated shape. It can be seen that SPH methodology can efficiently model the bubble evolution at submerged orifice but bubble dynamics after the detachment from the orifice mouth is not tracked well by this technique.

On the other hand, DI-SPH methodology tracked both the evolution of bubble as well as its rise through liquid column with a good accuracy in comparison to the results shown by Buwa et al. (2007). It needs to be mentioned further that the results of Buwa et al. (2007) replicates the experimental results of Zhang and Shoji (2001) and depicts an excellent agreement. In that regard the present DI-SPH solution also matches with the same experimental results very closely. As the bubble is attached at the orifice mouth, the force due to gas pressure is most dominant for the shape evolution. Basic SPH methodology tracks this force effectively which can be seen from the good agreement of the bubble at the orifice mouth. But after the detachment from the orifice mouth, bubbles no longer remain spherical due to the effect of buoyancy and surface tension forces. Inherent deficiency of the sharp interface technique in modelling the interfacial tension may be the possible reason for the mismatch in bubble shape after it is detached.

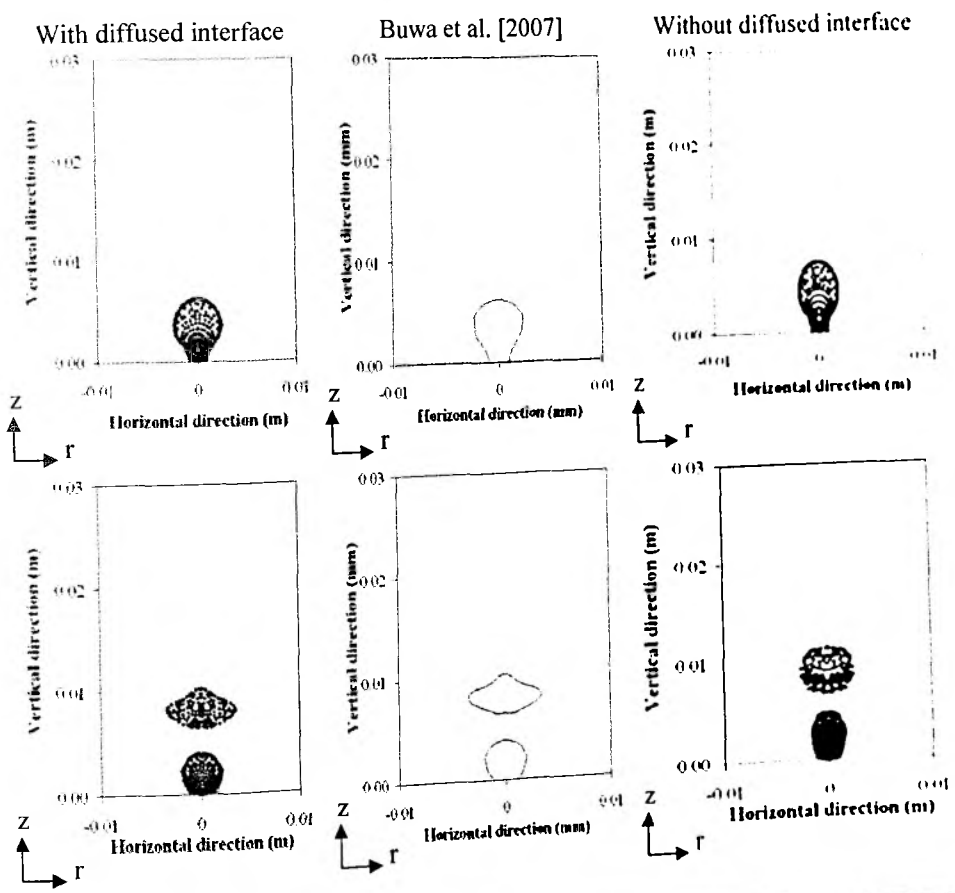

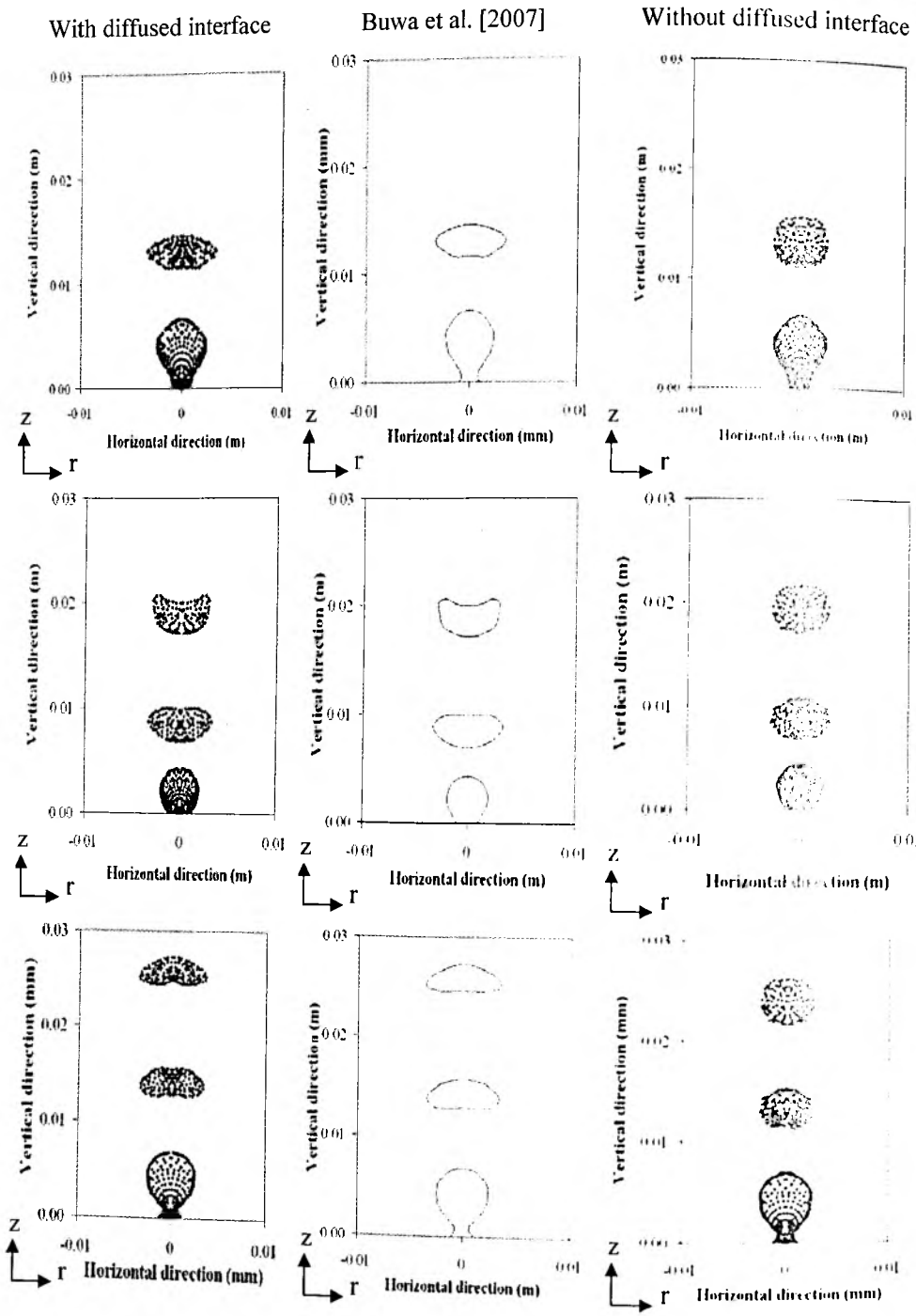

Fig. 4.3 Bubble evolution and its free rise in the liquid pool with and with out DI method

Once DI is incorporated in SPH, the algorithm enables the simulation of both free rising bubbles and the bubbles pinned at the orifice mouth with adequate accuracy. After the detachment the bubbles become oblate which is tracked well by DI-SPH but is not captured by basic methodology. Even change of bubble shape during its rise through the liquid column is well tracked by DI-SPH that can be observed from the results shown in the first column of Fig. 4.3. In Fig. 4.4 bubble frequency calculated using SPH methodology is compared with the experimental data of McCann and Prince (1969). Additionally, the simulation by DI-SPH for the same parametric combinations has also been superimposed in the same figure. The simulation through DI-SPH shows a better agreement with the experimental data and establishes the improvement due to the incorporation of DI.

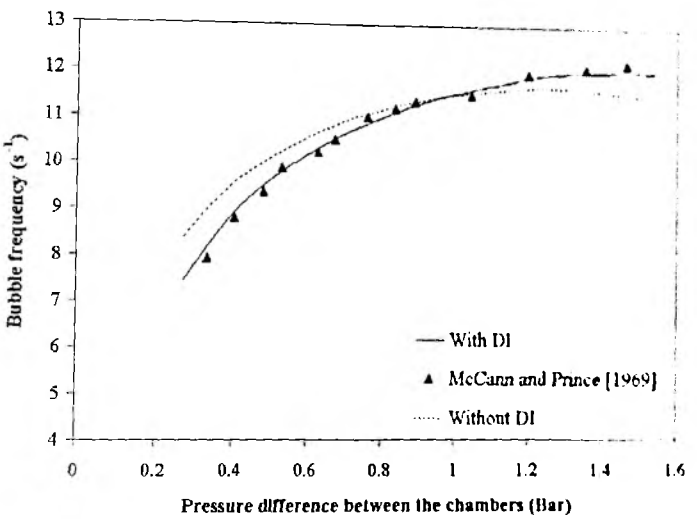

Fig. 4.4 Bubble frequency of different chamber pressure, prediction by DI-SPH and basic SPH

4.3.2. Drop in a shear flow

Deformation of a drop and its breakup into finer droplets are commonly encountered in various systems including micro fluidic devices and emulsification processes. The phenomenon is of fundamental importance in dispersion science and shows a great potential in micro mixing and micro reaction. To manipulate a drop in an immiscible matrix confined in a conduit, application of shear flow in the matrix is a common trend. Starting from initial work of G. I. Taylor (1932) several authors (Bentley and Leal, 1986; Loewenberg and Hinch,

1996; Guido et al., 2003) have attempted to analyze this problem in order to understand the complex interplay between the inertia, viscous and surface tension forces. The important non dimensional numbers governing the phenomena are Capillary number (Ca), Reynolds number (Re), and viscosity ratio (λ); and are defined as:

$$Ca = \frac{\mu_m \beta_s a_r}{\sigma}, \qquad \mathrm{Re} = \frac{\rho_m \beta_s a_r^2}{\mu_m} \qquad \text{and} \qquad \lambda = \frac{\mu_d}{\mu_m} \tag{4.8}$$

Here, β_s is the shear rate and m and d stands for matrix and droplet. a_r is the initial droplet radius.

Li et al. (2000) proposed a critical Ca over which the drop deforms into a dumbbell shape and daughter drops generate due to end pinching. Renardy and Cristini (2001) examined different stages of drop break up through VOF based numerical simulation. As per their study, a drop initially oscillates, then elongates and finally experiences a higher shear which divides it into two daughters. As drop deformation in shear flow is governed by various body and surface forces complex interfacial configurations are obvious. It is expected that the use of particle based methodology like SPH can successfully model the phenomena due to the inherent flexibility of the method in tracking dynamic interfaces. Further, improvement in simulation is possible by considering DI as the abrupt change in property across the interface can be avoided.

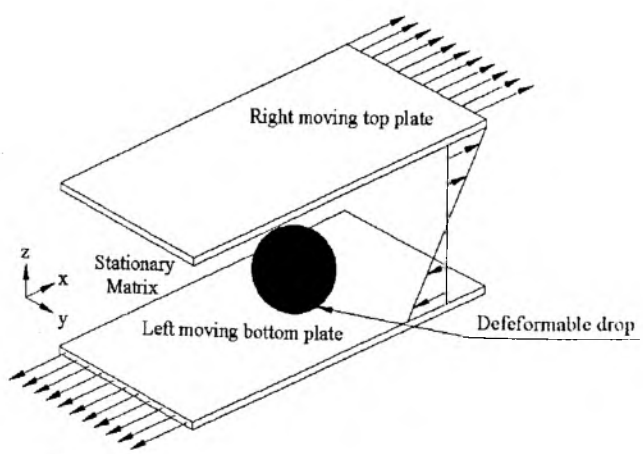

Fig. 4.5 Schematic diagram of a drop in a shear flow

The schematic representation of the problem considered is shown in Fig. 4.5. Initially a spherical fluid drop in the matrix of another immiscible fluid is confined between two

rectangular parallel plates. For simplicity, the density of drop and the matrix fluid is considered to be same. Due to the motions of the plates in reverse direction the centrally placed drop is subjected to a shear field. Drop deformation and break up in a shear flow is simulated using 3D DI-SPH algorithm for Ca = 0.054 and Re = 60. The drop is assumed as spherical at the beginning of the computation having a diameter 0.125 mm. For computation a rectangular prism (2 mm X 1 mm X 1 mm) is considered as the domain keeping the drop at its centre. Liquid and air particles are placed uniformly in the domain. Initial particle distribution and smoothing length are kept uniform and identical for both the simulations. A rigorous study has been made for initial choice of particle spacing. At 2.4 s the drop shape obtained using different particle spacing is shown in Fig. 4.6. It can be observed from the figure that 100 particles across the radius of the drop will give sufficiently accurate prediction in the drop shape. Based on this study particle spacing is maintained at a/100 in all the simulations Simulation is forward marched in steps of 10^{-4} s to attain a steady state solution or drop fragmentation. The motion of the matrix fluid through the finite length of the channel has been modeled using periodic boundary conditions at the channel ends. Viscosity and density of the drop and matrix is assumed to be the same for the simulation. The same problem has also been solved numerically using basic 3D SPH model.

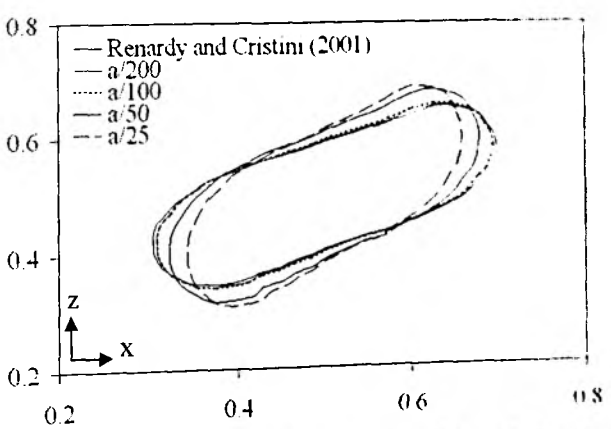

Fig. 4.6 Effect of particle spacing on the prediction of drop shape using DI-SPH

Results obtained from both the schemes are compared with the numerical data of Renardy and Cristini (2001) in Fig. 4.7. It may be noted that Renardy and Cristini (2001) used VOF to solve this problem. All the simulations indicate that the spherical droplet takes up an ellipsoidal shape to start with. The primary axis of the ellipsoid makes an angle with the

channel axis such that the leading edge points the positive x direction. The ellipsoid elongates further to form a two lobed drop with a narrow connecting finger. The two lobes finally break into two small drops and the connecting finger fragments into a number of tiny droplets. It can be observed that the numerical simulations through DI-SPH and the VOF based model of Renardy and Cristini (2001) produce excellent matching as far as drop shapes are concerned. The simulation through SPH with sharp interface gives noticeable deviations in the shape at every stages of drop evolution. The improvement due to the incorporation of DI in the basic SPH model is clear from this comparison.

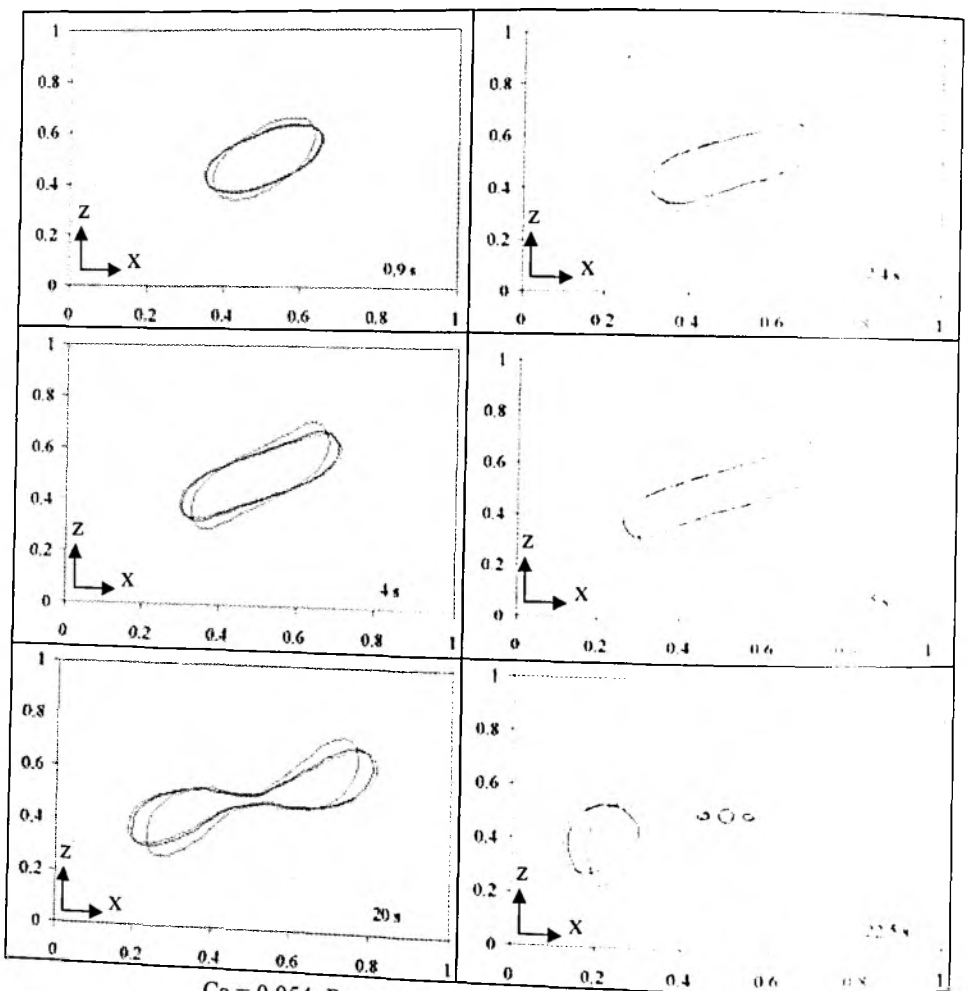

Ca = 0.054; Re = 60.0; same density and viscosity

——— Renardy and Cristini [2001] ——— With DI ——— Without DI

Fig. 4.7 Drop deformations and break up due to shear flow by DI-SPH and basic SPH

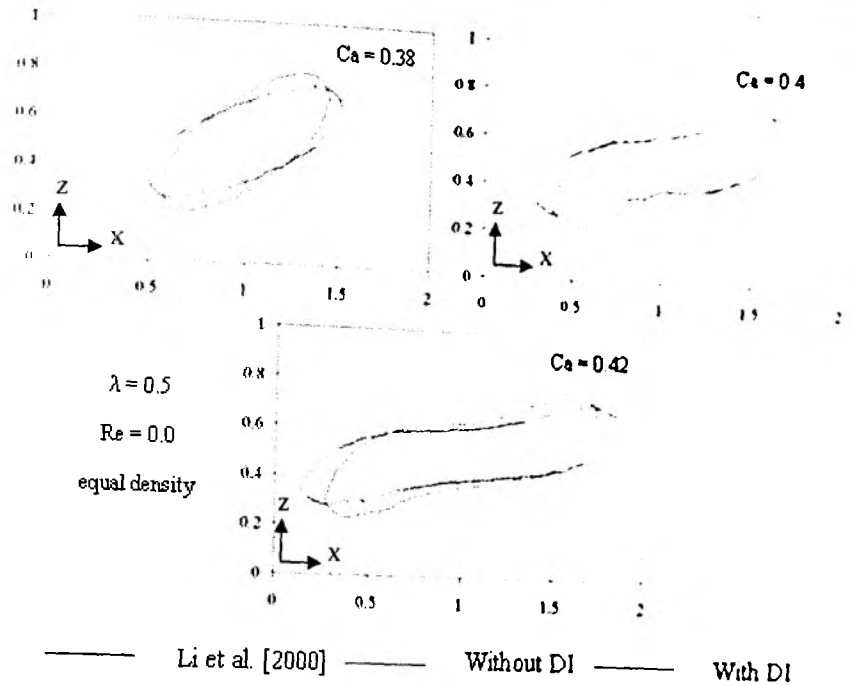

Fig. 4.8 Prediction of drop profile for various Ca number using DI-SPH method

To test the suitability of the developed methodology over a range of fluid properties simulations have next been done varying the non dimensional numbers. To examine the effect of surface tension drop shapes have been evaluated for different Ca. A high value of viscosity has been taken for the matrix fluid to avoid any breakage. This renders the Re close to zero. Drop viscosity is taken as half of the matrix viscosity. Equal densities have been taken for both the fluids. Drop motion and deformation have been simulated using SPH and DI-SPH for three different Ca (0.38, 0.4 and 0.42). It has been observed that drop becomes elongated in the reported ranges of Ca value and reaches at a stable shape from which further elongation is not observed. Fig. 4.8 shows the above simulation along with the results reported by Li et al. (2000). In this case also the DI-SPH simulation gives a closer agreement with the results of Li et al. (2000). For high Ca value drop elongation ultimately tends towards the pinch off.

Effect of the variation in drop viscosity is reported in Fig. 4.9. Viscosity of the drop is lowered in comparison to the viscosity of the matrix assuming very low density of both the fluids such that the Re is close to zero. In Fig. 4.9 simulated results for viscosity ratios of 0.1

and 0.5 and Ca = 0.4, are shown for the stable drop shape. As the viscosity ratio increases the drop becomes more slender and filamental. Nevertheless, like all the previous cases DI-SPH results agrees very well with the VOF based simulation of Li et al. (2000).

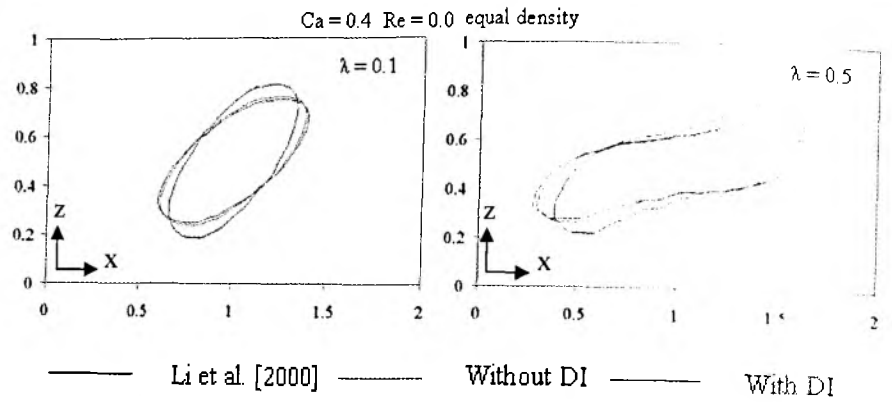

Fig. 4.9 Prediction of drop deformation for various viscosity ratio between drop and matrix using DI-SPH method

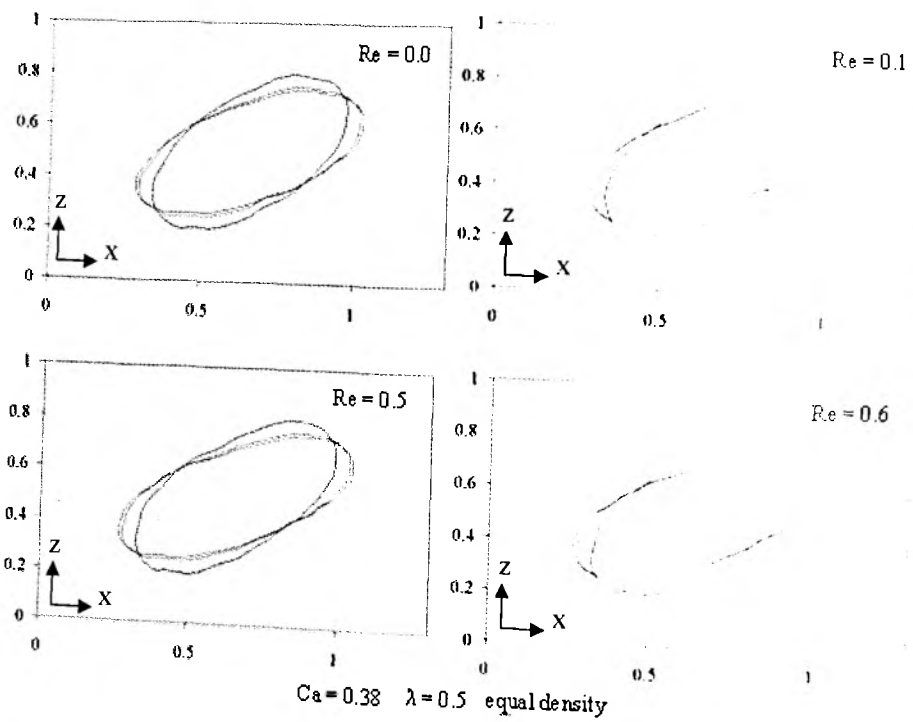

Fig. 4.10 Prediction of drop deformation for various Re using DI-SPH method

Similarly, the effect of Re on stable drop shape is shown in Fig. 4.10 for fixed values of λ and Ca and equal densities of the fluids. Increase in Re enhances the shearing action and elongates the drop as expected. The improvement in the prediction of the drop shape through the incorporation of DI is also obvious from this exercise.

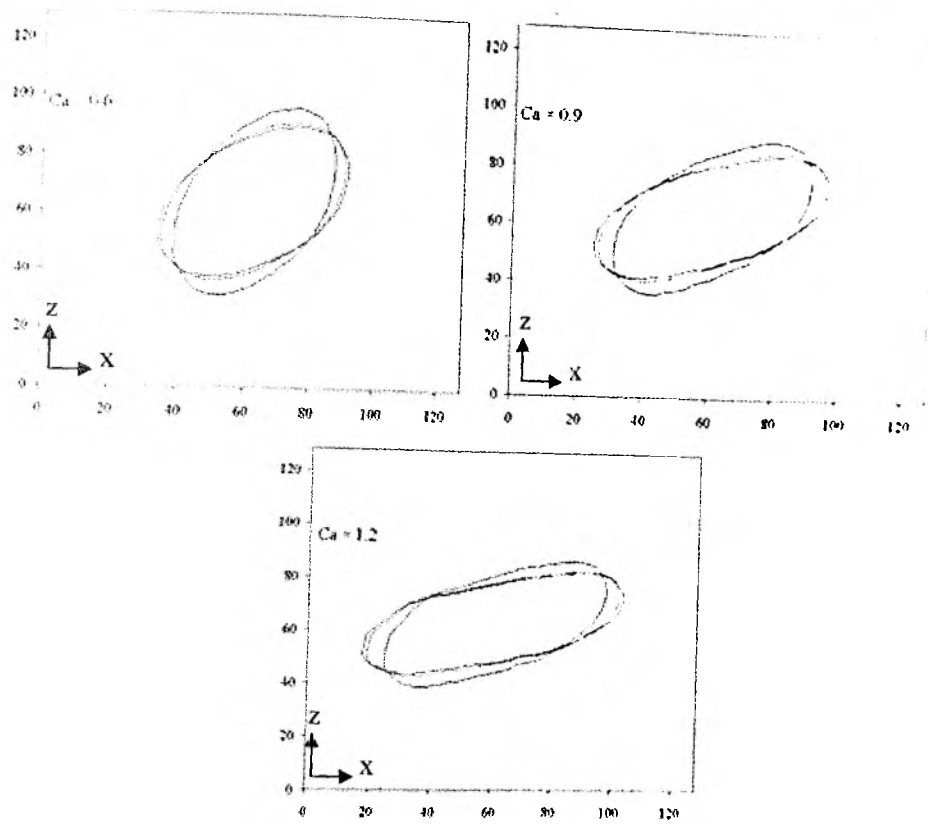

Initial drop diameter = 50.8 mm Re = 10 Pe = 0.1

——Badalassi et al. [2003] —— DI-SPH —— SPH

Fig. 4.11 Comparison of DI-SPH methodology with the numerical results of Badalassi et al. (2003)

Finally, the numerical results of the present methodology have been compared with the reported numerical simulation of Badalassi et al. (2003). Badalassi et al. (2003) used coupled Cahn-Hilliard/Navier-Stokes system for modelling of drop deformation under shear flow. Simulations have been made using the developed DI-SPH methodology for three different Ca number (0.6, 0.9 and 1.2) keeping the Re (0.1) fixed. Badalassi et al. (2003) used DI concept

and defined Peclet number based on the interface thickness and liquid mobility ($3X10^{-6}$). Identical parameters have been used for the present simulations. Fig. 4.11 shows the comparisons of drop shapes reported by Badalassi et al. (2003) and those obtained through numerical simulations using DI-SPH and SPH. It is clear from the figure that prediction of DI-SPH methodology is matching well with Badalassi et al. (2003) compared to basic SPH methodology. The above comparison once again establishes the improvement in the prediction of SPH method by the incorporation of DI.

From the above discussion it is seen that the drop elongates with the increase of both Ca and Re. Depending on the values of these two numbers one may get an elongated drop shape which does not change further and the drop break up is not encountered. Alternately, the elongation may continue and ultimately results in the break up of the drop. For a given Ca one can identify a critical Re above which the drop break up occurs. Li et al. (2000) have constructed a transition curve for drop break up in Ca-Re plane. The same exercise has been repeated using SPH simulation adopting both sharp and DI and the results are shown in Fig. 4.12. The DI-SPH prediction follows the curve by Li et al. (2000) closely while the prediction through basic SPH deviates from both these curves over a range of Ca. All the exercises in this section demonstrate that SPH can simulate the deformation of immiscible drops in shear flow successfully. However, incorporation of DI in the basic algorithm of SPH provides finite improvement in prediction.

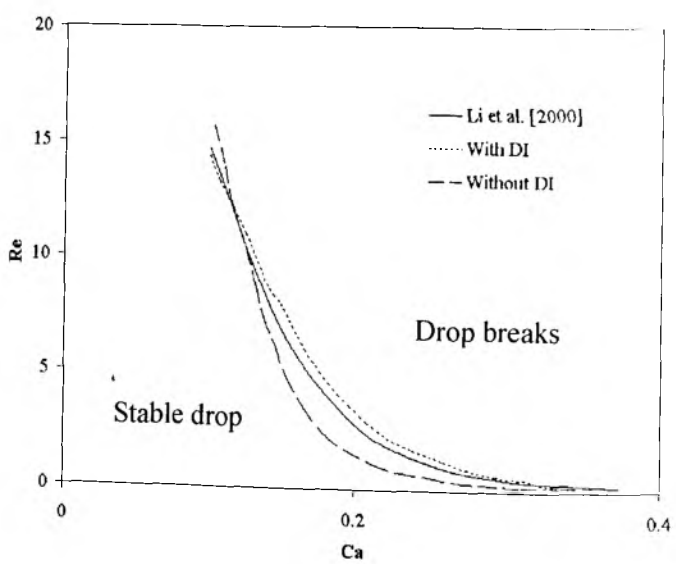

Fig. 4.12 Transition boundary for drop breakup

4.4. Case studies using DI-SPH methodology

In the present investigation the DI-SPH methodology has been used to simulate diverse problems of droplet spreading, their movement as well as breakage and joining of droplets. A unique physical mechanism for droplet manipulation namely wettability gradient has also been considered in some of the case studies.

4.4.1 Drop movement over an inclined surface

Sliding of drops over inclined planes is not only a topic of fundamental interest but is also relevant in many technological and biological applications. While fast droplet movement over wind shields, solar panels, green house covers is desirable, effective utilization of pesticides calls for a greater stability of droplets over plant foliages (Pieters et al., 1997; Wirth et al., 1991). Stability of droplets has a crucial importance in the transition from dropwise to filmwise condensation (Oron and Bankoff, 2001) over an inclined surface as it is also important in printing and coating techniques. Besides, manipulation of droplet movement over terrained surfaces (Abdelgawad et al., 2008) is of great interest in droplet microfluidics. In recent years interests have been shown to build super hydrophobic surfaces (Osawa et al., 2006). The basic understanding of droplet sliding can provide useful information in the design and development of such surfaces. Sliding of droplets is also important for the design of condensing surfaces.

In general, the shape, the stability and the motion of the liquid drops over solid surfaces rely on a number of physico chemical phenomena all of which are not well understood till date. Explanation of certain drop behaviours needs the consideration of interactions even at a molecular level. Nevertheless, tireless efforts have been made by the researchers over the decades to describe the same in terms of macroscopic forces and properties. However, the situation becomes different if the solid plate makes an angle with the direction of gravity. The drop no longer remains axisymmetric to start with and begins to slide down with the increase in plate inclination. Numerous efforts (Larkin, 1967; Brown et al., 1980; Lawal and Brown, 1982; Dussan and Chow, 1983; Rotenberg et al., 1984; Durbin, 1988; Iliev, 1997; Podgorski et al., 2001; Kim et al., 2002; Thiele et al., 2002; Le Grand et al., 2005) have been made to determine the drop shape over an inclined plane, inception of its sliding as well as its sliding velocity. In this connection contact angle hysterisis (Krasovitsky and Marmur, 2005) is a well accepted fact. Contact angles hysterisis refers to the difference of contact

angles at the leading and trailing edge of the drop resting on an inclined plane. For a drop resting on the inclined plane $\theta_a < \theta < \theta_b$. Beyond a critical inclination the drop starts sliding when this relationship is violated (Krasovitsky and Marmur, 2005).

Most of the experimental and theoretical studies (Larkin, 1967; Brown et al., 1980; Lawal and Brown, 1982; Dussan and Chow, 1983; Rotenberg et al., 1984; Durbin, 1988; Iliev, 1997; Podgorski et al., 2001; Kim et al., 2002; Thiele et al., 2002; Le Grand et al., 2005) aim at analyzing the static or at best the quasi static drop shapes just at the yield point. Based on asymptotic theory (Krasovitsky and Marmur, 2005) drop movement after the yield condition has also been investigated. Different postulations have been made to explain drop sliding over inclined planes. Frenkel (1948) explained the drop sliding considering the "pouring of the liquid" from the rear edge of the drop to its front edge along the fluid-fluid interface. He further stated that the drop leaves a thin unstable liquid film behind in case of perfect wetting. Though heterogeneity of the solid surface is thought (Krasovitsky and Marmur, 2005; Dettre and Jhonson, 1964; Joanny and de Gennes, 1984; de Gennes, 1985) to be the cause of a drop being pinned on an inclined surface there have also been alternate explanations (Roura and Fort, 2001). One of the initial attempts to predict the non axisymmetric shape of liquid drops over a sloped solid surface was made by Larkin (1967). He imposed a polar function of contact angle along the triple line in order to obtain a partial differential equation of capillarity. Brown et al. (1980) assumed the contact line to be circular and employed Galerkin finite element technique for the shape of the drop in an inclined plane. Following the same procedure, effort (Lawal and Brown, 1982) was also been made to evaluate the drop profile considering an oval contact line. Rotenberg et al. (1983) used an experimental functional relationship between the spatial contact angle and contact line velocity as the lower boundary. They solved a system of finite element equation which was obtained by minimizing the surface energy potential of a liquid drop. Durbin (1988) considered velocity slip near the contact line and assumed interface yield stress as the shear stress near the triple line. Equilibrium variation approach is used by Iliev (1997) to track the virtual motion of the three phase contact line. He modeled the effect of drop holdup on the contact surface by establishing the counteraction between the separating media. Kim et al. (2002) reported the sliding velocity of a liquid drop of known wetting characteristics by using a scaling law and established the distortion of free surface during its movement. Thiele and

coworkers (Thiele et al., 2001; Thiele et al., 2002) combined diffused interface theory and long wave approximation in order to study one dimensional periodic drop profiles sliding down an inclined plane. They also extrapolated their model for two dimensional drops and noticed front instabilities of the advancing drop front.

Though a large volume of work exists on drop shape, its spreading and stability on tilted plane, enough effort (Gao and McCarthy, 2006) has not been spent to analyze the drop movement down the plane. Gao and McCarthy (2006) postulated two mechanisms for drop motion. Droplets can move by sliding where the particles near the solid-liquid interface are exchanged with the gas-liquid interface ones in a tank and tread fashion keeping bulk of the fluid unaffected. On the other hand there could be rolling motion where entire fluid mass undergoes a circulatory movement. They did not rule out a combination of these two modes of motion in case of an actual drop movement. However, this postulation has not been explicitly demonstrated.

It is worth mentioning that many of the analytical models (Iliev, 1997; Kim et al., 2002; Thiele et al., 2002) simulate two dimensional drop or idealized the three dimensional drop as a planer drop (Krasovitsky and Marmur, 2005). Though the simulation of a three dimensional drop constitutes a considerable level of complexity the problem is solvable by a suitable numerical scheme. Apart from the three dimensionality of the problem, a common difficulty experienced by such techniques is the stress singularity at the triple line. A number of remedies have been prescribed for this. As the singularity arises from the small length scale associated with the triple line incorporation of a precursor film (de Gennes, 1985), surface tension relaxation (Shikhmurzaev, 1997) as well as slip length based level set (Spelt, 2005) methods have been suggested. Alternately, the sharp interface is replaced by a diffuse interface in a number of attempts (Jacqmin, 1996; Huang et al., 2005; Liu et al, 2006). Apart from the above mentioned works the contact line dynamics has not been studied in details and further study is needed for better understanding of the three dimensional phenomena.

Asymmetric shapes of a liquid drop over an inclined plane and contact line dynamics is studied using a hybrid DI-SPH methodology. A 100 mm X 100 mm X 100 mm cube is considered as computational domain where the drop is placed at the centre of the bottom most plane. Initially liquid and air particles are placed uniformly with constant smoothing length. Particle spacing is chosen through a rigorous spacing independence test and it has been decided that 100 particles will be accommodated across the radius of the drop foot print. The same spacing is followed in the other directions. Simulation is forward marched with a time

step 10^{-4} s to get a steady dynamics solution. The particle spacing and time step is kept constant for the other case studies related to drop dynamics. The focus of the study is on the estimation of sliding limit of the inclination angle for drops of different size and fluid-solid combination. The numerical results have been compared well with experimental data taken from various sources. Efforts have also been made to study the internal fluid structure of the drop over the solid surface during the rolling motion. Hybrid DI-SPH model is used to investigate numerically the movement of drop over an inclined plane. Most of the simulations have been done for water droplet (σ_{lv} = 0.072 N/m, ρ = 1000 kg/m^3 and μ = 10^{-3} Pa-s) sliding over a steel surface (contact angle 83°). Gas-liquid interface is simulated as a free surface i.e. pressure difference between two phases are generated only due to interfacial curvature. The model has been validated against available theoretical and experimental results.

Simulation has been started considering a static drop over a horizontal surface. The inclination of the surface has then been gradually increased until the drop starts sliding over the surface. Volume of the water drop is taken as 1.75 mm^3. At every inclination drop is allowed to take its stable shape before proceeding further. In Fig. 4.13 the non dimensional shapes of the stable drop for different inclination have been depicted by the liquid particles at the interface. It is clear from the figures that drop losses its symmetric shape as the solid surface at its base makes an inclination with the horizontal.

At any inclined position of the solid surface, the contact angle of the drop changes from point to point along its periphery. From Fig. 4.13 it can be seen that the drop thins down at the top and assumes a blunt shape towards the bottom due to the effect of gravity. As a result, one gets a substantial difference in the contact angles between the lowest and highest point of the droplet. Contact angle at the lower portion is called as advancing contact angle (θ_a) which exceeds the nominal contact angle of the fluid-solid pair. On the other hand contact angle associated with the upper corner or receding contact angle (θ_r) of the drop reduces as compared with the nominal one. An increase of advancing contact angle and a simultaneous decrease of receding contact angle continues as the inclination of the solid surface increases. Finally at a certain inclination force generated due to asymmetry becomes strong enough to overcome the frictional resistance of the solid surface and drop slides over the surface. The nature of the guiding force (F_c) is as follows:

$$F_c = \pi R \sigma_{lv} \left(\cos\theta_a - \cos\theta_r \right) \tag{4.9}$$

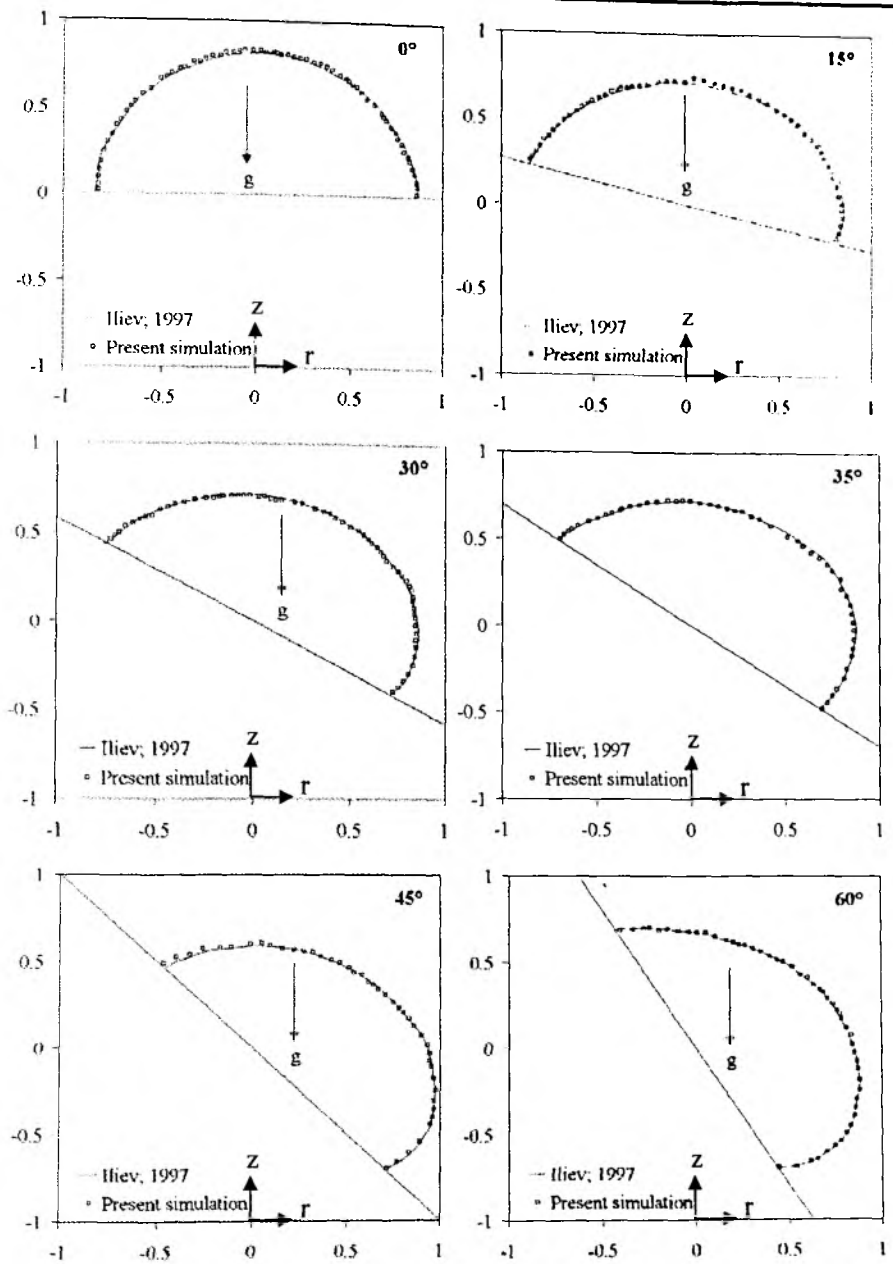

Fig. 4.13 Asymmetric drop shape at various angle of inclination

In Fig. 4.13 drop shape is shown for six different inclinations of the solid surface along with the analytical solution of Iliev (1997). While the drop is stationary for the first five

angles of inclination, it is sliding at 60°. A very good match can be seen between the present numerical simulations and analytical simulation (Iliev, 1997).

Study the drop foot print at various inclinations is made in order to investigate the contact line dynamics. As the inclination of the solid surface increases the drop starts losing its azimuthal symmetry. In Fig. 4.14 contact line is depicted for different angle of inclinations. It is evident from the figure that contact line remains more or less symmetric up to 30° inclination. Beyond that, asymmetry becomes prominent and over an inclination of 45° the drop movement starts. Analytical results of Iliev (1997), also present in Fig. 4.14, show the good predictability of the model. Once, the angle of inclination exceeds 45°, the drop slides down the inclined plane.

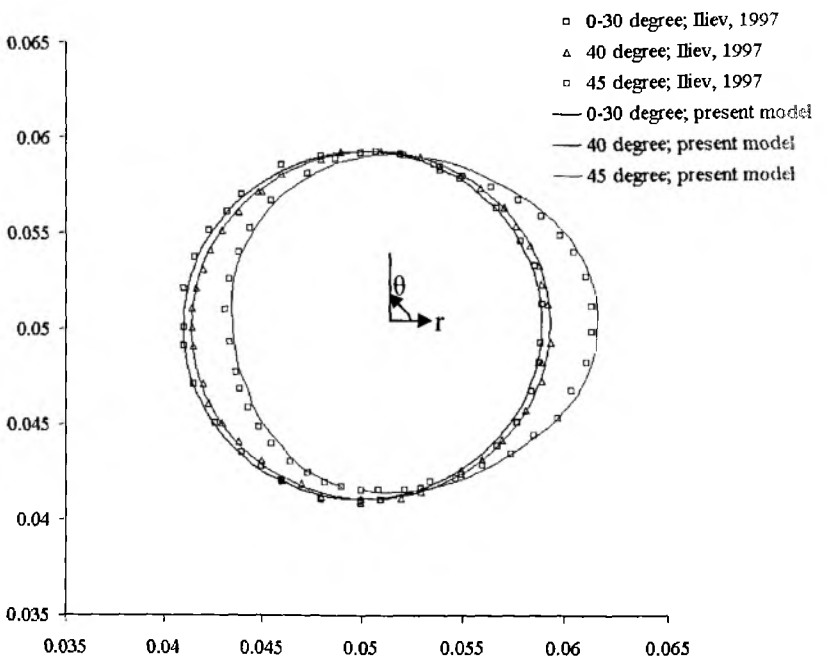

Fig. 4.14 Drop footprint at different angle of inclination

The unique CFD simulation adopted for the present study lends an opportunity to probe the interesting hydrodynamics during sliding of the drop. It is clear from the simulation results that the liquid drop undergoes a continuous change in its shape during its movement. The local interface curvature changes to produce a worm like peristalsis of the drop. Spatio-temporal ripples are generated at the interface and moves from one end of the drop to the

other. This alternate swelling-deswelling surface ripples are responsible for the bulk movement. The surface waves create an internal circulation. In Fig. 4.15 snapshots of the drop sliding down a 60° inclination are shown. The continuous change of the droplet shape is obvious from this figure.

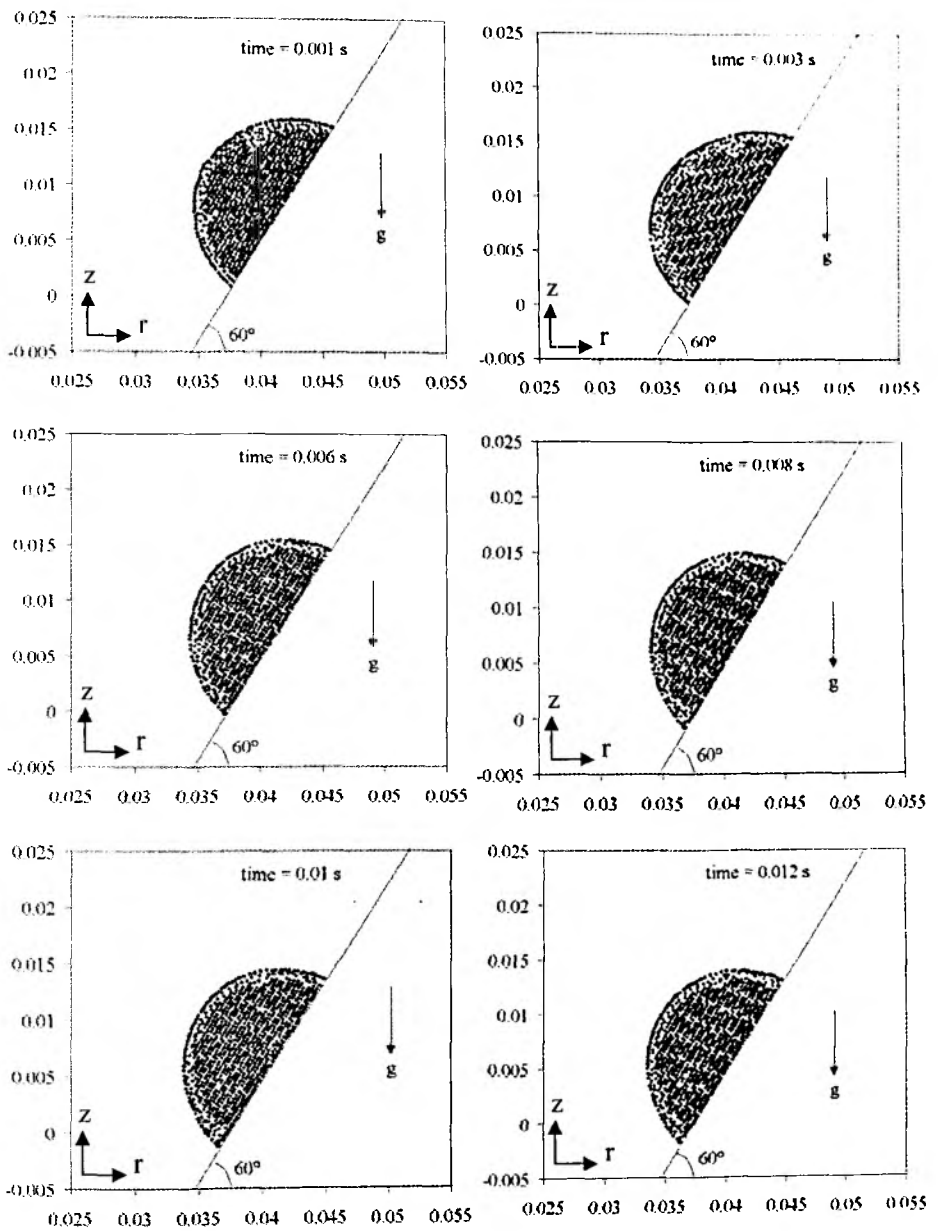

Fig. 4.15 Motion of the marked particles inside a drop sliding downward

Additionally, a bunch of marked fluid particles are traced during sliding. As shown in the figure, initially the marked particles are located just below the liquid-gas interface. During sliding they move down under the effect of gravity along the interface and reach the advancing front. In the next course of their motion they move up along the inclined solid surface. It may be noted that as the internal circulation of the drop does not contain a strong vortex the marked particle bunch retain its shape more or less intact during the downward motion. However, while climbing up the inclined plane, the bunch is stretched along the surface. This implies while the fluid lump rolls down the gas-liquid interface it undergoes a deformation near the solid-liquid contact surface due to presence of a strong shear field. After reaching the receding end the particles forms a lump once again due to sudden velocity drop. A book keeping of the particle numbers has also been done meticulously during each step of the movement. It has been noticed that near the advancing end one particle disappears from the two dimensional plane presented in the figure. The decrease in the number of marked particles, while passing near the advancing front, signifies the bulging of the leading tip of the drop. The missing particles shift to the other plane adjacent to the reported one and leads towards the asymmetry of the drop.

The above observation can also be supported by instantaneous velocity fields inside the droplets. In Fig. 4.16 velocity vectors are depicted for 50° and 60° inclinations for the same volume of the liquid drop. An internal circulation is clear from the velocity vector plot for both the inclination angles. Circulation becomes stronger as the inclination increases from 50° to 60°. The internal liquid motion obtained by the numerical simulation supports some of the earlier conjectures (Frenkel, 1948; Gao and McCarthy, 2006) regarding the mechanism of drop movement down a tilted plane. Out of two mechanisms namely sliding and rolling postulated by Gao and McCarthy (2006), the Figs. 4.15 and 4.16 present a picture very close to the description of rolling. For the range of parameters considered in the present study we did not come across a sliding motion where only the liquid adjacent to the solid surface is affected. This leaves of scope of further investigation for a wide variety of fluid properties.

Variation of contact angles for both advancing and receding corner of the drop (θ_a and θ_r) due to change in inclination angle is plotted in Fig. 4.17. At 0° inclination the drop is symmetric which makes both the contact angle same (83°). With the increase of the inclination angle a steep change in advancing contact angle is noticed. Receding contact angle is also decreased with the increase in inclination angle but its change is not so sharp. At 60°

inclination there is 90° variation in contact angle between the advancing and receding front. Difference between the contact angles generates a force as described in equation 4.13 which helps the rolling motion of the fluid particles inside the drop. The drop moves down the surface when the force generated due to difference in contact angle exceeds the pinning force of the solid liquid contact.

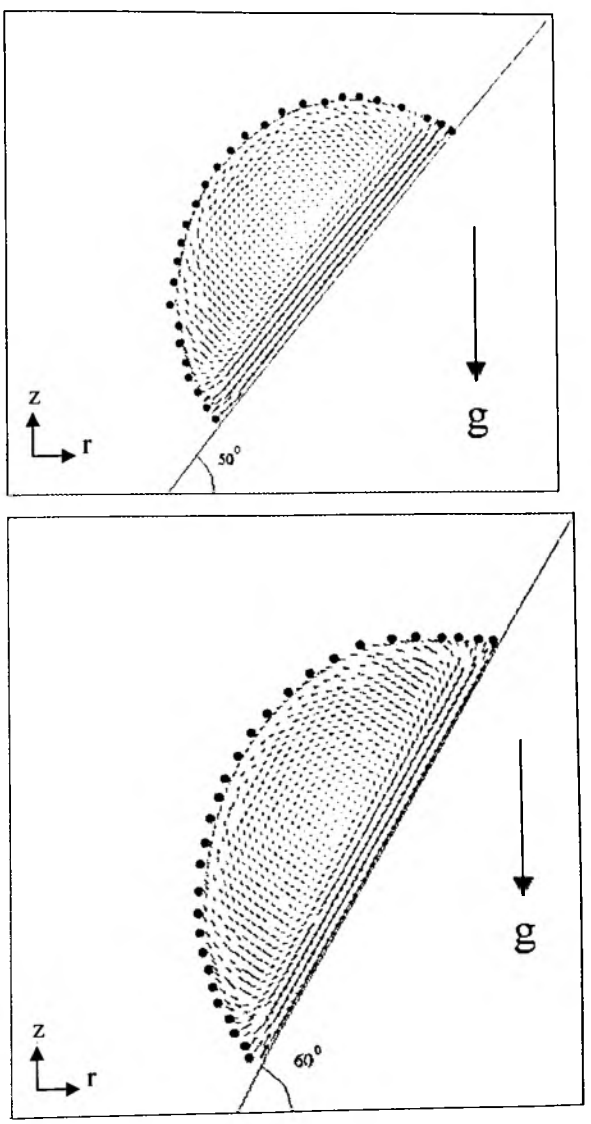

Fig. 4.16 Velocity field inside the drop at different angle of inclination

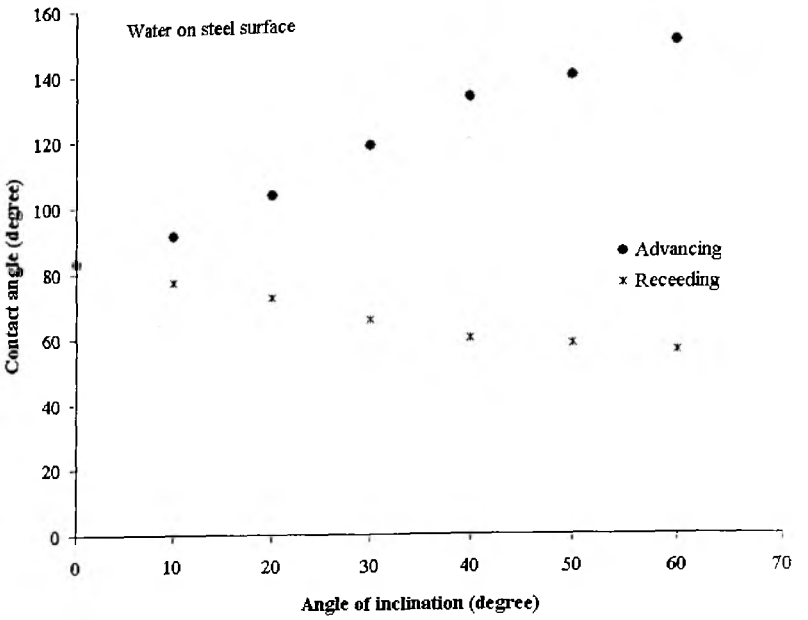

Fig. 4.17 Evolution of advancing and receding contact angle with a variation of inclination

Simulations have been done by increasing the inclination angle continuously to reach the limiting inclination angle beyond which a drop of a specified volume starts moving. A curve signifying this limit in inclination angle vs. volume plane is termed as sliding curve. The sliding curve for a water drop over a Polytetrafluoroethylene (PTFE) surface (Contact angle 109°) is reported in Fig. 4.18. The limiting inclination angle decreases with drop volume as can also be conceived intuitively. Experimental results of Ryley and Ismail (1978) plotted on the same figure shows a good agreement with the present simulation. Similar studies have been made for other fluids. It can be seen that the sliding curve of Kerosene (Contact angle 20°) (less viscous than water) over PTFE surface shifts up while the curve for Glycerin (Contact angle 105°) (more viscous than water) shifts down in comparison with that of water. As the contact between mercury and PTFE surface (Contact angle 150°) is almost non wetting, the sliding curve for this solid liquid pair indicates that a mercury drop will instantaneously roll down a PTFE surface at a nominal angle of inclination.

Another validation of the hybrid DI-SPH model for the prediction of sliding curve is presented in Fig. 4.19. Simulations using water drop over an Alkyl Ketene Dimmer (AKD)

surface (θ = 165°) is matched satisfactorily along with experimental results of Pierce et al. (2008).

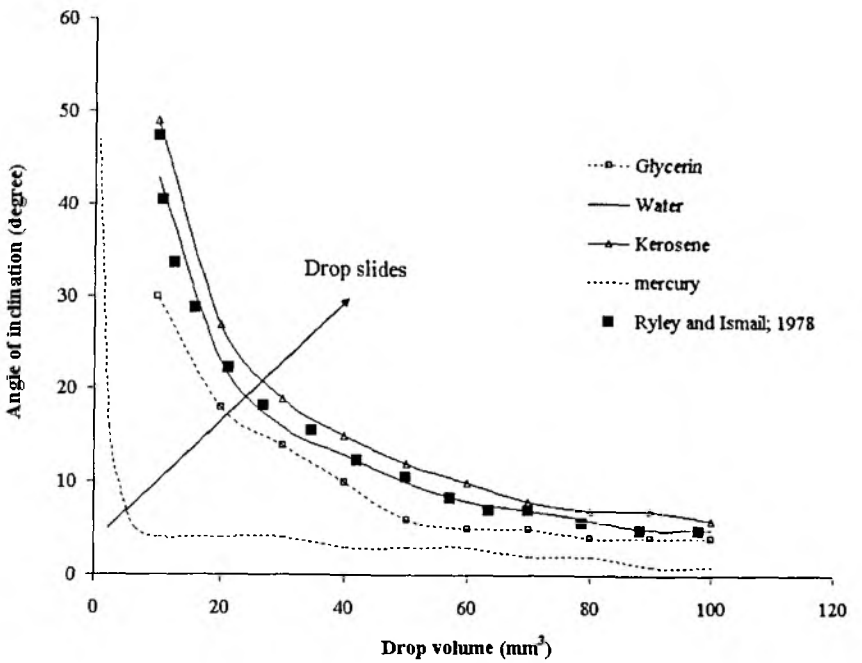

Fig. 4.18 Sliding curve for different fluids over PTFE surface

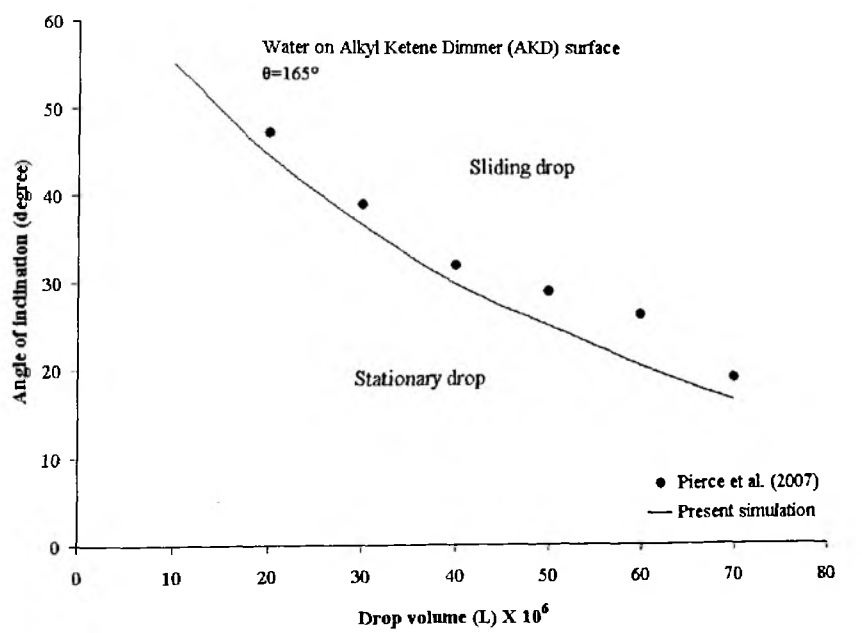

Fig. 4.19 Sliding curve of water over AKD surface

4.4.2 Droplet transportation over horizontal gradient surface

The translation of droplet over a solid surface having a gradient of contact angle is showing great potential for the developments of various lab-on-chip systems in micro fluidics (Gau et al. 1999; Gallard et al. 1999) and bio fluidics (Suda 2001). It basically employs the imbalance of surface tension in the circumferential plane of a droplet resting over a treated surface having wettability gradient. The driving force behind this autonomous transport is a direct function of the wettability of the heterogeneous surface. Wettability gradient can be produced using chemical, thermal, electrochemical and photochemical methods. Experimentally, it is first demonstrated by Greenspan (1978) and subsequently investigated by several researchers (Brochard, 1989; Chaudhury and Whitesides; 1992; Suda and Yamada; 2003). Daniel et al. (2001) showed that the drop velocity on a gradient surface can be very high even in comparison to the classical marangoni flows. They also reported improved heat transfer coefficient in gradient surface due to the high mobility of liquid drops over it. Moumen et al. (2006) experimentally showed that the drop velocity is not only a function of wettability gradient, it also depends on the drop volume as gravitational force is of the same order with the inertial force. Recently, Liao et al. (2007) showed that the movement of a drop over a gradient surface can be partitioned into two separate segments. At first, drop will accelerate and then decelerate before reaching the saturation point of the contact angle due to sheet formation. Apart from experimental investigations very few theoretical efforts have been made to understand the phenomena from the basic principle. In 1995 Iliev used a hybrid boundary-finite element method for probing into details of drop movement over gradient surface. Subramanian et al. (2005) approximated the drop shape over a gradient surface by lubrication theory and collection of wedges to evaluate the quasi steady speed against the hydrodynamics resistances. Numerical techniques have also been tried for the study of internal structures during the movement of the drop over a surface having wettability gradient. Huang et al. (2008) used lattice Boltzmann Method for wettability controlled movement of a liquid drop in lab-on-a-chip systems. They showed that the mobility of the three phase contact line is important for droplet motion. Liao et al. (2009) numerically simulated the equilibrium shape of a liquid drop on a surface having surface energy gradient using a finite element method. They have reported that unbalanced surface tension force generated by gradient surface causes the drops to be elongated up to a certain limit of contact

angle. This limit is governed by the transition of the drop centre of mass from hydrophilic to hydrophobic zone. But till date a very few investigation has been made for contact line dynamics using SPH. In this section DI-SPH formulation is used for the simulation of axisymmetric drop shape over a gradient surface. For simulation of drops 1000 to 21000 liquid particles are taken depending on the drop volume with uniform particle spacing (100 particles along the drop foot radius). Study of internal flow pattern of the drop has also been reported.

At the outset, the simulation results by the present technique have been calibrated against some published results of drop dynamics over linear wettability gradient. Liao et al. (2009) used finite element method to predict the shape and foot print of water drops (2μL in volume) during their spreading on a 5°/mm gradient surface. Similar situations have been modeled using the developed DI-SPH methodology. Properties of water used for the simulation is mentioned in Table 4.1. Results obtained from the numerical simulation are presented in Fig. 4.20 and 4.21. The drop spreads over the surface rapidly to attain the contact angle corresponding to the triple line. However, the drop spread is highly asymmetric and its receding edge remains almost pinned to the solid surface. It is evident from Figs. 4.20 and 4.20 that the present simulation agrees very well with the prediction of Liao et al. (2009) over a wide range of contact angle variation at the centre (from 36° to 95°). Fig. 4.21 also shows that the drop foot print elongates keeping the left most point of the drop pinned to the surface.

Table 4.1 Properties of fluids used

Type of fluid	Density (kg/m^3)	Viscosity (mPa-s)	Liquid-vapor Surface tension (mN/m)	Contact angle (°)
Water	1000	0.89	72.8	82.6
Tetra ethylene glycol	1125	16.1	48	40

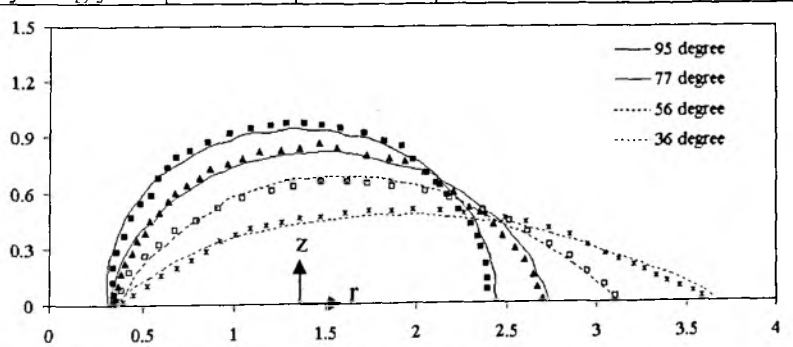

Fig. 4.20 Comparison of drop profile with Liao et al. (2009) at high wettability

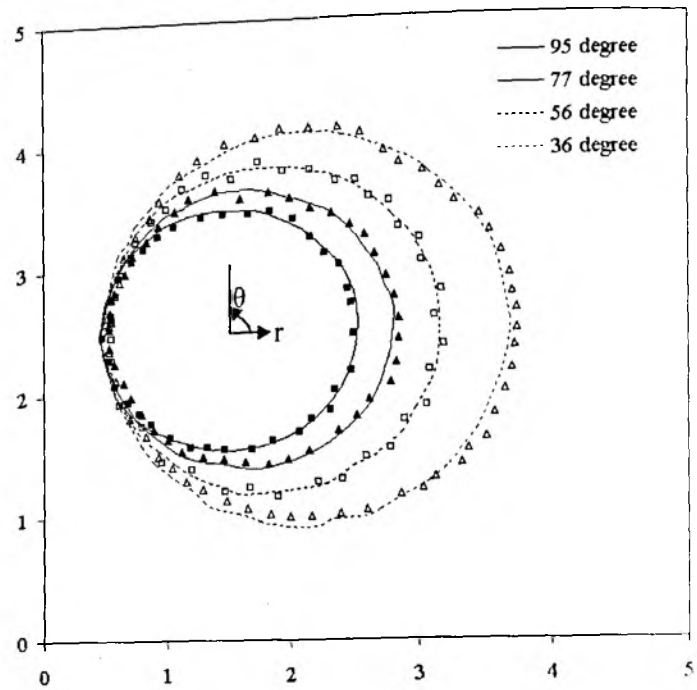

Fig. 4.21 Comparison of drop foot print with Liao et al. (2009) at high wettability

The above example shows that a drop placed on a gradient surface spreads till it assumes the equilibrium shape. In other words, there is a temporal evolution of the drop placed on a gradient surface. However, Liao et al. (2009) did not report this temporal evolution. In Fig. 4.22 the shape of a water drop over a gradient surface has been shown at four different time instants. A 2μL of water lump over a solid surface having 5°/mm wettability gradient has been considered as before. The spread of the droplet is evident from the "computational snapshots". To investigate the internal fluid movement during spreading, position of a group of particles is tracked with respect to time. In Fig. 4.22 two bunches of particles, one near the right most corner and other at the leftmost corner has been identified and are colored red and blue respectively. With the spread of the droplet the bunch of the red particles experience a small movement towards the right and finally occupies the rightmost corner. On the other hand the blue particles remain almost stationary. This implies that during spreading there is a small movement at the rightmost corner but the left corner is practically static and pinned to the surface. Due to the unidirectional wettability gradient drop spreads primarily in one direction.

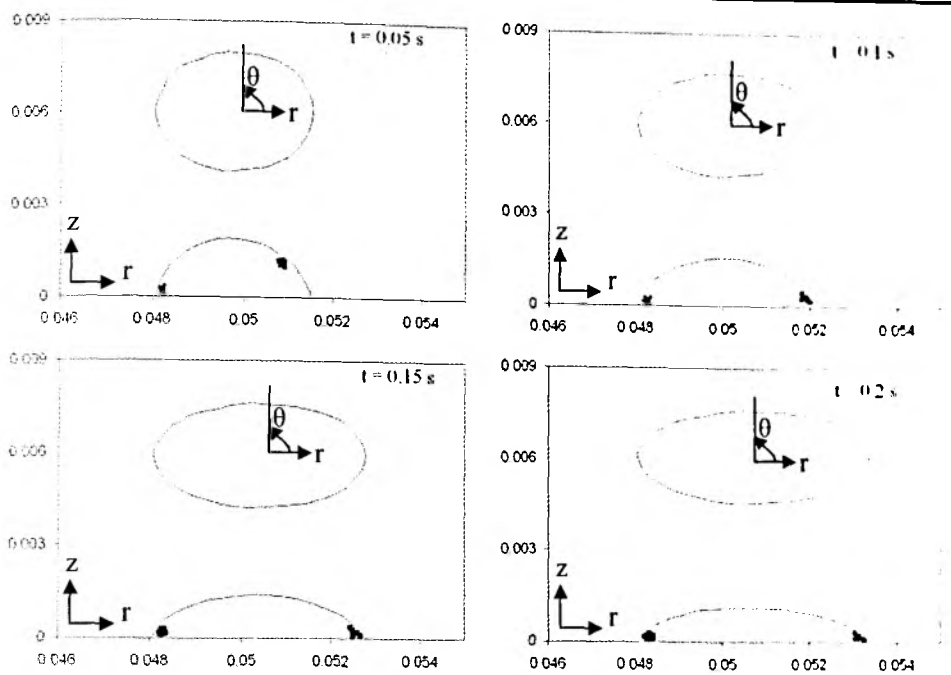

Fig. 4.22 Drop spreading at a high wettability gradient

It is needless to mention that the behavior of a droplet over a gradient surface is strongly influenced by the magnitude of the wettability gradient itself. This aspect has been thoroughly investigated in the present work. Simulations have also been made for the liquid drops over a surface having different wettability gradients. For a moderate value of wettability gradient the drop shapes and the foot prints as obtained from the simulation are depicted in Fig. 4.23 and 4.24 for a tetra ethylene drop over a steel surface having 1°/mm wettability. Properties used for the simulation of tetra ethylene drop are mentioned in Table 4.1. Drop volume is kept constant as in the previous case. Interestingly, the behavior of the droplet is distinctly different. There is no discernable change in the drop shape but the drop translates over the surface as depicted in Fig. 4.23. Drop velocity can be calculated using any of these figures. Rate of change of displacement of the centre of mass of the drop with respect to time is defined as the droplet velocity. In the present example the drop velocity can be estimated as 0.0017 mm/s.

It would be interesting to study the internal fluid motion during the bulk movement of the drop. Inside the translating drop a bunch of particles (marked red) are identified as shown in

Fig. 4.25. From the locus of the particle positions during the drop movement, an internal circulation of the fluid mass is evident. At low and moderate wettability gradient, forces due to surface tension become comparable with the gravitational forces. This generates a circulation cell inside the fluid drop and drop starts to translate over the surface.

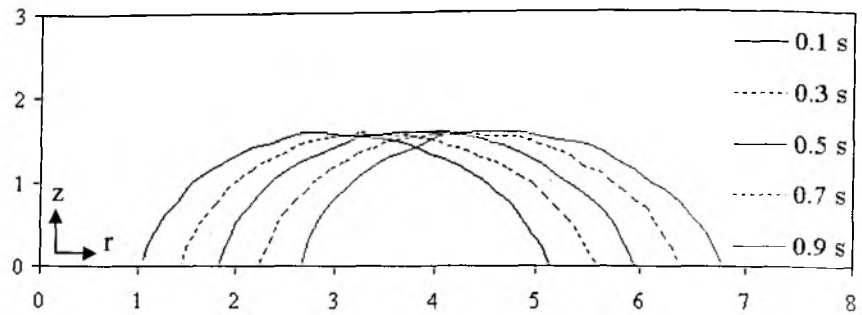

Fig. 4.23 Drop profile at various time steps over a surface having low wettability gradient

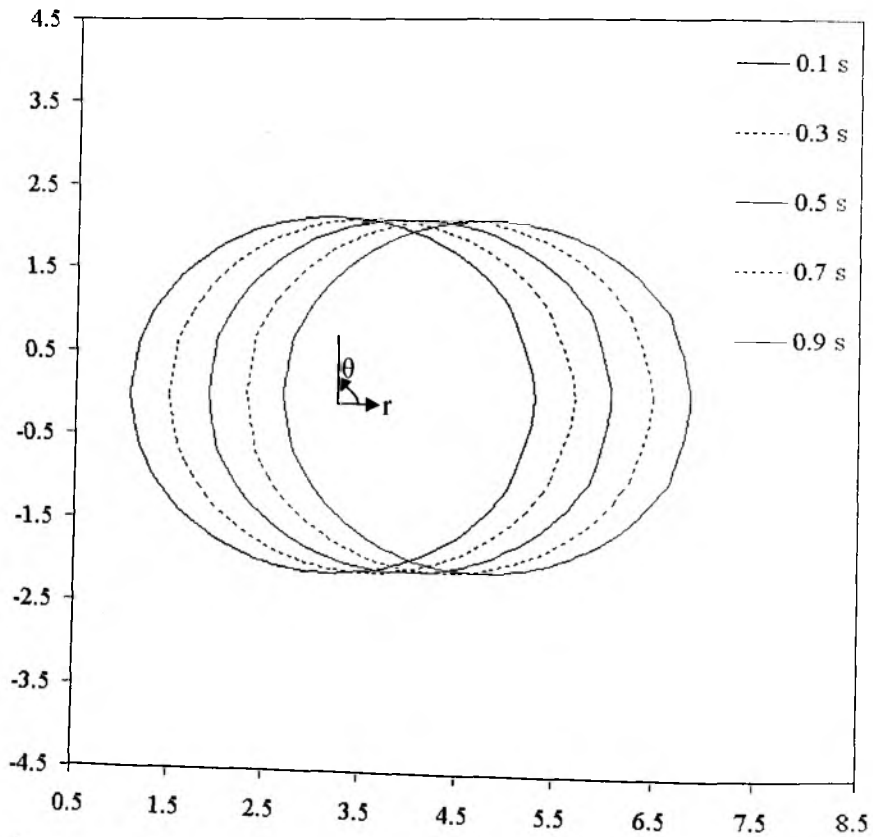

Fig. 4.24 Drop foot print at various time steps over a low wettability gradient surface

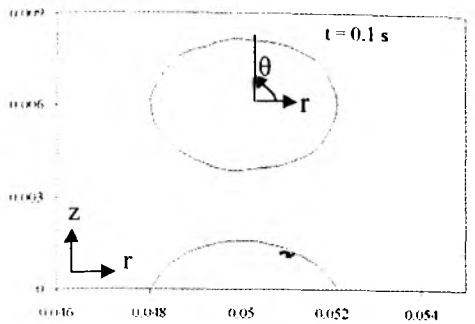
t = 0.1 s
θ
r
Z
r
0.046
0.048
0.05
0.052
0.054

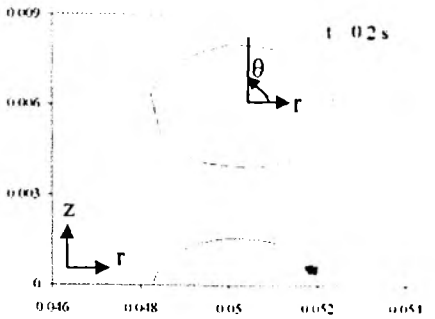
t = 0.2 s
θ
r
Z
r
0.009
0.006
0.003
0
0.046
0.048
0.05
0.052
0.054

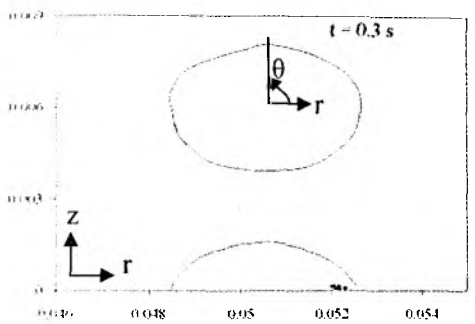
t = 0.3 s
θ
r
Z
r
0.048
0.05
0.052
0.054

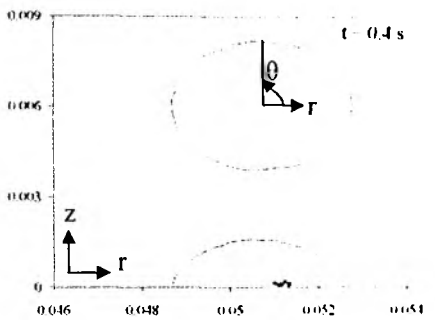
t = 0.4 s
θ
r
Z
r
0.009
0.006
0.003
0
0.046
0.048
0.05
0.052

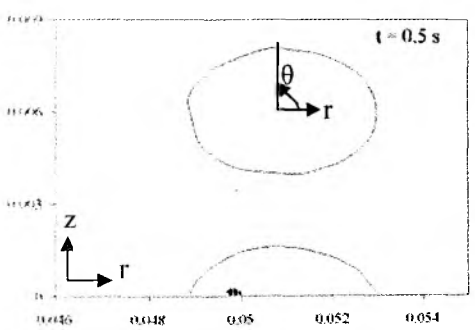
t = 0.5 s
θ
r
Z
r
0.048
0.05
0.052
0.054

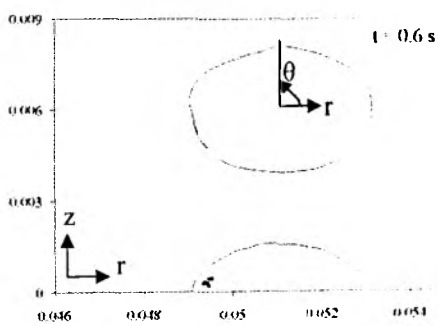
t = 0.6 s
θ
r
Z
r
0.009
0.006
0.003
0
0.046
0.048
0.05
0.052

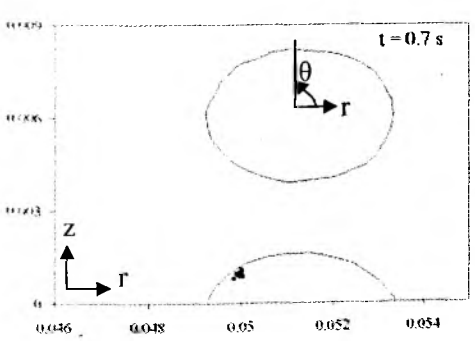
t = 0.7 s
θ
r
Z
r
0.046
0.048
0.05
0.052
0.054

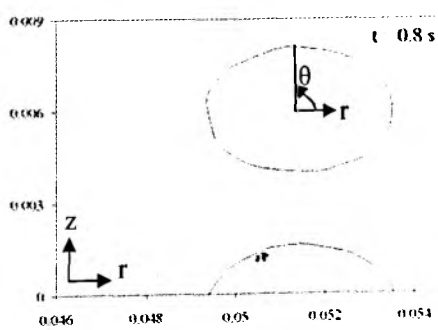
t = 0.8 s
θ
r
Z
r
0.009
0.006
0.003
0
0.046
0.048
0.05
0.052
0.054

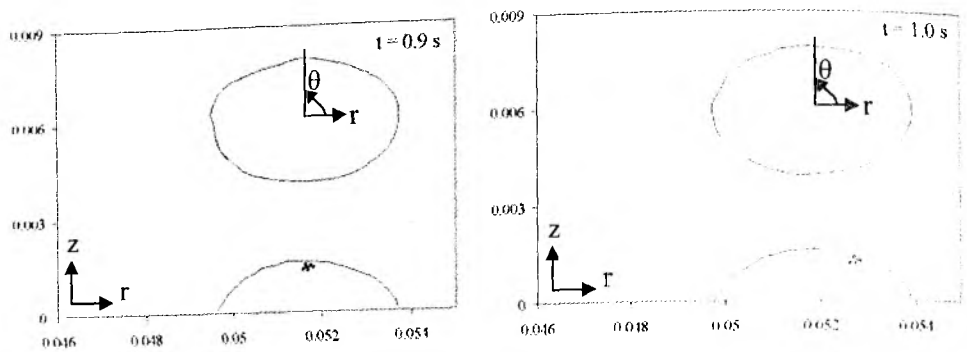

Fig. 4.25 Translation of a liquid drop at a low wettability gradient

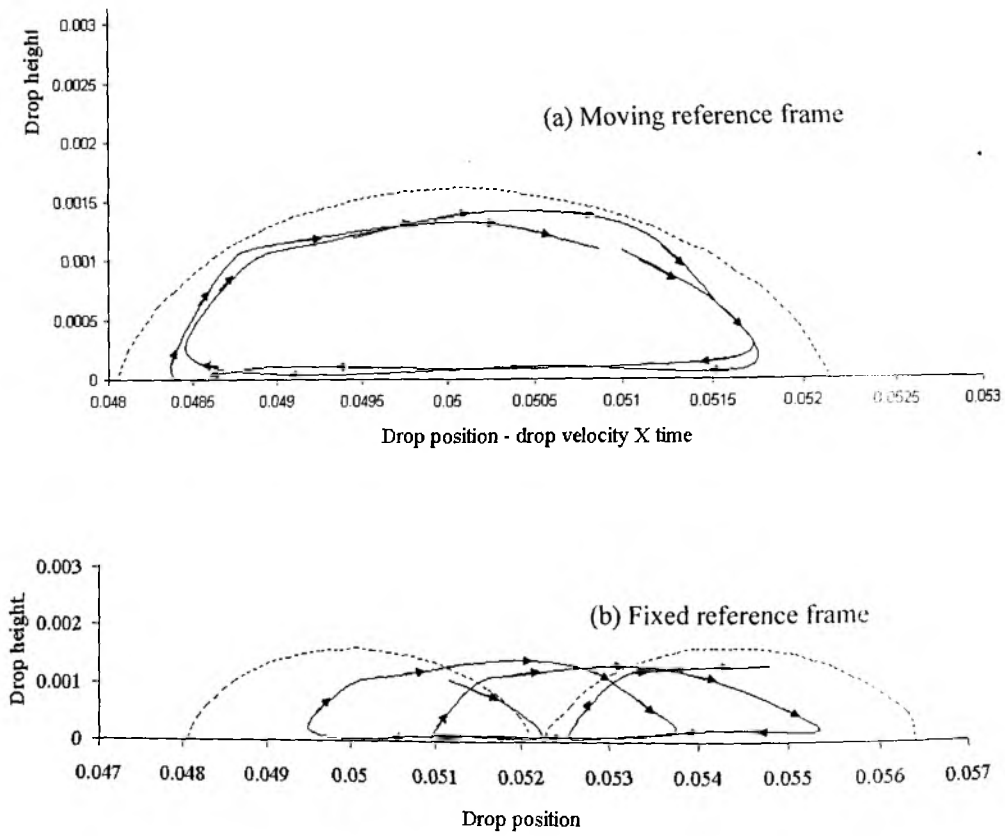

Fig. 4.26 Motion of a particle in moving and fixed reference frame during drop translation

In Fig. 4.26 locus of a particle is plotted as a function of time both in moving and fixed reference frames. A reference frame moving at a velocity of the drop is considered in Fig.

4.26a. Drop velocity is calculated as the average of the velocities of the advancing and receding front. Consideration of moving reference frame eliminates the effect of the drop translation and gives a clear indication of local circulatory motion under the combined action of surface tension force and gravity force. It may be noted that during the translation of the drop, the marker particle follows almost identical circulatory path. This shows a clear circulatory pattern inside the drop. In Fig. 4.26.b. reference frame is kept stationary to visualize the particle movement in an absolute sense. In this figure initial and final position of the drop is also depicted to compare the particle position along with the translation of the system. The figure makes it clear that with respect to a moving frame of reference the particle movement is a combination of circulation and translation.

In Fig. 4.27 velocity vectors have been plotted for water drop over a low (1°/mm) and a high (5°/mm) gradient surface. The effect of wettability gradient on the drop hydrodynamics can be understood well from the vector plots. For a low wettability gradient the internal circulation is clearly viscible with an upward movement of the fluid mass at the receding end and a downward movement at the advancing end. This typical pattern of fluid motion causes the receding end to retreat from the surface and creates an infinitesimally small new contact zone at the advancing end. A sequence of these events ultimately results in the translation of the drop. On the other hand, velocity vectors in a drop over a high wettability gradient surface show a different picture. Firstly, there is no strong circulatory pattern of the velocity vectors. At the advancing end a relatively high local velocity in the downward direction is observed whereas the local velocity is practically zero at the receding end. It essentially depicts the typical spreading pattern of the droplet. While it is pinned at the receding end it spreads by a change of drop height and contact angle.

It may be noted that though the movement of a droplet over a gradient surface has been observed in a number of investigations (Chaudhury and Whitesides, 1992; Suda and Yamada, 2003; Moumen et al., 2006) its spreading has been reported only by a few (Liao et al., 2007). Nevertheless, in none of the earlier works it has been pointed out that depending on the wettability gradient a drop may experience spreading or translation. To strengthen our observation we also calculated the drop energy. It is expected that a droplet will try to take a new configuration on a gradient surface either through spreading or translation so that its total energy is minimized. The drop energy is mainly constituted by the surface energy and the gravitational potential energy (Liao et al., 2009).

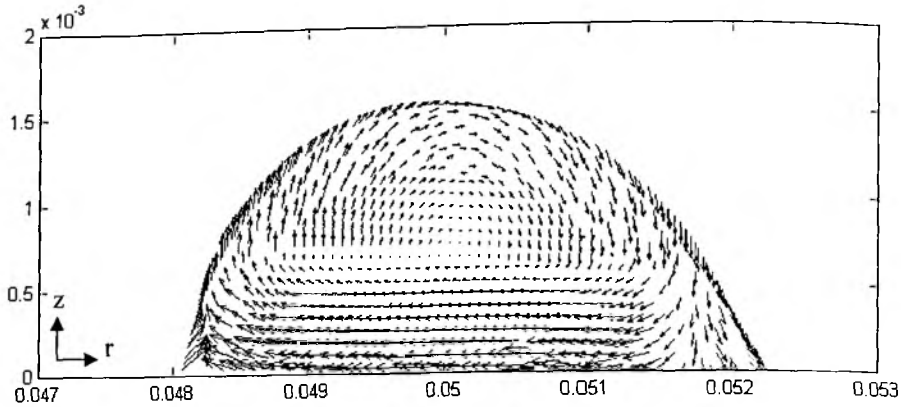

a) at low wettability

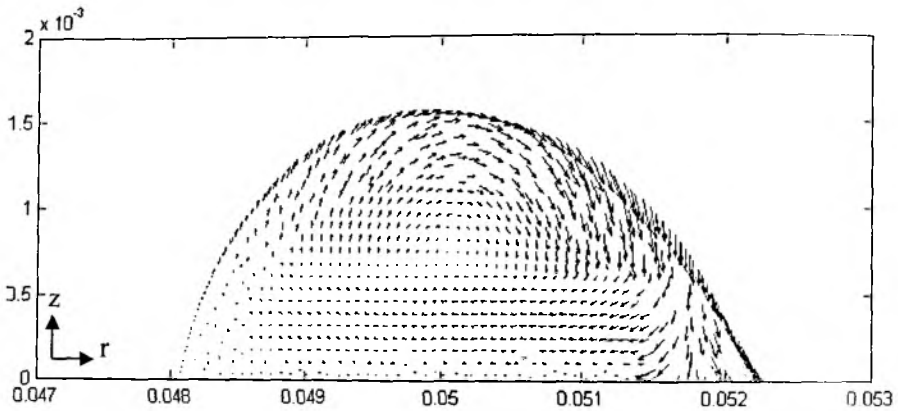

b) at high wettability

Fig. 4.27 Velocity field inside the drop at different levels of wettability

In Fig. 4.28 both these energies and their summation – the drop total energy is plotted for translation as well as spreading of water drop having 2μL volume. In both the cases total energy reduces with the movement of the drop centre of mass. However, a closer look into the diagram brings out some interesting features. In case of translation the drop height remains almost unchanged after a brief initial period. Change of potential energy clearly depicts that. The contact angle keeps on changing indicating a continuous change in surface energy as the drop moves over the gradient surface. As a result total drop energy also reduces. In a nutshell, on a low gradient surface the drop achieves energy minimization by movement. On a high gradient surface the drop spreads indicating a relatively larger change in its height. This is reflected in a continuous decrease in potential energy. The surface energy on the other hand

does not change appreciably. As surface energy is much higher compared to the potential energy the decrease of total energy is not very pronounced.

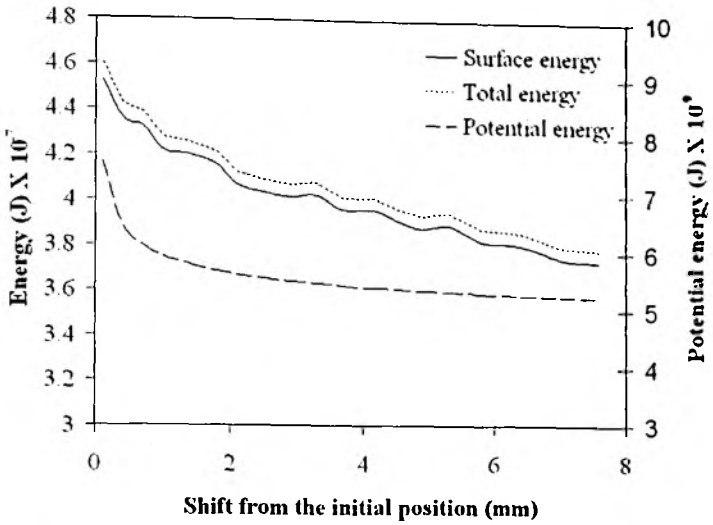

(a) at low wettability(1°/mm)

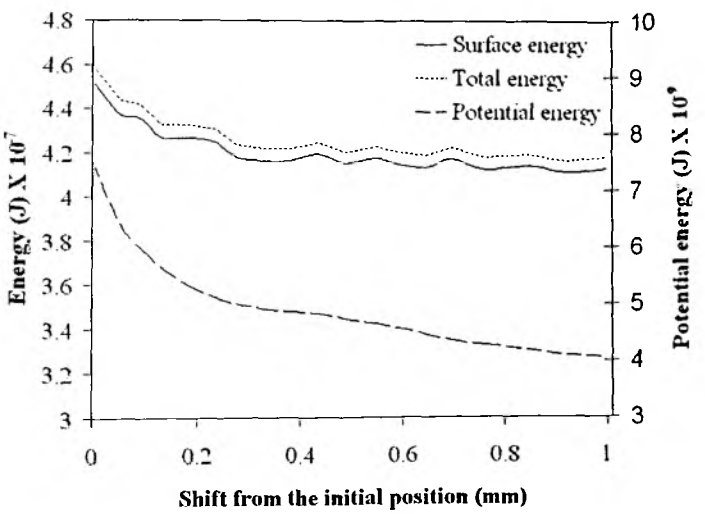

(b) at high wettability (5°/mm)

Fig. 4.28 Change of drop energy during its evolution on a gradient surface

Difference in the contact angles at the advancing and receding end is also tracked at different time instants. At low wettability gradient where the drop moves over the surface, advancing and receding contact angle is plotted along with the drop position in Fig. 4.29.

Simulation has been made for a 1.5 μL ethylene glycol drop over a surface having 5.3°/mm wettability gradient. Shift of the centre of the drop footprint is plotted in the abscissa of the figure. In this figure we can see that both advancing (from 75° to 15°) and receding (from 67° to 10°) contact angle is changing. In the same figure experimental results of Daniel and Choudhury (2002) is plotted to show the good predictability of the present model.

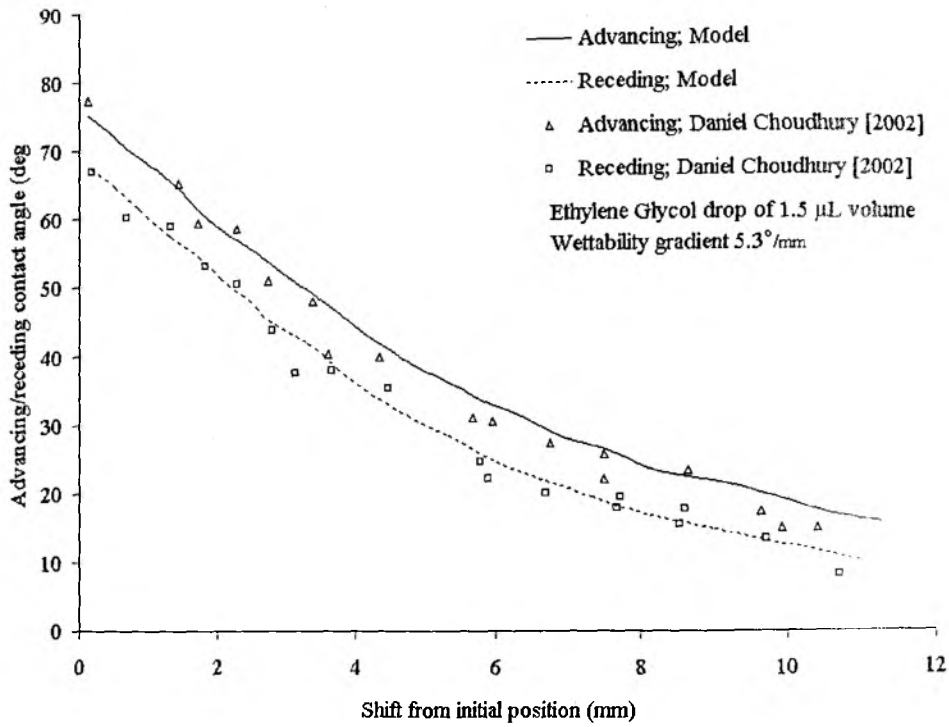

Fig. 4.29 Change of advancing and receding contact angle of a drop during its movement

It is obvious that the translational velocity of the drop depends on its volume. Simulations have been made by varying the drop size and the corresponding drop velocities have been determined. In Fig. 4.30 drop velocity is plotted as a function of drop foot radius. It is observed that the drop velocity increases with the increase in drop size. This is obvious as the magnitude of surface force increases with the drop size. Experimental results of Daniel and Choudhury (2002) is depicted in the same figure. A good match of the reported experimental observation with the numerical simulation shows the capability of the model in predicting the dynamics of asymmetric drops.

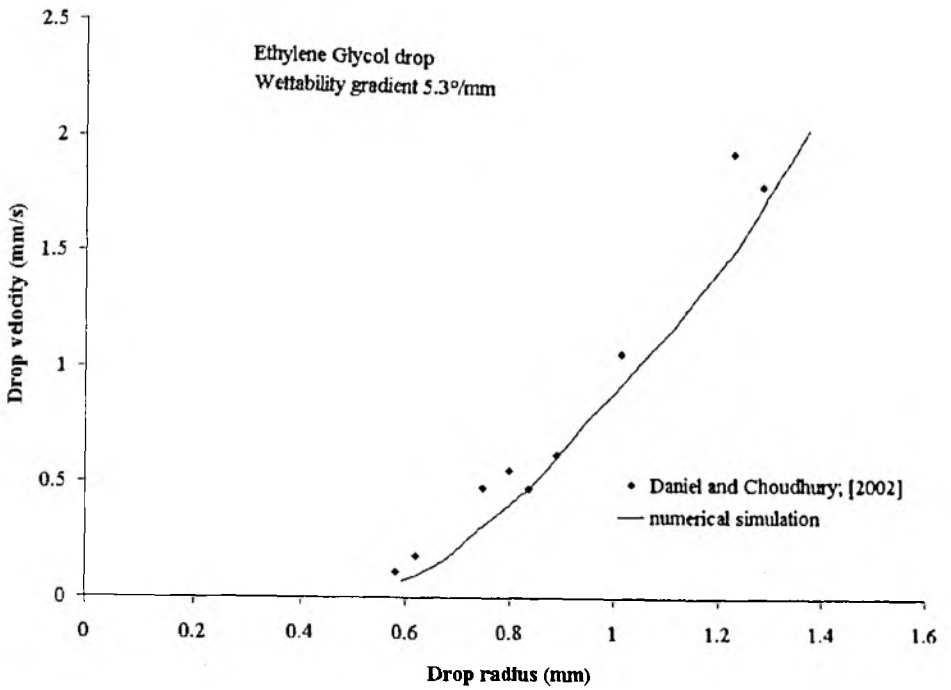

Fig. 4.30 Velocity of drop as a function of its size

The earlier results show that the contact angle gradient of a solid surface influences the dynamic behavior of a liquid droplet in a very unique way. To get a full appraisal of the fact the variation of the droplet velocity has been estimated as a function of the gradient of contact angle. The results for water and ethelyne glycol droplets of 1.5 μL are shown in Fig. 4.31. Velocities of three different points of the drop namely the receding edge, the advancing edge and the centre of mass have been monitored. To initiate the motion of a liquid droplet over a horizontal surface a finite value of the contact angle gradient is required. Obviously, this value depends on the fluid properties. Once the drop starts moving, the drop velocity increases continuously with the increase of the gradient. At this stage, along with the internal motion, the drop experiences a bulk movement. The identical velocities of the three points of the drops indicate this unambiguously. This trend continues up to a certain value of wettability gradient which again depends on the fluid. In the next phase the drop velocity decreases rapidly. Finally, the bulk movement of the drop ceases but it experiences a spreading on the surface. In the spreading stage the advancing end, the centre of mass and the receding end will have different velocities. The receding end has almost a zero velocity

indicating the drop is pinned to the surface at that point. A further increase in wettability gradient shows that the velocities of different points of the spreading drop are different. But the velocity of a particular point remains more or less constant. This shows that the drop is stretched towards the direction of wettability gradient.

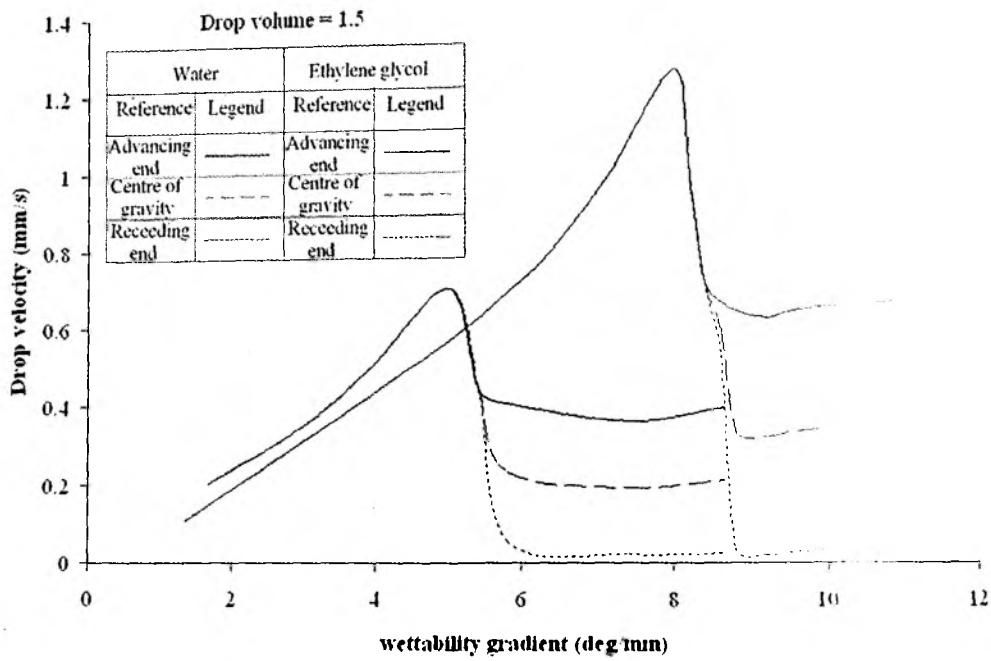

Fig. 4.31 Variation of drop velocity with wettability gradient

Above investigation clearly depicts that the behavior of a droplet over a gradient surface mainly depends on the value of the contact angle gradient, the liquid property and the drop volume. Variations of these parameters may result in no movement of the drop, its translation as well as its spreading. The drop dynamics with its entirety over a gradient surface can be represented on a two dimensional plane in the form of a regime map. Fig. 4.32a. and 4.32b show such regime maps for ethylene glycol and water respectively. A finite value of wettability gradient is needed to move a drop over the solid surface. It is expected that the inception of the drop movement occurs early as the volume reduces. This is supported by Fig. 4.32. The figure also shows the transition boundaries between drop translation and drop spreading.

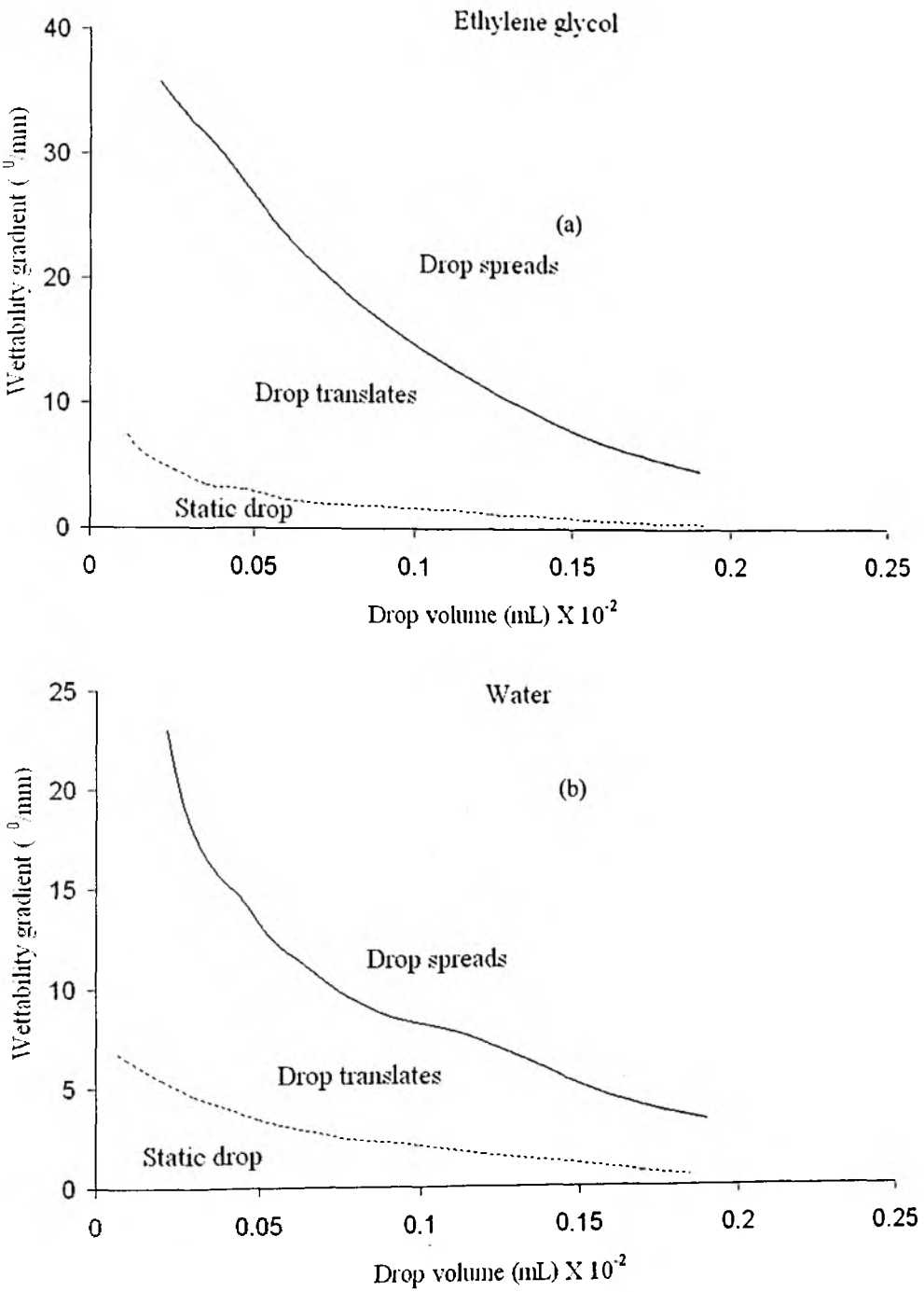

Fig. 4.32 Different regimes of drop dynamics for (a) ethylene glycol and (b) water

4.4.3 Uphill movement of a liquid drop over an inclined gradient surface

Drop over a solid surface can be transported by imposing gravitational force, thermal gradient (Ford and Nadim, 1994; Chen et al., 2005) or chemical wettability gradient (Greenspan, 1978; Hitoshi and Satoshi, 2003). Actuation of micro drops due to a chemical wettability gradient is few order faster compared to that motion produced by Marangoni flow and gravitational field. As a results, surface with gradient surface energy emerged as a potential candidate in MEMS applications nowadays (Daniel and Chowdhury, 2002; Moumen et al., 2006). Wettability gradient surface basically employs the imbalance of surface tension in its circumferential plane over a treated surface. The driving force behind this autonomous transport is a direct function of the wettability of the heterogeneous gradient surface. With the increase of wettability gradient of the surface it is possible to make the drop even climb upward against the gravity. It has been experimentally proven by Chowdhury and Whitesides (1992) when they translated water drop over a treated silicon wafer (7.2°/mm). They have polished the silicon wafer by decyltrychlorosilane to obtain a velocity in the order of few mm per second for drop of volume 1-2 μL. Not much attention has been given in this direction later either experimentally or numerically. Numerical or analytical techniques have been used successfully for translation of liquid drops over horizontal gradient surface by various researchers. But till date numerical techniques are not employed to investigate the internal fluid structures of a liquid drop during uphill movement over an inclined gradient surface. Using the developed hybrid DI-SPH methodology effort has been made to numerically simulate drop shape over an inclined gradient surface during up climbing. Particle spacing and time step is kept identical as has been mentioned in the earlier case. Study of internal flow pattern of the drop and drop mobility map have also been reported.

For this investigation the direction of increasing wettability gradient is kept in the opposite direction of gravity over the inclined surface. As a result surface force generated due to wettability gradient will oppose the force due to gravity over an inclined surface. But if the surface force is strong enough to overcome the resistance due to body force drop can move up. To circumvent this situation simulations have been made for a water drop of 2 μL volume over a surface having 15° inclination with horizontal plane. To counter the downward gravity force a wettability gradient of 1°/mm is considered along the surface. Position of the particles of water drop at different time step is presented in Fig. 4.33.

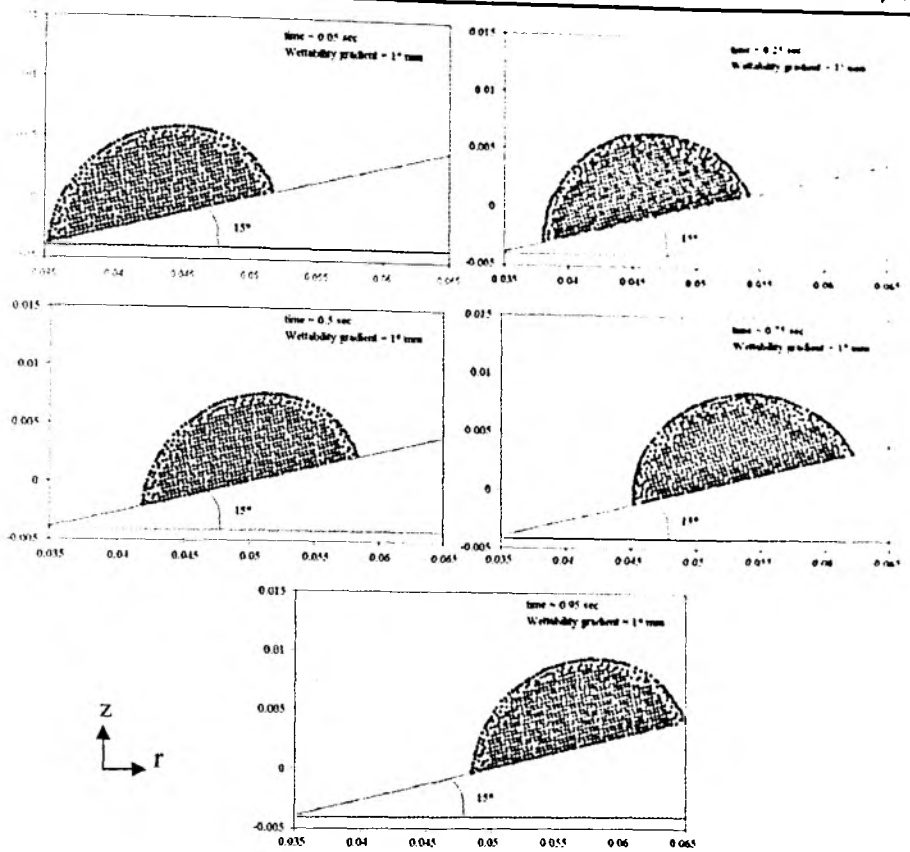

Fig. 4.33 Uphill movement of a liquid drop due to wettability gradient

It can be observed from the figure that the drop has been moved up due to the application of strong wettability gradient. Change of surface topology and contact angles are also visible from the drop shape at different time level. Incorporation of DI in the lagrangian SPH can be noticed from the loosely packed particles near the air water interface. A peristaltic motion in the drop shape can also be visible from the particle positions at different time step. Numerical simulation carried out using hybrid DI-SPH methodology has also been validated with pioneering experimental observation of Chowdhury and Whitesides (1992). Fig. 4.34 shows the drop shape and position at three different time level after positioning the drop over an inclined surface having wettability gradient along with the experimental drop shape as reported by Chowdhury and Whitesides (1992). To create the exact wettability situation we have simulated for 15° inclined surface with 7.2°/mm wettability gradient. Good match with the experimental observation and numerical simulation can be observed from Fig. 4.34.

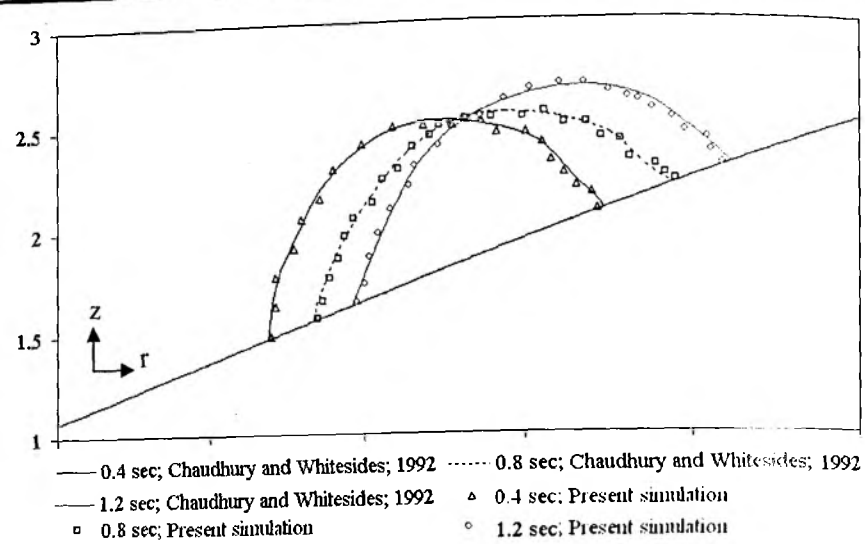

Fig. 4.34 Drop shape on an upwardly inclined gradient surface, comparison with the experiment of Chaudhury and Whitesides (1992)

Further, effort has been made to investigate the internal fluid structure during the motion of a liquid drop over the inclined gradient surface. We have simulated the drop for three different (7°/mm, 4°/mm and 1°/mm) wettability gradient strength of the solid surface which makes an angle 10° with the horizontal. Velocity vectors of the particles near the higher wettability corner try to wet the solid surface in front of it in order to maintain the local contact angle. Similarly particles near the lower wettability end try to move up to match with the lower contact angle. This generates a circulation current inside the drop due to wettability gradient which helps to gather the water particles from receding end to advancing end and hence move forward in the direction of gradient. At high (7°/mm) strength of gradient internal circulation is strong enough to overcome the gravitational opposing internal circulation generated due to inclination. On the other hand at low (1°/mm) wettability gradient, internal circulation due to gravity (Das and Das, 2009) dominates over the opposing circulation due to wettability gradient and forces the drop to move in the downward direction. At intermediate strength of wettability both the counter active circulations are dominant making the drop to stick with the solid surface. For a better visualization of that circulation pattern velocity vectors of the water particles are depicted in Fig. 4.35 for all three gradient strength separately.

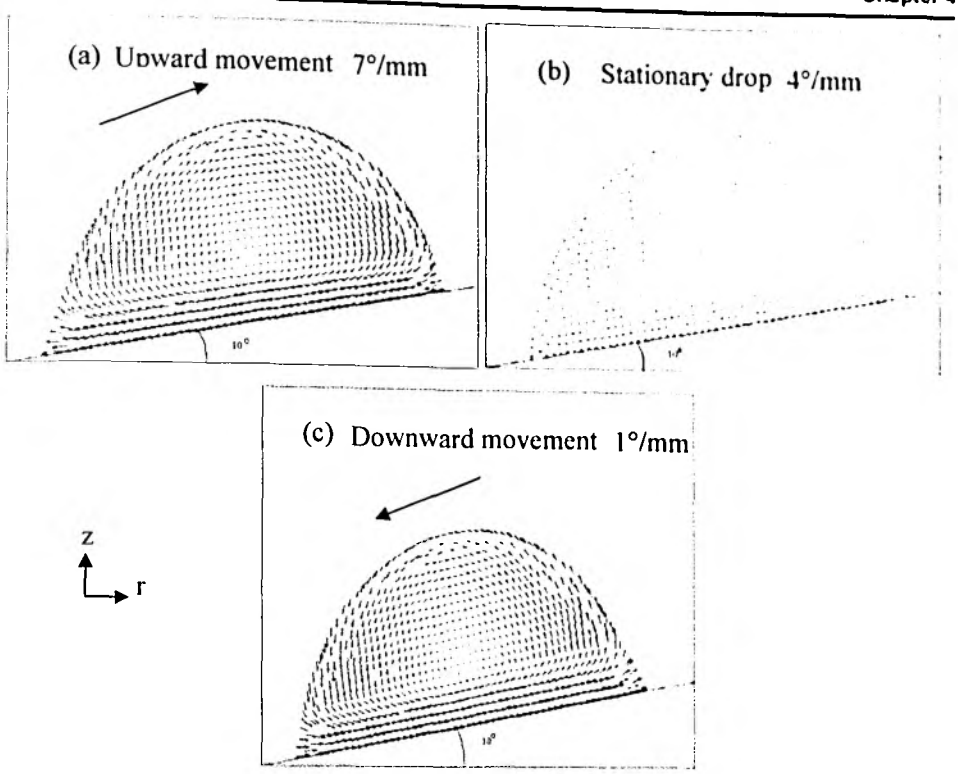

Fig. 4.35 Velocity field inside a drop on a upwardly inclined gradient surface

A clockwise circulation cell is clearly visible inside the drop from Fig. 4.35a as it is climbing up due to application of excessive wettability gradient (7°/mm) over the inclined surface while Fig. 4.35c shows counter clock wise circulation representing downward movement. Fig. 4.35b shows no resultant circulation as both forces due to wettability gradient and gravity are of similar order for stagnant drop.

Velocity in vertical direction has also been calculated for drop climbing over an inclined surface. In order to calculate the velocity, reference is taken at the equidistant point of drop from advancing and receding end over the surface. In Fig. 4.36 we have plotted the velocity of liquid drop as a function of wettability gradient. It has been observed that the velocity increases gradually as the gradient is increasing. This trend has been observed for all the drop sizes as reported in Fig. 4.36. Velocity of the different drop size (50 μL, 5 μL and 5 nL) over 15° inclined surface is considered in Fig. 4.36. It has been observed small drop (5 nL) requires more wettability gradient (11°/mm) compared to the larger drops (50 μL and 5 μL) over the surface to move in upward direction. Though the inertia of the small drop is not high

the wettability gradient requires to overcome it is very high due to its small foot print over the surface. At the same time drop velocity increases with drop size if the wettability gradient is fixed. This can be explained by strong circulation cell generated due to wettability gradient inside the large drop.

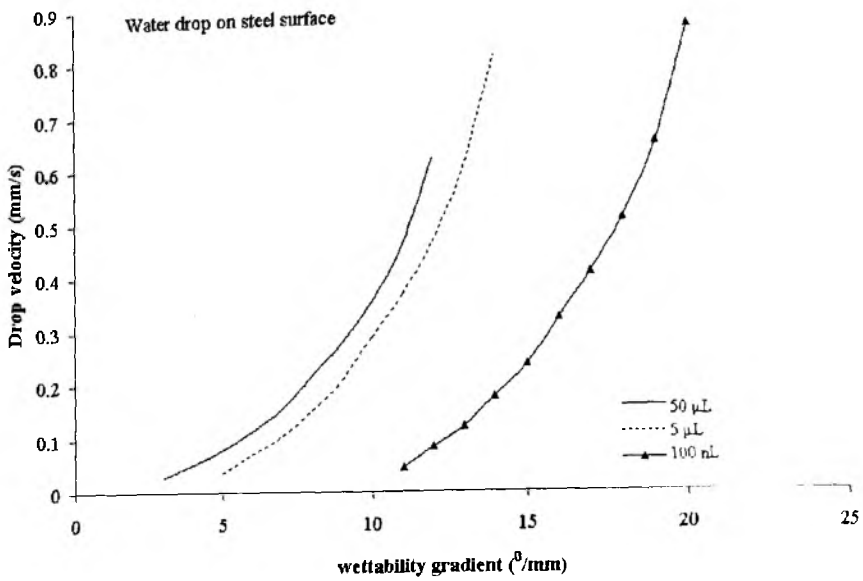

Fig. 4.36 Drop velocity in the upward direction at various wettability gradients

In Fig. 4.37 drop mobility curve has been reported for water drop of 50μL volume over gradient inclined surface. It has been observed that drop shows three different directional movements over inclined gradient surfaces. At a very small inclination drop initially remains static but it moves uphill as the wettability gradient increases. As the inclination increases drop climbs down the surface due to the action of gravitational force. With the increase of wettability gradient its downward movement seizes and a particular gradient strength drop again remains static over the surface. Further increase in gradient strength causes an upward movement. To describe different regimes in the mobility map we have plotted one vertical line in the plot which eventually signifies variation of wettability gradient for a surface having constant inclination. In the region where drop moves downward (region AB), an anticlockwise circulation cell is generated inside the drop. After providing some wettability gradient as we move up from point A to point B circulation strength decreases. At some

wettability gradient over point B drop become static though anticlockwise circulation still remains. In this region (region BO) anticlockwise circulation cell is not strong enough to overcome the drop inertia to move. At point O circulation cell changes its orientation and starts rotating in clockwise direction which helps in opposing the gravitational pull. But in region OC still gravity dominates and keeps the drop pinned over the surface. But beyond point C drop circulation strength in clockwise direction overcome the inertial resistance. As a result drop can be observed to move up. By varying the angle of inclination three regimes can be clearly identified for mobility of liquid drop. Most importantly one narrow region has been identified in the curve where drop will remain static over the surface. It separates two mobile regime of drop movement namely upward and downward. It has also been observed that the span of static zone is maximized at moderate angle of inclination but it narrows down at low and highly inclined gradient surface. Over slightly inclined gradient surface upward movement can be achieved at a low level wettability gradient which enhances the change of circulation direction and causes the static regime to be minimized. On the other hand at highly inclined surface downward movement is the prime motion and to generate upward motion a high amount of wettability gradient is necessary. It eventually narrows down the static zone at high angle of inclination. But at intermediate angle of inclination (8°-12° for 50 µL drop) both the regimes are dominant. So shift from one regime to other regime can not be abrupt that makes the static region widened.

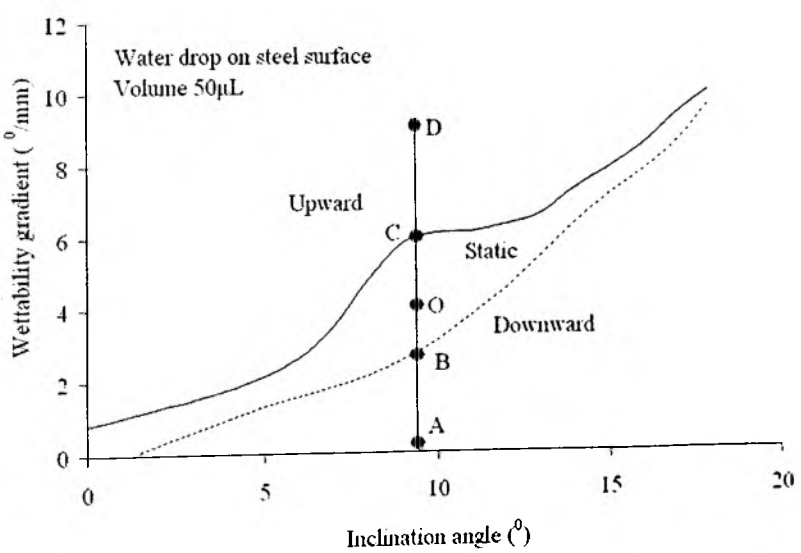

Fig. 4.37 Drop mobility map for water drop of 50 µL volume

Drop mobility curve has also been reported in Fig. 4.38 and 4.39 for drop of volume 5 μL and 100 nL. In those figures also three different regimes of upward movement, static drop and downward movement has been observed. But it is also to be mentioned that static zone has also been minimized as the drop size decreases which can be described from the minimization of inertial force due to decrease in volume. This seems realistic as the drop becomes more unstable in its mobility as the size minimizes. But the trend of static zone is same for all the drop sizes.

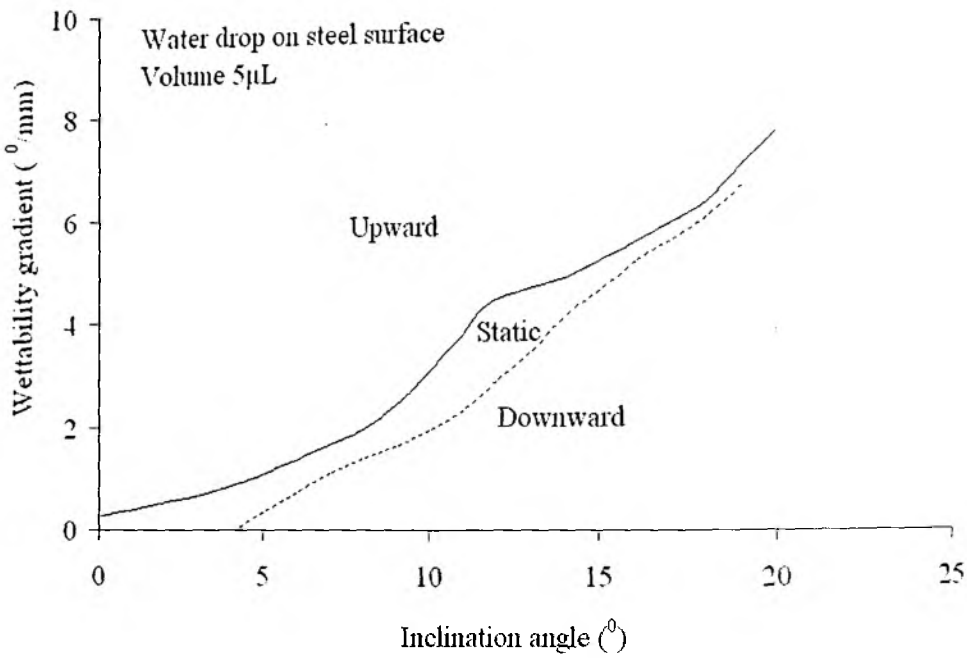

Fig. 4.38 Drop mobility map for water drop of 5 μL volume

A rigorous study has also been made to investigate the behavior of static drops over the inclined gradient surface. It has been observed from the mobility map that drop remains static over a large variation of wettability gradient strength at a moderate inclination of the solid surface. Numerical drop profile shows that though the drop remains static, the drop spreads as the gradient strength increases for a fixed inclination angle of the solid surface. We have shown one representative situation in Fig. 4.40 where a drop of 50 μL is placed over a 10° inclined gradient surface. It can be observed from the figure that drop foot radius is more for

5 mm strength compared to 3 mm. On the other hand drop height decreases as the gradient strength increases. As the drop becomes flattened for higher gradient strength, its centre of gravity also lowered compared to the lower strength of gradient. This makes the effect of surface energy more dominating over the effect of downward gravitational pull

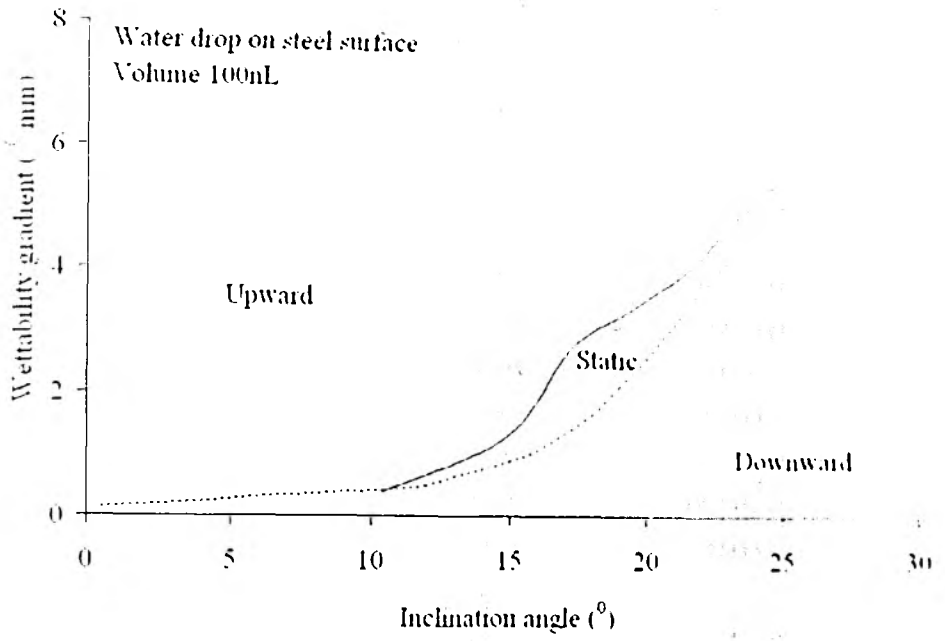

Fig. 4.39 Drop mobility map for water drop of 100 nL volume

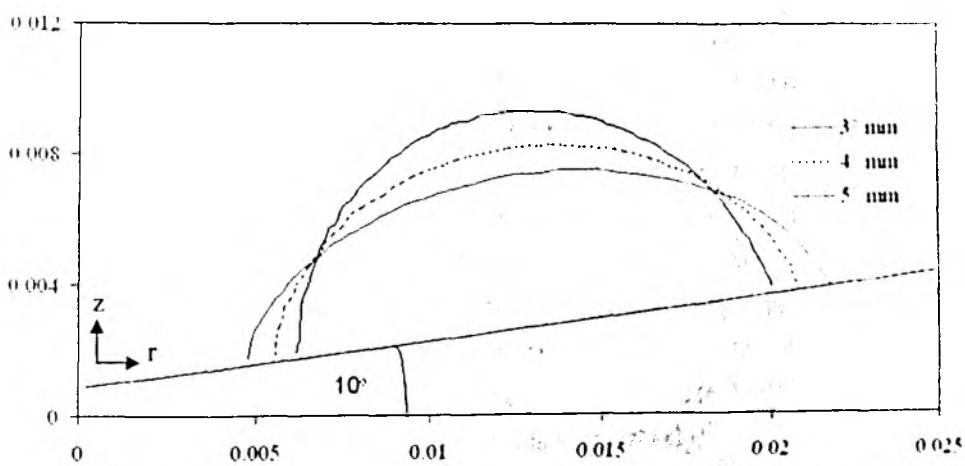

Fig. 4.40 Spreading of static drop with the increase of wettability gradient

4.4.4 Droplet fragmentation using patterned wettability gradient

With the fast development of miniaturized systems in mechanical, electronic, chemical and biomedical devices, dynamics of the mili and micron sized drops are becoming more prevalent in both commercial applications and scientific enquiries. Dynamics of a mini drop tends to be different from the fluid behavior we are familiar with in our daily life as the surface tension force dominates over the inertial ($We = \frac{\rho v^2 L}{\sigma} << 1$) and viscous forces ($oh = \frac{\mu}{\sqrt{\rho \sigma L}} << 1$; L is the characteristic length and v is the characteristic velocity) in these cases. Moreover the surface to volume ratio in case of small drops is high enough to make the characteristics length and time indeed small. Apart from the study of its dynamics, the generation of smaller drops from normal sized drop is utmost difficult due to the domination of surface forces. Various means are tried to fragment a drop into a number of daughter droplets by researchers for the last three decades. Application of shear flow over a drop is the common technique used for fragmentation. Starting from the pioneering work of G. I. Taylor (1932) several researchers (Bentley and Leal, 1986; Renardy and Cristini, 2001; Guido et al., 2003) experimentally or theoretically investigated the break up procedure using shear flow. But very small droplets cannot be generated using shear flow as magnitude of shear force which is the primary cause for drop breakup becomes smaller continuously with the drop characteristics length. Other methodologies for drop break up are also growing parallely to meet the trend of miniaturization. Walker (1980) analyzed break-up of a liquid-metal drop moving at high velocity across a non-uniform magnetic field. But as the application of magnetic field can only be done over metallic drops this method of drop fragmentation is unable to attract the interest of future researchers. As an alternative to the magnetic field, Pollack et al. (2002) applied differential electric fields for drop splitting. Later on, Cho et al. (2003), Yeo et al. (2007) and several researchers have experimentally and theoretically studied drop breakup using electrowetting phenomena. All these techniques required some active force from outside during breakup which forces the drop to shear against the adhesive surface tension forces. In the present investigation we propose the use of specially designed gradient surface (Greenspan, 1978; Brochard, 1989; Chaudhury and Whitesides; 1992; Suda and Yamada; 2003) for the break up of droplets.

Spatial wettability gradient may be provided along Y shaped path as shown in Fig. 4.41. Drop is initially placed at the root arm of the 'Y' path from where it starts to move towards the junction by minimizing the surface energy due to wettability gradient. In the arms of the 'Y' path favorable wettability gradient is given which pulls the drop into two segments. Patterned path is characterized in terms of the angles of the arm (α_1 and α_2) with the symmetry line and the wettability gradient in the arms (x_1°/mm and x_2°/mm). Four different patterns have been made for drop break up from the junction. In the first arrangement (Fig. 4.41a) arms of the 'Y' path is making equal angles ($\alpha_1 = \alpha_2$) with the symmetry line and having equal wettability gradient ($x_1 = x_2$). In the second pattern (Fig. 4.41b) angles made by the arms with the symmetry line are not equal ($\alpha_1 \neq \alpha_2$) but same wettability gradient ($x_1 = x_2$) is provided. Next, 'Y' path is kept geometrically symmetrical along the root arm ($\alpha_1 = \alpha_2$) with different wettability gradient ($x_1 \neq x_2$) in its arms as shown in Fig. 4.41c. In Fig. 4.41d three armed 'Y' pattern is shown where one arm is aligned along with the symmetry line and the other two arms are symmetrically ($\alpha_1 = \alpha_2$) made bilateral to the first arm. Wettability gradients at all the three arms are kept same in the patterned surface ($x_1 = x_2 = x_3$).

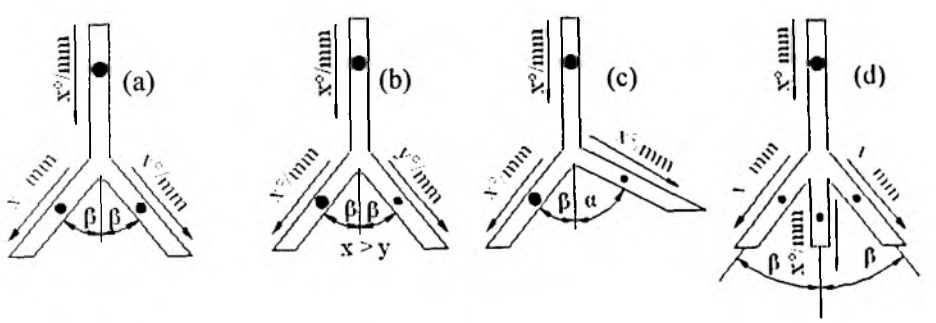

Fig. 4.41 Arrangements of directional wettability gradient for drop splitting

A particle redistribution scheme near the contact line is used to maintain the local contact angle (θ) which can be determined as:

$$\theta_i' = \cos^{-1}\left(\cos\left(\theta_{in} + \frac{d\theta}{dx}(x_i - x_{in})\right) - \frac{\sigma}{R\sigma_{lv}}\right). \tag{4.10}$$

here, θ_{in} is the contact angle at initial location x_{in} and $\frac{d\theta}{dx}$ is the wettability gradient along the pattern length.

In the arms of the 'Y' path $\frac{d\theta}{dx}$ will be replaced by $\cos\alpha\frac{d\theta}{dx}$ assuming α be the angle of the arm with the symmetry line.

DI-SPH methodology is used to study the motion of a drop over patterned surfaces as described in Fig. 4.41. Clusters of liquid particles over the patterned surface can be explicitly tracked which eventually shows the shape of the liquid drop at each time instant. Due to the inherent property of the adopted methodology no special treatment is required for gas-liquid interface reconstruction. Along with different shaped pattern of gradient surfaces, the strength of the wettability gradient is also varied as the drop forwards along the path by virtue of surface force minimization. In the root arm, drop moves forward towards the junction as a result of a continuous change of contact angles at leading and trailing edges. At the junction one half of the drop experiences a hysterisis force along one arm of the 'Y' path and the rest half on the other way. These forces which are not collinear, makes the drop to feel a yield force near the junction. Influenced by the hysterisis forces aligned with the arms of the 'Y' path, the advancing front of the drop bifurcates into two lobes and starts moving along the two branches. Continuous diversion of liquid from the base arm into the side arms of the 'Y' path eventually makes the drop to split into two paths. Hysterisis force generated by the wettability gradient in the side arms, acts upon a fraction of the drop volume which depends over the inclination of the side arms with the symmetry line and the strength of the hysteresis force.

To judge the break up of drop at the junction of a 'Y' shaped pattern of wettability gradient developed methodology has initially been applied for uniform wettability gradient (x°/mm at all the arms) along the length of the arms. Initially the patterned path is kept symmetrical along the root arm. It has been observed that in the above mentioned situation drop approaches towards the junction of the 'Y' arm in the root arm and finally breaks into two equal sized daughters in the side arms. In Fig. 4.42 one representative simulation has been shown where 60° angle is provided between the branch arms with root arm ($\alpha_1 = \alpha_2 = 60°$). For the simulation result shown in figure 2 5°/mm wettability gradient is provided along each arm of the Y channel. Other parts of the solid surface are simulated as non wettable surface. Particle positions of the liquid drop at different time steps ($\Delta t = 0.05s$) of the simulation are shown in Fig. 4.42. In Fig. 4.42a drop is placed in the root arm and it advances towards the junction. Fig. 4.42b shows with initiation of the break up and the advancement of

the lobes towards the arms. In the subsequent figures (Fig. 4.42c-4.42e) evolution of daughter drops from the mother drop is shown at various time levels. It is evident from Fig. 4.42f that by providing symmetric directional wettability gradient, water drop can be split into two equal segments. After the complete break up the two fragments of the parent drop undergo a change in shape so that the resulting surface minimizes the total energy for the given volume. Drop velocity in the side arms increases compared to the drop velocity in the root arm due to the decrease of base area of the daughters compared to their parent.

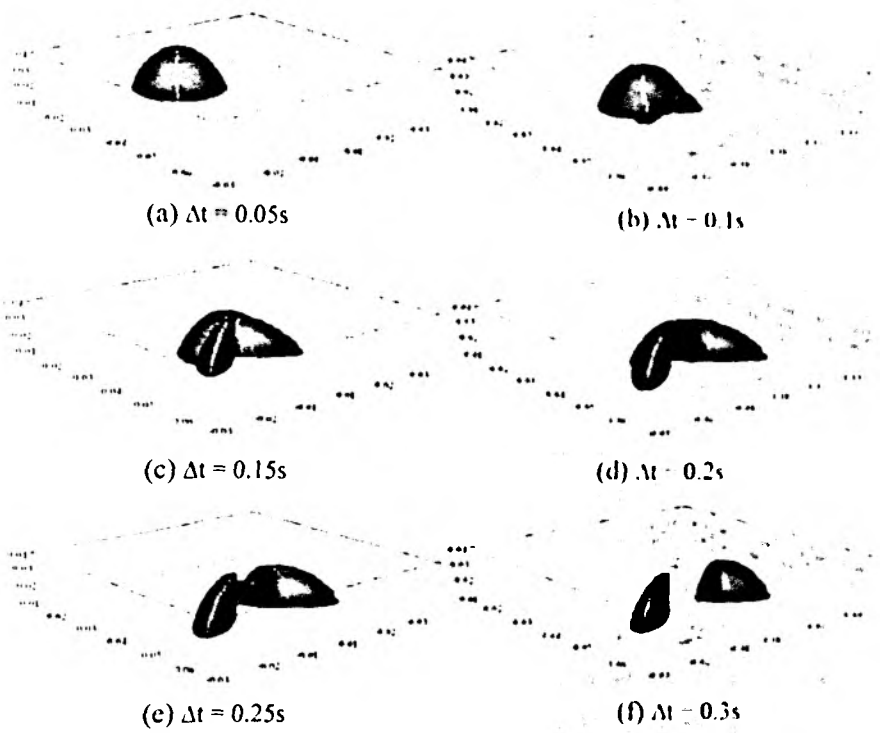

(a) $\Delta t = 0.05s$ (b) $\Delta t = 0.1s$

(c) $\Delta t = 0.15s$ (d) $\Delta t = 0.2s$

(e) $\Delta t = 0.25s$ (f) $\Delta t = 0.3s$

Fig. 4.42 Symmetric binary breakage of droplet (scheme a, Figure 4.41)

Breakage time of the drop into its daughters which can be defined as the time starting from the initial crater at the drop profile to the final pinching off the daughters depends upon the drop volume, wettability gradient and inclination of the side arms with the root arm. It is clear from the intuition that breakage time increases as the drop increases in volume. Here we have made an account of the breakage time for different wettability gradient at the root arms and inclination of the 'Y' arms with the symmetry line keeping the drop volume same (200 nL). Fig. 4.43 shows that drop breakage time increases as the angle between the side arm of

the 'Y' path and root arm increases for a particular wettability gradient in the arms. Breakage time is considered to the time difference between the appearance of the first crater in the drop and breakage of liquid film between the daughters. It has been observed that complete drop break up is not possible if the angle between the side arms and the root arm becomes very high. For wettability gradient of 8°/mm it has been observed that drop break up is not possible if the angle between the root arm and the side arm exceeds 87°. Upper limit of angle between the arms for successful drop break up decreases with the decrease of the wettability gradient.

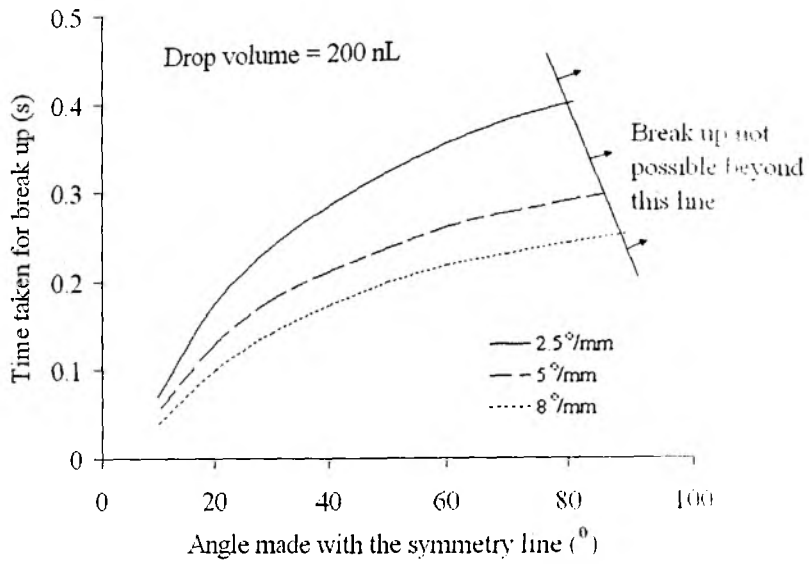

Fig. 4.43 Drop break up time for different angle of the branches and wettability gradient

Wettability gradients of the arms are varied to see the effect of intensity of hysteris force over the volume of the daughter drops in a symmetric patterned 'Y' path ($\alpha_1 = \alpha_2$) (Fig. 4.41b). Simulations have been made for a drop placed over the root arm of a patterned 'Y' path which has different wettability gradient ($x_1 \neq x_2$) at its two symmetric side arms ($\alpha_1 = \alpha_2$). It has been observed that though the drop starts to break up upon reaching the junction, the lobes generated are not symmetrical. The arm having more wettability gradient compared to the other contain the bigger lobe of the breaking drop (Fig. 4.44d). This process continues and after the complete detachment of one lobe from the other it has been observed that daughters are different in volume (Fig. 4.44f). The daughter drop moving over the side arm having high wettability gradient compared to the other is large in volume than the drop placed in the other

arm. In Fig. 4.44 similar situations have been shown using a symmetric Y channel having 60 angle of its side arms with root arm. Along one of its root arm 5°/mm wettability gradient is given and along the other 2.5°/mm gradient is adopted (Fig. 4.41b).

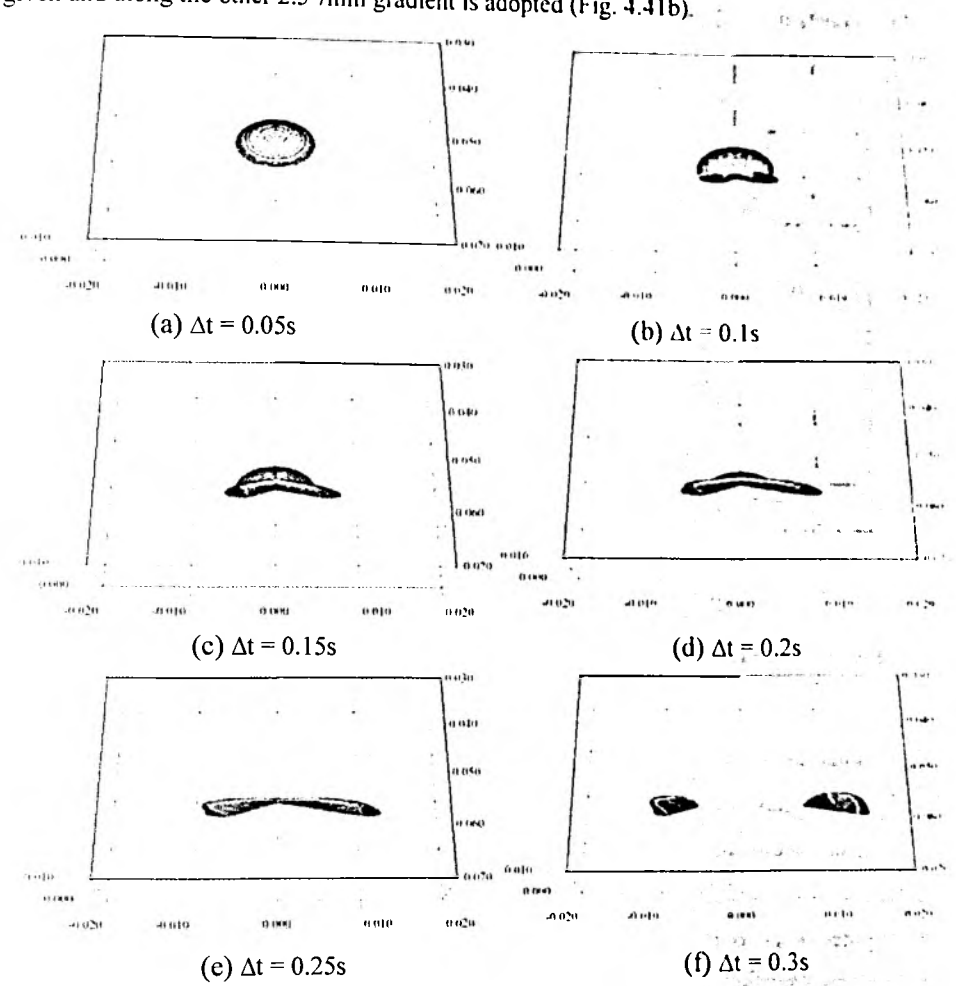

(a) $\Delta t = 0.05s$ (b) $\Delta t = 0.1s$

(c) $\Delta t = 0.15s$ (d) $\Delta t = 0.2s$

(e) $\Delta t = 0.25s$ (f) $\Delta t = 0.3s$

Fig. 4.44 Asymmetric binary breakage of droplet (scheme b, Figure 4.41)

In the figure liquid particle positions after certain time interval ($\Delta t = 0.05s$) is shown in several section which clearly depicts asymmetric splitting of droplet. Smaller drop is generated in the arm having lesser wettability gradient (right arm) compared to the other (left arm). Mobility of fluid particle is faster in the right arm compared to the left arm that causes two different sized drops. Studies have also been made to see the effect of different ratio of wettability gradient applied in the arms over the ratio of volume of the daughter drops. To

make the comparison a drop having volume 200 nL is placed over a patterned 'Y' path which makes an angle 60° between the root arm and the side arms. Wettability gradient of the left arm is kept constant and the wettability gradient of the right arm is varied.

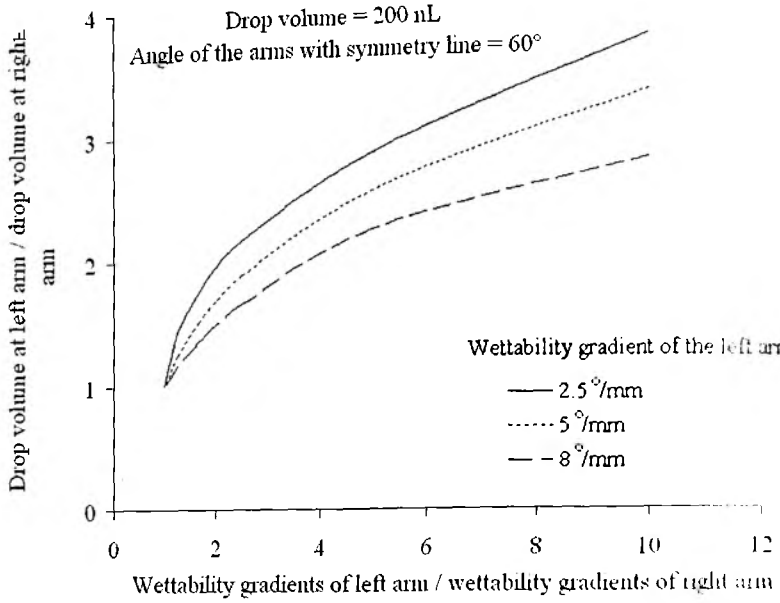

Fig. 4.45 Ratio of daughter drops for different wettability ratios of the arms

The simulation of drop break up has been made for three different wettability gradients at the left arm (2.5°/mm, 5°/mm and 8°/mm). It has been observed and shown in Fig. 4.45 that the daughter drops are similar in size when the wettability gradient is same at both the arms. But as the ratio of wettability gradient of left arm to right arm increases ratio of the volumes of the daughter drops at left to right arm increases. This trend is observed for all the three reported values of wettability gradient of the left arm. For a fixed wettability gradient ratio at left to right arm, ratio of drop volume generated at left and right arm increases as the reference wettability gradient provided in the left arm decreases. Though the ratio of wettability gradient is same between the arms, hysterisis force becomes much prominent for lower wettability gradient at the left reference arm.

Similarly, simulations are also made for drop break up when it is placed over a patterned asymmetric 'Y' shaped path ($\alpha_1 \neq \alpha_2$) having the same wettability gradients at the arms ($x_1 = x_2$) (Fig. 4.41c). For all the simulations of the above mentioned condition daughter drops

generated due to break up are not of equal size. It has been observed that the arm making a small angle with the root arm receives the major share of the mother drop (200 nl.). Numerical simulations of such situations are shown representatively in Fig. 4.46.

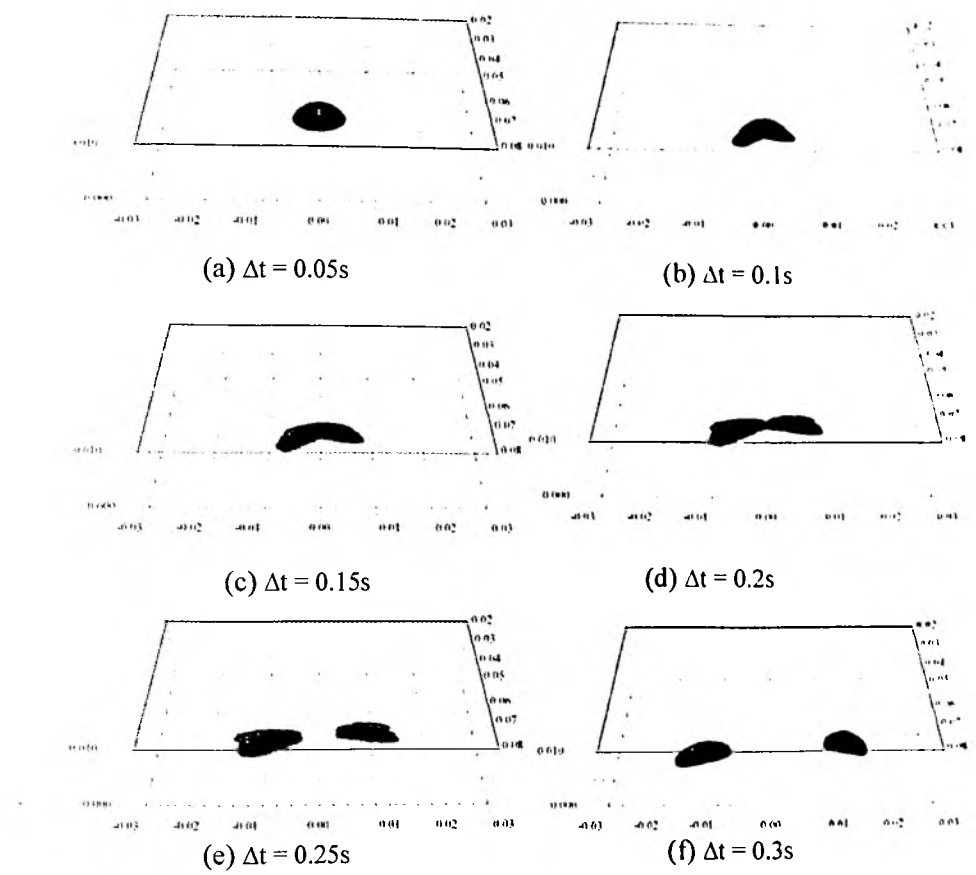

(a) $\Delta t = 0.05s$ (b) $\Delta t = 0.1s$

(c) $\Delta t = 0.15s$ (d) $\Delta t = 0.2s$

(e) $\Delta t = 0.25s$ (f) $\Delta t = 0.3s$

Fig. 4.46 Asymmetric binary breakage of droplet (scheme c, Figure 4.41)

In the figure temporal results of simulation of drop break up over patterned asymmetric 'Y' shaped channel is shown. Right arm of the 'Y' path makes 60° angle with the root arm whereas 30° angle is made by the left arm with the symmetry. Along the arms 5°/mm wettability gradient is provided to generate dissimilar drops. Fig. 4.46 shows the fluid particle positions at different instants ($\Delta t = 0.05s$) during the fragmentation of the drop. It is evident from the figures that branch arms having different inclination with the base arm can also produce two droplets having different size (Fig. 4.46e-4.46f).

Efforts have also been made to assess the ratio of the volumes of the daughter drops for different range of asymmetry in the construction of the 'Y' shaped patterns. This has been reported in Fig. 4.47. For this ranges of simulations drop size is kept constant (200nL) and wettability gradient is not varied (5°/mm) through out. To present the simulations angle between the left arm and the root arm (α_1) is kept constant. Angle of the right arm with the root arm (α_2) is varied to attain different ratio between α_1 and α_2. Results obtained from the simulations for the above mentioned situations are judged in terms of the volume ratio of the daughter drops. Volume of the daughter drops are equal in case of the left arm and right arm makes an equal angle with the root arm as depicted from Fig. 4.47.

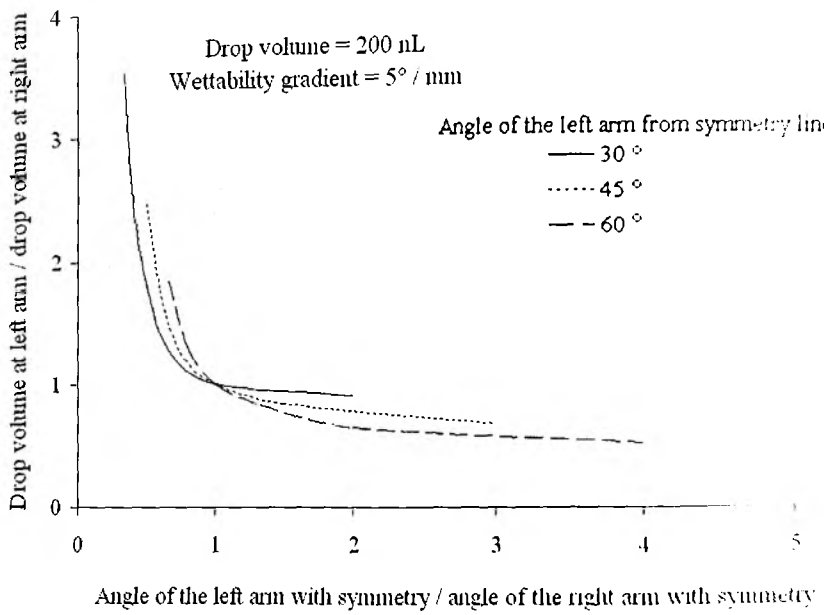

Fig. 4.47 Ratio of daughter drops for the asymmetry ratios of the arms

It has also been observed that as α_1/α_2 increases from 1.0 the ratio of the volumes of daughter drops in the left to right arm decreases. On the other hand, the volumes of daughter drops in the left to right arm increases as α_1/α_2 decreases from 1.0. A close look at the numerical values of the curves of Fig. 4.47 reveals that this phenomenon of asymmetric drop break up shows directional similarity. As a result the curve becomes steep when $\alpha_1/\alpha_2 < 1$ in comparison with $\alpha_1/\alpha_2 > 1$. This situation is valid for all the three reported values of the reference angle between the left arm and the symmetry line (α_1).

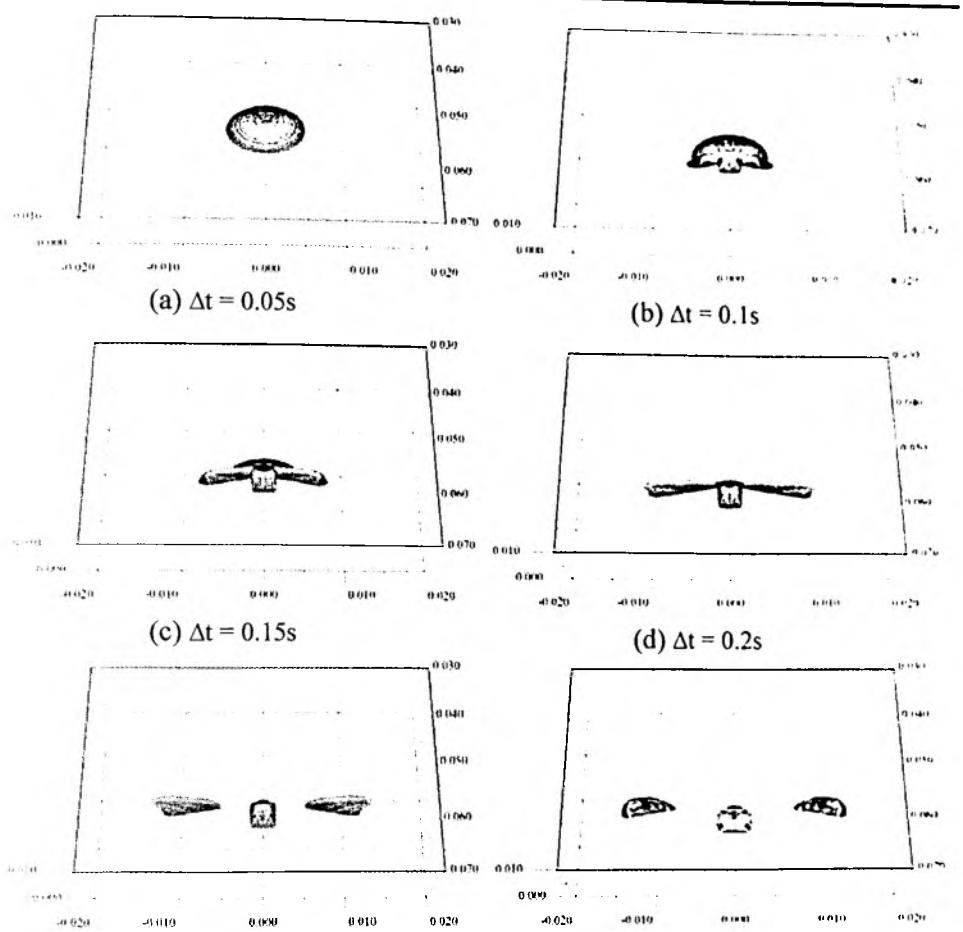

Fig. 4.48 Breakage of drop into three droplets (scheme d, Figure 4.41)

Finally, simulations have been forward marched to employ the concept of drop break up due to wettability gradient for generation of multiple drops from the mother drop. Three side armed pattern of 'Y' path as shown in Fig. 4.41d is simulated numerically. Middle arm which is aligned with the root arm makes an angle of 60° with the other side arms. Arrangements were made to provide wettability gradient of 5°/mm along all the arms. Simulated drop profiles after a particular instant (Δt = 0.05s) are shown in various sub figures of Fig. 4.48. At the junction the middle portion of the drop continues to move along the middle side arm while two side craters are made in the drop (Fig. 4.48b). It forces the drop to break into three parts which proceeds to march forward along the side arms (Fig. 4.48c-4.48d). Finally, three

different daughter drops are generated in the arms (Fig. 4.48e) and all three drops stabilizes (Fig. 4.48e) after certain period due to surface tension. From Fig. 4.48 it is clear that multi drop of similar size can be generated from a single drop using directional wettability gradient. This concept can be extrapolated for multiple different sized drops by providing unequal wettability gradient at different arms.

This concept can be extrapolated to develop multiple 'Y' shaped branched tree using wettability gradient using which various sized daughter drops can be obtained. Such an example is shown in Fig. 4.49. In this tree a drop is broken into three equal parts (1→11, 12 and 13). One of the daughter drops is then split into two equal sized drops (11→111 and 112). Later on asymmetric splitting using asymmetric 'Y' path but symmetric wettability gradient (12→121 and 122), symmetric 'Y' path but asymmetric wettability gradient (121→1211 and 1212) and both (1211→12111 and 12112). One three side arm 'Y' path is also used in the tree having different wettability gradient (122→1221, 1222 and 1223).

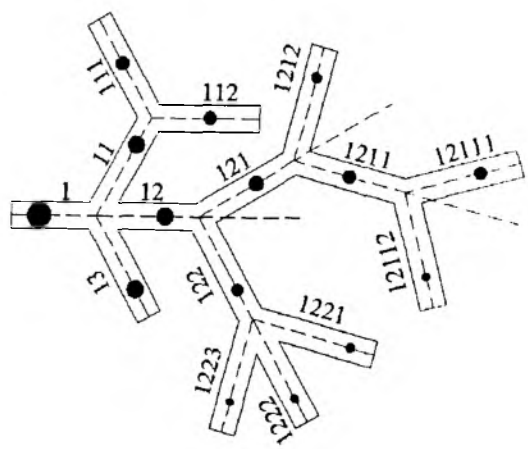

Fig. 4.49 Proposed scheme for the variation of wettability gradient for achieving drop fragmentation

Wettability of all the arms and the angle made by the side arms with the root arm is given in Table 4.2. Drop placed over 1 root arm will proceed towards the complex tree and produce different percentage of the initial drop as output from the end arms (111, 112, 1212, 12111, 12112, 1221, 1222, 1223 and 13) of the tree. The ratio daughter drop volume generated of the two arm pattern of 'Y' path having wettability gradient is taken from the Fig. 4.45 and 4.46. For symmetric splitting of three side arm 'Y' path with wettability gradient drop volume in

the side arm is considered as 1/3rd of the initial drop volume. For asymmetric splitting of the drop using asymmetric wettability gradient in three armed 'Y' path daughter drop volume is considered to be the same as their ratio of wettability gradient provided in the arms. Drop volume in each arm is calculated using above mentioned analogy is reported in the last column of Table 4.2 as the percentage of the initial drop placed on arm 1. It can be observed that using the patterned multiple 'Y' shaped tree drop can be divided into different ratio starting from 1.35% of the initial drop to 33.33% of the initial drop placed in arm 1. Finally, it can be said that present numerical tool (coupled DI-SPH) can capture intricate drop bifurcation into smaller daughter drops. However, we strongly feel that experimental verification is needed to confirm the numerical results proposed above.

Table 4.2 Daughter drop size as a percentage of the initial drop volume in the proposed patterned surface

Root arm	Side arm	Wettability gradient (°/mm)	Angle with root arm (°)	% of drop volume achieved (approximate)
1	11	x	60°	33.33
	12	x	0°	33.33
	13	x	60°	33.33
11	111	x	60°	16.67
	112	x	60°	16.67
12	121	x	30°	22.22
	122	x	60°	11.11
121	1211	x	45°	14.81
	1212	x/2	45°	7.41
1211	12111	x	30°	13.16
	12112	x/2	60°	1.65
122	1221	4x/3	45°	2.47
	1222	x	0°	3.70
	1223	2x/3	45°	4.93

4.4.5 Merging of two liquid drops using patterned wettability gradient

Merging of two droplets is essential for mixing in any microfluidic devices. Micro reaction between two drops of two different chemical components is a crucial process in microfluidics. It needs a precise control over the drop size and movement. In many microfluidic and bio fluidic devices the amounts of substrates to be handled are in microscale order. In this range of application the use of body forces like buoyancy etc will not be too effective as the volume to area ratio is not high. Rather several passive techniques like piezoelectric, electrostatic, thermopneumatic, electromagnetic and electroosmotic are extensively used by researchers in MEMS based chemical reactors. Though such methods are highly reliable, a considerable amount of sophistication and mechanical complicacy is always involved. In this segment an effort has been made to utilize the principle of drop actuation using wettability gradient for the controlled merging of two drops. Following pattern of wettability gradient as shown in Fig. 4.50 have been used for drop joining.

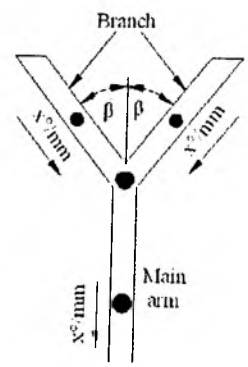

Fig. 4.50 Schematic diagram of the Y channel for drop merging

Here a pattern of wettability gradient is considered in the shape of a Y channel having equal angles of the side arms with the symmetry line. In the side arms of the Y path a positive wettability gradient (x°/mm) is provided towards the junction. The same wettability gradient is continued in the main arm also. Drops of different liquids are initially placed at the side arms of the 'Y' path from where these start to move towards the junction by minimizing the surface energy. At the junction both the drops collide with each other with same or different inertia depending on the wettability gradient provided in the side arms. After making contact with each other the drops starts to move in the root arm being associated with each other. This

scheme may be used to promote the chemical reaction between the drops of two different liquids. Total contact time depends on the combinations of the wettability gradient Considered in The Y path.

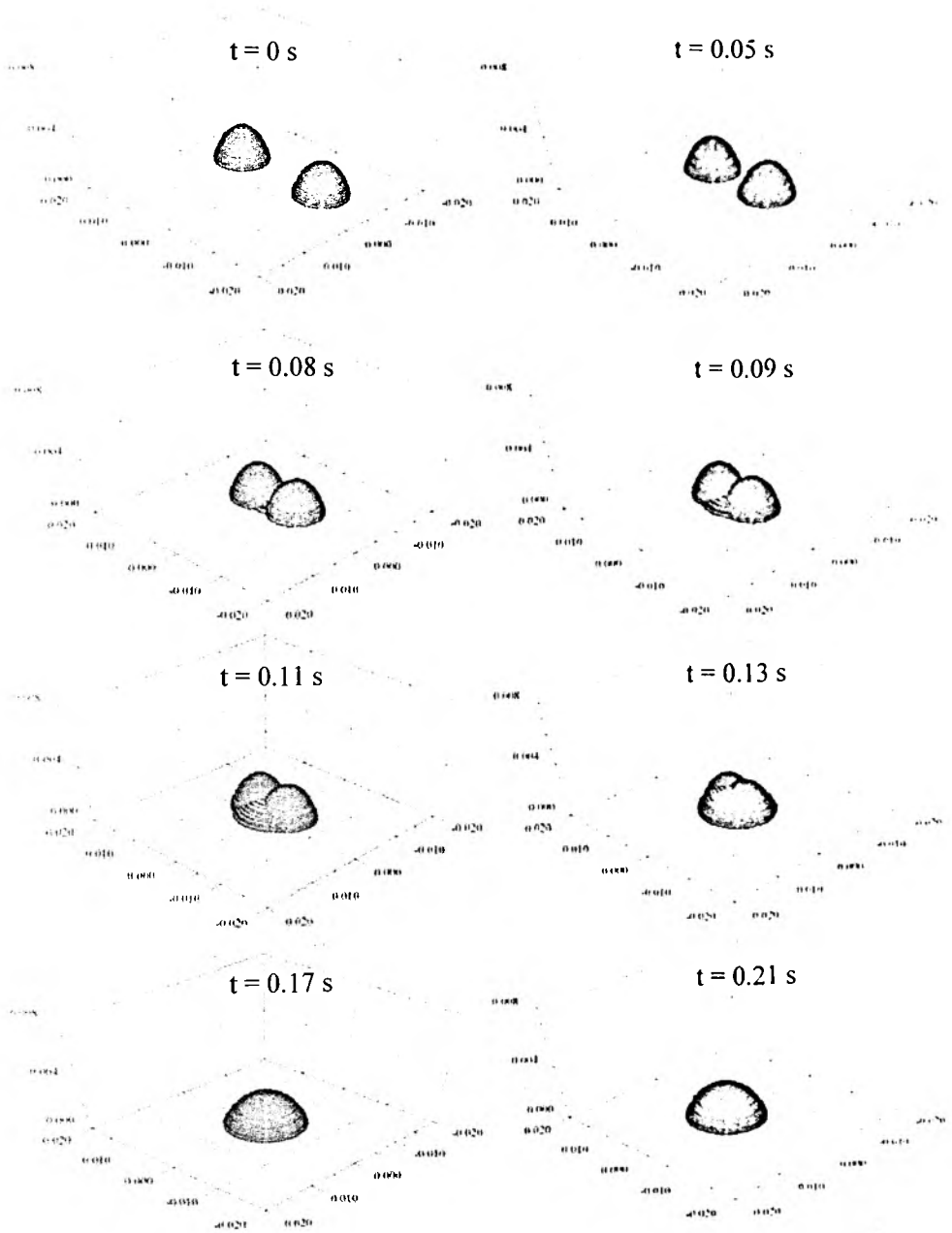

Fig. 4.51 Merging of drops in a 'Y' shaped path with directional wettability gradient

To simulate the drop advancement and merging in a Y shaped wettability gradient path DI based SPH is used. Incorporation of wettability gradient in the simulation is made based on equation 4.14. Simulation results for a wettability gradient of 5°/mm along the arms are depicted in Fig. 4.51. For the present simulation two water drops having 90 μL of volume are placed in the side arms. As no effort has been made for studying the chemical reactions in the SPH methodology drops with similar property is tested. Stresses have been given on the contact time as it is the prime factor which governs the reaction rate. It can be observed from the figure that the two drops advanced towards each other gathering some inertia and then collided with at the junction. As the wettability gradient is provided in the root arm the combined drop also moves along the root arm after collision. Total time required for complete merging under wettability gradient 5°/mm is 0.0796 s. Time required for complete merging depends on the rate of wettability gradient provided in the path.

Efforts have also been made to examine the time required for complete merging of liquid drops for different wettability gradient. Results obtained from the simulations are depicted in Fig. 4.52. It can be seen that at lower wettability gradient time required for complete merging is high which facilitates the desired reaction procedure. But a very low wettability gradient is also not desired as under such situation the drops are unable to generate adequate inertia force which prompts the drops to move forward towards the junction and collide. It can be concluded from the study that by applying suitable wettability gradient at the arms of the 'Y' path a control over the miniature chemical reaction can be achieved.

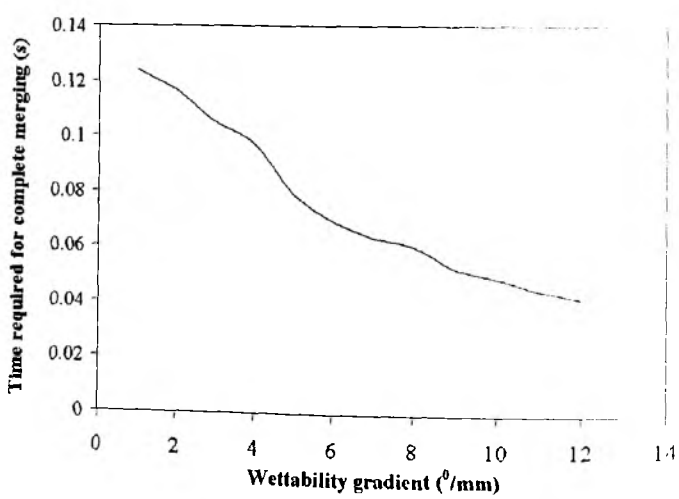

Fig. 4.52 Time taken for complete merging at different wettability gradients

4.5 Summary

In this chapter DI concept is incorporated in particle based SPH. This approach is new in origin and a very few efforts are reported earlier which combine DI with particle based methodology. The proposed methodology has been put to rigorous tests considering two different case studies namely i) evolution and free rise of a bubble from a submerged orifice and ii) drop deformation and break up in shear flow. In both the cases DI-SPH simulation provides discernable improvement over the SPH simulation with sharp interface.

The model is employed to study different problems of drop dynamics under the action of gravitational force and wettability gradient. It has been shown that present methodology can not only handle asymmetric shape of the drop, it can also successfully model drop breakage and merging due to wettability gradient.

CHAPTER 5 MODELING OF LIQUID-VAPOR PHASE CHANGE

5.1. Introduction

In the previous two chapters schemes have been developed for the modeling of interface and its evolution using SPH. The models have been employed for various examples of two phase flow. All the examples considered are adiabatic and do not involve any phase change. On the other hand, phase transfer is an extremely important physical process present in numerous engineering applications. The aim of the present chapter is to develop an algorithm based on SPH to handle phase change with a large density difference. Though the developed algorithm could be used in general for different types of phase change problems, emphasis has been given on liquid-vapor phase change due to evaporation and boiling.

It can be seen from the literature (Welch and Wilson, 2000; Esmaeeli and Tryggvason, 2004) that the tracking of interfaces in eulerian phase change problem is quite challenging. Moreover, film growth, film collapse and bubble nucleations are several new phenomena which are associated with breaking and making of complex interfaces. But till date lagrangian techniques are not elaborately employed for phase change problems. In a lagrangian particle based technique both the number of particle and their individual mass need to be conserved. Therefore, the implementation of the basic SPH scheme may pose a difficulty as many phase change problems involve a large change in density. For capturing the dynamic interface, particle redistribution was needed at regular intervals. Using SPH a 3D model of gas liquid phase change has been developed to overcome these numerical difficulties. In the next section a brief description of the developed methodology is presented. A number of examples for gas liquid phase change from both plane and curved surfaces have been taken up to establish the technique. In both the cases the nucleation of bubble is considered to be greater than 10^{-6} m.

5.2. Model development

5.1. Governing equations

For the phase change problem the conservation of mass, momentum and energy of each of the phases can be expressed using a Lagrangian description.

Continuity equation for the k^{th} phase can be written as:

$$\frac{D\rho_k}{Dt} + \rho_k \nabla . v_k = \sum_k \frac{dm_g}{dt}. \tag{5.1}$$

In equation 5.1, the right hand side denotes the mass transfer from one phase to another.

The conservation of momentum can be mathematically expressed as follows:

$$\frac{Dv_k^{\ \alpha}}{Dt} = \frac{1}{\rho}\frac{\partial \sigma_k^{\ \alpha\beta}}{\partial x^\beta} + g_\alpha \beta_{Tk}\left(T - T_0\right), \tag{5.2}$$

where,

$$\sigma^{\alpha\beta} = -P\delta^{\alpha\beta} + \mu_k\left(\frac{\partial v^\beta}{\partial x^\alpha} + \frac{\partial v^\alpha}{\partial x^\beta} - \frac{2}{3}(\nabla v)\delta^{\alpha\beta}\right). \tag{5.3}$$

The last term in the right hand side of equation 5.2 denotes the body force term due to change of density in a temperature field. As a usual practice the change of density is considered only in the body force term based on Boussinesq approximation. This term was not considered for adiabatic cases discussed in chapters 3 and 4. Surface tension force is not added in the momentum equation as it is separately applied to the interfacial particles following the CSF methodology as described in chapter 3. Instead of a sharp interface if a diffused interface is considered equation 5.2 needs to be modified as follows to accommodate the conservation of surface energy:

$$\frac{Dv_k^{\ \alpha}}{Dt} = \frac{1}{\rho}\frac{\partial \sigma_k^{\ \alpha\beta}}{\partial x^\beta} + g_\alpha \beta_{Tk}\left(T - T_0\right) - \frac{C_k}{Cap_k\ Cn}\frac{\partial \phi}{\partial x^\beta}. \tag{5.4}$$

The derivation of the surface energy term has been discussed in chapter 4.

The energy equation in case of a phase change problem needs to be derived carefully. In general, a fluid phase may not be in the saturated condition. As a result both latent and sensible heat transfer is present. As phase change occurs only at the interface, separate energy balance equations are considered for the bulk phases and the interface. Energy equation of the bulk phase involves sensible heat transfer and also contains a source term which assumes a non-zero value only at the solid boundary:

$$\rho_k c_{pk}\frac{DT}{Dt} = \nabla\left(k_k \nabla T\right) - P\nabla v + \mu_k\left(\frac{\partial v^\beta}{\partial x^\alpha} + \frac{\partial v^\alpha}{\partial x^\beta} - \frac{2}{3}(\nabla v)\delta^{\alpha\beta}\right)\frac{\partial v^\alpha}{\partial x^\beta} + \sum_k Q_k \delta\left(r - R_k\right). \tag{5.5}$$

It may be noted that viscous dissipation (third term of the right hand side) is also taken into consideration in the above equation. R_k is the radial location of the heat source and $\delta(x)$ is the delta function with following definition:

$$\delta(x) = \begin{matrix} 1 & \text{if } x = 0 \\ 0 & \text{if } x \neq 0 \end{matrix}. \tag{5.6}$$

The last term in the R.H.S. of the above equation is needed only when heat flux condition is imposed on the boundary. This term is omitted for a constant temperature wall condition.

At the interface, equation (5.5) transforms into equation (5.7) which includes also the rate of mass transfer due to phase change. It can be written in the following form:

$$\sum_k L_h \frac{Dm_g}{Dt} = \nabla\left(k_k \nabla T\right) - P\nabla u + \mu_k \left(\frac{\partial v^\beta}{\partial x^\alpha} + \frac{\partial v^\alpha}{\partial x^\beta} - \frac{2}{3}\left(\nabla v\right)\delta^{\alpha\beta} \right) \frac{\partial v^\alpha}{\partial x^\beta} . \tag{5.7}$$

It needs to be mentioned that the formulation for the diffuse interface is applied only in the momentum equation. No special term has been added in the energy equation for considering the surface energies.

Equations 5.1-5.7 are recast in SPH formalism using a smoothing kernel W(x, h) and the following equations are obtained:

Continuity:
$$\frac{D\rho_i}{Dt} - \sum_k m_k \left(v_i - v_k\right).\nabla W_{ik} = \sum_k \frac{dm_{gk}}{dt} W_{ik} , \tag{5.8}$$

Momentum (sharp interface):

$$\frac{Dv_i^\alpha}{Dt} = \sum_{j=1}^{N} m_j \left(\frac{\sigma_i^{\alpha\beta} + \sigma_j^{\alpha\beta}}{\rho_i \rho_j} \right) \frac{\partial W_{ij}}{\partial x_i^\beta} + g_\alpha \beta_T \left(T_i - T_0\right), \tag{5.9}$$

Momentum (diffuse interface):

$$\begin{aligned} \frac{Dv_i^\alpha}{Dt} = & \sum_{j=1}^{N} m_j \left(\frac{\sigma_i^{\alpha\beta} + \sigma_j^{\alpha\beta}}{\rho_i \rho_j} \right) \frac{\partial W_{ij}}{\partial x_i^\beta} + g_\alpha \beta_T \left(T_i - T_0\right) - \\ & \sum_{j=1}^{N} \frac{m_j}{\rho_i \rho_j} \frac{\left(\frac{C_i}{Cap_i Cn_i} + \frac{C_j}{Cap_j Cn_j} \right)\left(\phi_i - \phi_j\right)}{\left|r_{ij}\right|} \frac{\partial W_{ij}}{\partial r_{ij}}, \end{aligned} \tag{5.10}$$

where $\sigma_i^{\alpha\beta}$ can be evaluated following equation 3.10. Discretization of chemical potential (φ) is also described in Chapter 4.

Energy (bulk phase):

$$\begin{aligned} c_{pa} \frac{DT_a}{Dt} = & \sum_b \frac{m_b}{\rho_a \rho_b} \frac{4k_a k_b}{\left(k_a + k_b\right)} \left(T_a - T_b\right) F_{ab} - \sum_k \frac{m_k P_k}{\rho_k} \left(v_i - v_k\right).\nabla W_{ik} \\ & + \mu_i \left(\frac{\partial v_i^\beta}{\partial x_i^\alpha} + \frac{\partial v_i^\alpha}{\partial x_i^\beta} - \frac{2}{3}\left(\nabla v_{ij}\right)\delta^{\alpha\beta} \right) \frac{\partial v_i^\alpha}{\partial x_i^\beta} + \frac{1}{\rho_a} \sum_k Q_k \xi_k W\left(r_a - R_k\right), \end{aligned} \tag{5.11}$$

Energy (at interface):

$$\begin{aligned} \frac{1}{\rho_a} \sum_k L_h \frac{Dm_{gk}}{Dt} \xi_I W\left(r_a - R_I\right) = & \sum_b \frac{m_b}{\rho_a \rho_b} \frac{4k_a k_b}{\left(k_a + k_b\right)} \left(T_a - T_b\right) F_{ab} \\ & - \sum_k \frac{m_k P_k}{\rho_k} \left(v_i - v_k\right).\nabla W_{ik} + \mu_i \left(\frac{\partial v_i^\beta}{\partial x_i^\alpha} + \frac{\partial v_i^\alpha}{\partial x_i^\beta} - \frac{2}{3}\left(\nabla v_{ij}\right)\delta^{\alpha\beta} \right) \frac{\partial v_i^\alpha}{\partial x_i^\beta}, \end{aligned} \tag{5.12}$$

where, $\frac{1}{\xi_k} = \sum_b \frac{m_b}{\rho_b} W(r_b - R_k, h)$ and $F_{ab} = \frac{1}{(r_a - r_b)} \nabla W(r_a - r_b, h)$. (5.13)

It may be noted that equation 5.11 is the generalized form of the energy equation as it contains also the heat flux condition (last term of R.H.S.). All the problems considered in the later sections involve constant temperature boundary condition and naturally this term is omitted.

5.2. Algorithm for tracking the interface with phase change

To treat the spatio-temporal evolution of phases the following steps are proposed apart from solving equation (5.8-5.13) numerically.

- Domains of two separate phases are discretized into finite number of particles having individual mass and properties.
- For a clear definition of the interface which is x unit away from the left boundary, a separate set of particles are positioned between the particles of the two different phases. These particles are termed as pseudo particles.
- Pseudo particles are used as temporary storage of mass before the redistribution of the particles of two adjacent phases. Initially pseudo particles have no mass while they are assigned the properties of a particular phase (the gaseous phase in the present case). One typical example of positioning the pseudo particles is shown in Fig. 5.1(a). In this figure solid black circles are representing the vapor domain and hatched circles denote liquid particles. At the interface, array of blank circular pseudo particles are positioned.
- The interfacial mass transfer between the liquid and vapor particles (equation 5.12) is calculated by simultaneous solution of equations 5.8-5.13. In case of boiling or evaporation mass lost by the liquid particles are considered as mass gained in the pseudo particles (Fig. 5.1b-c).
- Pseudo particles are treated as gaseous particles during the solution of equations 5.8-5.13 with modified mass and smoothing length. Effect of pseudo particles over bulk particles is also considered following equations 5.8-5.11. Mass of pseudo particles increases as time progresses.

- Based on a pre assigned criterion (mentioned in equation 5.14) the mass and position of the liquid and gas particles are redistributed keeping their total number fixed (Fig. 5.1d). The criterion for redistribution can be set as follows:

$$\left.\frac{m_{pseudo}}{m_{gas}}\right|_{for\ all\ pseudo\ particles} = x \qquad 0 < x < 1 \tag{5.14}$$

Value of x governs the frequency of redistribution. A value of x close to zero indicates that redistribution is done in almost every step. Lower value of x increases the accuracy of prediction but with a penalty of computational effort. The value of x may be selected from a balance between the accuracy and the computational effort. Further, it varies from problem to problem and depends also on the complexity of the interface.

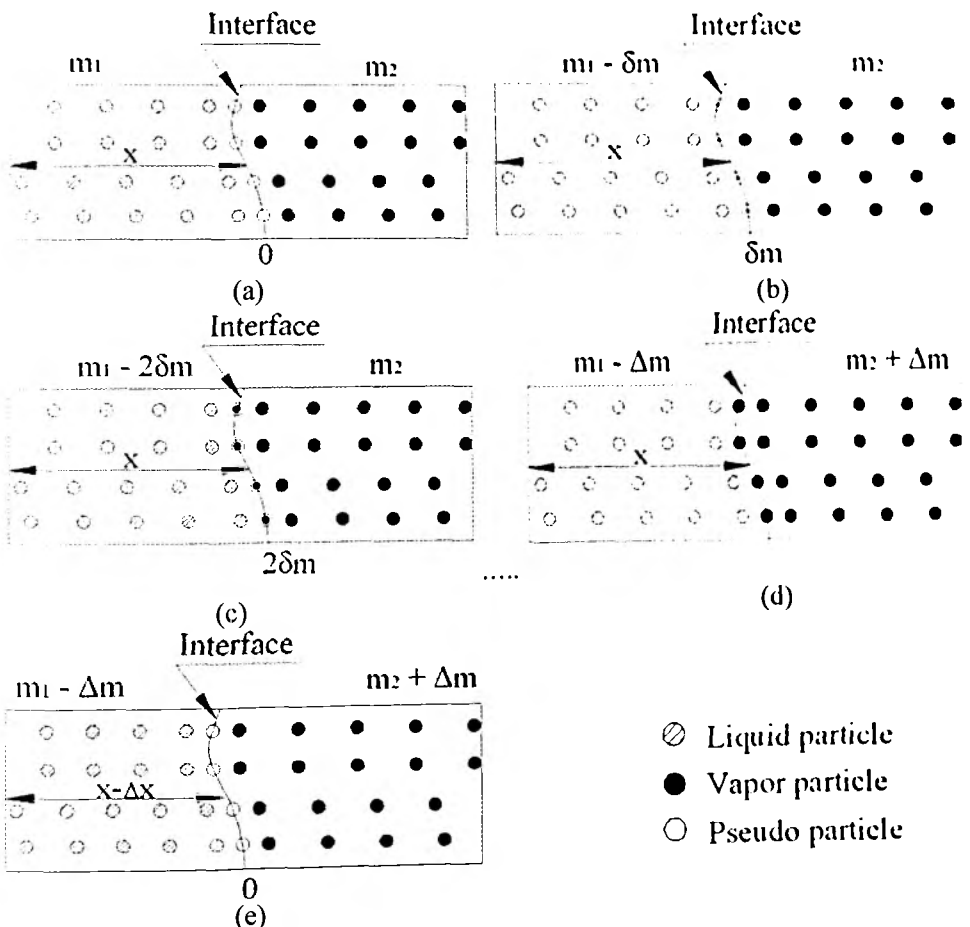

Fig. 5.1 The scheme of particle redistribution for an evolving interface

- Once the particles of the neighboring phases are redistributed a layer of fresh pseudo particles are introduced at the interface (Fig. 5.1e) which is now shifted Δx unit towards the left wall.

The above mentioned redistribution scheme is valid only for homogeneous growth of vapor film in every direction. But for the cases where growth of vapor film is not uniform remeshing is done after certain time step when any one of the pseudo particle becomes as heavy as the vapor particle.

Choice of kernel function is of vital importance for the SPH methodology. In the earlier chapters the use of cubic spline kernel could produce sufficiently accurate results. The complexity of phase change process demands an interpolation function with a higher accuracy. Accordingly, a piecewise smooth polynomial is used. The used function is described below:

$$\text{for } 2<\left|\frac{r_j}{h}+\frac{r_i}{h}\right| \qquad W_{ij}\left(r_i,r_j,h\right)=\frac{1}{hr_ir_j}\begin{cases}\frac{7}{10}-C\left(\left|\frac{r_j}{h}-\frac{r_i}{h}\right|\right), & 0\le\left|\frac{r_j}{h}-\frac{r_i}{h}\right|<1\\ \frac{8}{10}-D\left(\left|\frac{r_j}{h}-\frac{r_i}{h}\right|\right), & 1\le\left|\frac{r_j}{h}-\frac{r_i}{h}\right|<2\end{cases},$$

$$\text{for } 1<\left|\frac{r_j}{h}+\frac{r_i}{h}\right|\le 2 \quad W_{ij}\left(r_i,r_j,h\right)=\frac{1}{hr_ir_j}\begin{cases}-\frac{1}{10}+D\left(\left|\frac{r_j}{h}+\frac{r_i}{h}\right|\right)-C\left(\left|\frac{r_j}{h}-\frac{r_i}{h}\right|\right), & 0\le\left|\frac{r_j}{h}-\frac{r_i}{h}\right|<1\\ D\left(\left|\frac{r_j}{h}+\frac{r_i}{h}\right|\right)-D\left(\left|\frac{r_j}{h}-\frac{r_i}{h}\right|\right), & 1\le\left|\frac{r_j}{h}-\frac{r_i}{h}\right|<2\end{cases},$$

$$\text{for } \left|\frac{r_j}{h}+\frac{r_i}{h}\right|\le 1 \qquad W_{ij}\left(r_i,r_j,h\right)=\frac{1}{hr_ir_j}\left(C\left(\left|\frac{r_j}{h}+\frac{r_i}{h}\right|\right)-C\left(\left|\frac{r_j}{h}-\frac{r_i}{h}\right|\right)\right), \quad (5.15)$$

where,

$$C(q)=q^2+\frac{3}{4}q^4-\frac{3}{10}q^5$$

and

$$D(q)=2q^2+2q^3-\frac{3}{4}q^4+\frac{1}{10}q^5.$$

Appropriate surface tension force and no penetration force are employed near the interface as discussed in Chapter 3. The model is applied for several cases involving a transient growth of vapor film. For all the cases a constant pressure boundary condition is assumed for the extreme outer boundary.

5.3. Case studies

Following case studies has been taken into consideration for the validation of the developed model i) Vapor film growth around a sphere without gravity ii) Vapor film growth around a sphere under normal gravity and iii) Vapor bubble formation and departure from film over a horizontal surface

5.3.1. Vapor film growth around a sphere without gravity

The suitability of the developed algorithm was first tested for investigating the vaporization and the growth of vapor film around a hot solid sphere. As the simulation of the phase change with a large density difference is the prime concern certain idealizations have been made to simplify the problem. The effects of gravity, property variation and radiative heat exchange have been neglected. Radiative heat exchange could be significant in film boiling particularly when the wall temperature is high. However, in a number of computational modelling (Son and Dhir, 2007; Welch and Wilson, 2000) the radiation effect has been neglected as the simulation of the complex interface becomes the main challenge. We have also taken the queue from the earlier works. Nevertheless, the incorporation of radiative heat exchange is expected to improvise the prediction and could be taken as a future scope of work. Absence of gravity ensures a spherical growth of vapor. For such a simplified problem analytical models are available (Robinson and Judd, 2004). This leaves a scope for validating the present computational predictions. As the surface temperature is maintained at a high degree of superheat a growth of vapor film have been considered from the very inception of the problem. It has been assumed that initially the total domain is filled with liquid particles having 2×10^{-4} m. Particle spacing has been fixed after a rigorous grid independence test. The solid boundary is described by particles with constant temperature around the periphery. The present case study has been done based on sharp interface.

Proposed redistribution scheme is employed for the present case when the mass of the pseudo particles become equal to the mass of the vapor particles. Fig. 5.2 shows the vapor film growth at different time interval around a solid sphere of 5 mm diameter, maintained at 473 K and immersed in a pool of water (ρ = 1000 kg/m^3, k = 0.0025 W/m-K, $\sigma = 5.67 \times 10^{-8}$ W) at atmospheric pressure. As the effect of gravity has been neglected the vapor film exhibits a perfectly spherical growth. Only one half of the symmetric film is shown in alternate side as time progresses. To start with the vapor film grows rapidly but as expected the rate of growth decreases as the film becomes thicker.

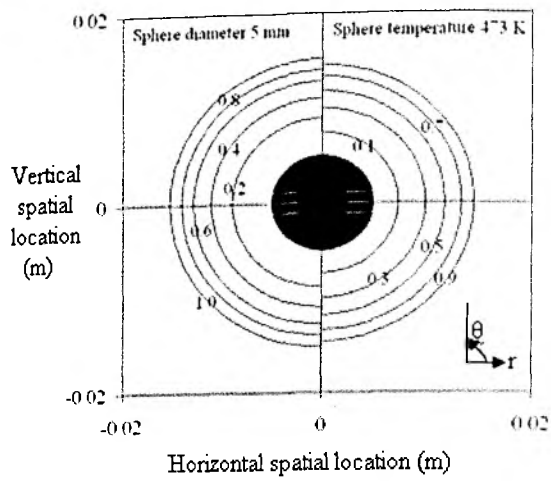

Fig. 5.2 Growth of vapor film over a sphere without gravity (diameter 5 mm, surface temperature 473 K)

Instantaneous film thickness around the sphere and its velocity is obtained from the numerical simulation and is depicted in Figs. 5.3a and 5.3b respectively. Bejan et al. (1997) simulated the similar type of problem using finite difference approximation of the mixture equation. In both the figures numerical results of Bejan et al. (1997) are also depicted. A good match can be seen between the results of present numerical simulation and observations of Bejan et al. (1997). The maximum error is around 5.3%. It has been observed that interface velocity decreases as time progresses. The continuous fall in the interface velocity is consistent with the decreasing rate of vapor film growth depicted in Fig. 5.2.

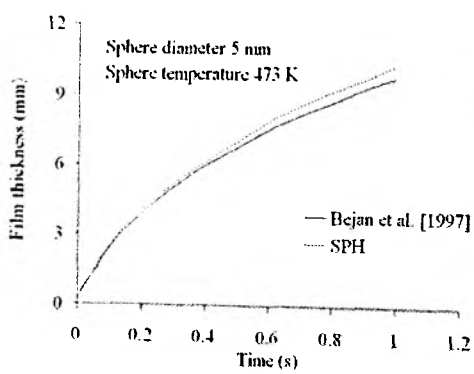

(a) film thickness

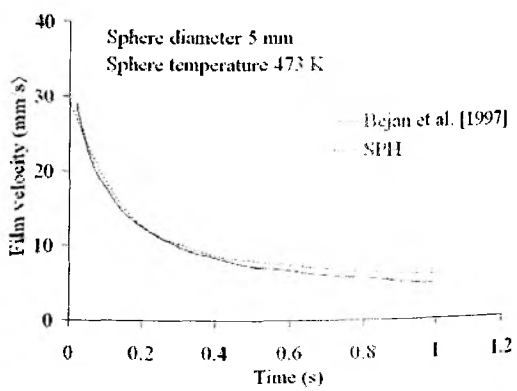

(b) interface velocity

Fig. 5.3 Comparison of film thickness and interface velocity with Bejan et al. (1997); sphere diameter 5 mm, temperature 473 K

Next simulations have been made for a sphere maintained at 2295 K temperature. At such a high surface temperature the vapor generation rate is very high. Either one can adopt a smaller time step or a scheme of frequent redistribution of particles to tackle such a situation. Both the strategies are computationally intensive. To avoid this difficulty a sphere of smaller diameter namely 1 mm has been considered. Similar redistribution technique, as discussed earlier, is applied to the vapor particles. Redistribution is done when the mass of the pseudo particle becomes more or less comparable to the neighboring gaseous particles. Fig. 5.4 shows the growth of the vapor film around a sphere of diameter 1 mm. Comparing Fig. 5.4 and 5.2, film growth is relatively fast in case of high temperature of the solid surface.

Thickness of the vapor film (Fig. 5.5a) and its subsequent velocity (Fig. 5.5b) are also calculated at different time level to show the nature of film generation around the sphere at high temperature. It has been observed that film thickness increases but the rate of advancement is diminishing in nature. Reported results of Bejan et al. (1997) are also depicted in the figures. Though the trend is predicted well by proposed SPH methodology, it has been observed that there exist an over prediction compared to the results of Bejan et al. (1997) after certain time instants. They have included the heat transfer due to radiation in their model which is not considered in the present model. At such a high temperature (2295 K) radiation heat loss cannot be completely ignored. A better model incorporating radiation heat transfer in particulate SPH methodology may improve the predictions at high temperatures.

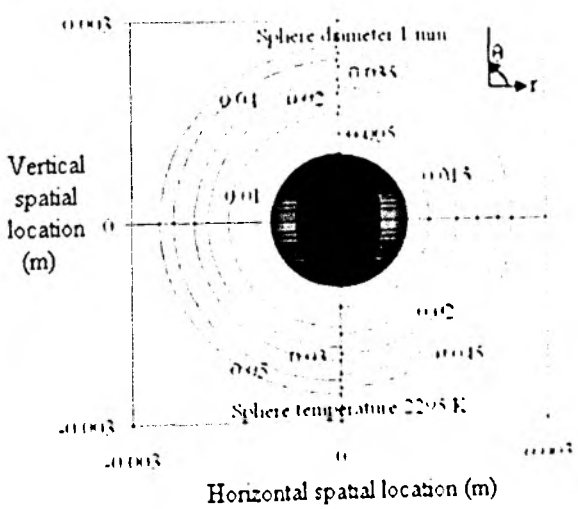

Fig. 5.4 Growth of vapor film over a sphere without gravity (diameter 1 mm, surface temperature 2295 K)

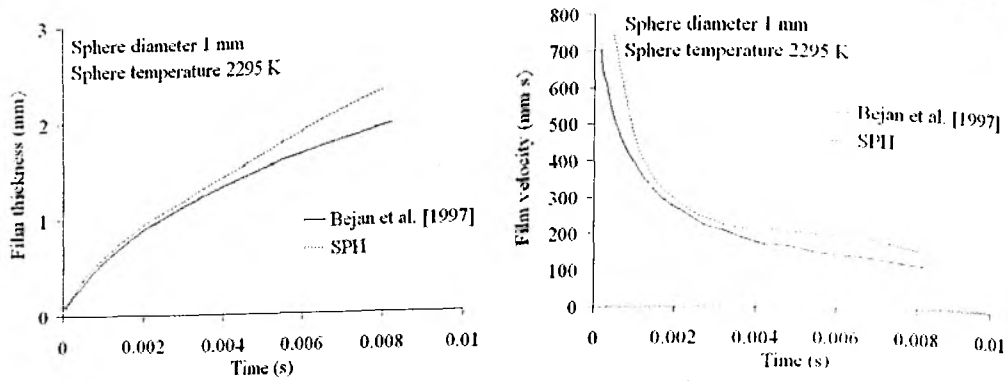

(a) film thickness (b) interface velocity

Fig. 5.5 Comparison of film thickness and interface velocity with Bejan et al. (1997); sphere diameter 1 mm, sphere temperature 2295 K

Adoption of Lagrangian particle based SPH methodology makes it possible to investigate the spatial variations of the parameters like vapor temperature and velocity. In Figs. 5.6a and 5.6b representative temperature and velocity contours of the superheated vapor around a solid sphere having 100° superheat are depicted. Water is taken as the test fluid. It can be observed from the figures that iso-contours are concentric around the sphere in the absence of gravity. Vapors near the hot solid are more superheated compared to the interfacial zone. Vapor particles near the hot solid show almost no mobility. Vapor particles near the interface follows the interface velocity but the intermediate vapor particles show higher mobility compared to the others.

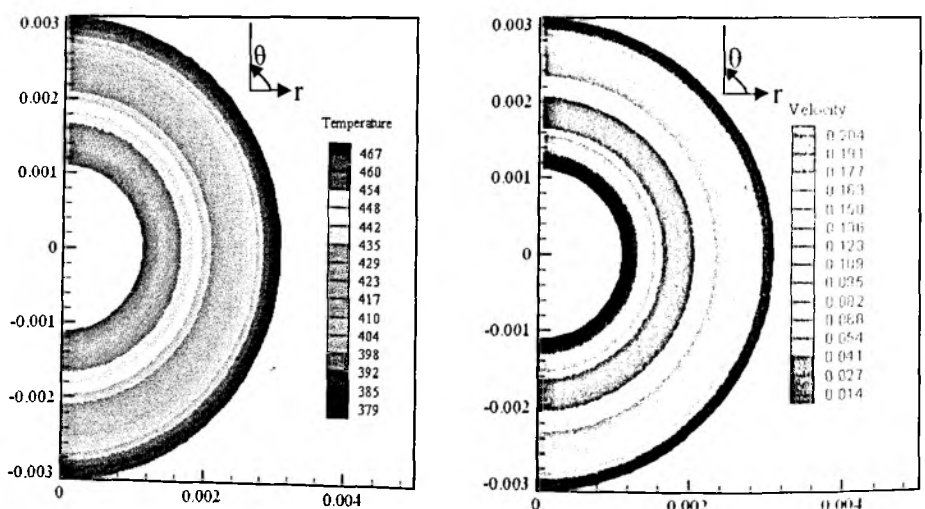

(a) temperature contour (b) velocity contour

Fig. 5.6 Temperature and velocity contour of the film generated around a sphere; 2 mm diameter and 100 K superheat

Efforts have also been made to study the radial distribution of temperature and velocity of the vapor particles generated due to evaporation. To compare the temperature distributions at several time instants non dimensional temperature, $(T_r-T_{sat})/(T_s-T_{sat})$ and non dimensional radius $(r_r-r_s)/(r_l-r_s)$ is taken into consideration. Here, T_{sat} and T_s stand for saturation temperature and sphere temperature respectively. r_s and r_l denote the radius of the hot sphere and radial location of the interface. Velocity of the individual particles are divided by the interface velocity (v_l) to make the study non dimensional. Figs. 5.7a and 5.7b show the radial temperature and velocity distribution transients around a sphere having 5 mm diameter and maintained at 2295 K (T_s). Water (T_{sat} = 373 K) is taken as the test fluid. It can be observed from Fig. 5.7a that particles adjacent to the sphere are maintained at T_s whereas interfacial particles are at T_{sat}. Initially, the temperature gradient is almost constant throughout the radial plane but nonlinearity sets in as time progresses keeping both the extremities constant. Particles near the sphere are almost stationary (Fig. 5.7b) whereas interfacial particles maintain its velocity as a whole. Similar observation is also reported in Fig. 5.6b for lower temperature. A zone near the solid sphere inside the vapor film can be identified where the particles show greater mobility (1.7 times) compared to the interface. Mobility of this zone increases as the time progresses.

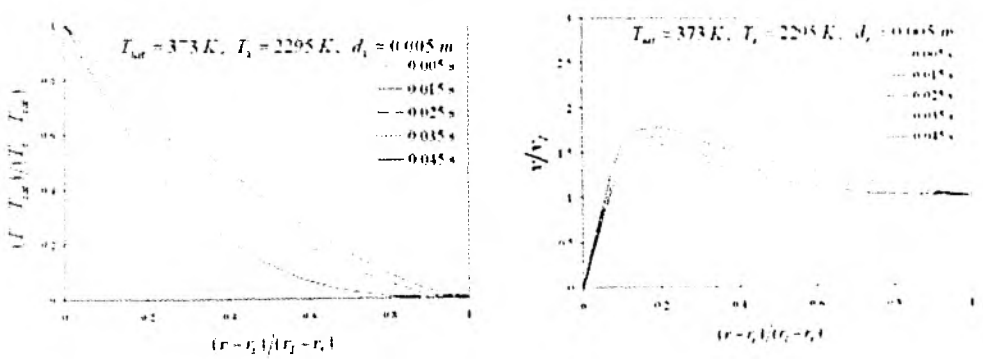

(a) temperature distribution (b) velocity distrtibution

Fig. 5.7 Radial temperature and velocity distribution inside the vapor film around a sphere; 5 mm diameter and 2295 K superheat

Fig. 5.8 depicts a comprehensive picture on how vapor film grows for different diameters (3 mm, 4 mm and 5 mm) and temperatures (473 K, 523 K and 573 K) of the sphere. Locations of the symmetric film for six different time instants (0.1 s, 0.2 s, 0.3 s, 0.4 s, 0.5 s and 0.6 s) are shown for every situation. From the figure it can be observed that film thickness increases as the sphere diameter and temperature increases. It is quite obvious as the amount

of thermal energy input increases with the increase in surface area of constant temperature boundary or increase in surface temperature of constant boundary area.

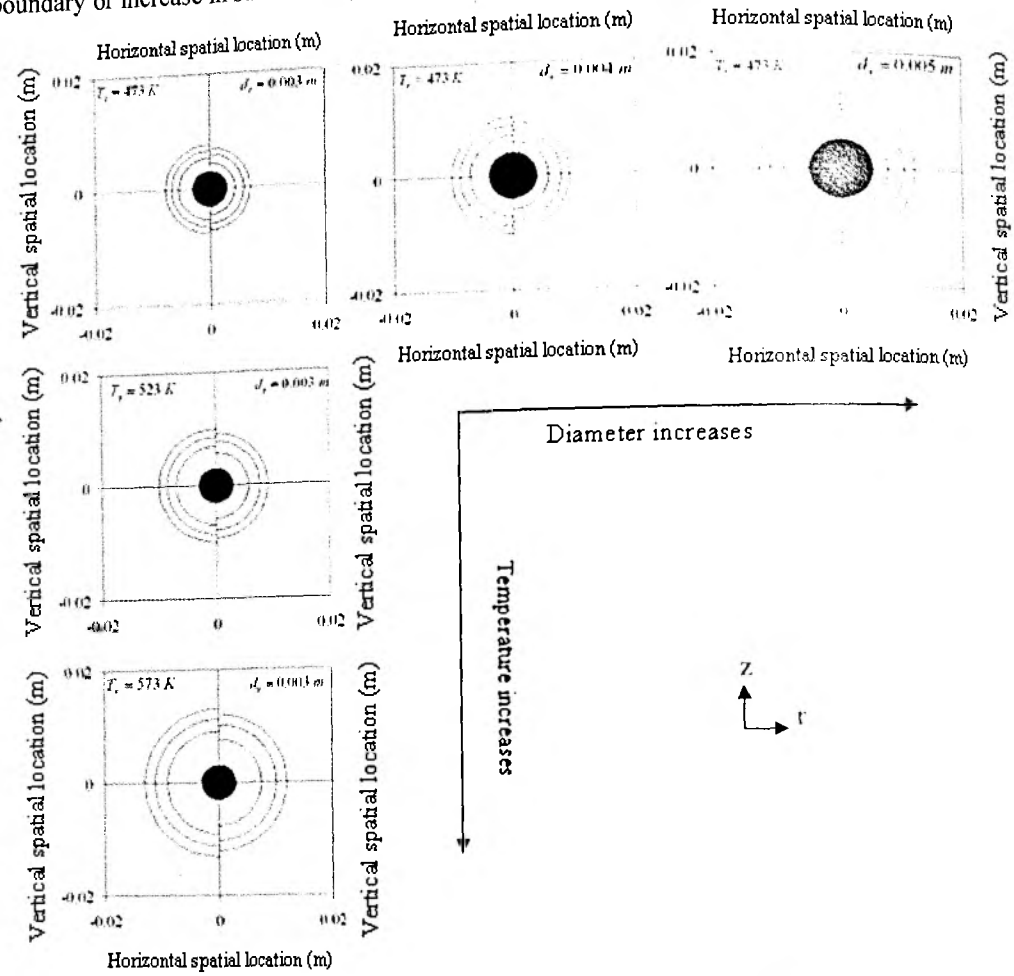

Fig. 5.8 Effect of sphere diameter and temperature on the growth of vapor film

Dependence of sphere diameter and sphere temperature on radial temperature and velocity distribution of the film is studied numerically. Though the particles near the interface and sphere maintains respective boundary conditions, the temperature and velocity distribution of the interior particles is important to understand the kinetics of the vapor film. In Figs. 5.9a and 5.9b, radial temperature and velocity distribution of vapor film at 0.7 s for 3 mm, 4 mm and 5 mm diameter sphere is plotted. All the spheres are kept at 473 K in the atmosphere of saturated water at atmospheric pressure. It can be observed from Fig. 5.9a that the radial temperature becomes nonlinear as the diameter of the sphere increases. The

intermediate zone within the film thickness shows greater mobility (Fig. 5.9b) in all the cases. From Figure 5.9b it can be observed that the mobility of this zone increases with the increase of sphere diameter keeping the extremities constant. The location of this high mobility zone also shifts towards the sphere as diameter increases.

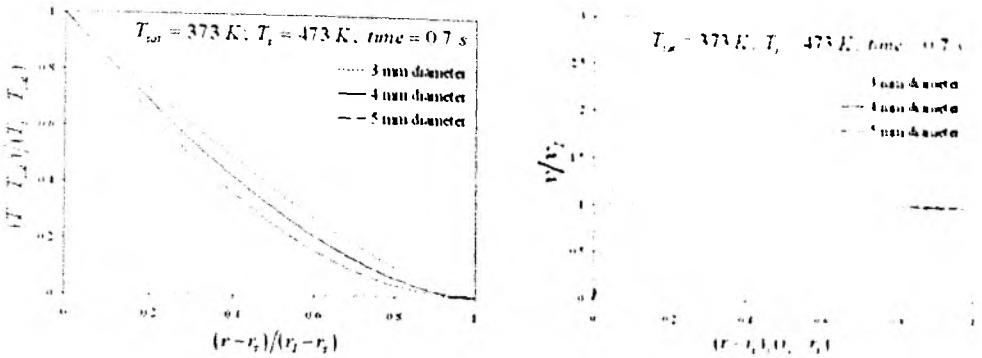

(a) temperature distribution (b) velocity distribution

Fig. 5.9 Effect of sphere diameter on radial temperature distributions and velocity keeping the degree of superheat fixed

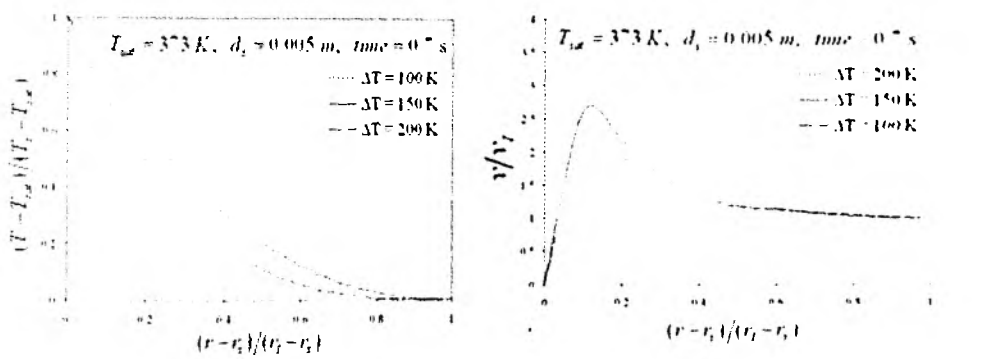

(a) temperature distribution (b) velocity distribution

Fig. 5.10 Effect of superheat on radial temperature and velocity distributions keeping the sphere diameter fixed

Similar study has been made keeping the sphere diameter constant (5 mm) with varying superheat of the solid (100 K, 150 K and 200 K). Numerical results for radial temperature distribution and interface velocities are depicted in Figs. 5.10a and 5.10b for these situations. The figure shows that non linearity of the temperature distribution as the superheat increases. This is quite obvious as the vapor particles show higher mobility at high degree of superheat. It is obvious that mobility of the intermediate zone increases as the sphere temperature

increases. As the diameter of the sphere has not been changed the location of the high mobility zone also remained more or less at the same location. This shows that though the particles near the solid sphere and interface satisfies the boundary condition intermediate particles follow their own kinetics based on basic fluid mechanics and heat transfer conjectures.

Finally, it can be concluded from the above study that described model along with the proposed redistribution scheme is well efficient in predicting the advancing film thickness during phase change under zero gravity situation.

5.3.2. Vapor film growth around a sphere under normal gravity

In the earlier section vapor formation from a hot sphere has been considered in the absence of gravity. Low gravity or zero gravity situations are particularly important for space applications and in flight simulations. The simulation results also approximate the growth of vapor phase at a very early stage and vaporization in case the density of liquid and vapor phase are close. Primarily the exercise of the earlier section has been taken up for the establishment of the computational algorithm and its validation against available analytical results. Inter particle spacing is kept identical (2×10^{-4} m) as have been mentioned in the previous case. As the density of the generated vapor due to phase change is quite low compared to the density of the surrounding liquid vapor mass always tries to move upward against gravity. This induces a non uniformity in the film thickness and vapor velocity around the sphere. This upward movement of vapor along with the effect of surface tension gives rise a typical distribution of vapor film which is substantially different from that observed in the previous section.

For the advancement of vapor front, particle redistribution scheme as described earlier in this chapter is employed after a time interval when the mass of the pseudo particles becomes equal to that of the neighboring vapor particle.

Fig. 5.11 presents the simulation results for the process of vaporization around a sphere of 5 mm diameter. The surface temperature of the sphere is kept at 473 K while it is surrounded by liquid water saturated at 373 K. the effect of property variation and radiative exchange have been neglected for the sake of simplicity.

Initially it has been observed that a symmetrical vapor film is generated around the sphere (Fig. 5.11a). As the film grows further the magnitude of the buoyancy force over the vapor

mass becomes stronger. It starts to develop an azimuthal asymmetry in the vapor film around the sphere (Fig. 5.11b-e). In the vertical elongation of vapor mass as a protrusion a small neck formation is observed due to surface tension force (Fig. 5.11f). This neck formation continues along with the increment of film thickness around the sphere (Fig. 5.11g-j). It eventually forms a vapor bubble over the solid sphere. At the final stage of the growth the neck narrows down to pinch the bubble off from the topmost position of the film (Fig. 5.11k). After departure, the bubble becomes spherical (Fig. 5.11l) while the truncated vapor film around the sphere starts to generate another bubble.

For a very small period of time, the film around the sphere remains uniform. As the film grows, asymmetry sets in. In Fig. 5.12 the thickness of the film at three different circumferential locations has been reported over a period of time.

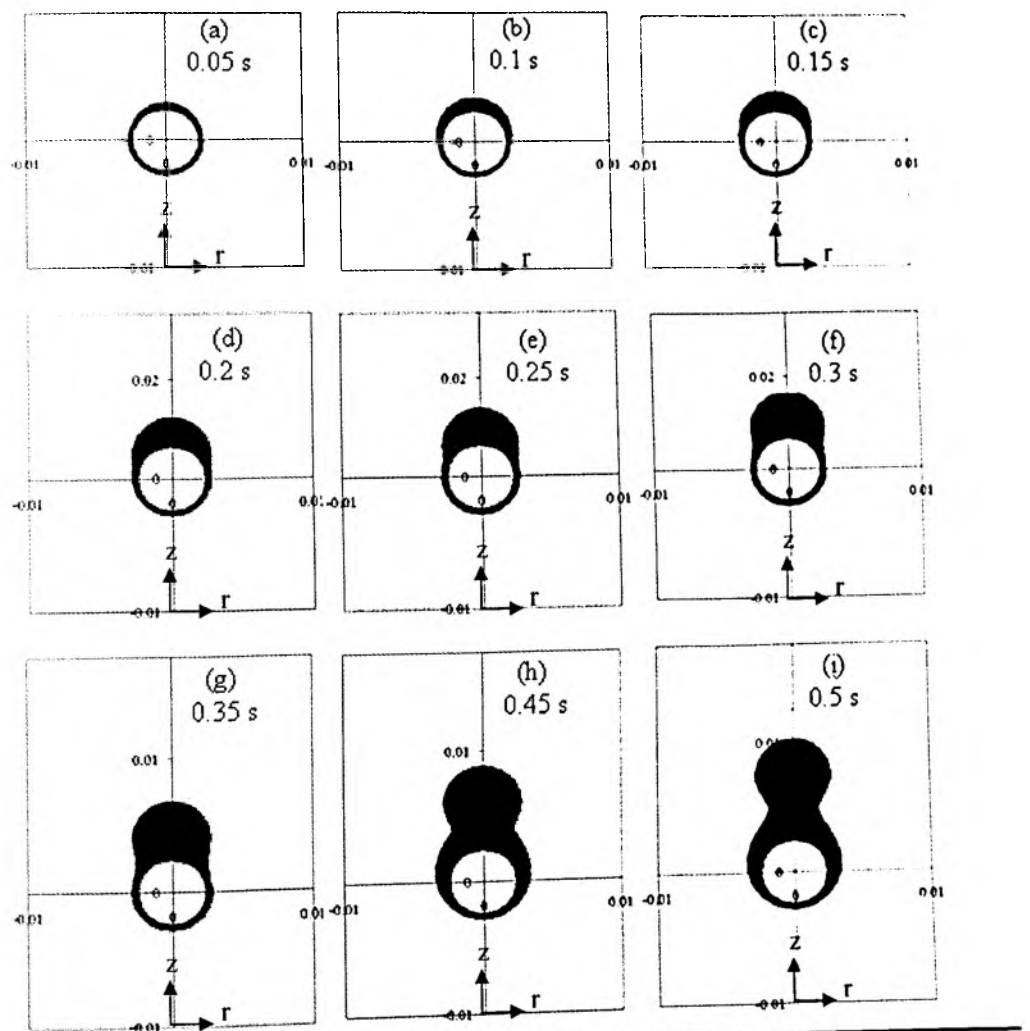

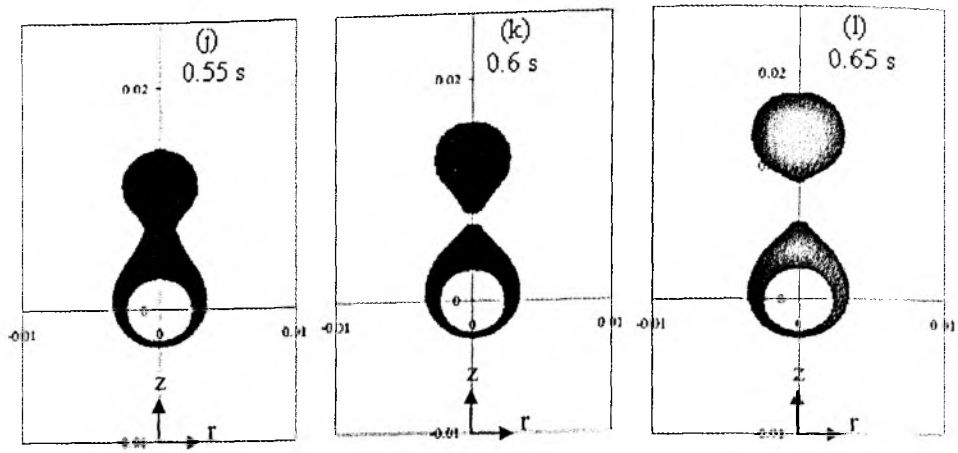

Fig. 5.11 Evolution of vapor film around a sphere; diameter 5 mm, sphere temperature 473 K

It can be seen that though initially for a very small period of time the vapor film grows uniformly, asymmetry sets in very quickly (≈0.03 s). After this initial period at the topmost position vapor tries to gather due to gravity which causes the thickness of the film to grow more compared to the film at the bottom most position.

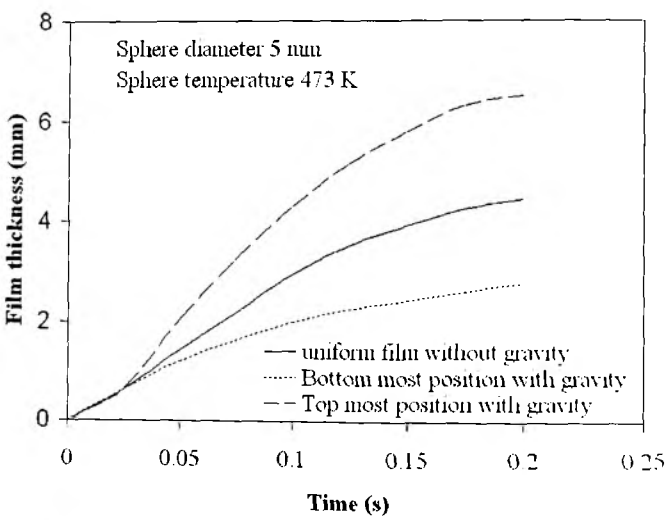

Fig. 5.12 Comparison of film thickness at the topmost portion and bottom most portions in the presence of gravity.

In the above case the size of the released bubble is of the similar order with the hot solid sphere. However, the size of the vapor bubble detached from to the hot sphere is not identical

in all the cases. Simulations have also been made for film boiling over a sphere of 10 mm diameter. The temperature of the outer surface is kept identical to the earlier case for the sake of comparison. Surrounding liquid temperature is kept at the saturation point. No superheated liquid layer is allowed in the simulation. For an initial period, a uniform vapor film is observed to form around the sphere similar to the earlier case. With the increase in the diameter of the hot sphere the initial vapor layer is observed to grow at a slower rate. It remains almost uniform over the periphery except on a small area at the top of the sphere. At the topmost position vapor is accumulated in the form of a bulge or protrusion (Fig. 5.13a-d). The accumulated vapor mass elongates upward and forms a finger like structure due to the effect of buoyancy (Fig. 5.13e-h). Gradually the vapor finger elongates but it also becomes narrower. At one point a neck is observed to form in the vapor finger (Fig. 5.13i). The neck radius decreases (Fig. 5.13j) with the passage of time making the situation conducive for vapor bubble release from the topmost position of the vapor finger (Fig. 5.13k). After the release, the vapor bubble becomes almost spherical (Fig. 5.13l).

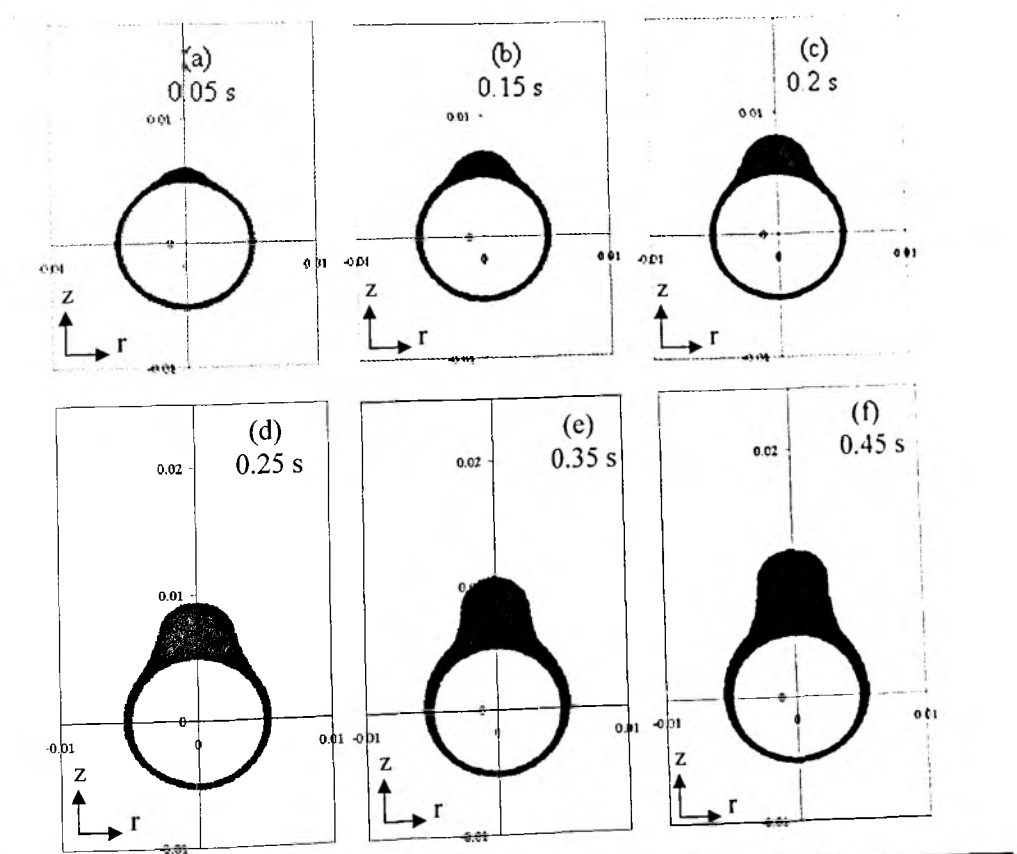

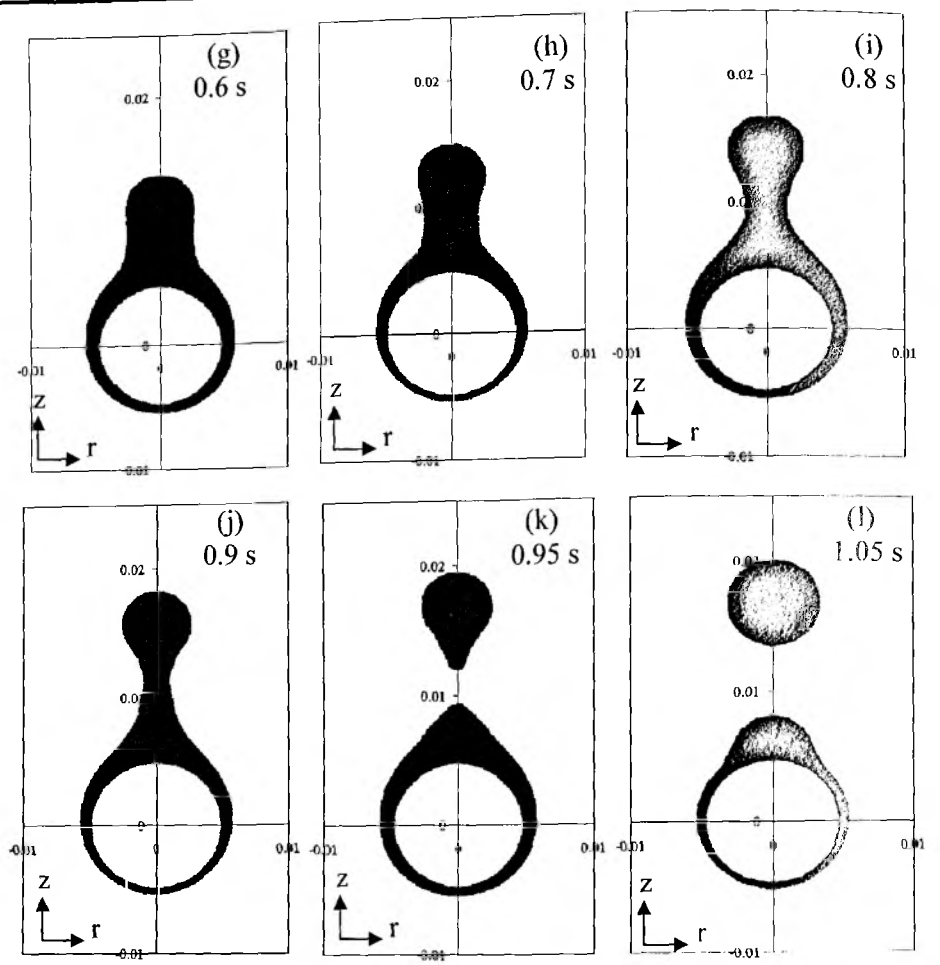

Fig. 5.13 Evolution of vapor film around a cylinder; sphere diameter 10 mm, sphere temperature 473 K

A comparison between the Fig. 5.11 and 5.13 readily brings out the difference in the process of the vapor growth and bubble release. It clearly shows that these phenomena are strongly influenced by the size of the sphere. It has been observed that bubble period is higher in case of bigger sphere (10 mm) compared to the small sphere (5 mm). Freud et al. (2009) described that the bubble release pattern from a heated sphere varies depending on its diameter. They described that in saturated water, a single columnar vapor release is observed up to a diameter of 8.83 mm. If the sphere diameter exceeds this limit a single vapor dome is observed during the bubble release.

In the present simulation the released vapor from 5 mm sphere closely resemblance a columnar shape. On the other hand a well formed vapor dome is observed in case of a sphere of 10 mm diameter. Therefore, the present simulation agrees with the experimental observation of Freued et al (2009). They also observed multiple vapor domes for spheres with diameter more than 13.6 mm. But using the present methodology multiple vapor domes have not been observed. Probably incorporation of instability mechanism of the long vapor liquid interface may produce such regimes of vapor release.

Tso et al. (1990) reported a combined analytical-experimental study to calculate the vapor film thickness in case of saturated film boiling over a sphere. Their analytical solution assumes zero thickness of the film at the bottom most position of the sphere. But this initial condition for forward marching the solution is away from reality. In the original situations a thin layer of vapor always covers the sphere even at its bottom most point.

Fig. 5.14 compares the thickness of the vapor film predicted by the present work with that predicted by Tso et al. (1990). The agreement between the two predictions is excellent except for the fact that the estimation by the present model is marginally higher compared to the analytical results at all the angular positions of the sphere. The possible cause of this mismatch may be the assumption of zero film thickness at the bottom of the sphere made by Tso et al. (1990). Similar trend is also observed for a sphere of 10 mm diameter.

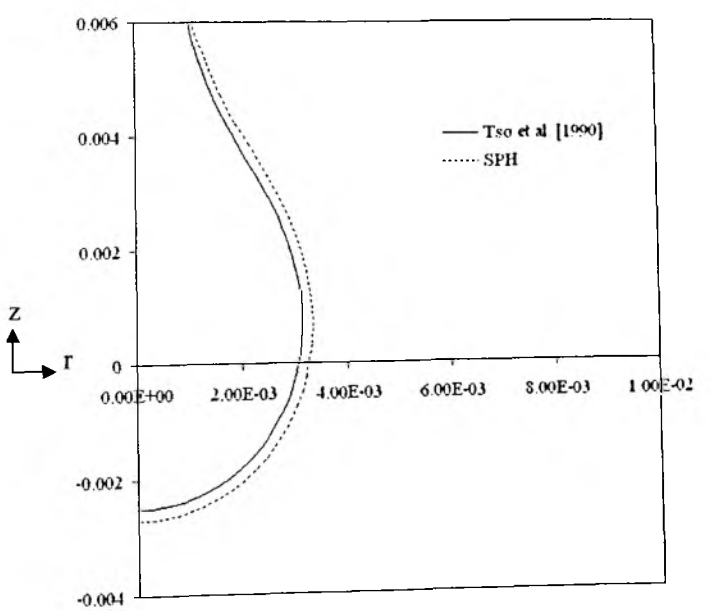

Fig. 5.14 Prediction of vapor film thickness along with the results of Tso et al. (1990) - sphere diameter 5 mm, sphere temperature 473 K

Both Fig. 5.11 and 5.13 depicts the formation of a bulging vapor mass at the top of the heated sphere, its gradual growth and finally its release and departure from the sphere. This phenomenon is periodic in nature. In other words, the vapor film thickness at the top of the sphere experiences a cycle of growth and decay. The average heat transfer coefficient or the Nusselt number should also follow a trend of periodic variation due to this.

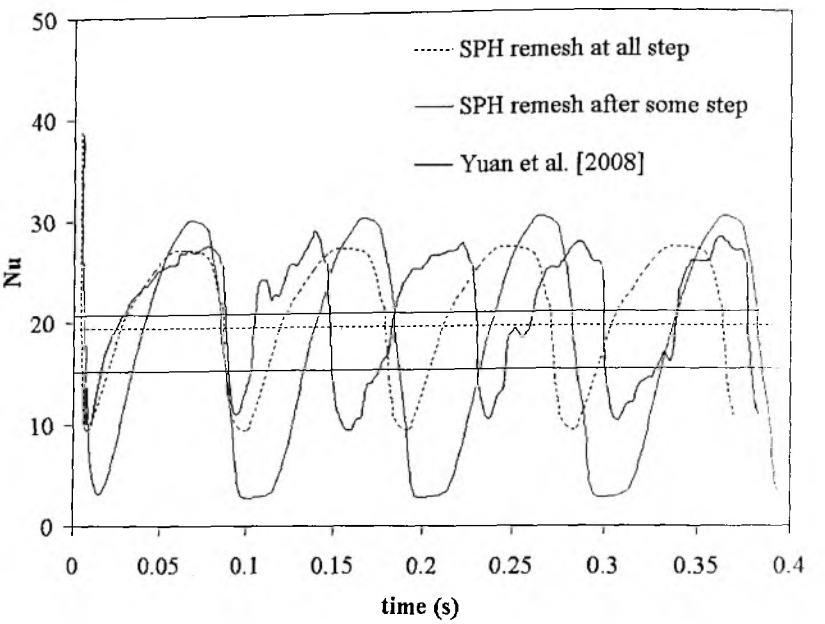

Fig. 5.15 Prediction of averaged Nussult number and comparison with Yuan et al. (2008)

Using the simulation, the variation of Nusselt number has been predicted for certain duration as depicted in Fig. 5.15. Nusselt number has been calculated by two different schemes of SPH. In the first scheme remeshing has been done after the interval of a few iterations. In the second scheme remeshing has been done after every iteration. The second method demands a substantially large computational effort due to remeshing at every time step. In Fig. 5.15 the numerical prediction of Yuan et al. (2008) has been shown. It has been observed that results from none of the scheme exactly match with the numerical results of Yuan et al. (2008). The amplitude of Nu predicted by the second scheme matches well with the amplitude predicted by Yuan et al. (2008) whereas the frequencies predicted by these two methods do not agree. However, the average Nusselt number calculated by the second scheme (remeshing after every iteration) is almost identical to that computed by Yuan et al. (2008).

5.3.3. Vapor bubble formation and departure from a hot horizontal surface

Nucleate boiling is different from film boiling in the sense where vaporization takes place from the entire surface of the later case, in the former vapor generation is there only from discrete nucleation sites. As a result the numerical simulation of nucleate boiling is complex compared to that of the film boiling. An effort has been made to simulate nucleate boiling under some idealized situation using the present algorithm.

Recently Lee et al. (2003) reported a study of nucleate boiling of R113 under saturated condition through a meticulously controlled experiment. They observed onset of nucleate boiling at a temperature of 61° C for a saturation temperature of the pool at 47.5° C. Bubbles at discrete locations were observed. For a single location they have recorded the entire cycle of bubble growth and departure photographically along with the parametric measurements. The same situation has been modeled in the present work with initial particle spacing 5×10^{-4} m. The spacing has been decided after a rigorous study of particle independence test. A single bubble nucleation has been considered (equation 5.5) and the solid surface surrounding the nucleation point was allowed to retain the prescribed degree of superheat without vapor formation. As the bubble grows in size additional numbers of pseudo particles are placed between the liquid and vapor particles to simulate the growing interface. Redistribution is made at every time step to get an accurate shape of the generated bubble.

Generated results are depicted in Fig. 5.16 along with the experimental observation of Lee et al. (2003) at different time levels. It has been observed that the vapor generation of vapor at the preferred location where pseudo particles are present, makes a small bubble nucleation site (Fig. 5.16a). The bubble grows in size as time progresses increasing the total number of pseudo particles aligned along the interface. Bubble size increases as is evident from Fig. 5.16b-e. After that, surface tension force dominates over the inertial force due to evaporation. As a result bubble growth is no longer dominant while its shape becomes smoother due to the effect of surface tension in this period. At 3.248 ms bubble necking starts (Fig. 5.16f-g). This prompts the bubble to get released from the site mouth subsequently (Fig. 5.16h). After the detachment of vapor bubble from the site mouth bubble motion is fully governed by buoyancy force and surface tension force. This makes the departing bubble to be spherical at far downstream (Fig. 5.16i). In Fig. 5.16 experimental observation of Lee et al. (2003) is also depicted side by side to make the comparison. It has been observed from Fig. 5.16 that present numerical simulation works efficiently and depicts a good match with experimental observations made by Lee et al. (2003).

Time	Present SPH simulation	Lee et al. [2003]
(a) 0.248 (ms)	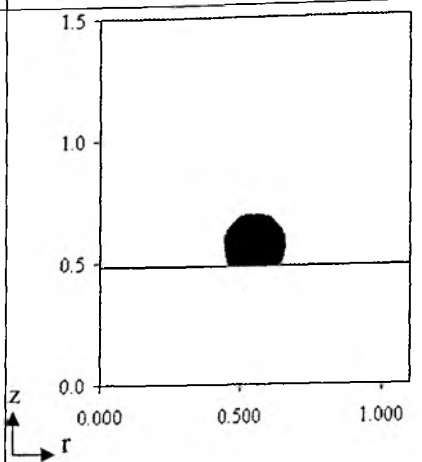	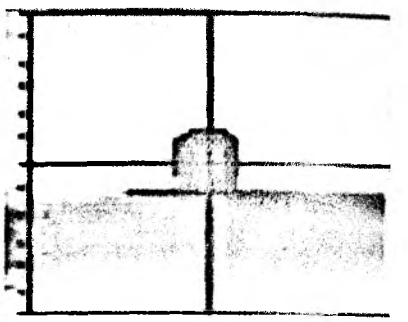
(b) 0.748 (ms)	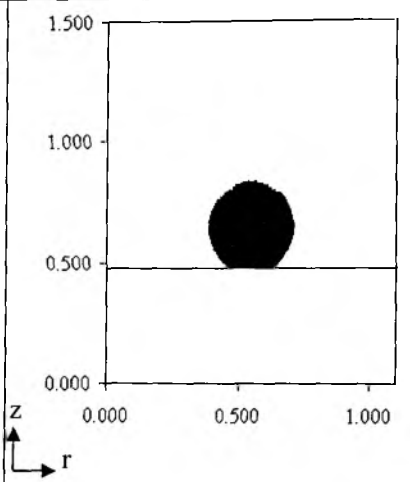	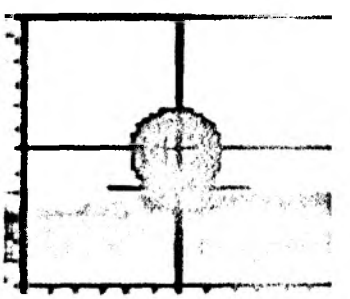
(c) 0.998 (ms)	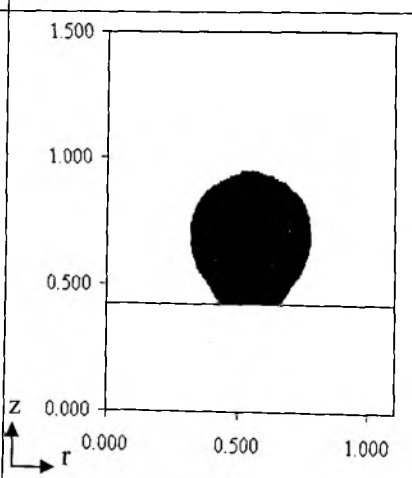	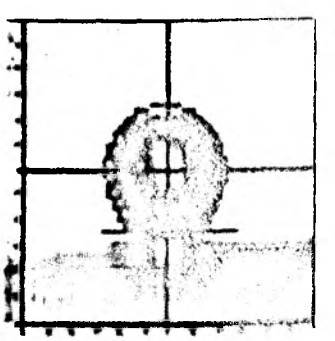

Time	Present SPH simulation	Lee et al. [2003]
(d) 1.498 (ms)	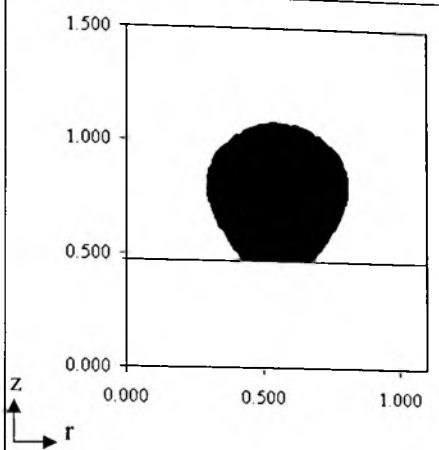	
(e) 2.998 (ms)	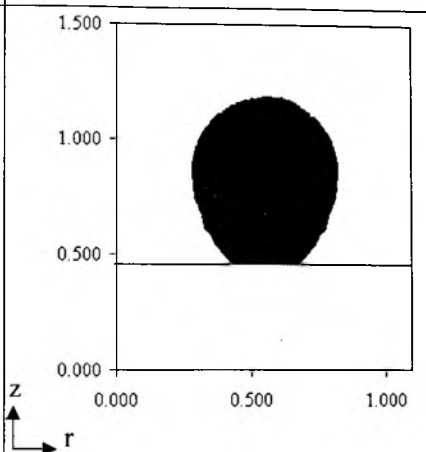	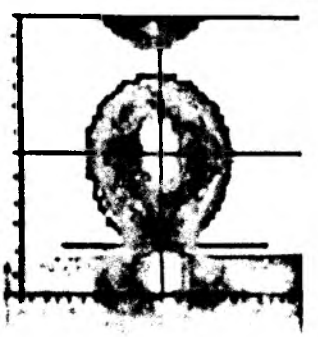
(f) 3.248 (ms)	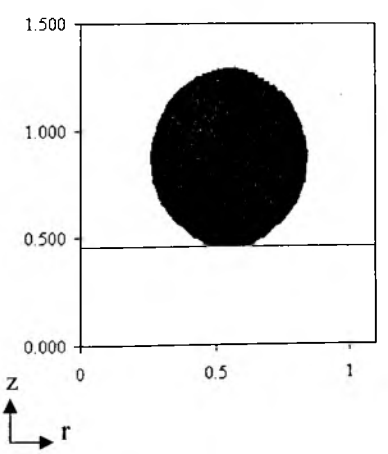	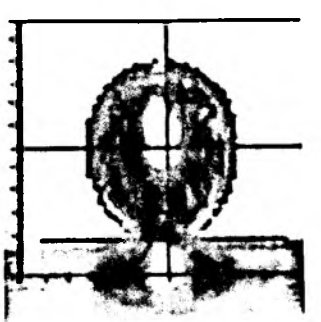

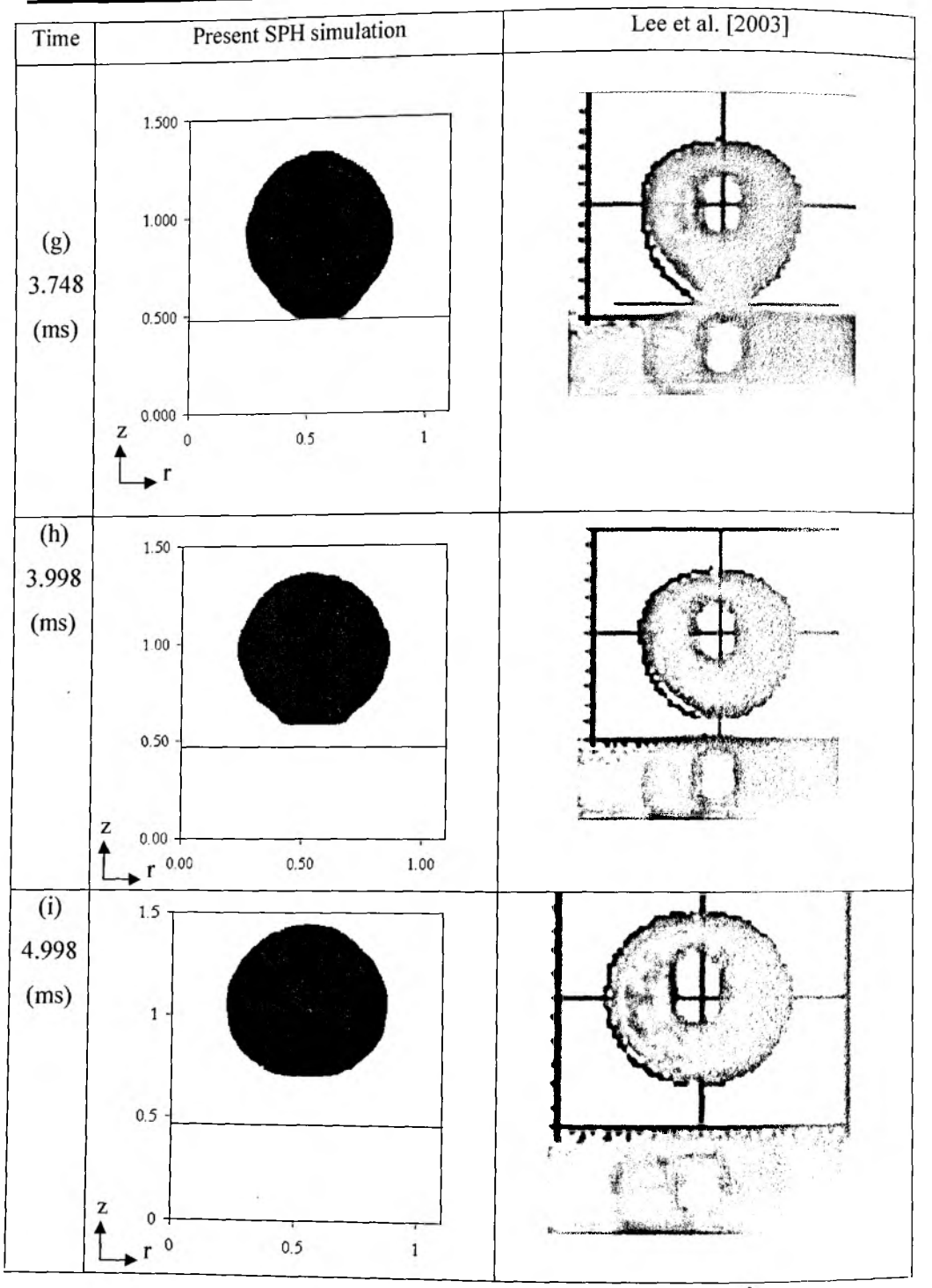

Fig. 5.16 Boiling and bubble release pattern over a horizontal hot surface

5.3.4. Summary

A new algorithm has been proposed based on particle based SPH methodology for gas-liquid phase change. Placement of zero mass pseudo particles along the interface and its mobility to construct new location of interface is described. Using the methodology film boiling around a hot solid sphere is simulated with and without considering the effect of gravity. Finally, efforts have also been made to model vapor bubble formation and its departure over a horizontal solid surface. In all the cases prediction of the simulated result is compared successfully with available literature.

CHAPTER 6 SUMMARY, CONCLUSIONS AND SCOPE OF FUTURE WORK

In this dissertation efforts have been made to develop computational algorithms for the simulation of diverse multiphase flow problems. Algorithms suitable for two broad categories of problems have been developed. The first one is based on averaged two fluid model coupled with the population balance technique. The model is suitable for dispersed two phase flow and has been employed for various aspects of gas-liquid bubbly flow. The second algorithm is developed using the Lagrangian SPH methodology. After establishing the capability of the basic model it has been modified further to incorporate the concept of diffuse interface. The coupled DI-SPH model has been used to analyze diverse problems of drop dynamics and drop manipulation over solid substrates. Additionally, another improvement has been incorporated in the SPH formulation to simulate phase change problems with a large density difference in the phases. A very brief summary of the work done and the salient conclusions are outlined below.

6.1. Simulation through two-fluid-population-balance technique

- Two fluid formulation is combined with the population balance equation to develop a numerical model for gas-liquid bubbly flow. Interfacial drag forces along with wall resistive forces are considered as the force terms used in the momentum equations. Coalescence of two similar or different sized bubbles and homogeneous and non homogeneous binary break up of a bubble has been considered in the population balance model.
- For the calculation of turbulent energy dissipation a simple formulation based on mixture velocity is used to capture the local hydrodynamic effect. This approach eliminates rigorous turbulence calculation but gives reasonably accurate prediction of void distribution and flow pattern transition for a wide range of flow velocities, inlet bubble diameter and tube diameter.
- In the model possible bubble size is divided into equal volume subgroups. This facilitates the redistribution of newly born bubbles due to coalescence without any numerical complicacy.
- A new transition criterion has been proposed for the transitions of bubbly flow into slug flow based on the CFD simulation. The transition criteria depend on i) the breakage and coalescence frequency ii) bubble volume count below and above the

bubble size introduced at the inlet and iii) local maximum bubble size. The prediction based on the present criteria exhibits excellent agreement with the experimental data (Taitel et al., 1980).

- At higher liquid velocity the simulation results show a suppression of coalescence and a dominance of the breakup process- a situation conducive for dispersed bubbly flow. Simulation results have been generated to obtain the maximum bubble size needed for a transition to disperse bubbly flow. A good agreement has been obtained with the model prediction and available literature (Brauner, 2001).
- The capability of the model for predicting different peaked structure of void distribution in bubbly flow has been demonstrated. A regime map has been constructed showing near wall peak, wall peak, two peak and core peak. This diagram makes a clear demonstration of the transformation to slug flow from a low voidage bubbly flow by gradual increase in the gas flow rate through the change of local concentration of the void distribution.
- The model has convincingly demonstrated that phase superficial velocities are not the sole parameters to dictate the transition of flow regimes. Inlet bubble size plays a crucial role in the axial development of bubbly flow and its transition to slug flow. When uniform sized bubbles are introduced at the inlet the regime boundary experiences an upward shift with a decrease in bubble size.
- When bubbles of different sizes are considered at the inlet plane the shift in regime boundary becomes complex. As a result, mismatch between different experimental observations is not unexpected. Present simulation also depicts that the tube diameter has an influence both on void distribution and on the transition boundary.
- Developed model is also employed for the prediction of transition from bubbly flow to the neighboring flow regimes during gas liquid two phase upflow through vertical annuli. The regime boundary for bubbly flow to slug flow in annuli compares well with the reported experimental observations (Kelessidis and Dukler, 1989) and theoretical predictions (Das et al., 1999). Outer wall peaking, both wall peaking, three peak and core peak can be separately identified for different ranges of phase velocities inside the annuli.
- Further, the influence of the annular gap over void distribution has been studied. For narrow annular passages wall forces dominate over the interfacial forces prompting

the bubbles to come close to the outer wall of the annular geometry. With an increase in the annular spacing interfacial forces become comparable to the wall forces. Finally, it has been observed that at a high liquid flow rate the bubble size decreases even with an increase in the air flow rate.

6.2. Basic SPH model- sharp interface

- Lagrangian particle based smoothed particle hydrodynamics (SPH) is used for the simulation of time and space variant interfaces. Surface tension is modeled by continuum surface force method. The developed model was validated against some well known analytical solution for free surface variation due to acceleration.
- Using the model efforts have been made to capture bubble formation and its detachment from an orifice mouth surrounded by a stagnant liquid pool. A good match in bubble frequency with the experimental observations (McCann and Prince, 1969) shows the validity of the present model. Volume of the bubble at the instant of departure is also compared satisfactorily with the available experimental observation (Davidson and Schuler, 1960).
- The dynamic bubble profile is also obtained by the present simulation matches excellently with the published analytical (Gerlach et al., 2005) and experimental results (Teresaka and Tsuge, 1990). The computed velocity contours help in explaining the hydrodynamics during the growth of a bubble.
- Developed model is also used to study the influence of surrounding liquid thermo physical properties like density, viscosity and surface tension on the process of bubbling through a submerged orifice. It has been seen that both the duration of bubble growth and bubble size at the time of departure increases with the decrease in liquid density.
- Similarly, bubbles become bigger in size and take more time to depart from the orifice mouth when it is surrounded by a more viscous liquid. Liquids having a low viscosity allow the bubble to form and detach easily at the orifice mouth. Surface tension of the liquid determines the bubble sticking time with the orifice and also governs its shape. At a low surface tension bubbles are smaller and they depart early from the orifice mouth.

- Necking process is examined carefully using the present methodology for a variation in density, surface tension and viscosity of the liquid over the orifice. In general, the duration of necking and the change of bubble volume in this duration decreases with density. Effects of surface tension and viscosity are just the reverse.

6.3. Incorporation of diffused interface in SPH formulation

- Diffused interface (DI) concept is incorporated in the basic formulation of particle based smoothed particle hydrodynamics to track the complex interfacial configurations of two phase flow. It may be noted that the incorporation of DI in particle based algorithm is of very recent origin. In that regard the present algorithm is unique as it models the DI using chemical potential in the paradigm of SPH.
- Superiority of the combined diffused interface based smoothed particle hydrodynamics model over the basic model is established by modelling two dynamic problems namely evolution and free rise of a bubble from a submerged orifice and drop deformation and break up in shear flow.
- Drop movement over an inclined surface is studied using the developed methodology to understand the contact line dynamics under the gravitational force. It has been shown that an internal circulation of the liquid drop causes its asymmetric shape and the subsequent downward movement. A regime map has also been developed for different fluids to describe the mobility of the drop of various sizes over an inclined surface.
- Next, efforts have been made to model the translation or spreading of a liquid drop over a horizontal surface having wettability gradient. Underlying physics behind the spreading and translation kinetics is described based on the internal fluid flow of the drop. By calculating the surface energy and gravitational energy it has been shown that drop tries to adopt a configuration to minimize its total energy for both spreading and translation. From the drop velocity curve over a gradient surface it has been described that drop spreading and its translation depend on the gradient strength and drop size. Finally, an effort has been made to separately identify the spreading and translating regime over the drop mobility curve for various gradient strength and drop size.

- Through experiments (Chaudhury and Whitesides; 1992) it has been observed that a drop can climb upward over an inclined plane due to favorable wettability gradient. The present numerical study also corroborates the same. Detailed study has also been made to understand the multi mode dynamics of a liquid drop over an inclined gradient surface. Analyzing the internal fluid flow downward and upward movement of the drop over the inclined plane is studied. Moreover a separate zone has been identified where the drop remains pinned to the surface without showing any mobility under the application of wettability gradient. Extensive simulations have been made to identify separate zones of drop motion over an inclined gradient surface of various strength and inclination.
- A new methodology for drop breakup into two or three different smaller droplets of equal or unequal sizes is proposed using developed methodology. Drop dynamics over the 'Y' shaped pattern having wettability gradient is studied numerically. It has been observed that the drop breaks up from the junction of the 'Y' path into two equal or unequal segments. The ratio of the volumes of the daughter drop depends over the ratio of the wettability gradient in the side arms and the angle made by the side arms with the root arm or symmetry line. Finally giving an example of a combination of different arrangements of the 'Y' paths having wettability gradient it has been shown that drop can be broken into multiple drops having unique volume fraction of the initial drop volume.
- It has been observed that the present algorithm can well track the merging of two drops efficiently. Accordingly, a new technique for fusion of drops without employing any active forces from outside is proposed.

6.4. Modeling of liquid-vapor phase change

- Till date, only a few attempts (Monaghan et al., 2005) have been made to apply SPH for phase change problems. Mostly (Monaghan et al., 2005) solid-liquid phase change, where density change is marginal, has been addressed. We have devised a new technique in SPH. It can take care of the large density change during phase transformation through temporary mass storage at the interface and subsequent redistribution of the particles in the computational domain.

- Pseudo particles with zero mass are used as temporary storage of mass before the redistribution of the particles in the two adjacent phases. Redistribution scheme is valid only for homogeneous growth of vapor film in every direction. But for the cases where growth of vapor film is not uniform remeshing is done after certain time step when any one of the pseudo particle becomes as heavy as the vapour particle.
- The model is initially validated for film boiling around a hot solid sphere in the absence of gravity. Instantaneous film thickness around the sphere derived from the numerical simulation matches well with the available literature (Bejan et al., 1997).
- The developed model is applied for the prediction of vapor film growth and its departure from the hot sphere under the normal gravity. Two different types of growth modes are observed depending on the sphere diameter. For a smaller diameter of the sphere, a single vapor dome is generated whereas with the increase in diameter, a columnar bubble is observed. These two types of vapor zone formation is earlier reported in literature (Freud et al., 2009) and present model can efficiently track the phenomena.
- Finally, the formation of vapor bubble over a horizontal hot surface has been simulated. Bubble nucleation, its growth, neck formation and detachment in the surrounding fluid is modeled using the present methodology. It has been observed that present numerical simulation works efficiently and depicts a good match with experimental observations (Lee et al., 2003) published in literature.

6.5. Scope of future work

During the investigation it was always felt that there are many aspects which warrant further studies. The major issues for future studies may be identified as:

(a) Developed model on two fluid-population balance equation involves several constitutive relationships for interfacial forces as well as breakage and coalescence phenomena. Rigorous models eliminating all the correlations are still possibility better predictions.

(b) Turbulence structure in two phase flow is not yet well understood. Only option is to use single phase turbulence models with modified coefficients without going into the details of the turbulent structures. To avoid this we have deduced turbulent dispersion coefficients based on local resultant velocities. A suitable model for two

phase turbulence should be incorporated in the basic two fluid population balance equation for the better simulation of the local phenomena.

(c) The present two fluid model is axisymmetric. Comparison with a meticulous 3D simulation can only ascertained how far the assumption of axisymmetric is valid.

(d) Reported experimental results indicate flow regime depends also on the design of the injector. CFD simulation for different designs of inlet geometry has not been done.

(e) In the present work only the transition of bubbly flow has been modeled through CFD. It would be interesting to investigate transition of other flow regimes using the suitable computational technique.

(f) In the DI-SPH formulation along with density other properties may be allowed to vary across the interface. Such a scheme is expected to improve the prediction.

(g) Diffused interface based smoothed particle hydrodynamics has been used for studying drop dynamics over surfaces having wettability gradient. Though the techniques for drop breakage and merging are established numerically, experimental verification is always a possibility of future research work.

(h) In the fifth chapter nucleate boiling heat transfer from a single site is modeled with several assumptions. Simulation of actual nucleate boiling considering the nucleation site density needs a substantial research effort.

(i) With an optimistic note it may be stated that the future research should aim at developing all the boiling regimes namely nucleate boiling, boiling crisis, transition boiling and film boiling through a generalized computational model.

Finally, it is reasonable to claim that the present developments of numerical models are encouraging towards the development of unique techniques for modelling of multiphase situations. Efforts have been made not only to use the developed model for simulating some of the well known phenomena but also to understand some fundamental physics. New techniques for drop manipulation are also proposed using the numerical simulation. These can find implementation in several micro fluidic operations.

REFERENCES

Alder, B. J. and Wainwright, T. (1958), Studies in molecular dynamics I. General method, Journal of Chemical Physics Vol. 31, pp. 459-466.

Anderson, T. B. and Jackson, R. (1967), A fluid mechanical description of fluidized beds: Equations of motion, Industrial and Engineering Chemistry Fundamentals Vol. 6, pp. 527–539.

Anderson, D. M. McFadden, G. B. and Wheeler, A. A. (1998), Diffuse-interface methods in fluid mechanics, Annual Review of Fluid Mechanics Vol. 30, pp. 139-165.

Antanovskii, L. K. (1995), A phase field model of capillarity, Phys. Fluids Vol. 7, pp. 747-753.

Badalassi, V. E. Ceniceros, H. D. and Banerjee, S. (2003), Computation of multiphase systems with phase field models, Journal of Computational Physics Vol. 19, pp. 371-397.

Bejan, A. Dan, N. Cacuci, D. G. and Schutz, W. (1997), On the thermodynamic efficiency of energy conversion during the expansion of a mixture of hot particles, steam and liquid water, Energy Vol. 22 (12), pp. 1119-1133.

Belytschko, T. Lu, Y. Y. and Gu, L. (1994), Element-free galerkin method, Int. J Numer. Methods Engrg. Vol. 37, pp. 229–256.

Bentley, B. J. and Leal, L. G. (1986), An experimental investigation of drop deformation and breakup in steady, two-dimensional linear flows, J. Fluid Mech. Vol. 167, pp. 241-283.

Benzing, R. A. and Mayers, J. E. (1955), Low-frequency bubble formation at horizontal circular orifices, Industrial Engineering Chemistry Vol. 47, pp. 2087-2090.

Bilicki, Z. and Kestin, J. (1987), Transition criteria for two phase flow patterns in vertical upward flow, International J. of Multiphase Flow Vol. 13, pp. 283-294.

Bosnjakovic, F. (1930), Verdampfung und fluessigheitsueberhitzung, Tech. Mech. Und Therm. Vol. 1, pp. 358-362.

Bourlioux, A. (1995), A coupled level-set volume-of-fluid algorithm for tracking material interfaces. in: Proceedings of Sixth International Symposium on Computational Fluid Dynamics, Lake Tahoe, CA, USA.

Brackbill, J.U. Kothe, D.B. and Zemach, C. (1992), A continuum method for modelling surface tension, J. Comput. Phys. Vol. 100, pp. 335–354.

Brauner, N. (2001), The prediction of dispersed flows boundaries in liquid-liquid and gas-liquid systems, International J. of Multiphase Flow Vol. 27, pp. 885-910.

Brochard, F. (1989), Motions of droplets on solid surfaces induced by chemical or thermal gradients, Langmuir Vol. 5, pp. 432-438.

Brown, R. A. Orr, F. M. and Scriven, L. E. (1980), Static drop on an inclined plate: Analysis by the finite element method, J. Colloid Interface Sci. Vol. 73, pp. 76-87.

Burns, A. D. Frank, T. Hamill, I. Shi, J. (2004), The Farve averaged drag model for turbulent

dispersion in eulerian multi-phase flows, in: Proc. of the Fifth International Conference on Multiphase flow, Yokohama, Japan.

Buwa, V. V. Gerlach, D. Durst, F. and Schlucker, E. (2007), Numerical simulation of bubble formation on submerged orifices: period-1 and period-2 bubbling regimes, Chemical Engineering Science Vol. 62, pp. 7119-7132.

Caetano, E.F. (1984), Two-phase flow in a vertical annulus, in: TUFFP Report, University of Tulsa, OK.

Caetano, E.F. Shoham, O. and Brill, J.P. (1992), Upward vertical two-phase flow through an annulus, Part I: single phase friction factor, Taylor bubble rise velocity and flow pattern prediction, in: Proceedings of 4th Int. Conf. on Multiphase Flow, Nice, France.

Cahn, J. W. and Hilliard, J. E. (1958), Free energy of a non uniform system. I. Interfacial free energy, J. of Chemical Physics Vol. 28, pp. 258-267.

Cahn, J. W. (1961), On spinodal decomposition, Acta Metall. Vol. 9, pp. 795-801.

Carrica, P. M. and Clausse, A. A. (1993), Mathematical description of the critical heat flux as nonlinear dynamic instability, in: Instabilities in Multiphase Flow (Gouesbet G., Berlemont A., ed), Plenum Press, New York.

Chaudhury, M. K. and Whitesides, G. M. (1992), How to make water run uphill, Science Vol. 256 (6), pp. 1539-1541.

Chen, S. and Doolen, G. D. (1998), Lattice boltzmann method for fluid flows, Annu. Rev. Fluid. Mech. Vol. 30, pp. 329-364.

Chen, J.K. Beraun, J.E. and Jih, C.J. (1999), An improvement for tensile instability in smoothed particle hydrodynamics, Comput. Mech. Vol. 23, pp. 279-287.

Chen, J. Z. Troian, S. M. Darhuber, A. A. and Wagner, S. (2005), Effect of contact angle hysterisis on thermocapillary droplet actuation, Journal of Applied Physics Vol. 97, pp. 014906-1-9.

Chesters, A. K. (1991), The modelling of coalescence processes in fluid- liquid dispersions: a review of current understanding, Trans. Inst. Chem. Engineering Vol. 69, pp. 259-270.

Chisholm, D. (1973), Pressure gradient due to friction during the flow of evaporating two phase mixtures in smooth tubes and channel, Int. J. Heat Mass transfer Vol. 16, pp. 347–358.

Cho, S. K. Moon, H. and Kim, C.J. (2003), Creating, transporting, cutting, and merging liquid droplets by electrowetting-based actuation for digital microfluidic circuits, Journal of Microelectromechanical Systems Vol. 12, pp. 70-80.

Coulaloglou, C. A. and Tavlarides, L. L. (1977), Description of interaction processes in agitated liquid–liquid dispersions, Chemical Engineering Science Vol. 32, pp. 1289–1297.

Daniel, S. Chaudhury, M. K. and Chen, J. C. (2001), Fast drop movements resulting from the phase change on a gradient surface, Science Vol. 291 (1), pp. 633-636.

Daniel, S. and Chaudhury, M. K. (2002), Rectified motion of liquid drops on gradient surfaces induced by vibration, Langmuir Vol. 18 (9), pp 3404–3407.

Das, G. Das, P. K. Purohit, N. K. and Mitra, A.K. (1999), Flow pattern transition during gas

liquid upflow through vertical concentric annuli - part I: experimental investigations, ASME J. of Fluids Engineering Vol. 121, pp. 895–901.

Das, A. K. And Das, P. K. (2009). Bubble evolution through submerged orifice using smoothed particle hydrodynamics: Basic formulation and model validation, Chemical Engineering Science Vol. 64 (10), pp. 2281-2290.

Das, A. K. and Das, P. K. (2009), Simulation of a sliding drop over an inclined surface using smoothed particle hydrodynamics, Langmuir Vol. 25 (19), pp. 11459-11466.

Datta, R. L. Napier, D. H. and Newitt, D. M. (1950), The properties and behaviour of gas bubbles formed at a circular orifice, Transactions of the Institution of Chemical Engineers Vol. 28, pp. 14-26.

Davidson, J. F. and Schuler, B. O. G. (1960), Bubble formation at an orifice in a viscous fluid, Transactions of the Institution of Chemical Engineers Vol. 38, pp. 144-154.

de Gennes, P. G. (1985), Wetting : statics and dynamics, Rev. Mod. Phys. Vol. 57, pp. 827-863.

Dettre, R. H. and Johnson, R. E. (1964), Contact angle hysteresis. II. Contact angle measurements on rough surfaces, in: Advances in chemistry series (Gould R. F., ed), Los Angeles, American Chemical Society, pp. 136-144.

Di Macro, P. Grassi, W. and Memoli, G. (2003), Experimental study on rising velocity of nitrogen bubbles in FC-72, International Journal of Thermal Sciences Vol. 42, pp. 435-443.

Ding, H. and Spelt, P. D. M. (2007), Inertial effects in droplet spreading: a comparison between diffuse-interface and level-set simulations, Journal of Fluid Mechanics Vol. 576, pp. 287-296.

Drew, D. A. and Passman, S. L. (1999), Theory of multicomponent fluids, Appl. Math. Sci. Vol. 135, New York, Springer.

Dukler, A. E. and Taitel, Y. (1977), Flow regime transitions for vertical upward gas liquid flow, in: Progress Report No. 2, NUREG-0163, Houston University, U.S.

Dukler, A. E. and Taitel Y. (1986), Flow pattern transitions in gas-liquid systems: measurement and modeling, in: Multiphase science and technology (Hewitt G. F., Delhaye J. M., and Zuber N., Ed), Hemisphere Publishing Corporation, Washington, USA, Vol. 2, pp. 1-94.

Durbin, P. A. (1988), Considerations on the moving contact-line singularity, with application to frictional drag on a slender drop, J. Fluid Mech. Vol. 197, pp. 157-169.

Dussan, V. E. B. and Chow, R. T. P. (1983), On the ability of drops or bubbles to stick to non-horizontal surfaces of solids, J. Fluid Mech. Vol. 137, pp. 1–29.

Ekambara, K. Sanders, R. S. Nandakumar, K. and Masliyah, J. H. (2008), CFD simulation of bubbly two-phase flow in horizontal pipes, Chemical Engineering Journal, Vol. 144, pp. 277-288.

Ekberg, N.P. Ghiaasiaan, S.M. Abdel-Khalik, S.I. Yoda, M. and Jeter, S.M. (1999), Gas–liquid two-phase flow in narrow horizontal annuli, Nuclear Engineering and Design Vol. 192, pp. 59–80.

Esmaeeli, A. and Tryggvason, G. (2004), A front tracking method for computations of boiling in complex geometries, Int. J. Multiphase Flow Vol. 30, pp. 1037–1050.

Esmaeeli, A. and Tryggvason, G. (2004), Computations of film boiling, part i-numerical method, International Journal of Heat and Mass Transfer Vol. 47, pp. 5451-5461.

Esmaeeli, A. and Tryggvason, G. (2004), Computations of film boiling, part ii: multi-mode film boiling, Int. J. Heat Mass Transfer Vol. 47, pp. 5463-5476.

Ford, M. L. and Nadim, A. (1994), Thermocapillary migration of an attached drop on a solid surface, Phys. Fluids Vol. 6, pp. 3183-3185.

Forster, H. K. and Zuber, N. (1955), Dynamics of vapor bubbles and boiling heat transfer, A.I.Ch.E. Journal Vol. 1 (4), pp. 531-535.

Francois, M. and Shyy, W. (2003), Computations of drop dynamics with the immersed boundary method part 2: drop impact and heat transfer, Numerical Heat Transfer Part B Vol. 44, pp. 119–143.

Frenkel, Y. I. (1948), On the behavior of liquid drops on a solid surface 1. The sliding of drops on an inclined surface, J. Exptl. Theoret. Phys. (USSR) Vol. 18, pp. 659-668.

Freud, R. Harari, R. and Sher, E. (2009), Collapsing criteria for vapor film around solid spheres as a fundamental stage leading to vapor explosion, Nuclear Engineering and Design Vol. 239 (4), pp. 722-727.

Fu, X. Y. (2001), Interfacial area measurement and transport modeling in air-water two-phase flow, Ph. D. Thesis, School of Nuclear Engineering, Purdue University, West Lafayette, IN, USA.

Fu, X. Y. and Ishii, M. (2002), Two-group interfacial area transport in vertical air-water flow I. Mechanistic model, Nuclear Engineering and Design Vol. 219, 143-168.

Gallardo, B. S. Gupta, V. K. Eagerton, F. D. Jong, L. I. Craig, V. S. Shah, R. R. and Abbott, N. L. (1999), Electrochemical principles for active control of liquids on submillimeter scales, Science Vol. 283, pp. 57-60.

Gao, L. and McCarthy, T. J. (2006), Contact angle hysteresis explained, Langmuir Vol. 22, pp. 6234-6237.

Gau, H. Herminghaus, S. Lentz, P. and Lipowsky, R. (1999), Liquid morphologies on structured surfaces: from microchannels to microchips, Science Vol. 283, pp. 46-49.

Gauss, C. F. (1830), Principia generalia theoriae figurae fluidorum in statu aequilibrii, Werke Vol. 5, pp. 29-77.

Gerbeau, J. F. and Vidrascu, M. (2003), A quasi-newton algorithm based on a reduced model for fluid-structure interaction problems in blood flows, Modélisation mathématique et analyse numérique Vol. 37 (4), pp. 631-647.

Gerlach, D. Biswas, G. Durst, F. and Kolobaric, V. (2005), Quasi-static bubble formation on submerged orifices, International Journal of Heat and Mass Transfer Vol. 48, pp. 425-438.

Gerlach, D. Alleborn, N. Buwa, V. and Durst, F. (2007), Numerical simulation of periodic bubble formation at a submerged orifice with constant gas flow rate, Chemical Engineering Science Vol. 62, pp. 2109-2125.

Gibbs, J. W. (1876), On the equilibrium of heterogeneous substances, Trans. Conn. Acad. Vol. 3, pp. 108-248.

Gingold, R. A. and Monaghan, J. J. (1977), Smoothed particle hydrodynamics: theory and application to non-spherical stars, Monthly Notices of the Royal Astronomical Society Vol. 181, pp. 375–389.

Gomez-Gesteira, M. Robert, A. and Dalrymple, F. (2004), Using a three-dimensional smoothed particle hydrodynamics method for wave impact on a tall structure, J Waterway Port Coastal Ocean Eng. Vol. 130 (2), pp. 145–154.

Gomez, H. Calo, V. M. Bazilevs, Y. Hughes, T. J. R. (2008), Isogeometric analysis of the Cahn-Hilliard phase-field model, Computer Methods in Applied Mechanics and Engineering, Vol. 197, 4333-4352.

Gould, T. L. (1974), Vertical two-phase steam water flow in geothermal wells, Journal of Petroleum Technology Vol. 26, pp. 833-842.

Govier, G. W. Aziz, K. (1972), The flow of complex mixtures in pipes, Van Nostrand-Reinhold, New York, U.S., pp. 388-389.

Greenspan, H. P. (1978), On the motion of a small viscous droplet that wets a surface, Journal of Fluid Mechanics Vol. 84, pp. 125-143.

Griffith, P. and Wallis, G. B. (1961), Two-phase slug flow, J. Heat Transfer Vol. 83, pp. 307-320.

Guido, S. Simeone, M. and Greco, F. (2003), Effects of matrix viscoelasticity on drop deformation in dilute polymer blends under slow shear flow, Polymer Vol. 44, pp. 467-471.

Gunstensen, A. K. and Rothman, D. H. (1993), Lattice boltzmann studies of immiscible two phase flow through porous media, Journal of Geophysical Research Vol. 98, pp. 6431-6441.

Hasan, A. R. and Kabir, C. S. (1992), Two-phase flow in vertical and inclined annuli, International J. of Multiphase Flow Vol. 18 (2), pp. 279-293.

Hibiki, T. and Ishii, M. (2000), Two-group interfacial area transport equations at bubbly-to-slug flow transition, Nuclear Engineering and Design Vol. 202, pp. 39–76.

Hibiki, T. and Ishii, M. (2000), One-group interfacial area transport of bubbly flows in vertical round tubes, Int. J. Heat Mass Transfer Vol. 43 (15) pp. 2711-2726.

Hibiki, T. and Ishii, M. (2002), Interfacial area concentration of bubbly flow systems, Chemical Engineering Science Vol. 57, pp. 3967–3977.

Hibiki, T. Situ, R. Mi, Y. and Ishii, M. (2003), Local flow measurements of vertical upward bubbly flow in an annulus, International Journal of Heat and Mass Transfer Vol. 46, pp. 1479-1496.

Higuera, F. J. and Succi, S. (1989), Simulating the flow around a circular cylinder with a lattice Boltzmann equation, Europhys. Lett. Vol. 8, pp. 517-521.

Higuera, F. (2005), Injection and coalescence of bubbles in a very viscous liquid, Journal of Fluid Mechanics Vol. 530, pp. 369-378.

Hinze, J. (1955), Turbulence, McGrawhill, New York, USA.

Hirt, C. W. Amsden, A. A. and Cook, J. L. (1974), An arbitrary lagrangian-eulerian computing method for all speeds, J. Comput. Phys. Vol. 14, pp. 227–253.

Hirt, C. W. and Nichols, B. D. (1981), Volume of fluid (VOF) method for the dynamics of free boundaries, Journal of Computational Physics Vol. 39, pp. 201-225.

Hitoshi, S. and Satoshi, Y. (2003), Force measurements for the movement of a water drop on a surface with a surface tension gradient, Langmuir Vol. 19(3), pp. 529-531.

Hong, H. S. Rana, S. Barrigan, L. Shi, A. Zhang, Y. and Zhou, F. (2009), Inhibition of Alzheimer's amyloid toxicity with a tricyclic pyrone molecule in vitro and in vivo, J Neurochem. Vol. 108, pp. 1097–1108.

Hoogerbrugge, P. J. and Koelman, J. M. V. A. (1992), Simulating microscopic hydrodynamic phenomena with dissipative particle dynamics, Europhys. Lett. Vol. 19, pp. 155-160.

Hsu, S. H. Lee, W. H. Yang, Y. M. Chang, C. H. and Maa, J. R. (2000), Bubble formation at an orifice in surfactant solutions under constant flow conditions, Industrial Engineering Chemical Research Vol. 39, pp. 1473-1479.

Hu, H. G. Zhang, C. (2007), A modified k–ε turbulence model for the simulation of two-phase flow and heat transfer in condensers, International Journal of Heat and Mass Transfer Vol. 50, pp. 1641-1648.

Huang, H. Meakin, P. and Liu, M. (2005), Computer simulation of twophase immiscible fluid motion in unsaturated complex fractures using a volume of fluid method, Water Res. Research Vol. 41, pp. 1-12.

Huang, J. J. Shu, C. and Chew, Y. T. (2008), Numerical investigation of transporting droplets by spatiotemporally controlling substrate wettability, Journal of Colloid and Interface Science Vol. 328, pp. 124-133.

Iliev, S. D. (1995), Iterative method for the shape of static drops, Computer Methods in Applied Mechanics and Engineering Vol. 126 (3–4), pp. 251-265.

Iliev, S. D. (1997), Static drops on an inclined plane: equilibrium modeling and numerical analysis, J. Colloid Interface Sci. Vol. 194, pp. 287-300.

Ioannou, K. Hu, B. Matar, O. K. Hewitt, G. F. and Angeli, P. (2004), Phase inversion in dispersed liquid–liquid pipe flows, in: Proc. Fifth International Conference on Multiphase Flow, Yokohama, Japan.

Ishii, M. (1975), Thermo-fluid dynamic theory of two-phase flow, Eyrolles, Paris.

Ishii, M. (1977), One-dimensional drift-flux model and constitutive equations for relative motion between phases in various two-phase flow regimes, Argonne National Lab Report, ANL 77-47.

Ishii, M. Mishima, K. (1981) Study of two-fluid model and interfacial area correlation for liquid entrainment in annular two-phase flow of low viscous fluid, Argonne National Laboratory, ANL 80-111.

Ishii, M. and Mishima, K. (1984), Two-fluid model and hydrodynamic constitutive relations, Nuclear Engineering and Design Vol. 82, pp. 107–126.

Ishii, M. and Kim, S. Development of one-group and twogroup interfacial area transport equation, Nucl Science and Eng, Vol. 146 (3), pp. 257-273.

Ishii, M. Paranjape, S. S. Kim, S. and Sun, X. (2004), Interfacial structures and interfacial area transport in downward twophase bubbly flow, International Journal of Multiphase Flow Vol. 30 (7-8), pp 779-801.

Ishii, M. and Hibiki, T. (2006), Thermo-fluid dynamics of two-phase flow, Springer, New York, USA.

Jacqmin, D. (1996), J. Calculation of two-phase navier–stokes flows using phase-field modeling, Comput. Phys. Vol. 155, pp. 96-127.

Jacqmin, D. (2000), Contact-line dynamics of a diffuse fluid interface, Journal of Fluid Mechanics Vol. 402, pp. 57-88.

Jamialahmadi, M. Zehtaban, M. R. Muller-Steinhagen, H. Sarrafi, A. and Smith, J. M. (2001), Study of bubble formation under constant flow conditions, Transaction of IChemE Vol. 79, pp. 523-532.

Joanny, J. F. de Gennes, P. G. (1984), A model for contact angle hysteresis, J. Chem. Phys. Vol. 81, pp. 552-562.

Juric, D. and Tryggvason, G. (1998), Computations of boiling flows, Int. J. Multiphase Flow Vol. 24, pp. 387–410.

Kelessidis, V.C. Dukler, A.E. (1989), Modeling flow pattern transitions for upward gas-liquid flow in vertical concentric and eccentric annuli, International J. of Multiphase Flow Vol. 15 (2), pp. 173-191.

Khurana, A. K. and Kumar, R. (1969), Studies in bubble formation- III., Chemical Engineering Science Vol. 24, pp. 1711-1723.

Kim, S. (1999), Interfacial Area Transport Equation and Measurement of Local Interfacial Characteristics, Ph.D. Thesis, School of Nuclear Engineering, Purdue University, West Lafayette, IN, USA.

Kim, H. Y. Lee, H. J. and Kang, B. H. (2002), Sliding of Liquid Drops Down an Inclined Solid Surface, J. Colloid Interface Sci. Vol. 247, pp. 372-380.

Kim, S. Ishii, M. Sun, X. and Beus, S. G. (2002), Interfacial area transport and evaluation of source terms for confined air-water bubbly flow, Nucl. Eng. Des. Vol. 219 (1), pp 61-65.

Kinjo T. and Matsumoto, M. (1998), Cavitation processes and negative pressure, Fluid Phase Equili. Vol. 144, pp. 343–350.

Kocamustafaogullari, G. and Ishii, M. (1995), Foundation of the interfacial area transport equation and its closure relation, Int. J. Heat and Mass Transfer Vol. 38 (3), pp. 481-493.

Kolev, K. I. (2002), Multiphase flow dynamics 2: Mechanical and thermal interactions, Springer Verlag, Berlin.

Korteweg, D. J. (1901), Sur la forme que prennent les équations du mouvements des fluides si l'on tient compte des forces capillaries causées par des variations de densité considérables mais continues et sur la théorie de la capillarité dans l'hypothése d'une variation continue de la densité, Arch. Néerl. Sci. Exactes Nat. Ser. II Vol. 6, pp. 1-24.

Koshizuka, S. Nobe, A. and Oka, Y. (1998), Numerical analysis of breaking waves using the moving particle semi implicit method, International Journal for Numerical Methods in Fluids Vol. 26, pp. 751-769.

Kostoglou, M. Karabelas, A. J. (1998), Theoretical analysis of steady state particle size distribution in limited breakage process, J. Phys. A: Math. Gen. Vol. 31, pp. 8905-8921.

Kostoglou, M., Karabelas, A. J. (2006), Towards a unified framework for the derivation of breakage functions based on the statistical theory of turbulence, Chemical Engineering Science Vol. 60, pp. 6584-6595.

Krasovitsky, B. Marmur, A. Drops down the hill: theoretical study of limiting contact angles and the hysteresis range on a tilted plate, Langmuir Vol. 21, pp. 3881-3885.

Krussenberg, A. K. Prasser, H. M. and Schaffrath, A. (1999), A new criterion for the bubble slug transition in vertical tubes, in: Proc. 9th International Topical Meeting on Nuclear Reactor Thermal Hydraulics (NURETH-9), San Francisco, CA, USA.

Kulkarni, A. A., and Joshi, J. B. (2005), Bubble formation and bubble rise velocity in gas liquid systems: A review, Industrial Engineering Chemical Research Vol. 44, pp. 5873-5931.

Kumar, R. and Kuloor, N. R. (1970), The formation of bubbles and drops, Advances in Chemical Engineering Vol. 8, pp. 255-368.

Lahey, R. T. and Drew, D. A. (1989), The three-dimensional time and volume averaged conservation equations of two-phase flow, Adv. Nuclear Sci. Technol. Vol. 20, pp. 1-69.

Lahey, R. T. and Drew, D. A. (2001), The analysis of two-phase flow and heat transfer using a multidimensional, four field, two-fluid model, Nucl. Eng. Design Vol. 204 (1–3), pp. 29–44.

Lahey, R. T., and Drew, D. A. (2002), On the Multidimensional Analysis of Two-Phase Flows, in: Transactions of Workshop on Scientific Issues in Multiphase Flow, University of Illinois, Urbana-Champaign, USA.

Laplace, P. S. (1805), Mécanique Céleste, Vol. 10, Courier, Paris.

Larkin, B. K. (1967), Numerical solution of the equation of capillarity, J. Colloid Interface Sci. Vol. 23, pp. 305-312.

Lastiwka, M. Basa, M. and Quinlan, N. (2005), Application of 3D smoothed particle hydrodynamics to a shock tube flow: effect and control of particle distribution, in: Proc. of the 17th AIAA Computational Fluid Dynamics Conference, Toronto, Canada.

Lawal, A. and Brown, R. A. (1982), The stability of an inclined pendent drop, J. Colloid Interface Sci. Vol. 89, pp. 332-345.

Lee, R. C. and Nyadhl, J. E. (1989), Numerical calculation of bubble growth in nucleate boiling from inception to departure, Journal of Heat Transfer Vol. 111, pp. 474-479.

Lee, H. C., Oh, B. D., Bae, S. W. and Kim, M. H., (2003), Single bubble growth in saturated pool boiling on a constant wall temperature surface, Int. J. Multiphase Flow Vol. 29, pp. 1857–1874.

Le Grand, N. Daerr, A. and Limat, L. (2005), Shape and motion of drops sliding down an inclined plane, J. Fluid Mech. Vol. 541, pp. 293-315.

Li, J. Renardy, Y. Y. and Renardy, M. (2000), Numerical simulation of breakup of a viscous drop in simple shear flow through a volume-of-fluid method, Physics of Fluids Vol. 12(2), pp. 269-282.

Liao, Q Wang, H. and Zhu, X. (2007), Experimental study on movement characteristics of droplet on the surface with gradient surface energy, Journal of Engineering Thermophysics Vol. 28 (1), pp. 134-136.

Liao, Q Shi, Y. Fan, Y. Zhu, X. and Wang, H. (2009), Numerical simulations of the equilibrium shape of liquid droplets on gradient surfaces, Applied Thermal Engineering Vol. 29, pp. 372-379.

Libersky, L. D. and Petscheck, A. G. (1991), Smoothed particle hydrodynamics with strength of materials, in: Proceedings of The Next Free Lagrange Conference Vol. 395, pp. 248-257.

Liow, J. L. (2000), Quasi-equilibrium bubble formation during top submerged gas injection, Chemical Engineering Science Vol. 55, pp. 4515-4524.

Liszka, T. and Orkisz, J. (1980), The finite difference method at arbitrary irregular grids and its application in applied mechanics, Comput. and Structures Vol. 11, pp. 83–95.

Liu, W. K. Jun, S. Li, S. Adee J. and Belytschko, T. (1995), Reproducing kernel particle methods for structural dynamics, Int. J. Numer. Methods Engrg. Vol. 38, pp. 1655–1679.

Liu, G. R. and Gu, Y. T. (2001), A point interpolation method for two dimensional solids, International Journal for Numerical Methods in Engineering Vol. 50, pp. 937-951.

Liu, M. B. Liu, G. R. Zong, Z. and Lam, K. Y. (2001), Numerical simulation of incompressible flows by SPH, in: International Conference on Scientific and Engineering Computer, Beijing, China.

Liu, M. B. Liu, G. R. and Lam, K. Y. (2002), Investigations into water mitigations using a meshless particle method, Shock Waves Vol. 12(3), pp. 181-195.

Liu, G. R. and Liu, M. B. (2003), Smoothed Particle Hydrodynamics – a mesh free particle method, World Scientific, Toh Tuck Link, Singapore.

Liu, C. and Shen, J. (2003), A phase field model for the mixture of two incompressible fluids and its approximation by a Fourier-spectral method, Physica D Vol. 179, pp. 211-228.

Liu, G. R. Zhang, G. R. Gu, Y. T. and Wang, Y. Y. (2005), A meshfree radial point interpolation method (RPIM) for three-dimensional solids, Computational Mechanics Vol. 36(6), pp. 421–430.

Liu, M. B. Xie, W. P. and Liu, G. R. (2005), Modeling incompressible flows using finite particle method, Applied Mathematical Modeling Vol. 29, pp. 1252-1270.

Liu, M. Meakin, and P. Huang, H. (2006), Computer simulation of two-phase immiscible fluid motion in unsaturated complex fractures using a volume of fluid method, Water Res. Research Vol. 43, pp. 1-12.

Liu, X. and Xiao, Y. P. (2006), Meshfree numerical solution of two-phase flow through porous media, in: Computational Methods, Springer, Netherlands, pp. 1547-1553.

Lo. S. (1996), Application of population balance to CFD modelling of bubbly flow via the MUSIG model, Technical Report AEAT-1096, AEA Technology plc.

Loewenberg, M. and Hinch, E. J. (1996), Numerical simulation of a concentrated emulsion in shear flow, J. Fluid Mech. Vol. 321, pp. 395-419.

Lovick, J. (2004), Horizontal oil-water flows in the dual continuous flow regime, Ph.D. Thesis, University College London, England.

Lucas, D. Krepper, E. and Prasser, H. M. (2005), Development of co-current air-water flow in a vertical pipe, International Journal of Multiphase Flow, Vol. 31, pp. 1304-1328.

Lucas, D. Krepper, E. and Prasser, H. M. (2007), Use of models for lift, wall and turbulent dispersion forces acting on bubbles for poly-disperse flows, Chemical Engineering Science, Vol. 62(15), pp. 4146-4157.

Lucy, L. B., (1977), A numerical approach to the testing of the fusion process, Astron. J. Vol. 88, pp. 1013–1024.

Luo, H. and Svendsen, H. F. (1996), Theoretical model for drop and bubble breakup in turbulent dispersions, A.I.Ch.E J. Vol. 42, pp. 1225–1233.

Martin, M. Montes, F. J. and Galan, M. A. (2006), Numerical calculation of shapes and detachment times of bubbles generated from a sieve plate, Chemical Engineering Science Vol. 61, pp. 363-369.

Martin, M. Montes, F. J. and Galan, M. A. (2006), On the influence of liquid physical properties on bubble volumes and generation times, Chemical Engineering Science Vol. 61, 5196-5203.

Matuszkiewicz, A. Flamand, J. C. and Boure, J. A. (1987), The bubble slug flow pattern transition and instabilities of void fraction waves, International J. of Multiphase Flow, Vol. 13, pp. 199-217.

Maxwell, J. C. (1876), Capillary action, Encyclopedia Britannica, 9th ed., New York.

McCann, D. J. and Prince, R. G. H. (1969), Bubble formation and weeping at a submerged orifice, Chemical Engineering Sci. Vol. 24, pp. 801-814.

Mercadier, Y. (1981), Contribution al'etude des propagations de perturbations de taux de vide dans les ecoulements diphasiques eau-air a' bulles, The'se, Universite' Scientifique et Me'dicale, Institut National Polytechnique de Grenoble, France.

Mikic, B. B. Rohsenow, W. M. and Griffith, P. (1970), On bubble growth rates, Int. J. Heat Mass Transfer Vol. 13, pp. 657–665.

Millies, M. Drew, D. A. and Lahey, R. T. (1996), A first order relaxation model for the prediction of the local interfacial area density in two-phase flows, Int. J. Multiphase Flow Vol. 22, pp. 1073- 1104.

Mishima, K. and Ishii, M. (1984), Flow regime transition criteria for upward two-phase flow in vertical tubes, Int. J. Heat Mass Transfer Vol. 27, pp. 723–737.

Monaghan, J. J. and Gingold, R. A. (1983), Shock Simulation by the Particle Method SPH, Journal of Computational Physics Vol. 52, pp. 374-389.

Monaghan, J. J. (1992), Smoothed particle hydrodynamics, Ann. Rev. Astron. Astrophys. Vol. 30, pp. 543–574.

Monaghan, J. J. (1994), Simulating free surface flows with SPH, J. Comput. Phys. Vol. 110, pp. 399–406.

Monaghan, J. J. Thompson, M. C. and Hourigan, K. (1994), Simulation of free surface flows with SPH, ASME FED Vol. 196, pp. 375–380.

Morel, C. Goreaud, N. and Delhaye, J. M. (1999), The local volumetric interfacial area transport equation: derivation and physical significance, Int. J. Multiphase Flow Vol. 25, pp. 1099-1128.

Morris, J. P. Fox, J. P. and Yi, Z. (1997), Modeling low Reynolds number incompressible flows using SPH, J. Comput. Phys. Vol. 136, pp. 214–226.

Morris, J. P. (2000), Simulating surface tension with smoothed particle hydrodynamics, Int. J. Numer. Meth. Fluids Vol. 33, pp. 333-353.

Monaghan, J. J. Huppert, H. E. and Worster, M. G. (2005), Solidification using smoothed particle hydrodynamics, Journal of Computational Physics Vol. 206, pp. 684–705

Moumen, N. Subramanian, R. S. and McLaughlin, J. B. (2006), Experiments on the motion of drops on a horizontal solid surface due to a wettability gradient, Langmuir Vol. 22 (6), pp. 2682-2690.

Nakoriakov, V. E. Kashinsky, O. N. Randin, V. V. and Timkin, L. S. (1996), Gas liquid bubbly flow in vertical pipes. Data Bank contribution, J. Fluid Engineering Vol. 118, pp. 377–382.

Naude, J. and Mendez, F. (2007), Numerical analysis of an asymptotic model for the collapse of a vapor bubble, Heat and Mass Transfer Vol. 43 (4), pp. 325–331.

Nayroles, B. Touzot, G. and Villon, P. (1992), Generalizing the finite element method: diffuse aproximation and diffuse elements, Comput. Mech. Vol. 10, pp. 307–318.

Noh, W. F. and Woodward, P. (1976), SLIC /simple line interface calculation, in: International Conference on Numerical Methods in Fluid Dynamics, Netherlands.

Oguz, H. and Prosperetti, A. (1993), Dynamics of bubble growth and detachment from a needle, Journal of Fluid Mechanics Vol. 257, pp. 111-145.

Ohnuki, A. and Akimoto, H. (2000), Experimental study on transition of flow pattern and phase distribution in upward air-water two-phase flow along a large vertical pipe, Int. J. Multiphase Flow Vol. 26 (3), pp. 367–386.

Osamasali, S. I. and Chang, J. S. (1988), Two-phase flow regime transition in a horizontal pipe and annulus flow under gas–liquid two-phase flow, ASME Fluid Engineering Division Vol. 72, pp. 63–69.

Osher, S. and Sethian, J. A. (1988), Fronts propagating with curvature-dependent speed: algorithms based on Hamilton-Jacobi formulations, Journal of Computational Physics Vol. 79, pp. 234–246.

Oshinowo, T. and Charles, M. E. (1974), Vertical two-phase flow. Part 1: Flow pattern correlations, Can. J. Chem. Eng. Vol. 52, pp. 25–35.

Panton, R. L. (1984), Incompressible flow, Wiley, New York.

Paranjape, S. S. Kim, S. Ishii, M. and Kelly, J. M. (2003), Interfacial structure in downward two-phase flow, ICONE 11, Shinjuku, Tokyo, Japan.

Peng, W. L., Yang, G, and Fan, L. S. (2002), Experimental studies of liquid weeping and bubbling phenomena at submerged orifices, Industrial Engineering and Chemical Research Vol. 41, pp. 1666-1677.

Picasso, M. Rappaz, J. Reist, A. Funk, M. and Blatter H. (2004), Numerical Simulation of the Motion of a Two Dimensional Glacier, Int. J. Num. Meth. Engrg. Vol. 60, pp. 995–1009.

Pierce, E. Carmona, F. J. and Amirfazli, A. (2008), Understanding of sliding and contact angle results in tilted plate experiments, Colloids and surf. A: Physicochem. Eng. Aspects Vol. 323, pp. 73-82.

Plesset, M. S. and Zwick, S. A. (1954), The growth of vapor bubbles in superheated liquids, J. Appl. Phys. Vol. 25, pp. 493-500.

Podgorski, T. Flesselles, J. M. and Limat, L. (2001), Corners, Cusps, and Pearls in Running Drops, Phys. Rev. Lett. Vol. 87, pp. 036102–036105.

Poisson, S. D. (1832), Nouvelle Théorie de l'action capillaire, Annalen der Physik Vol. 101(6), pp. 270-287.

Pollack, M. G. Shenderov, A. D. and Fair, R. B. (2002), Electrowetting-based actuation of droplets for integrated microfluidics, Lab Chip Vol. 2, pp. 96-101.

Prasser, H. M. Beyer, M. Carl, H. Gregor, S. Lucas, D. Pietruske, H. Schütz, P. and Weiss, F. P. (2007), Evolution of the structure of a gas-liquid two phase flow in a large vertical pipe, Nuclear Engineering and Design, Vol. 237, pp. 1848-1861.

Prosperetti, A. and Tryggvason, G. (2007), Computational methods for multiphase flow, Cambridge University Press, Cambridge, UK.

Quigley, C. J. Johnson, A. I. and Harris, B. L. (1955), Size and mass transfer studies of gas bubbles, Chemical Engineering Progress Symposium Series Vol. 16, pp. 31-45.

Radovicich, N. A. and Moissis, R. (1962), The transition from twophase bubble flow to slug flow, Technical Report No. 7-7633-22, MIT Report, U.S.

Rakhmatulin, K. A. (1956), Fundamentals of gas dynamics of interpenetrating motions of compressible media, Prikl. Mat. Mekh. Vol. 20(2), pp. 184-195.

Ramkrishna, D. (2000), Population balances- Theory and applications to particulate systems in engineering, Academic Press, San Diego.

Ramakrishnan, S. Kumar, R. and Kuloor, N. R. (1969), Studies in bubble formation – I bubble formation under constant flow conditions, Chemical Engineering Science Vol. 24, pp. 731-748.

Randles, P. W. and Libersky, L. D. (1996), Smoothed particle hydrodynamics: some recent improvements and applications, Computer Methods in Applied Mechanics and Engineering Vol. 139, pp. 375-408.

Rao, N. M. (2002), Investigations on buoyancy induced circulation loops, Ph.D. Thesis, IIT Kharagpur, India.

Lord Rayleigh, (1892), On the theory of surface forces-II Compressible fluids, Phil. Mag. Vol. 33, pp. 209-220.

Renardy, Y. Y. and Cristini, V. (2001), Effect of inertia on drop breakup under shear, Physics of Fluid Vol. 13(1), pp. 7-13.

Richter, H. J. (1983), Separated two-phase flow model: application to critical two phase flow, Int. J. Multiphase Flow, Vol. 9(5), pp. 511–530.

Robinson, A. J. and Judd, R. L. (2004), The dynamics of spherical bubble growth, International Journal of Heat and Mass Transfer Vol. 47, pp. 5101–5113.

Rotenberg, Y. Boruvka, L. and Neumann, A. W. (1984), The shape of non-axisymmetric drops on inclined planar surfaces, J. Colloid Interface Sci. Vol. 102, pp. 424-434.

Roura, P. and Fort, J. (2001), Equilibrium of drops on inclined hydrophilic surfaces, Physical Review E Vol. 64, pp. 0116011-0116015.

Ryley, D. J. and Ismail, M. S. B. (1978), The shape of sessile water drops on inclined plane surfaces, J. Colloid Interface Sci. Vol. 65, pp. 394-396.

Sadatomi, M. Sato, Y. and Saruwatari, S. (1982), Two-phase flow in vertical noncircular channels, International J. of Multiphase Flow Vol. 8 (6), pp. 641-655.

Satyanarayana, A. Kumar, R. and Kuloor, N. R. (1969), Studies in bubble formation - II, Bubble formation under constant pressure conditions, Chemical Engineering Science Vol. 24, pp. 749-761.

Scardovelli, R. and Zaleski, S. (1999), Direct numerical simulation of free-surface and interfacial flow, Annu. Rev. Fluid Mech. Vol. 31, pp. 567-603.

Schumann, U. (1975), Subgrid scale model for finite difference simulations of turbulent flows in plane channels and annuli, J. Comp. Phys. Vol. 18, pp. 376–404.

Scriven, L. E. (1959), On the dynamics of phase growth, Chem. Engng. Sci. Vol. 10, pp. 1–13.

Sekoguchi, K. Fukui, H. and Sato, Y. (1981), Flow characteristics and heat transfer in vertical bubble flow, in: Proc. Two-Phase Flow Dynamics, Japan-U.S. Seminar, Hemisphere, Washington D.C., USA, pp. 59-74.

Serizawa, A. Kataoka, I. and Michiyoshi, I. (1975), Turbulence structure of air-water bubbly flow-II local properties, International J. of Multiphase Flow, Vol. 2, pp. 235-246.

Serizawa, A. and Kataoka, I. (1987), Phase distribution in two-phase flow, in: Proc. ICHMT Int. Seminar on Transient Two-Phase Flow, Dubrovnik, Yugoslavia, pp. 24-30.

Serizawa, A. and Kataoka, I. (1988), Phase distribution in twophase flow, in: Transient Phenomena in Multiphase Flow, (Afgan N., Ed), Hemisphere, Washington, DC, U.S., pp. 179–224.

Shen, X. Mishima, K. and Nakamura, H. (2005), Two-phase phase distribution in a vertical large diameter pipe, Int. J. of Heat and Mass Transfer, Vol. 48(1), pp. 211-225.

Shikhmurzaev, Y. D. (1997), Moving contact lines in liquid/liquid/solid systems, J. Fluid Mech. Vol. 334, pp. 211-249.

Shiotsu, M. and Hama, K. (2000), Film boiling heat transfer from a vertical cylinder in forced flow of liquids under saturated and subcooled conditions at pressures, Nuclear Engineering and Design Vol. 200, pp. 23–38.

Son, G. and Dhir, V. K. (1997), Numerical simulation of saturated film boiling on a horizontal surface, J. Heat Transfer Vol. 119, pp. 525–533.

Son, G. and Dhir, V. K. (1998), Numerical simulation of film boiling near critical pressures with a level set method, J. Heat Transfer Vol. 120, pp. 183–192.

Son, G. Dhir, V. K. and Ramanujapu, N. (1999), Dynamics and heat transfer associated with a single bubble during nucleate boiling on a horizontal surface, Journal of Heat Transfer Vol.121, pp. 623-632.

Son, G. and Hur, N. (2002), A coupled level set and volume-of-fluid method for the buoyancy-driven motion of fluid particles, Numer. Heat Transfer B Vol. 42, pp. 523–542.

Song, Q. Luo, R. Yang, X. Y. and Wang, Z. (2001), Phase distributions for upward laminar dilute bubbly flows with non-uniform bubble sizes in vertical pipe, International J. of Multiphase Flow, Vol. 27, pp. 379-390.

Sorour, M. M. El-Beshbeeshy, M. S. (1986), Void fraction and pressure fluctuations of bubbly flow in a vertical annular channel, Experiments in Fluids Vol. 4, pp. 163-170.

Souto Iglesias, A. Delorme, L. Perez-Rojas, L. and Abril-Perez, S. (2006), Liquid moment amplitude assessment in sloshing type problems with smooth particle hydrodynamics, Ocean Engineering Vol. 33, 1462-1484.

Splet, P. D. M. (2005), A level set approach for simulations of flows with multiple moving contact lines with hysteresis, J. Compt. Phys. Vol. 207, pp. 389-404.

Sternling, V. C. (1965), Two-phase theory and engineering decision, Award Lecture, AIChE Annual Meeting.

Subramanian, R. S. Moumen, N. and McLaughlin, J. B. (2005), Motion of a drop on a solid surface due to a wettability gradient, Langmuir Vol. 21 (25), pp. 11844-11849.

Suda, H. (1993), Origin of friction derived from rupture dynamics, Langmuir Vol. 17, pp. 6045-6047.

Suda, H. and Yamada, S. (2003), Force measurements for the movement of a water drop on a surface with a surface tension gradient, Langmuir Vol. 19, pp. 529-531.

Sun, X. (2001), Two-group interfacial area transport equation for a confined test section, Ph.D. Thesis, School of Nuclear Engineering, Purdue University, West Lafayette, IN, USA.

Sun, B. Wang, R. Zhao, X. and Yan, D. (2002), The mechanism for the formation of slug flow in vertical gas-liquid two phase flow, Solid-state electronics Vol. 46, pp. 2323-2329.

Sun, X. Kuran, S. and Ishii, M. (2004), Cap bubbly-to-slug flow regime transition in a vertical annulus, Experiments in Fluids Vol. 37, pp. 458-464.

Sussman, M. and Fatemi, E. (1999), An efficient, interface preserving level set redistancing algorithm and its application to interfacial incompressible fluid flow, SIAM Journal on Scientific Computing Vol. 20, pp. 1165-1191.

Sussman, M. and Puckett, E. G. (2000), A coupled level set and volume-of-fluid method for computing 3D axisymmetric incompressible two-phase flows, J. Comput. Phys. Vol. 162, pp. 301–337.

Taitel, Y. Bornea, D. and Dukler, A. E. (1980), Modelling flow pattern transitions for steady upward gas-liquid flow in vertical tubes, AICHE Journal Vol. 26 (3), pp. 345-354.

Takeda, H. Miyama, S. M. and Sekiya, M. (1994), Numerical simulation of viscous flow by smoothed particle hydrodynamics, Prog. Theor. Phys. Vol. 92, pp. 939-960.

Tapia, J. J. and Lopez, P. G. (2009), Adaptive pseudospectral solution of a diffuse interface model, Journal of Computational and Applied Mathematics Vol. 224, pp. 101-117.

Tartakovsky, A. M. Ferris, K. F. and Meakin, P. (2009), Lagrangian particle model for multiphase flows, Computer Physics Communications Vol. 180, 1874-1881.

Taylor, G. I. (1932), The viscosity of a fluid containing small drops of another fluid, Proc. R. Soc. London Ser. A Vol. 138, pp. 41-48.

Terasaka, and K. Tsuge, H. (1990), Bubble formation at a single orifice in highly viscous liquids, Journal of Chemical Engineering of Japan Vol. 23, pp. 160-165.

Thiele, U. Velarde, M. G. Neuffer, K. Bestehorn, M. and Pomeau, Y. (2001), Sliding drops in the diffuse interface model coupled to hydrodynamics, Physical Review E Vol. 64, pp. 0616011-0616012.

Thiele, U. Neuffer, K. Bestehorn, M. Pomeau, Y. and Velarde, M. G. (2002), Sliding drops on an inclined plane, Colloids and surf. A: Physicochem. Eng. Aspects Vol. 206, pp. 87-104.

Tomar, G. Biswas, G. Sharma, A. and Agrawal, A. (2005), Numerical simulation of bubble growth in film boiling using CLSVOF method, Physics of Fluids Vol. 17 (1), pp. 112103-1-13.

Tomar, G. Biswas, G. Sharma, A. Welch, S. W. J. (2008), Multimode analysis of bubble growth in saturated film boiling, Phys. Fluids Vol. 20, pp. 092101-1-7.

Tomiyama, A. Nakahara, Y. Adachi, Y. and Hosokawa, S. (2003), Shapes and rising velocities of single bubbles rising through an inner subchannel, J. Nucl. Sci. Technology Vol. 40, pp. 136-142.

Tryggvason, G. and Unverdi, S. O. (1999), The shear breakup of an immiscible fluid interface, in: Fluid Dynamics at Interfaces, (Shyy W. and Narayanan R., Ed), Cambridge University Press, Cambridge, UK, pp. 142–155.

Tso, C. P. Low, H. G. and Ng, S. M. (1990), Pool film boiling from spheres to saturated and subcooled liquids of Freon-12 and Freon-22, International J. of Heat and Fluid Flow Vol. 11(2), pp. 154-159.

Tsouris, C. and Tavlarides, L. L. (1994), Breakage and coalescence models for drops in turbulent dispersions, A.I.Ch.E J. Vol. 40, pp. 395-406.

Tuckerman, M. E. Berne, B. J. and Martyna, G. J. (1991), Molecular dynamics algorithm for multiple time scales: Systems with long range forces, J. Chem. Phys. Vol. 94, pp. 6811-6815.

van der Sman, R. G. M. and van der Graaf, S. (2008), Emulsion droplet deformation and breakup with lattice boltzmann model, Computer Physics Communications Vol. 178, pp. 492-504.

Van der Waals, J. D. (1894), The thermodynamic theory of capillarity under the hypothesis of a continuous variation of density, Zeitschrift für Physikalische Chemie Vol. 13, pp. 657-725.

van der Waals, J. D. (1893), The thermodynamic theory of capillarity under the hypothesis of a continuous variation of density, Verhandel. Konink. Akad. Weten. Amsterdam, Vol. 1(8), pp. 21-65.

Vasilev, A. S. (1970), Laws governing the outflow of a jet of gas into a liquid, Theoretical Foundation of Chemical Engineering, Vol. 4(5), pp. 727-729.

Venneker, B. C. H. Derksen, J. J. and Van den Akker, H. E. A. (2002), Population balance modeling of aerated stirred vessels based on CFD, A.I.Ch.E. J. Vol. 48, pp. 673–685.

Vince, M. A. and Lahey, R. T. (1982), On the development of an objective flow regime indicator, International Journal of Multiphase Flow Vol. 8, pp. 93-124.

Walker, J. S. (1980), Deformation and break-up of a liquid-metal drop moving across a non-uniform magnetic field, In: Proceedings of the Tenth Southeastern Conference, Knoxville, Tenn.

Wallis, G. B. (1969), One dimensional two phase flow, McGraw Hill, New York.

Wang, T. Wang, J. and Jin, J. (2003), A novel theoretical breakup kernel function for bubbles/droplets in a turbulent flow, Chemical Engineering Science Vol. 58, pp. 4629–4637.

Wang, T. Wang, J. and Jin, J. (2006), A CFD-PBM coupled model for gas-liquid, AIChE Journal Vol. 52, pp. 125–140.

Welch, S. W. J. and Wilson, J. (2000), A volume of fluid based method for fluid flows with phase change, J. Comput. Phys. Vol. 160, pp. 662–682.

Wong, H. Rumschitzki, D. and Maldarelli, C. (1998), Theory and experiment on the low-Reynolds-number expansion and contraction of a bubble pinned at a submerged tube tip, Journal of Fluid Mechanics Vol. 356, pp. 93-124.

Wongwises, S. Pipathattakul, M. (2006), Flow pattern, pressure drop and void fraction of two-phase gas–liquid flow in an inclined narrow annular channel, Experimental Thermal and Fluid Science Vol. 30, pp. 345–354.

Wu, Q. Kim, S. Ishii, M. and Beus, S. G. (1998), One-group interfacial area transport in vertical bubbly flow, Int. J. Heat Mass Transfer Vol. 41 (8-9), pp. 1103-1112.

Xu, Z. Meakin, P. and Tartakovsky, A. M. (2009), Diffuse-interface modelling for smoothed particle hydrodynamics, Physical Review E Vol. 79, pp. 036702-1-7.

Yan, Y. Y. and Ji, C. Y. (2008), Molecular dynamics simulation of behaviours of non-polar droplets merging and interactions with hydrophobic surfaces, Journal of Bionic Engineering Vol. 5(4), pp. 271-281.

Yeo, L. Y. Craster, R. V. and Matar, O. K. (2007), Drop manipulation and surgery using electric fields, J. Colloid Interface Sci. Vol. 306, pp. 368-378.

Young, T. (1805), On the cohesion of fluids, Philosophical Transaction Vol. 95, pp. 65-87.

Yuan, M. H. Yang, Y. H. Li, T. S. and Hu, Z. H. (2008), Numerical simulation of film boiling on a sphere with a volume of fluid interface tracking method, International J. of Heat and mass transfer Vol. 51, pp. 1646-1657.

Zeng, L. Z. Klausner, J.F. Bernhard, D.M. and Mei, R. (1993), A unified model for the prediction of bubble detachment diameters in boiling systems – II. Flow boiling, Int. J. Heat Mass Transfer

Vol. 36, pp. 2271–2279.

Zeng, L. Z. Klausner, J. F. and Mei, R. (1993), A unified model for the prediction of bubble detachment diameters in boiling systems-I. Pool boiling, International J. of Heat and Mass Transfer Vol. 36, pp. 2261-2270.

Zhang, D. Z. and Prosperetti, A. (1993), Ensemble averaged euler equations and added mass for linearized flows, gas-liquid flows, FED American Society of Mechanical Engineers, New York, Vol. 165.

Zhang, D. Z., and Prosperetti, A. (1994), Averaged equation for inviscid dispersed two-phase flow, Journal of Fluid Mechanics Vol. 267, pp. 185-219.

Zhang, L. and Shoji, M. (2001), Aperiodic bubble formation from a submerged orifice, Chemical Engineering Science Vol. 56, pp. 5371-5381.

Zuber, N. (1964), On the dispersed two phase flow in the laminar flow regime, Chemical Engineering Science Vol. 19, pp. 897-917.

Zuber, N. and Findlay, J. A. (1965), Average volumetric concentration in two phase flow systems, Journal of Heat Transfer Vol. 87, pp. 453-468.

Zun, I. (1990), The mechanism of bubble non-homogeneous distribution in two-phase shear flow, Nuclear Engineering and Design, Vol. 118, pp. 155-162.

List of Publications

1. Das A.K., Das P.K., "Bubble evolution through submerged orifice using smoothed particle hydrodynamics: Basic formulation and model validation" **Chemical Engineering Science Vol. 64, Issue 10, 2009, pp. 2281-2290.**

2. Das A.K., Das P.K., Thome J.R., "Transition of bubbly flow in vertical tubes: new criteria through CFD simulation" **ASME Journal of Fluids Engineering Vol. 131, Issue 9, 2009, pp. 091303-1-12.**

3. Das A.K., Das P.K., Thome J.R., "Transition of bubbly flow in vertical tubes: effect of bubble size and tube diameter" **ASME Journal of Fluids Engineering Vol. 131, Issue 9, 2009, pp. 091304-1-6.**

4. Das A.K., Das P.K., "Bubble evolution through submerged orifice using smoothed particle hydrodynamics: effect of different thermo physical properties" **Industrial Engineering and Chemistry Research Vol. 48, Issue 18, 2009, pp. 8726-8735.**

5. Das A.K., Das P.K., "Simulation of a sliding drop over an inclined surface using smoothed particle hydrodynamics" **Langmuir Vol. 25, Issue 19, 2009, pp. 11459-11466.**

6. Das A.K., Das P.K., "Modelling bubbly flow and its transitions in vertical annuli using population balance technique" **International Journal of Heat and Fluid Flow Vol. 31, 2010, pp. 101-114.**

7. Das A.K., Das P.K., "Equilibrium shape and contact angle of sessile drops of different volumes- computation by SPH and its further improvement by DI" **Chemical Engineering Science (Accepted).**

About the Author

The author was born on April 18, 1980. He had graduated in Mechanical Engineering from Jadavpur University, Kolkata, India in 2003. After his graduation he had joined Department of Mechanical Engineering, Indian Institute of Technology Kharagpur as a junior project assistant and obtained M.S. in Engineering in 2006. He has received the Best Thesis Award from Indian national Academy of Engineers for his Master's work. Since then he is continuing his doctoral study in the Department of Mechanical Engineering, IIT Kharagpur. He is the recipient of prestigious National Doctoral Fellowship from All India Council for Technical Education during his doctoral study. He had visited École Polytechnique Fédérale de Lausanne, Switzerland for a period of 3 months to conduct part of his doctoral research under a project funded by Indo-Swiss Bilateral Research Initiative.

He has one patent and published 14 papers (till date) in reputed International Journals from his Master's and Doctoral work. He has participated in several international and national workshops, seminars and presented papers in conference related to his studies.